1992

Coal cleaning in an inclined open-channel fluidized bed

Timothy J. Schmitt
Lehigh University

AUTHOR:

Schmitt, Timothy J.

TITLE:

Coal Cleaning in an Inclined Open-Chennel Fluidized Bed

DATE: May 31, 1992

COAL CLEANING IN AN INCLINED OPEN-CHANNEL FLUIDIZED BED

by

Timothy J. Schmitt

A Thesis

Presented to the Graduate Committee

of Lehigh University

in Candidacy for the Degree of

Master of Science

in

Mechanical Engineering

Lehigh University

1992

Certificate of Approval

This thesis is accepted and approved in partial fulfillment of the requirements for the degree of Master of Science.

Date: April 27, 1992

Thesis Advisor: _____
(Edward K. Levy)

Chairman of Department: _____
(Robert P. Wei)

ACKNOWLEDGEMENTS

I wish to express immeasurable appreciation to my family for their love, understanding, and ever-present support during my entire formal education. Thank you, Tracy, for your love, patience, and help during the production of this manuscript; your assistance made it possible. I appreciate the technical support and advice of Dr. Edward K. Levy and the very helpful staff of the Energy Research Center.

The work in this thesis was made possible as part of a project on coal cleaning funded by Atlantic Electric, Empire State Electric Energy Research Corporation, the Electric Power Research Institute, Minnesota Power Company, the Pennsylvania Energy Development Authority, and Pennsylvania Power and Light. I am thankful and greatly appreciative of their support.

I wish to thank the "team" with whom the continuous cleaning experiments were performed. Thank you, Rich Curran, Mark D'agostini, Mark Harris, Dr. Levy, Ridvan Sahan, John Salmento, Dick Trethaway, and Tunc Ulge. Also, thank you, Dr. Bulent Kozanoglu, for helping me grasp the fundamentals of the project.

An additional appreciation is extended to Rich Curran for tolerating me as a roommate for two years and to Mark Harris for working with me an entire summer, which was crucial to the completion of this work.

This is a blank page

Table of Contents

List of Tables

List of Figures

Abstract

Pollutant emissions and ash from coal combustion can be reduced by removing the sulfur and ash prior to combustion. Fluidizing coal and magnetite at proper conditions allows the denser coal fractions, which have higher sulfur and ash concentrations and lower energy content per mass, to segregate from the lighter fractions. Large scale utilization requires implementation of a continuous system, such as an inclined open-channel fluidized bed. In an inclined fluidized bed coal cleaning system developed at Lehigh University, the mixture of coal and magnetite flow down the open channel, the dense particles segregate and the product and refuse streams are mechanically separated near the end of the bed.

To understand the flow behavior of solids in the aerated open channel, measurements were made of bed heights and float residence times in a bed of flowing magnetite at combinations of five solids mass flow rates, seven superficial gas velocities, and three angles of inclination. Level bed height profiles and bed heights corresponding to efficient coal cleaning were attained, but low mass feed rates were required to achieve adequate processing time.

In cleaning trials performed on several coals the sulfur reduction and ash reduction achieved in the continuous cleaning trials were compared to cleaning results obtained in a batch bed under similar operating conditions.

The Upper Freeport coal cleaning trial produced a 44.0% sulfur reduction and 42.3% ash reduction at 83% energy recovery, which matched the batch bed results at a processing time of 13.1 seconds.

The Rushton coal continuous cleaning trials produced 49.8% sulfur reduction and 60.1% ash reduction at 73% energy recovery, and 31.7% sulfur reduction and 44.6% ash reduction at 89% energy recovery. The Rushton coal cleaning results did not match the batch bed cleaning performance, and this is believed to have been caused by a storage of the dense fractions of the Rushton coal onto the surface of the distributor.

1 Introduction

Fluidization occurs when gas flows upward through a bed of particulate solids at a sufficient velocity to create enough drag force to suspend the particles within the bed. At slightly higher velocities, voids, also known as bubbles, form, and drive a segregation phenomenon. Due to this segregation, denser and larger particles tend to settle toward the bottom of the bed, and smaller and lighter particles tend to move to the top of the bed. This fluidized bed segregation process can be used to remove impurities from coal by separating the dense from the light fractions.

Coal typically has a wide density range due to the manner in which the minerals are distributed within the coal. The two major impurities are sulfur and ash. Sulfur appears primarily in two forms, organic or pyritic. The organic form of sulfur is chemically attached to the carbon atoms of the coal. Because the pyritic sulfur is physically, not chemically, attached to the coal, it can be liberated by crushing the coal, but it then must be separated from the coal. Ash is defined simply as any substance remaining after the combustion of the carbon in the coal. In general, the sulfur and ash are much more heavily concentrated in the denser fractions of the coal, and the lighter fractions have the larger heating values.

By fluidizing the coal at the appropriate conditions, the light and the dense fractions will segregate. After segregation, the bed material must be physically separated, generating coal product and refuse streams. To aid in the cleaning process,

the layer of coal to be cleaned is initially placed on top of a layer of magnetite powder; the two materials then mix and form an inhomogeneous binary mixture. The magnetite aids the segregation process, acting as a buffer in the physical separation.

The above described cleaning procedure has proven to work well in a batch bed operation [11,15], but a continuous system would be necessary for any commercial application. In the present study, an inclined open-channel fluidized bed was used to continuously clean coal (see Figure 1.1). In this system, the magnetite was fed from a hopper and flowed a short distance down the channel to where the coal was fed from another hopper. The coal and the magnetite mixture flowed from that point towards the discharge end of the bed. As the mixture bubbled, segregation proceeded, until the particles reached the separator gap, which was a narrow slit, 2 to 3 mm wide, in the base of the channel perpendicular to the flow direction. This slit allowed a portion of the binary mixture to separate from the bed, discharging downward as refuse. The remaining clean coal product and magnetite were removed from the end of the bed. The coal and magnetite mixtures were later magnetically separated.

The objective of the study was to determine the flow characteristics of a co-flowing mixture of coal and magnetite. In addition, experiments were performed to measure the efficiencies of ash and sulfur removal using the inclined fluidized bed.

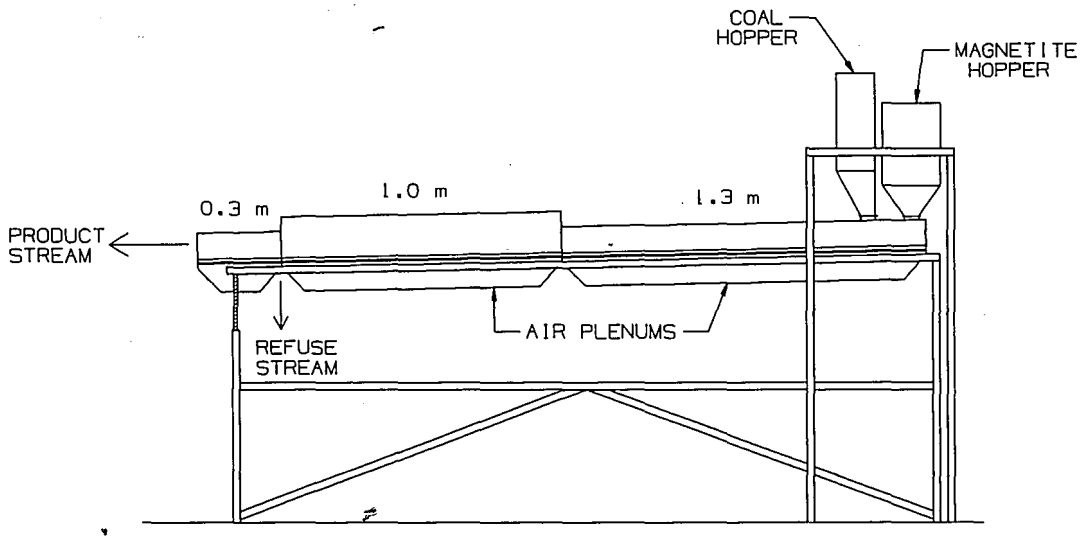

Figure 1.1
Inclined open-channel fluidized bed

2 Fluidization and coal cleaning

2.1 The concept of fluidization

Fluidization occurs when a gas or liquid is passed at high enough velocities through a bed of solid particles. This operation transforms the bed into a liquid-like state through suspension of the solids in the gas or liquid. At low gas velocities, the fluid percolates through the existing voids and the pressure drop across the bed varies nearly proportionally to the gas velocity. As the gas velocity increases, particles move apart and vibrate locally, and the bed begins to expand. As the gas velocity further increases, the particles become supported vertically by the upward flowing gas. The frictional forces of the fluid contacting the particle counterbalance the weight of the particles. This state is known as "minimum" or "incipient" fluidization, and the pressure drop is approximately equal to the weight of the fluid and particles in the bed. A bubbling bed exists when the gas velocity exceeds that of minimum fluidization, u_{mf}, which causes instabilities in the bed structure. This instability manifests itself in the form of bubbles which convey the excess gas above that which is required for fluidization. The larger the superficial gas velocity (volume gas flow per bed cross-sectional area), u_o, the more vigorous the agitation and movement of the particles. As the bubbles rise, they coalesce and grow. A slug forms when the bubble diameter is of the same order of magnitude as the bed diameter or other cross-sectional length dimension; therefore, slugging is more prominent in taller, narrow beds. As if pushed by a piston, the slug of bed

material rises, allowing material to rain down gently until the slug is dispersed. The repeated sequence of slug creation and dispersion demonstrates an extreme oscillatory bed behavior.

In dense-phase fluidization, the bed surface is clearly discernable; however, as the gas velocity exceeds the terminal velocity of the particles, the bed enters the lean phase. The lean phase is akin to dilute gas-solid pneumatic transport and is not applicable to coal cleaning. In contrast, the dense phase is of great interest, and it exhibits strong similarities to a liquid. A bubbling dense-phase fluidized bed does look like a boiling liquid, but it has significant gas-solid inhomogeneity. Some of the similarities between dense-phase fluidized solids and liquids follow in Table 2.1 [16].

Table 2.1
Similarities between fluidized solids and liquids

1.	Large light objects will float.
2.	When a container is tipped, the surface remains horizontal.
3.	Two connected beds will equalize the levels.
4.	Pressure difference across a bed is approximately the static head.
5.	Fluidized solids exhibit liquid-like flow in pipes and open channels. The fluidized material will flow from vessel to vessel, and will "gush" from holes.

Bubbles in a dense-phase gas fluidized bed cause mixing and segregation of the particles, two competing mechanisms based on size and density differences within the bed material. This combination of phenomena can be controlled by properly adjusting

the bed heights and gas velocities, in order to create the best bubbling for optimal segregation. This density segregation is directly applicable to coal cleaning.

2.2 Parameters and features of fluidization

The density, size, and size distribution of fluidized particles greatly affect the behavior of the fluidized bed. The minimum fluidization velocity decreases and the bed expansion ratio increases with reduction in particle size and density.

2.2.1 *Particle size, shape, and density*

Particles of many different descriptions can be fluidized. However, it immediately becomes evident that the behavior is very dependent on the particle density, shape, size, and size distribution. To describe the shape of the particle, a term referred to as the sphericity, ϕ, is defined as the surface area of a sphere divided by the surface area of a particle, where the sphere and particle each have the same volume.

$$\phi = \left(\frac{surface\ area\ sphere}{surface\ area\ particle} \right)_{same\ volume} \qquad (2.1)$$

The sizes of a group of particles are generally distributed and an average effective diameter must be determined. For intermediate-sized particles, a weight fraction, x_i, of a narrow size range may most easily be determined by a sieve analysis. By appropriately combining narrow size range weight fractions, an overall average

diameter is found. At first glance, one would probably consider using the following weighted average for the average diameter:

$$\bar{d}_{wm} = \sum_{i=1}^{n} x_i d_i \tag{2.2}$$

However, it has been found that fines disproportionately affect the fluidized behavior. To account for the greater effect of the fines, a weighted volume surface mean diameter is more appropriate:

$$\bar{d}_{vsm} = \left(\sum_{i=1}^{n} \frac{x_i}{d_i} \right)^{-1} \tag{2.3}$$

The density of particles has several definitions, each useful in different situations. The density types are:

- Particle density, ρ_p
- Packed bed bulk density, ρ_b
- Fluidized density, ρ_{fl}

The particle density is the mass of the particle per the volume of the particle only:

$$\rho_p = \frac{m_p}{v_p} \tag{2.4}$$

The bulk density is the mass of the solid particles and the mass of the fluid per the combined volume of the solid and fluid, generally with no fluid flow:

$$\rho_b = \frac{m_p + m_f}{v_p + v_f} \tag{2.5}$$

The fluidized density is the bulk density of the fluidized solids. These definitions are interrelated by the void fraction, ϵ, of the bulk material. The void fraction is the volume of the interstitial voids per the total volume of the bed. So, rigorously speaking, the bulk density is:

$$\rho_b = \rho_p(1-\epsilon) + \rho_f\epsilon \tag{2.6a}$$

When using dry bulk solids and gas, Equation 2.6a can be simplified to:

$$\rho_b = \rho_p(1-\epsilon) \tag{2.6b}$$

For most gas fluidized solids systems, the bed expands as it approaches minimum fluidization, so:

$$\rho_{fl} \simeq \rho_p(1-\epsilon_{mf}) \tag{2.7}$$

The parameter ϵ_{mf} is the void fraction under minimum fluidizing conditions.

Geldart [11] classified powders according to their size and density [16]. In summary, powders are divided into four categories, types A, B, C and D. (See Figure 2.1). Geldart Type A particles have small particle sizes and/or densities, very significant bed expansion between u_{mf} and u_{mb}, and slugging may be a problem at certain gas

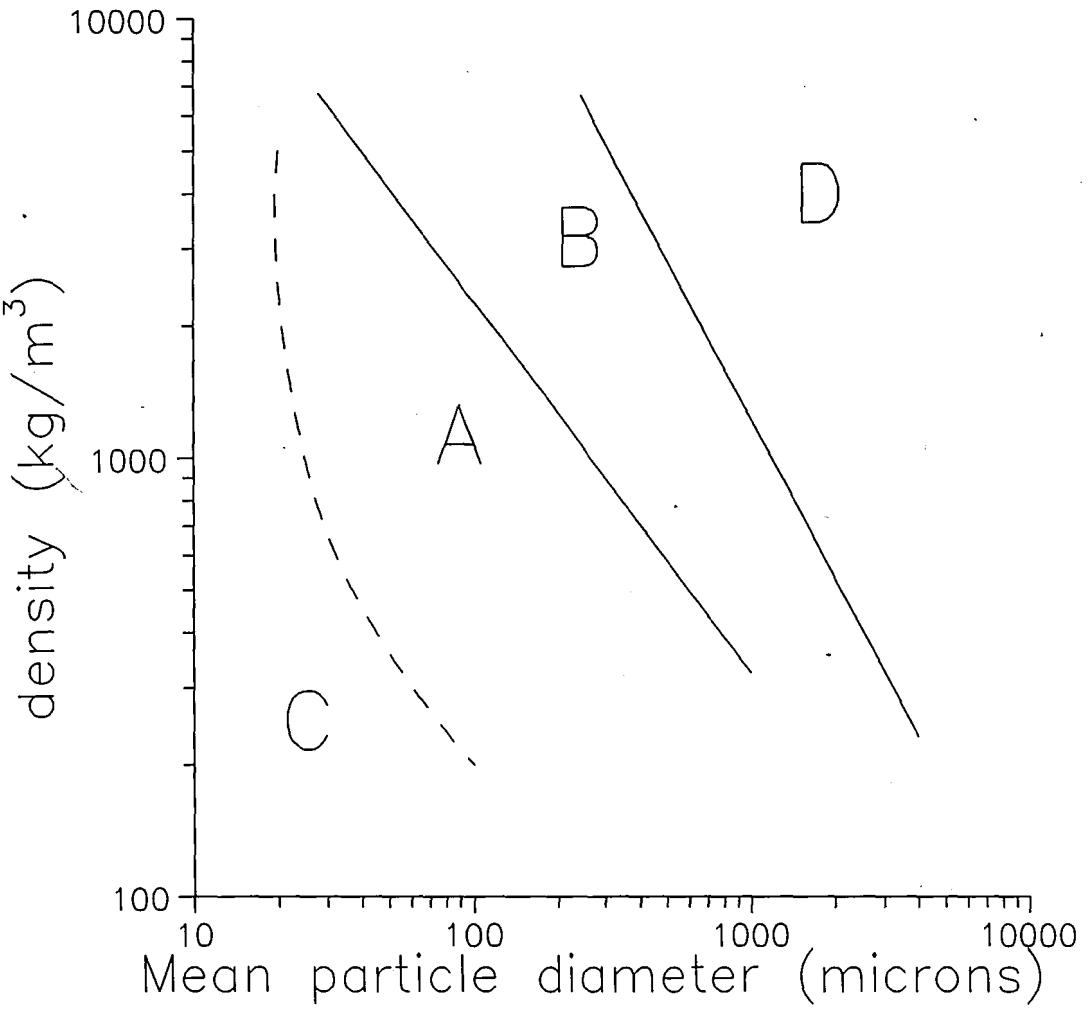

Figure 2.1
Geldart particle classification [11]

velocities. Geldart Type B particles are larger and denser, and bubbling begins very close to u_{mf}. Type B particles behave very predictably. Type C particles are very small and have large cohesive forces and electrostatic effects. These solids may fluidize as plugs or, in larger beds, channels form, eliminating fluidization and bubbling. Geldart Type D particles are the largest and densest, and behave very similarly to Type B particles. Type D particles also have rapid bubble growth to large bubbles, and tend to "spout" under certain gas inlet conditions.

2.2.2 *Minimum fluidization velocity*

The onset of fluidization occurs when the drag force exerted by the upward flowing gas on the bed particles equals the weight of the particles. In terms of pressure drop:

$$\frac{\Delta P_b}{L_{mf}} = W = (1-\epsilon_{mf})(\rho_s - \rho_g)g \qquad (2.8)$$

A plot of the pressure drop, ΔP_b, across the bed versus superficial gas velocity, u_o, is very useful to determine fluidization quality. Prior to fluidization, a fixed bed has a pressure drop nearly proportional to superficial gas velocity, u_o, and, after fluidization occurs, the pressure drop is almost constant with respect to u_o. A typical plot of ΔP_b versus u_o is shown in Figure 2.2. For uniformly sized particles with increasing u_o, a maximum pressure drop occurs at u_{mf} , which takes place since the particles in the fixed bed "unlock" after fluidization. Aside from this maximum pressure drop, the point of minimum fluidization is quite distinct. For fixed beds of particles of wide size

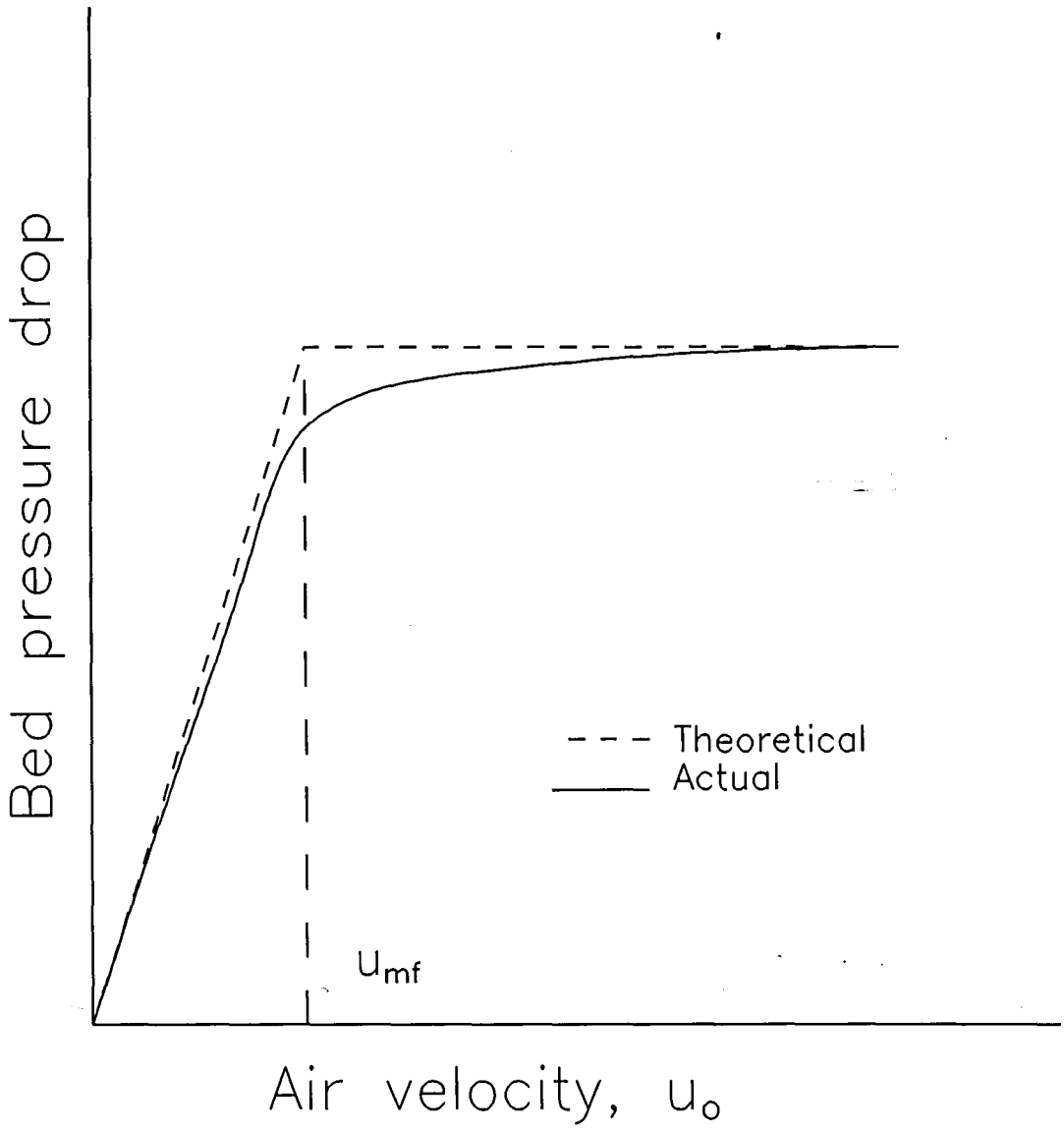

Figure 2.2
Typical pressure drop behavior across an aerated bed-of solids

distribution, the point of minimum fluidization is much less distinct, since the finer particles begin to fluidize within the voids of the larger particles prior to the entire bed being fluidized. In mixed particle systems, u_{mf} is defined by convention as the intersection of the fixed bed ΔP versus u_o line with the W/A_t line [16].

2.2.3 *Bubbling fluidized beds*

The two phase theory postulates that the excess gas flows through the bed as gas voids when the superficial gas velocity is greater than the minimum fluidization velocity. If the void dimension is smaller than that of the bed, these voids are referred to as bubbles. Bubbles rising through the bed drag solid particles in the bubble wake, creating an upward flowing wake phase. The remaining dense phase, the emulsion phase, flows downward to conserve mass in the circulating bed. The circulation and bubbling acts as the pump driving the competing mixing and segregation phenomena (see Figure 2.3).

2.2.3.1 *Physical model*

The bubbles in a fluidized bed originate at the distributor at an initial bubble diameter, D_{BO}. As the bubbles rise, the bubble diameter, D_B, grows as smaller bubbles coalesce, and the pressure around the bubble decreases at positions closer to the free surface. The bubbles eventually reach a maximum attainable bubble diameter, D_{BM}. The bubble rise velocity depends on the amount of excess gas and the size of the bubble. Various correlations have been used to describe this behavior (see Table 2.2).

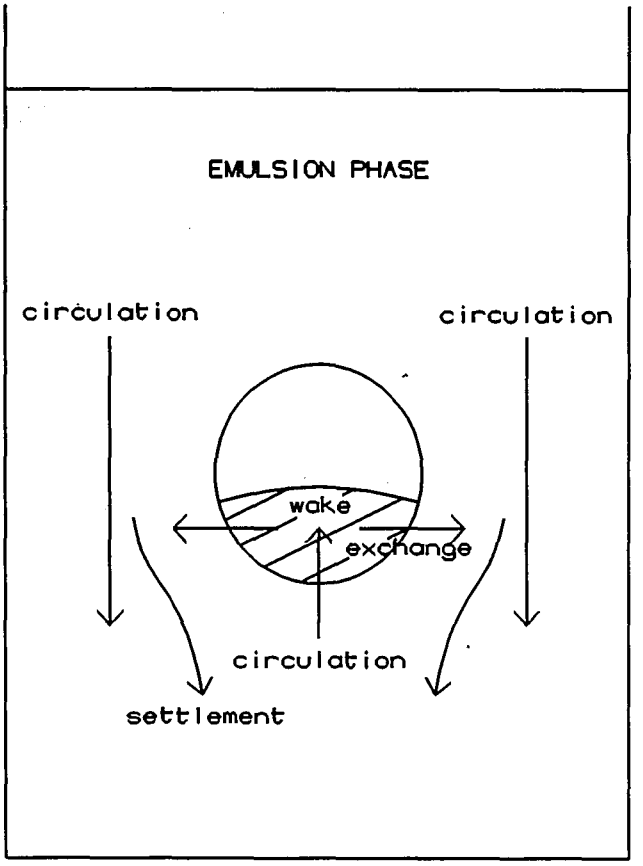

Figure 2.3
Schematic of competitive phenomena of mixing and segregation [15]

Table 2.2
Bubble size correlations [15]

Mori and Wen	$D_B = D_{BM} + (D_{BO} - D_{BM}) \exp(-0.3\ h/D_t)$ $D_{BO} = 0.00376\ (u_o - u_{mf})^2$ $D_{BM} = 0.652\ [A(u_o - u_{mf})]^{0.4}$
Rowe	$D_B = (u_o - u_{mf})^{0.5}\ (h + h_o)^{0.75}\ g^{-0.25}$ $h_o = 1.61\ [A_o^{1.6}\ g^{0.2}\ (u_o - u_{mf})^{-0.4}]^{0.33}$
Darton	$D_B = 0.54\ (u_o - u_{mf})^{0.4}\ (h + 4.0\ A_o^{0.5})^{0.8}\ g^{-0.2}$
Kato and Wen	$D_B = 0.327\ [A_o(u_o - u_{mf})]^{0.4} + 1.4\ d_p\ \rho_p\ (u_o/u_{mf})\ h$
Chiba	$D_B/D'_{BO} = [(2^{1.166} - 1.0)\ (h - h_{BO}) / D'_{BO} + 1.0]^{0.285}$ $D'_{BO} = 0.327\ [A_o\ (u_o - u_{mf}) / k_B]^{0.4}$ $h_{BO} = h'_o + 0.856\ D'_{BO};\ h'_o = 0.5$ cm

2.2.3.2 *Minimum bubbling velocity*

The minimum bubbling velocity, u_{mb}, is the velocity at which bubbles are first observed. For larger particles, the bed will begin to bubble very close to u_{mf}. Finer particles (i.e., Geldart Type A) tend to collect more air within the bed and continue to expand beyond u_{mf}. The parameter u_{mb} can be determined visually or by finding the point above u_{mf} at which the bed height remains almost constant.

2.2.3.3 *Bubbling mechanisms*

A bubbling fluidized bed has three mechanisms associated with the bubbles:

- Circulation
- Exchange
- Settlement

which generate the mixing-segregation competition. The aforementioned upward wake phase and downward emulsion phase cause the circulation in the bed. Exchange is the movement of particles between the wake region and the emulsion region; exchange proceeds at a wake exchange rate. Settlement occurs when density or size variations exist in the bed, which cause the denser and larger particles to tend to settle to the bottom of the bed.

2.3 Coal cleaning

Coal is a major source of available energy. However, coal has some very serious inherent drawbacks for use as a source for power generation. Coal, unlike crude petroleum sources, varies greatly in energy content and ash and mineral composition. For this reason, it is much easier to purify petroleum sources consistently than it is to purify coal. On the other hand, with the current ratio of use of energy, it is necessary to utilize the large natural stores of coal. Unfortunately, either the coal or the resultant combustion products of coal must be processed to protect the environment and ecosystems from excess SO_2 concentration.

One method of reducing the amount of post-combustion processing required is either to use a "cleaner" coal or to clean a "dirtier" coal prior to combustion. Coal cleaning is the act by which one optimally removes sulfur and ash from the coal, while retaining as much energy in the coal as possible. Several commercial methods exist currently to clean coal; however, most are wet processes or they do not adequately clean

fine particles (less than 300 μm). Wet processes cause problems with coal freezing in storage hoppers in winter and the wet coal must be de-watered prior to transportation or combustion. It is advantageous to clean finer size coal since the process of crushing to below a certain size generates many fines. It is therefore desirable to develop a dry process with the ability to handle small particle sizes to remove sulfur and ash from coal.

The general procedure for cleaning coal is to segregate the coal according to density variations in the coal. Depending on the type of coal, a wide range of densities may exist, due to significant amounts of heavy minerals. The lighter density fractions of the coal have highly concentrated amounts of energy; the denser fractions have larger quantities of sulfur and ash. Several common coal cleaning techniques are summarized below [23]:

1. Jigging - A hydraulic process used primarily for coarser coal. Clean, low-density particles concentrate on the top of a pulsating upward-flowing coal-water suspension.

2. Wet concentrating tables - Hydraulically sluicing the coal over rifles in a cross-wise flow cleans finer particles.

3. Hydrocyclones - Coal water slurries enter a cyclone, and the denser particles tend to flow to the edge of the conical section.

4. Heavy media cleaning - Coal is slurried in water with an easily mechanically separated heavy medium (i.e., magnetite). This slurry is fed into a cyclone for separation of the coal density fractions.

5. Froth flotation - Cleaning is based on differences in surface properties. The purer particles cling to surface bubbles or froth on a suspension. These bubbles are collected, thus obtaining a clean fraction of coal.

2.3.1 *Bubbling and cleaning: Mixing versus segregation*

By bubbling a fluidized bed containing coal, the coal's different density fractions will eventually reach an equilibrium distribution based on rates of mixing and segregation determined by the fluidization conditions. Magnetite and coal are combined in a fluidized bed and bubbled at appropriate conditions for a period of time. During the bubbling process, the three bubbling mechanisms, circulation, exchange, and settlement, segregate the dense fractions of coal from the lighter fractions using the magnetite as a buffer to aid in particle motion and, eventually, in controlled separation. When the bubbling process is completed, the bed must be mechanically separated at one or more positions along the bed height. The top portions of the bed have much higher energy content and lower sulfur and ash concentrations when compared to the bottom portions (see Figures 2.4 and 2.5). The process performance is very sensitive to the fluidizing conditions. To predict performance and to determine regions of efficient operation, Kozanoglu [15] developed a computer model based on the bubbling mechanisms and the changes in density fraction concentrations. Use of this code has determined the important fluidization parameters and identified the conditions required for high efficiency cleaning.

2.3.2 *Coal cleaning parameters*

Finding regions of proper operation requires defining parameters to describe the independent conditions in the bed. These independent conditions control the bubbling behavior, which, in turn, determines the density segregation and cleaning performance.

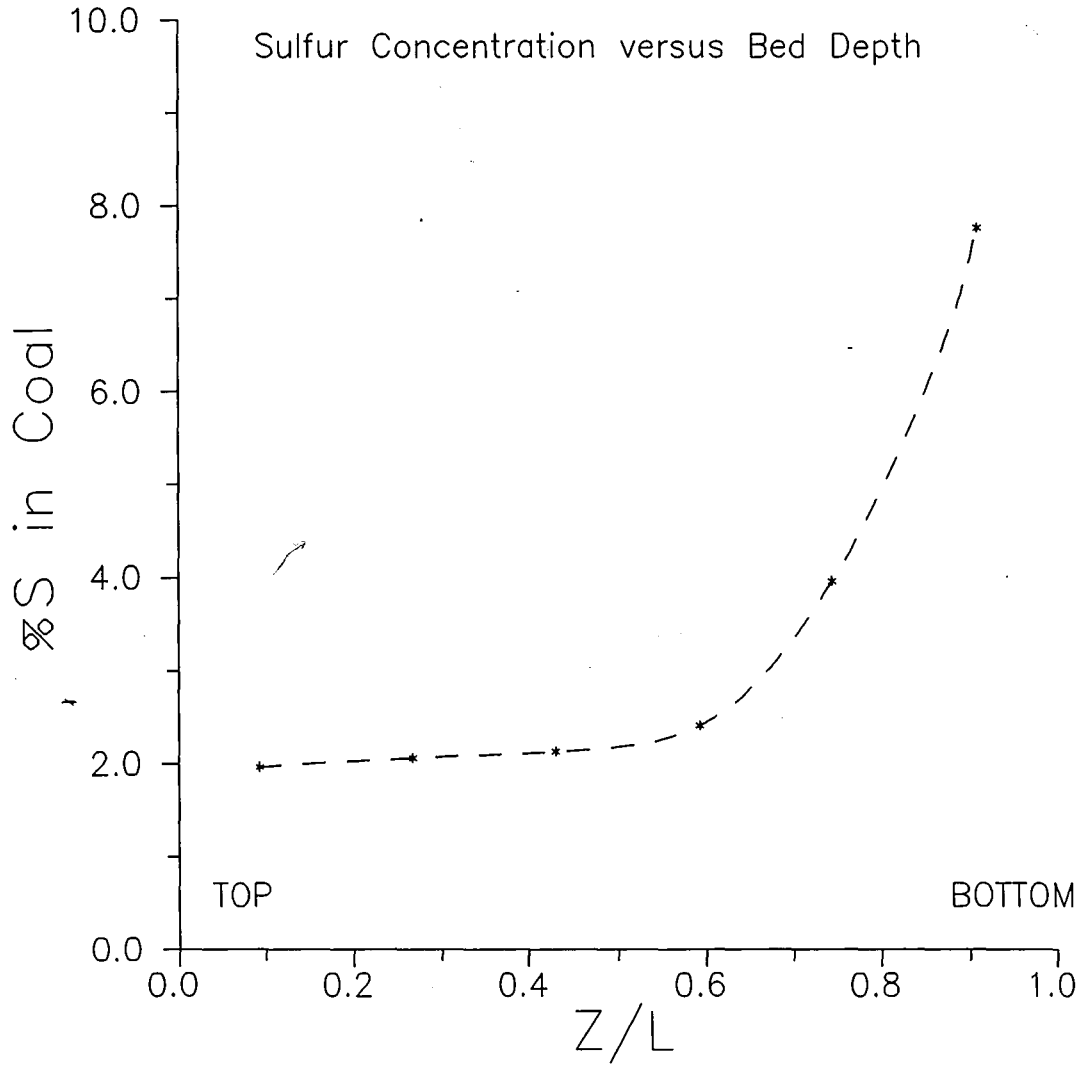

Figure 2.4
Typical profile of the sulfur concentration in coal versus bed depth

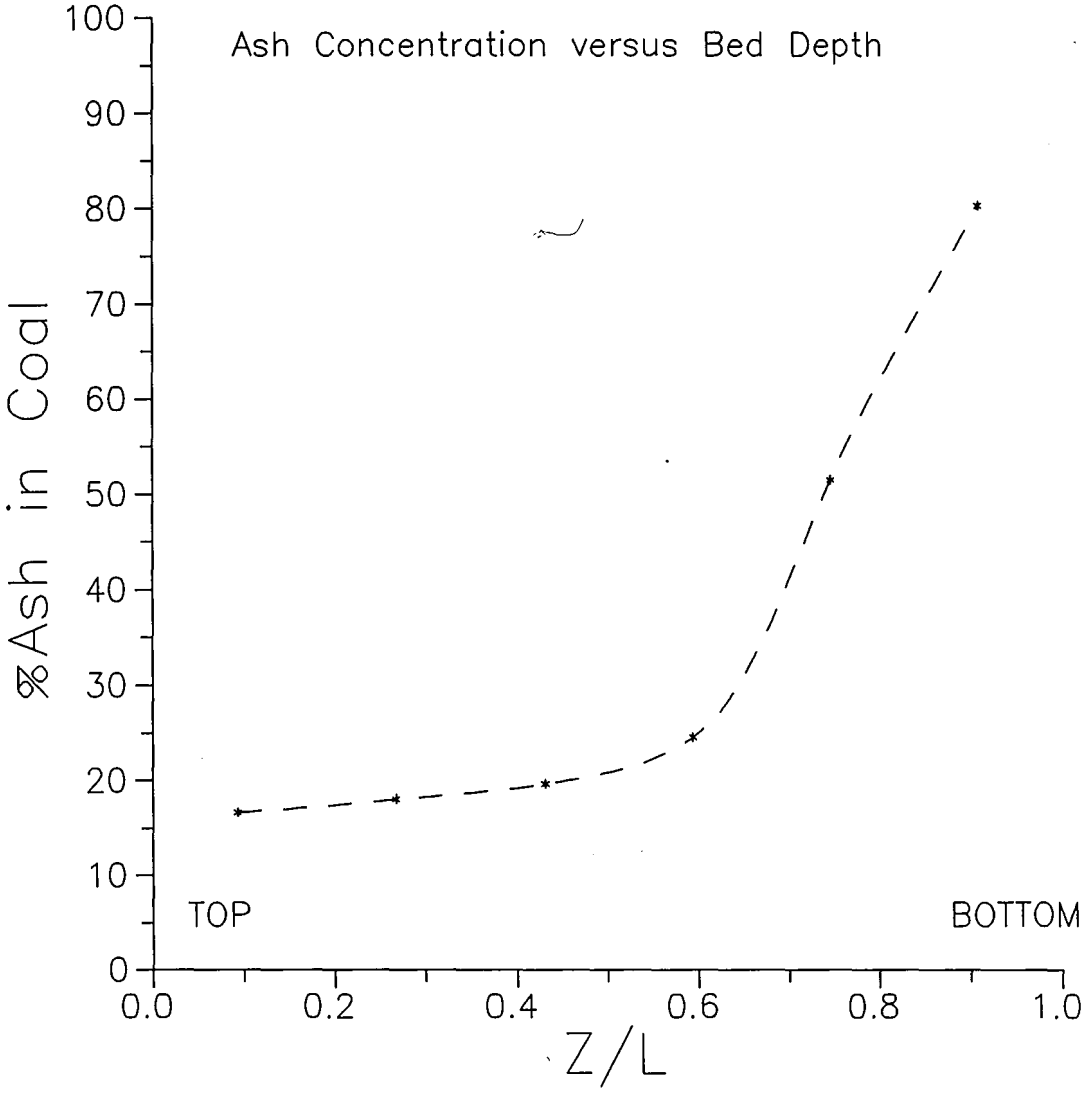

Figure 2.5
Typical profile of the ash concentration in coal versus bed depth

The important independent parameters are the mass ratio or volumetric ratio of coal to magnetite; the ratio of superficial gas velocity to minimum fluidization velocity of magnetite, u_o/u_{mfm}; bed height; and processing time. The magnetite size to use with a certain coal size is also an important criterion.

The mass ratio, m_c/m_m, is the mass of coal per mass of magnetite. The volumetric ratio, mm, follows from the computer code discussed above, and is typically the number of equal volume layers of magnetite in a total of fifteen layers. Therefore, m_c/m_m and mm are related as:

$$mm = \frac{15}{1 + \frac{\rho_m}{\rho_c}\frac{m_c}{m_m}} \qquad \textbf{(2.9a)}$$

where ρ_c and ρ_m are the respective bulk densities of coal and magnetite. If $\rho_c \approx 0.88$ g/cm^3 and $\rho_m \approx 1.8$ g/cm^3, then Equation 2.9a simplifies to:

$$mm = \frac{15}{1 + 2.045\frac{m_c}{m_m}} \qquad \textbf{(2.9b)}$$

2.3.3 *Coal cleaning performance*

The goal of coal cleaning is to remove the maximum amount of impurities while retaining the maximum amount of energy. The terms Sulfur Reduction (S.R.), Ash Reduction (A.R.), and Energy Recovery (BTUR) quantify the performance. The weight

recovery (WTR) measures the fraction of the coal that is kept as the product. The definitions of the above terms use mass quantities of impurities and energy quantities in both the refuse portion and the product portion of the coal.

The definitions are as follows:

$$S.R. = \frac{Mass\ of\ Sulfur\ in\ Refuse\ Portion}{Total\ Mass\ of\ Sulfur\ in\ Refuse\ and\ Product\ Portions}$$

$$A.R. = \frac{Mass\ of\ Ash\ in\ Refuse\ Portion}{Total\ Mass\ of\ Ash\ in\ Refuse\ and\ Product\ Portions}$$

$$BTUR = \frac{Energy\ in\ Product\ Portion}{Total\ Energy\ in\ Refuse\ and\ Product\ Portions}$$

$$WTR = \frac{Mass\ of\ Product\ Portion}{Total\ Mass\ in\ Refuse\ and\ Product\ Portions}$$

The above quantities are found using the mass, the sulfur and ash mass concentrations, and the energy content per mass of the product and refuse portions. These definitions show directly that if all the coal is in the product portion, S.R. and A.R. are 0.0 and BTUR is 1.0. Conversely, if all the coal is in the refuse portion, S.R. and A.R. are 1.0 and BTUR is 0.0. In practice, the desired energy recovery generally determines where to divide the coal into product and refuse portions. However, the division can be systematically varied to determine very useful relations of S.R. and A.R. versus BTUR. (See Figures 2.6 and 2.7.)

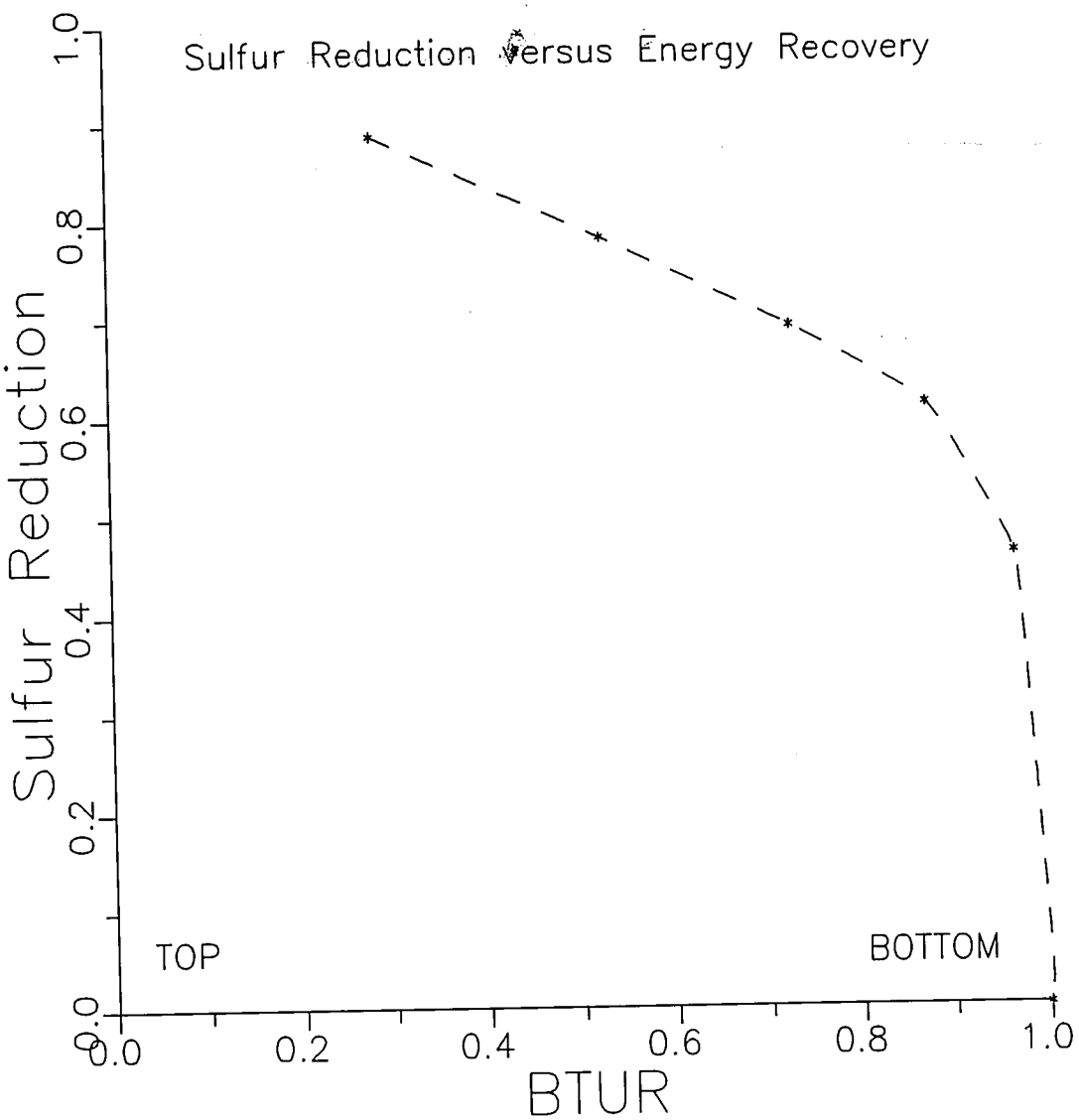

Figure 2.6
Typical sulfur reduction versus energy recovery

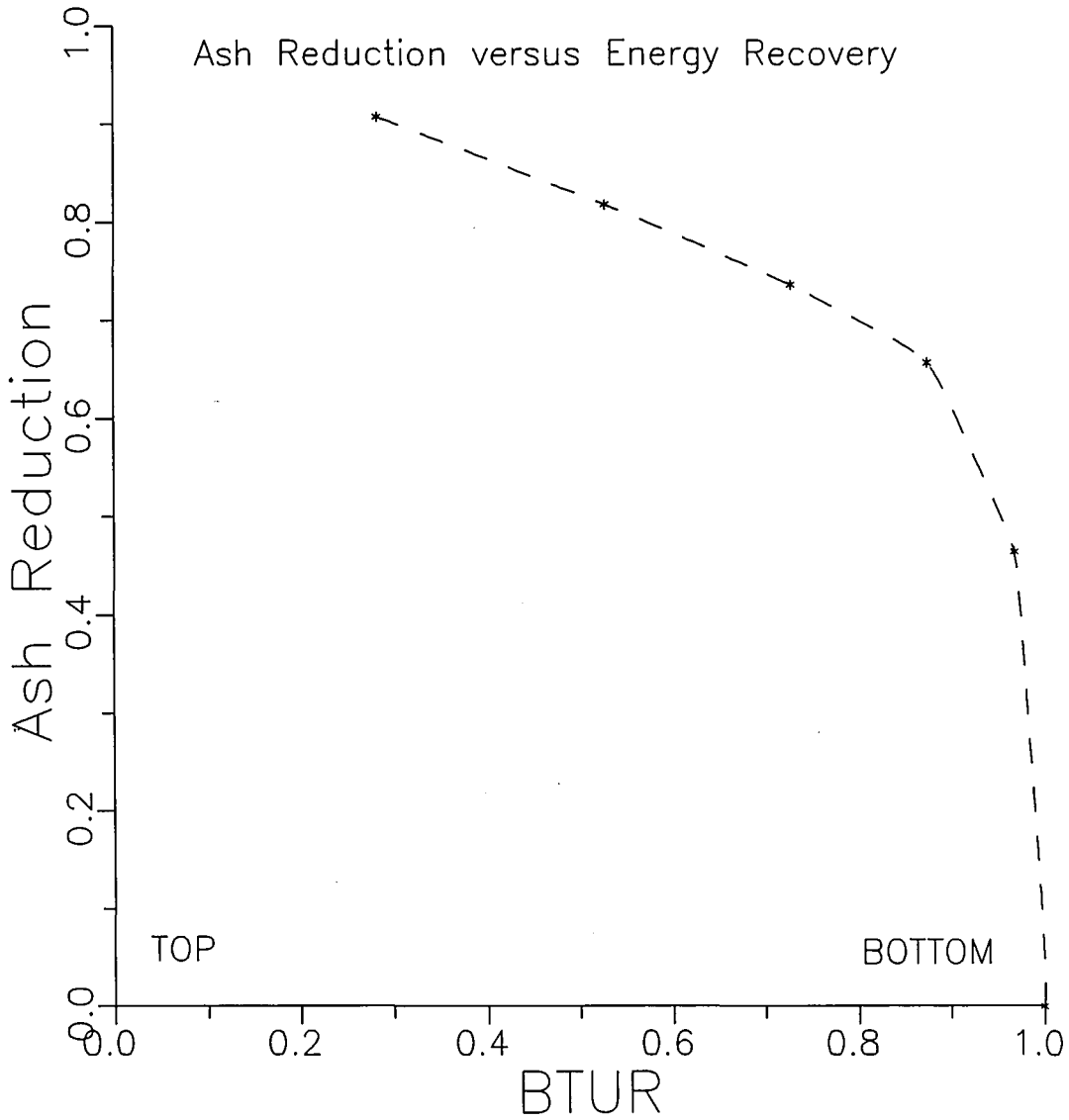

Figure 2.7
Typical ash reduction versus energy recovery

A generalized distribution is another method employed to characterize the cleaning performance of any coal cleaning system. Either a pre-set criterion or the use of actual experimental samples determines the division of the clean product and refuse portions of the coal. This criterion could be a required BTUR, S.R., A.R., or sulfur or ash mass concentration. The curve is then the fraction of the total mass of a density fraction, which is in the product portion, RTCC, versus the specific gravity of a density fraction.

The values of S.G.S., E_p, and GE_p come from the generalized curve. The parameter S.G.S., the specific gravity of separation, is the specific gravity at which RTCC is equal to 0.5. The parameter E_p, the Eckhart probability, and GE_p, the generalized Eckhart probability, represent probable error in the separation when compared to a perfect separation. (See Figures 2.8 and 2.9.)

$$E_p = \frac{S.G.(.75) - S.G.(.25)}{2}$$

and,

$$GE_p = \frac{E_p}{S.G.S.}$$

Better cleaning performance occurs at lower values of E_p, GE_p, and S.G.S.

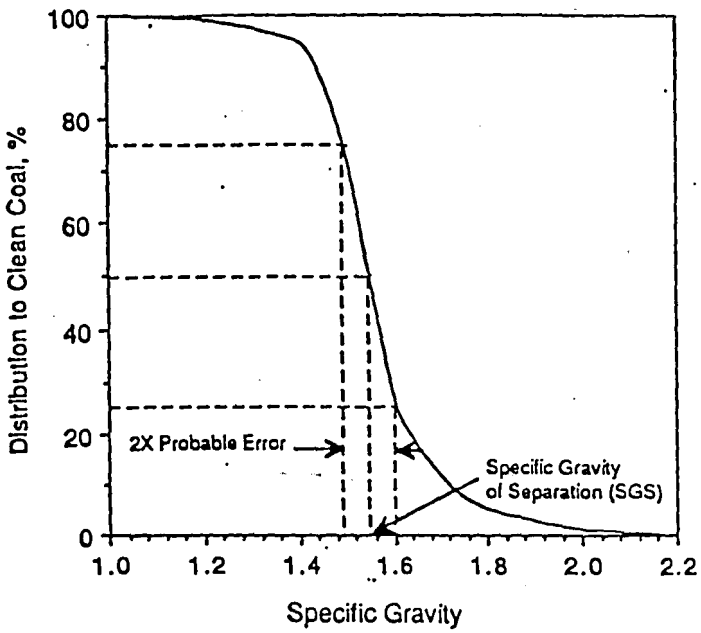

Figure 2.8
Typical distribution curve illustrating specific gravity of separation [23]

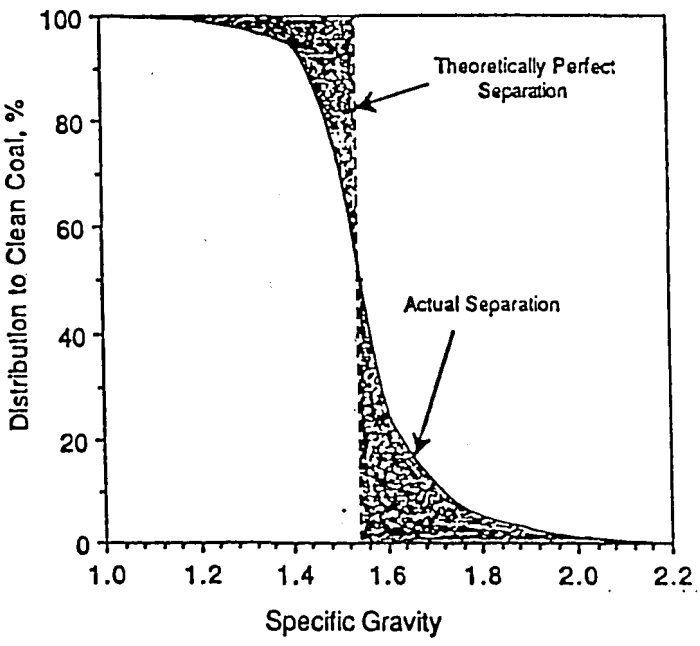

Figure 2.9
Error area as a measure of the difference between an actual and theoretical distribution curve [23]

2.3.4 *Density segregation*

As discussed previously, density segregation drives the coal cleaning process. The sulfur removal performance is often described as being dependent on the type or form of sulfur (e.g., pyritic or organic). In contrast, if the forms of sulfur are similarly distributed among the density fractions (i.e., all forms are more heavily concentrated in the denser fractions), the sulfur removal will not depend on the form of sulfur. The sulfur and ash removed will be the sulfur and ash in the denser fractions, which segregate away from the lighter, purer, energy-richer fractions.

According to a density segregation, the best performance available occurs with the complete separation of the density fractions from each other. Tables 2.3 and 2.4 show typical washability analyses for -50 +80 mesh Upper Freeport coal and -30 +50 Rushton coal, describing the sulfur, ash, and energy content, and overall weight percent of individual density fractions. By making the product-refuse split between two density fractions, the S.R., A.R., BTUR, and WTR can be calculated. Tables 2.5 and 2.6, and Figures 2.10 and 2.11 show the end result of the optimal cleaning through a density segregation procedure. Using the above procedure, a quick qualitative evaluation can be made of the potential to clean a certain coal by a physical density separation.

2.3.5 *Batch bed coal cleaning*

Studies performed using a small-scale stationary fluidized bed (batch bed) indicated the parameters for optimal performance. (See References [23] and [28].) Initially, Kozanoglu's [15] computer model gave ranges in which to perform actual coal

Table 2.3
Washability data of -50 +80 Upper Freeport coal

Specific Gravity Range	Wt %	Wt % S	Wt % Ash	Energy Content [Btu/lb_m]
Float - 1.3	38.04	0.78	2.20	15340
1.3 - 1.4	23.29	1.25	8.53	14257
1.4 - 1.6	12.65	1.80	18.38	12525
1.6 - 1.8	3.99	3.18	30.50	10214
1.8 - 2.0	1.89	4.78	44.90	7655
2.0 - 2.45	2.59	7.11	60.19	5058
2.45 - 2.9	11.87	2.06	86.23	638
2.9 - Sink	5.67	21.11	72.81	2275

Table 2.4
Washability data of -30 +50 Rushton coal

Specific Gravity Range	Wt %	Wt % S	Wt % Ash	Energy Content [Btu/lb_m]
Float - 1.3	26.33	1.14	3.14	15362
1.3 - 1.4	17.27	1.55	9.74	14122
1.4 - 1.6	9.76	2.01	24.40	11450
1.6 - 1.8	6.59	2.09	43.70	8153
1.8 - 2.0	5.52	2.30	56.48	5961
2.0 - 2.45	10.08	2.60	73.69	2926
2.45 - 2.9	18.78	3.19	86.87	722
2.9 - Sink	5.77	38.42	63.79	2760

cleaning experiments. The experiments consisted of placing a layer of coal on top of a layer of magnetite, using the desired mass and volume ratios and packed bed height. The bed was bubbled at a desired superficial air velocity for a period of time, usually thirty seconds. After stopping the flow of air, the bed material was collected layer-by-layer using a suction device. The resulting six samples were weighed, magnetically separated to remove the magnetite from the coal, and sent to a chemical laboratory for sulfur, ash,

Table 2.5
Results of perfect segregation coal cleaning for -50 +80 Upper Freeport coal

Fraction	S.R.	A.R.	BTUR	WTR
1	0.8884	0.9638	0.5018	0.3804
2	0.7789	0.8780	0.7874	0.6134
3	0.6932	0.7775	0.9236	0.7399
4	0.6455	0.7249	0.9587	0.7798
5	0.6155	0.6882	0.9711	0.7987
6	0.5422	0.6208	0.9824	0.8246
7	0.4503	0.1784	0.9889	0.9433
8	0.0000	0.0000	1.0000	1.0000

Table 2.6
Results of perfect segregation coal cleaning for -28 +50 Rushton coal

Fraction	S.R.	A.R.	BTUR	WTR
1	0.9272	0.9785	0.4456	0.2623
2	0.8620	0.9346	0.7154	0.4350
3	0.8142	0.8724	0.8390	0.5326
4	0.7806	0.7972	0.8984	0.5985
5	0.7497	0.7159	0.9348	0.6537
6	0.6859	0.5220	0.9674	0.7545
7	0.5400	0.0961	0.9824	0.9423
8	0.0000	0.0000	1.0000	1.0000

and energy content analysis in each layer. With these data, the S.R. and A.R. versus BTUR were calculated. (See Figures 2.4 - 2.7.)

Generally speaking, the optimal parameters found were a 3.0 cm bed height, a thirty-second processing time, $m_c/m_m \approx 1.5$, and $u_o/u_{mfm} \approx 2.0$. The optimal mass ratio and fluidizing air velocity ratio varied with particle size and coal type as shown in Figures 2.12 and 2.13.

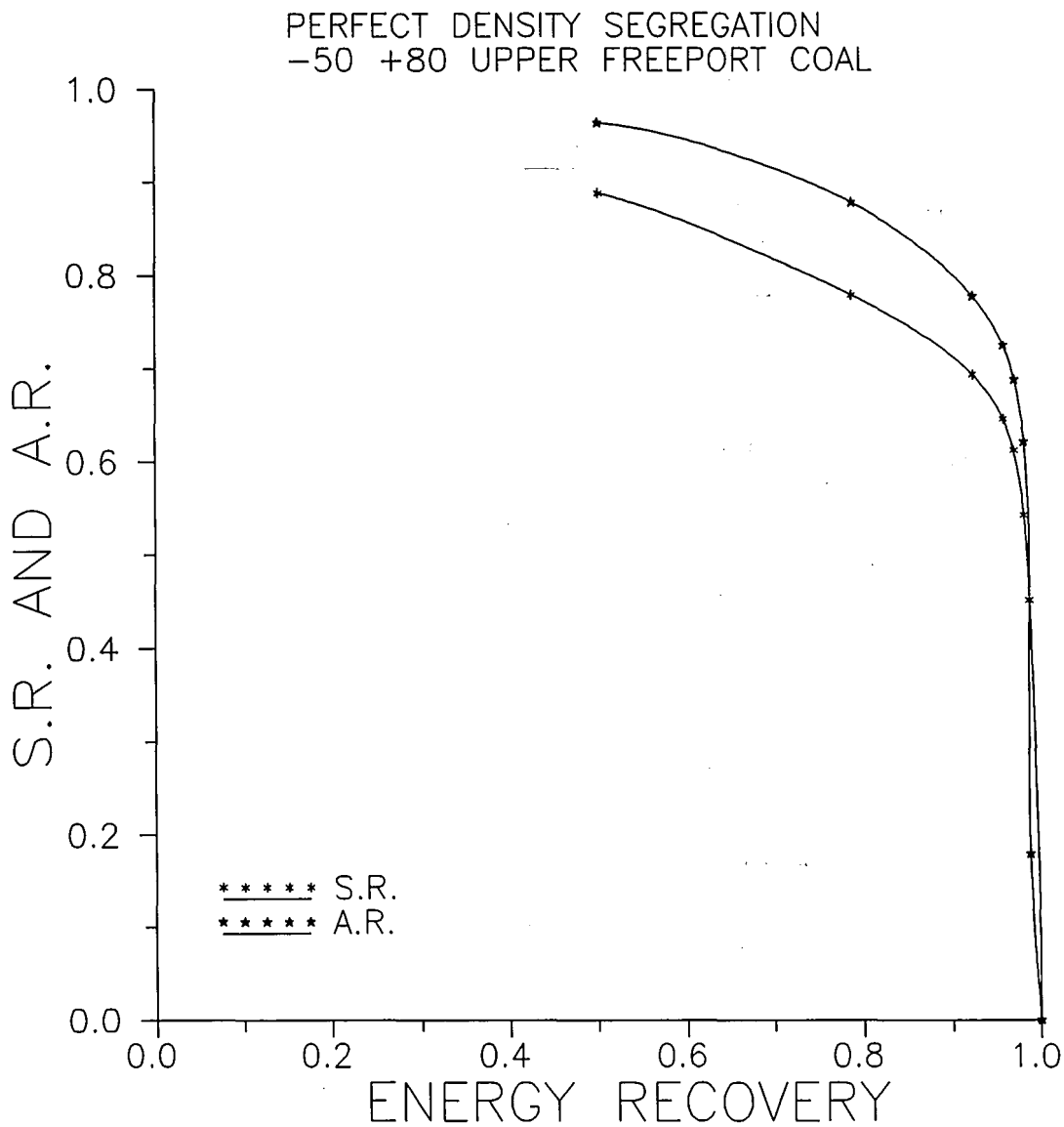

Figure 2.10
Cleaning performance of perfect density segregation of -50 +80 Upper Freeport coal

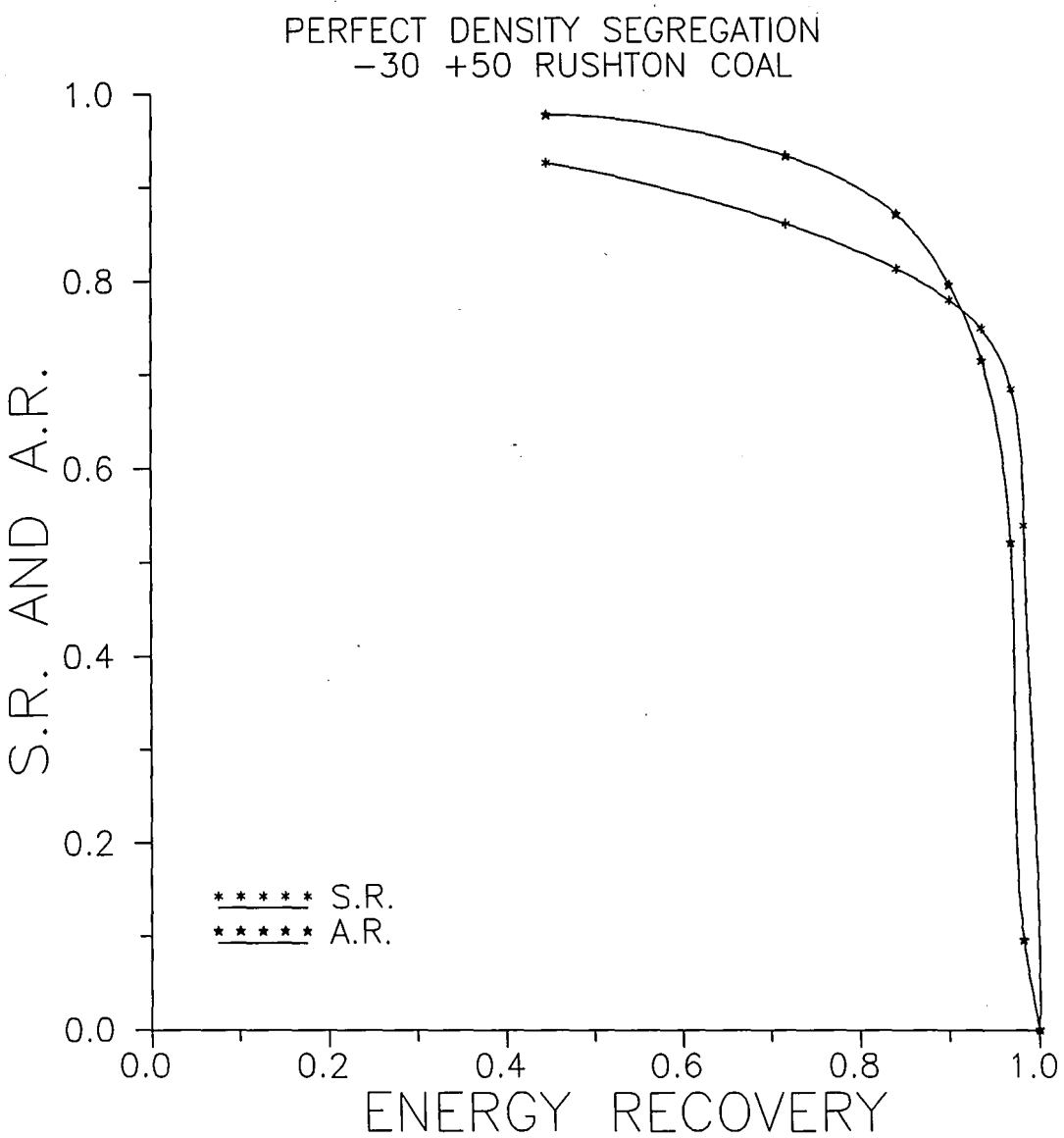

Figure 2.11
Cleaning performance of perfect density segregation of -30 +50 Rushton coal

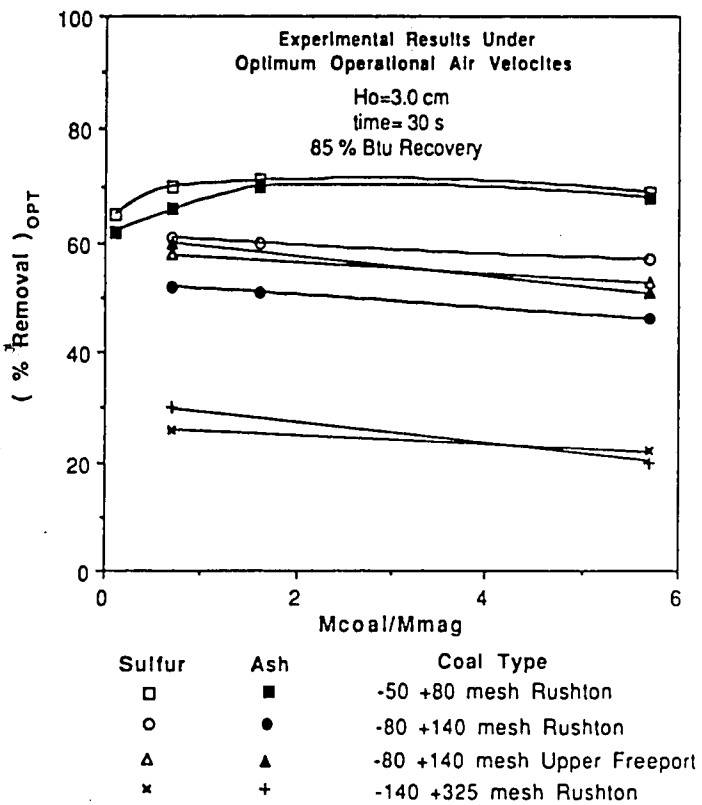

Figure 2.12
Experimental results under optimum fluidizing air velocities
regarding the effect of coal type and particle size on cleaning performance [23]

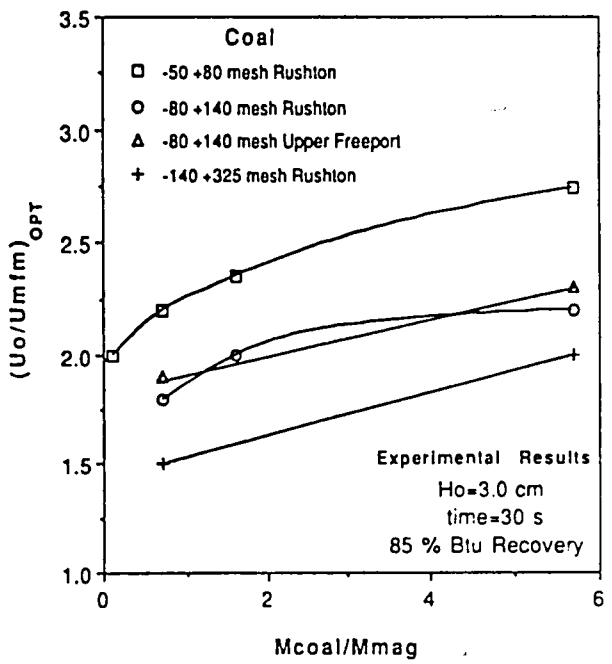

Figure 2.13
Experimental data of the effect of the coal to magnetite mass ratio on cleaning performance, while varying coal particle size and type [23]

2.3.6 *Continuous cleaning system*

A stationary batch bed system is not feasible for commercial application. In order to put an air-fluidized bed coal cleaning operation to use, it must be capable of continuously processing several tons per hour. An inclined open-channel fluidized bed is one means of continuous cleaning; a schematic is shown in Figure 2.14. The coal and magnetite flow from feed hoppers into the open channel. Fluidizing air from below a distributor increases the solids' flowability, allowing solids to flow down the channel. The inclined channel must be angled properly and have appropriate solids mass flow in order to give good cleaning conditions (bed height, m_c/m_m, and processing time at a given u_o/u_{mfm}). Most importantly, the performance in the continuous cleaning system needs to match the cleaning performance in the batch bed cleaning system, when the operating conditions of the continuous system are comparable to those conditions of efficient cleaning in the batch bed system.

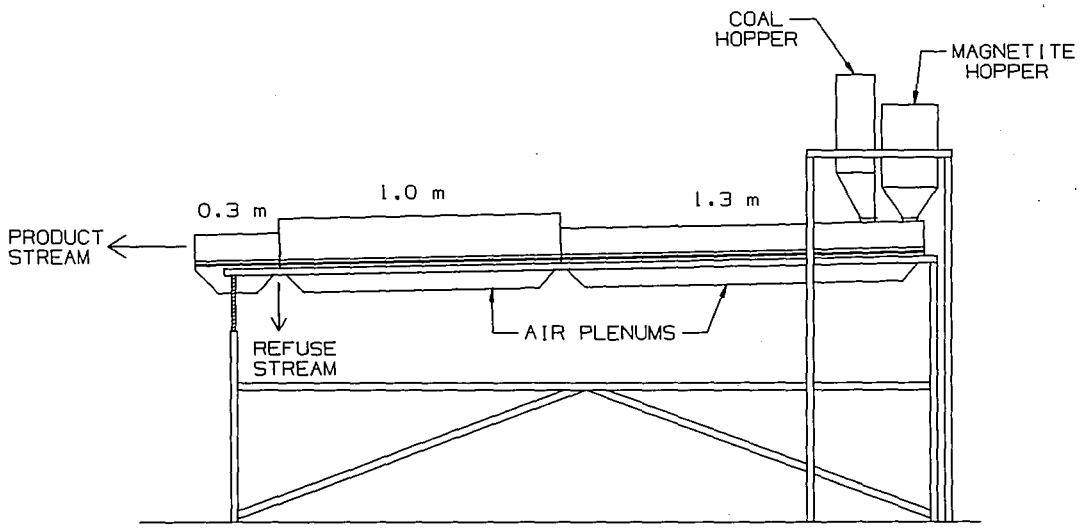

Figure 2.14
Schematic of continuous coal cleaning system -- fluidized inclined open channel

3 Inclined open-channel aerated solids flow

3.1 Introduction

Solid particulate material will flow along an open channel under the proper conditions. Typically, to achieve flow, the material is fed from a hopper into an inclined open channel, which, if desired, has fluidizing air flowing from a plenum through a porous-medium distributor. Conditions permitting, the solids will flow down the channel at a particular longitudinal velocity and bed height, depending on the energy and momentum demands of the system and the flow resistances.

In the absence of fluidizing air, the bed must be inclined beyond the angle of repose of the powder. The angle of repose is generally about 35°, but it depends on a combination of properties of the material (i.e., particle size, density, and sphericity), termed its "flowability" [31]. In order for the material to flow at smaller angles, or, in other words, with a smaller driving force, the "flowability" must be increased. If one supplies air to the material, the solid particles begin to lose their ability to hold a shear stress statically, thereby beginning to behave as a fluid. At low superficial gas velocities, the air creates an air layer, or slip region, between the channel surface and the particles, sharply reducing the shear stresses. At air velocities which are high enough to cause fluidization, the air reduces the particle contact forces, causing partial or full fluidization. This fluidization is, in fact, the primary cause of increased "flowability" once the minimum fluidization velocity is exceeded.

Ishida, et al. [13] divided the flow into five classifications, as follows:

- Sliding flow
- Immature sliding flow
- Splashing flow
- Bubbling flow
- Gliding flow

Sliding, immature sliding, and splashing flows all occur below or at the minimum fluidization velocity, and bubbling and gliding flows occur above the minimum fluidization velocity. The main flow type of concern for coal cleaning is bubbling flow, since the bubbling action is responsible for the density segregation. Further discussion will deal primarily with bubbling flow.

When designing an open-channel flow system for material conveying, one desires to know the resultant bed height for a required mass flow rate. In order to do so, one needs relationships of the height and longitudinal material velocity with respect to the superficial gas velocity, angle of inclination, solids mass flow rate, and solid particle properties. These relationships can either be found experimentally for narrow ranges of the above flow parameters, or one can attempt a theoretical model. The theoretical models available to date generally rely on some experimental data input. The theory can be based on a micro-scale inter-particle model or on a macro-scale model, such as a liquid analogy model. As such, the form of the model required for fluidized solids is most distinctly non-Newtonian in nature. Previous investigations have attempted to account for non-Newtonian behavior using an apparent viscosity based on relationships of shear stress versus shear rate.

The most important differences between a real fluid and flowing fluidized beds are [5]:

- The inherent anisotropy of a flowing bed of fluidized particles
- The presence and growth of bubbles
- The problem of air distribution

Even considering the above differences, the method most widely used for the theoretical modelling of aerated inclined open-channel flow relies on the liquid analogy.

3.2 Non-Newtonian fluids

3.2.1 *Introduction*

Unlike most gases and simple liquids, a non-Newtonian fluid does not follow a linear relationship between shear stress and shear rate. A simple Newtonian fluid follows the relation:

$$\tau = \mu \frac{du}{dy} \tag{3.1}$$

where μ is the coefficient of dynamic viscosity. More generally, the shear stress of a non-Newtonian fluid is a function of shear rate and time. A Newtonian fluid is a special case of this general model, where the shear stress is directly proportional to the shear rate, expressed as the velocity gradient.

The shear stress relationships of many types of non-Newtonian fluids are described as functions of shear rate and time. Fluidized solids flow does not have a time

dependence, so it is neither thixotropic (time-thinning) nor rheopectic (time-thickening). However, fluidized solids flow has been found to be pseudo-plastic (shear-thinning), dilatant (shear-thickening), or even perhaps Bingham plastic. A Bingham plastic's shear stress relationship requires a yield stress in order to have a finite positive shear rate. Figures 3.1a and 3.1b show typical rheograms for these types of non-Newtonian fluids.

3.2.2 *Modelling of non-Newtonian flow*

In general, the time-independent shear stress relationship can be described as:

$$\tau = f(\gamma) \tag{3.2}$$

The simplest way to model either pseudo-plastic or dilatant materials is using a power law model, as described by Ostwald and de Waale [22]:

$$\tau_{xy} = -k\left|\frac{du_x}{dy}\right|^{n-1}\frac{du_x}{dy} \tag{3.3a}$$

or, more simply:

$$\tau = k\,\gamma^n \tag{3.3b}$$

3.2.2.1 *Parameters of the power law model*

In Equations 3.3a and 3.3b, the values of k and n are constants. The "consistency factor," k, gives an indication of the consistency of the fluid. The larger

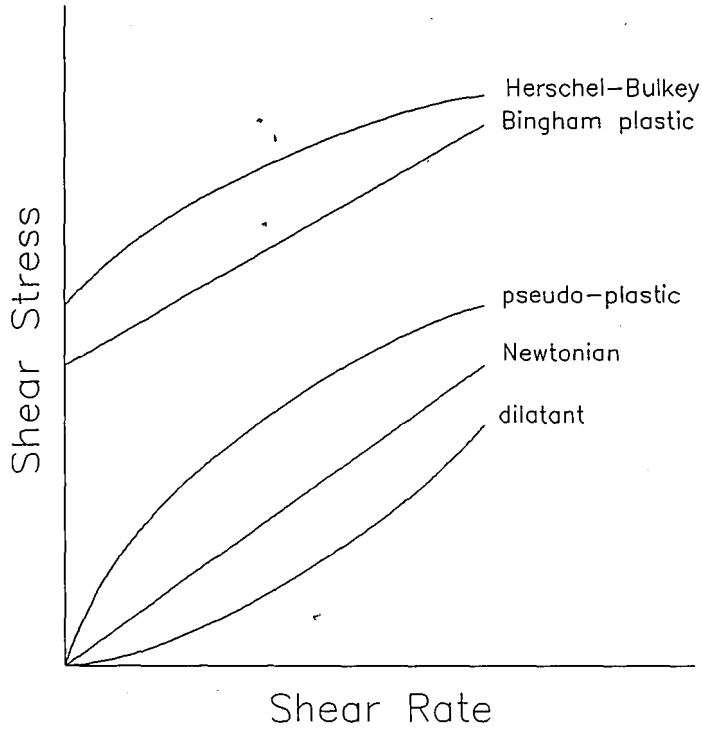

Figure 3.1a
Rheograms of non-Newtonian fluids

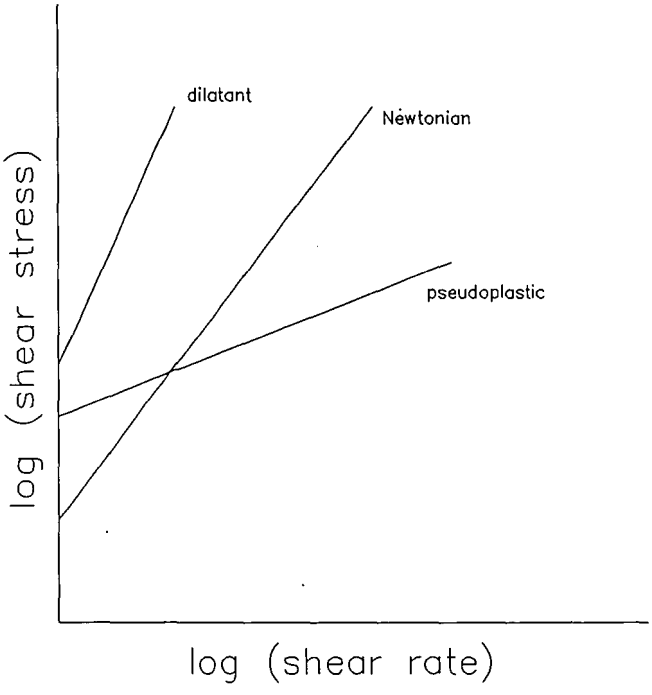

Figure 3.1b
Rheograms on logarithmic axes for
power law models

the value of k, the more "viscous" the fluid. The "flow index," n, indicates the amount of deviation from non-Newtonian behavior [17]. This is illustrated in Figure 3.1b on a logarithmic plot as:

$$\log \tau = \log k + n \log \gamma \tag{3.4}$$

In a similar fashion to Newtonian flow, we can define an apparent viscosity as:

$$\mu_{app} = \frac{\tau}{\gamma} \tag{3.5}$$

or, for the power law model:

$$\mu_{app} = k\,\gamma^{n-1} \tag{3.6}$$

According to Latkovic [17], the power law model has proved to be very useful, but it has inherent limitations:

- Equation 3.6 suggests that μ_{app} becomes infinite at zero shear rate for $n < 1$.
- For fluidized solids, n is not likely to remain constant over the entire range of flow conditions.
- The consistency factor, k, has dimensions which depend upon the value of the flow index, n.

3.2.2.2 *The Metzner-Reed Model*

Using a power law model for the shear stress-shear rate relationship, Metzner and Reed [19] developed a correlation for non-Newtonian laminar flow in pipes with no slip at the walls. Beginning with Mooney's [20] rearranged equation and allowing the average bulk flow velocity to be:

$$V = \frac{4Q}{\pi D^2} \tag{3.7}$$

and, letting n′ be defined such that:

$$\frac{1}{n'} = \frac{d\left[\ln\left(\frac{8V}{D}\right)\right]}{d\left[\ln\left(\frac{D\Delta P}{4L}\right)\right]} \tag{3.8}$$

they derived an expression for the shear rate at the wall:

$$-\left.\frac{du}{dr}\right|_{wall} = \frac{3n'+1}{4n'}\frac{8V}{D} \tag{3.9}$$

The advantages of this expression are [19]:

- Simplicity, and
- The logarithmic plot of $\frac{D\Delta P}{4L}$ versus $\frac{8V}{D}$ gives a nearly constant slope over a wide range of shear stresses for many non-Newtonian fluids, requiring that n′ be nearly constant.

If n′ is essentially a constant, then, upon integration :

$$\frac{D\Delta P}{4L} = k'\left(\frac{8V}{D}\right)^{n'} \tag{3.10}$$

It has been found experimentally [19] that k′ and n′ are constant over wide ranges of $\frac{8V}{D}$ or $\frac{D\Delta P}{4L}$. Even so, one must use care that k′ and n′ are valid for a desired range.

From the above relationships, it should be noted that the shear stress, τ_w, is equal to $\frac{D\Delta P}{4L}$ and the shear rate is $\left.\frac{du}{dr}\right|_{wall}$. Therefore,

$$\tau_w = k'\left(\frac{4n'}{3n'+1}\right)^{n'}\left(-\frac{du}{dr}\right)\Big|_{wall}^{n'} \tag{3.11}$$

Equation 3.11 is consistent with the power law model if n′ is constant and equal to n and $k = k'\left(\frac{4n'}{3n'+1}\right)^{n'}$. The values of n′ determine the type of fluid as follows:

i)	$n' = 1$	Newtonian
ii)	$n' < 1$	Pseudo-plastic
iii)	$n' > 1$	Dilatant

Furthermore, Metzner and Reed [19] defined a generalized Reynolds number in order to describe transition to turbulence according to the Fanning friction factor:

$$N'_{Re} = \frac{D^{n'} V^{2-n'} \rho}{k' 8^{n'-1}} \qquad (3.12)$$

and:

$$f_f = \frac{16}{N'_{Re}} \qquad \textit{(Laminar Flow)} \quad (3.13)$$

It has been found by Botterill, et al. [3] that this relation is valid for flowing fluidized solids, but the fluidized solids always remain in laminar flow. Interestingly, the constant coefficient (i.e., 16) may vary with particle and distributor properties.

To make use of these relations, Metzner and Reed felt that the only requirement was a good viscometer. A rotating viscometer, and not a capillary tube viscometer, must be used with fluidized solids.

The primary objection to the above model is the possibility of a Bingham plastic material. However, a slug profile, like that of a Bingham plastic, can be developed using a low flow index, n′ (approximately 0.2). Botterill, et al. [8] have also looked into the development of a slug profile for a flowing Bingham plastic fluidized solid and found a low flow index to give such a result.

3.3 Theoretical modelling

The modelling of open-channel aerated solids transport has been approached from both micro-scale and macro-scale viewpoints. On the micro-scale, equations describing the inter-particle forces require knowing sufficient information about the particles. From an engineer's standpoint, this is often not feasible, so approximations are made, and a macro-scale model is utilized instead. The most prominent type of such models is a liquid analogy model.

In deriving a liquid analogy model, the two phenomena, fluidization of particulate material and the flow of liquids in an open channel, must be combined [32]. In some respects, the liquid analogy seems quite applicable to the flow of fluidized solids, because they exhibit surface and standing wave motion like normal liquids. However, because of the non-Newtonian nature of this flow and the occurrence of defluidization on surface contact, the validity of this analogy should not be over-emphasized or over-extended. A non-Newtonian flow model requires an appropriate treatment of the density and viscosity to properly account for the fluidization phenomena.

3.3.1 τ *versus* γ

A popular liquid analogy which relies on the shear stress versus shear rate relation was used by Botterill, et al. [3,4,5,6,7,8]. This model attempts to define an

"effective" or "apparent" viscosity for a given flow. Following the Metzner-Reed model, the shear stress and shear rate are given respectively as:

$$\tau = \frac{\Delta P D_e}{4L} \tag{3.14}$$

and:

$$\gamma = \frac{3n'+1}{4n'}\frac{8V}{D_e} \tag{3.15}$$

where D_e is the equivalent hydraulic diameter and is given as:

$$D_e = \frac{4 \times Flow\ Area}{Wetted\ Perimeter} = \frac{4wh}{2h+w} \tag{3.16}$$

Since this model for the shear stress - shear rate relationship is an analogy to flow in circular pipes, the shear-rate coefficient of 8 is only exactly appropriate for the effect of drag on a cylindrical wall in fully developed laminar flow with no slip at the walls.

Later, it was found that τ_{wall} and τ_{dist} differ and the variation is dependent on the aspect ratio of the flowing bed. Accordingly, Botterill, et al. [5] changed the definition of equivalent diameter to:

$$D_e' = \frac{4wh}{Kw+2h} \tag{3.17}$$

where K is either:

$$K = \frac{Base\ Drag}{Total\ Drag} \qquad [5] \qquad \textbf{(3.18)}$$

or:

$$K = \frac{\tau_{dist}}{\tau_{wall}} \qquad [8] \qquad \textbf{(3.19)}$$

Even though both definitions for K must be measured experimentally, the second definition for K may be more useful, since it better represents the ratio of the drag forces at the wall and distributor. The authors offered the caveat that the use of an equivalent diameter is always questionable.

Using experimental data for the shear stress - shear rate relationship on a logarithmic plot, the values for k′ and n′ can be used in an expression for the shear stress, $\tau_{\Delta P}$.

$$\tau_{\Delta P} = k'\left(\frac{4n'}{3n'+1}\right)^{n'}\left|\frac{du}{dy}\right|^{n'-1}\frac{du}{dy} = k'\left(\frac{8V}{D_e'}\right)^{n'} \qquad \textbf{(3.20)}$$

The velocity profiles at a given height along a horizontal plane can be determined following the finite difference approximation approach of Wheeler and Wissler [29].

3.3.2 *Energy Balance*

Singh, et al. [27] approached the modelling of fluidized open-channel flow with a generalized energy equation:

$$\Delta\left(\frac{U_m^2}{2\beta}\right)+\Delta(gy)+\int_1^2\frac{1}{\rho}dP+\sum_1^2 F+W_f=0 \qquad (3.21)$$

In this equation, β is a kinetic energy correction factor for the velocity profile, where, for fully developed Newtonian flow:

$\beta = 0.5$	Laminar flow
$\beta = 1.0$	Turbulent flow

Also, the flow is incompressible and does no work, so:

$$\int_1^2\frac{1}{\rho}dP=0$$

and,

$$W_f=0$$

Again, using the analogy of liquid flow in pipes:

$$D_e'=\frac{4wh}{Kb+2h} \qquad (3.22)$$

and:

$$U_m = \frac{Q}{\rho b H} \tag{3.23}$$

See Figure 3.2 for a description of the coordinate system for these derivations.

For a Newtonian liquid, the energy equation becomes:

$$\frac{dH}{dl} = -\frac{\frac{32\mu U_m}{\rho g D_e^2} + \sin\alpha}{1 - \frac{U_m^2}{\beta g H}} \tag{3.24}$$

Assuming $\frac{dH}{dl} = 0$, the energy equation yields:

$$U_m = \frac{\rho g D_e^2}{32\mu} \sin\alpha \tag{3.25}$$

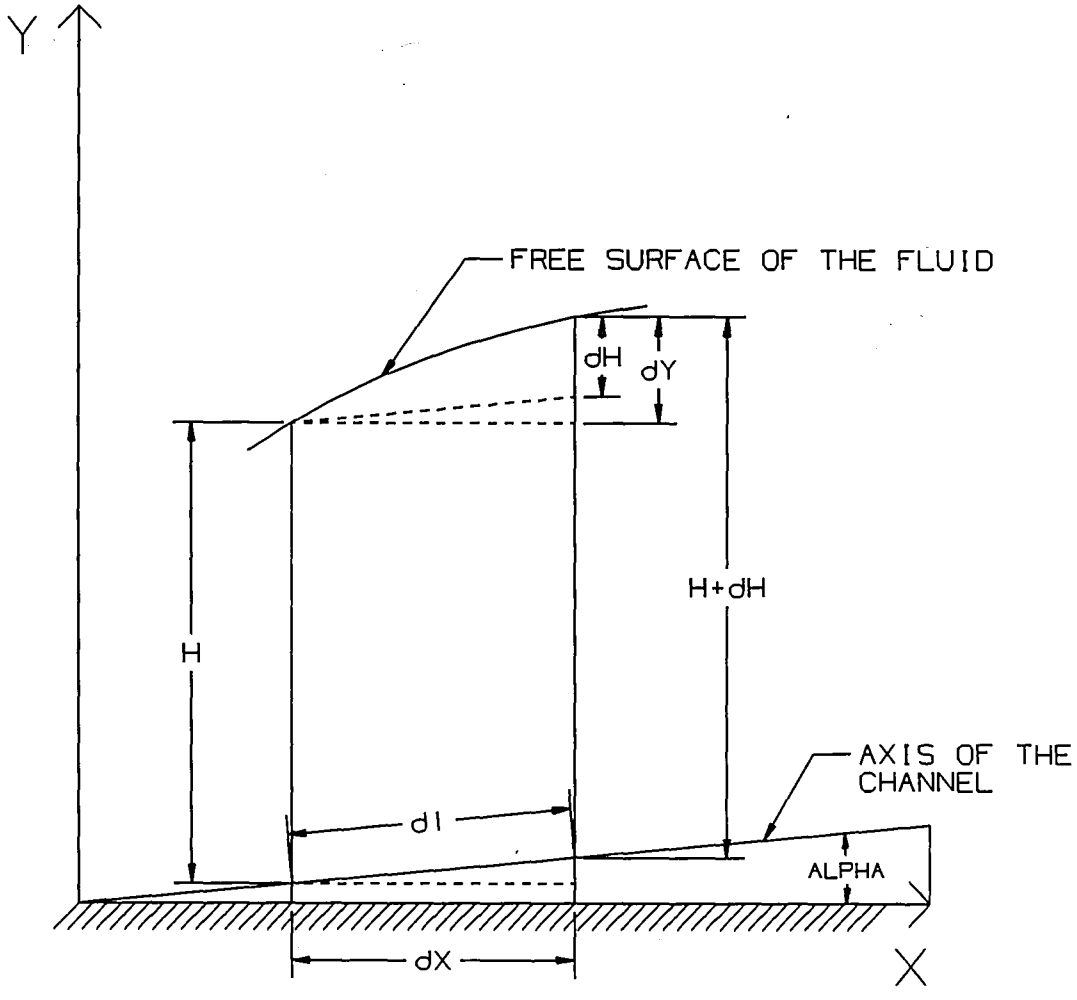

Figure 3.2
Coordinate system of inclined open-channel flow from Singh, et al. [27]

For a non-Newtonian open-channel flow:

$$\frac{dH}{dl} = \frac{-\left[\frac{2k}{\rho g c}\left(\frac{3n+1}{4n}\right)^n U_m^n + \sin\alpha\right]}{1-\frac{U_m^2}{\beta g H}} \tag{3.26}$$

where:

$$\beta = \frac{(2n+1)(5n+3)}{3(3n+1)^2} \tag{3.27}$$

It should be noted that:

Flow Index	K. E. Factor	Notes
n = 0	$\beta = 1$	Slug Profile
n = 1	$\beta = 0.5$	Newtonian Laminar Flow
n → ∞	$\beta = 0.370$	Extreme Dilatant Flow

The correlation for β is consistent with the type of profile and appropriate kinetic energy correction factor for a pseudo-plastic, Bingham-plastic, Newtonian, or dilatant fluid. A low index pseudo-plastic or Bingham plastic has a nearly slug profile, the Newtonian fully developed laminar profile is parabolic, and a dilatant profile should be even more peaked than the Newtonian parabolic profile.

The factor c is defined as:

$$c = \left[\frac{D_e'}{2} \right]^{n+1} \tag{3.28}$$

and k and n are defined from the power law model:

$$\tau = k\gamma^n \tag{3.29}$$

To test the model, the following divergence should be very close to zero:

$$D = \left[1 - \frac{U_m^2}{\beta g H} \right] \frac{dH}{dl} + \sin\alpha + \frac{2k}{\rho g c} \left[\frac{3n+1}{4n} \right]^n U_m^n \approx 0 \tag{3.30}$$

The parameters k and n must be estimated by minimizing the variance (D^2), while solving the above equation numerically, possibly using a Runge-Kutta routine, as Singh, et al. did. Singh, et al. [27] argued that the flow parameters (k and n) should be independent of flow rate, inclination, and channel dimensions. Even though Singh, et al. found the predicted results to match the experimental results quite well, k and n are not independent parameters. The inclination and flow rate affect the shear rate and all three parameters above affect the aspect ratio, thereby affecting the shear stress - shear rate power law and the equivalent hydraulic diameter. Their results did actually show some variation with the flow index parameters.

Ishida, et al. [13] developed an integral of energy terms:

$$J = \int_0^H \left[k_\tau y \frac{dv_z}{dh} + \frac{k_\mu}{2} y \left(\frac{dv_z}{dh} \right)^2 - \rho g v_z \sin\alpha \right] dh \qquad (3.31)$$

According to their approach, the particles will flow with a profile such that J is a minimum. The parameters k_τ and k_μ are characteristic constants of the flow. The following were derived using this variational method:

$$v_z = \frac{\rho g \sin\alpha - k_\tau}{k_\mu} h; \qquad for\ \sin\alpha > \frac{k_\tau}{\rho} \qquad (3.32a)$$

$$v_z = 0; \qquad for\ \sin\alpha \le \frac{k_\tau}{\rho g} \qquad (3.32b)$$

and:

$$\tau_{yz} = k_\tau y - k_\mu y \frac{dv_z}{dh} \qquad (3.33)$$

The model for the shear stress is similar to a Bingham-plastic fluid, but the yield stress $k_\tau y$ and the apparent viscosity $k_\mu y$ are proportional to the distance from the free surface, or, in other words, the normal stress associated with the hydrostatic pressure.

3.3.3 *Modelling by Woodcock and Mason*

Woodcock and Mason [30] have stated that various attempts have been made to find a way of predicting the flow characteristics from measurements of an "apparent

viscosity" of the material in the fluidized state. The majority of workers rely on a non-Newtonian liquid analogy. However, there has as yet been no agreement on a clear definition of the apparent viscosity or on a method of measuring it.

3.3.3.1 *Previous models summarized*

Woodcock and Mason [32] have summarized previously published models which were based on a liquid analogy using the mass flow rate, density, bed height, and factors to account for an effective flow viscosity. The mass flow of an inclined open-channel Newtonian flow with uniform bed height, no slip at the walls, and total slip at the base can be described by integrating the Navier-Stokes equation and integrating the resultant velocity profile to yield:

$$\dot{m} = \frac{\rho^2 g b^3 h \sin\alpha}{12\mu} \tag{3.34}$$

Assuming constant density and viscosity, Siemes and Hellmer [25] tried the approach,

$$\dot{m} = K b^3 h \sin\alpha \tag{3.35}$$

where K is a constant:

$$K = \frac{\rho^2 g}{12\mu} \tag{3.36}$$

This prediction for mass flow did not work well, so, later, Siemes and Hellmer [26] proposed the following:

$$\dot{m} = \frac{\rho b^2 h g \sin\alpha}{\mu} F\left(\frac{h}{b}\right) \tag{3.37}$$

For the simple Newtonian model, F becomes:

$$F\left(\frac{h}{b}\right) = \frac{b}{12h} \tag{3.38}$$

Descamps and Jodlowski [10] continued in this direction, trying:

$$\dot{m} = K b^n h^{4-n} \sin\alpha \tag{3.39}$$

where:

$$n = 1 \qquad for\ \frac{h}{b} < 0.5$$

$$n = 3 \qquad for\ \frac{h}{b} > 0.5$$

A major problem with the above model is the discontinuous correlation for n. Chandelle [9] developed the following continuous correlation for n in Equation 3.39.

$$n = 1 \qquad \frac{h}{b} \ll 0.5 \tag{3.40}$$

$$n = 2 \qquad \frac{h}{b} \approx 0.5$$

$$n = 3 \qquad \frac{h}{b} > 0.5$$

It should also be noted that according to data obtained by Woodcock and Mason with P.V.C. powder, K seems to be dependent on the aspect ratio (h/b).

Siemes and Hellmer [26] manipulated Equation 3.37 to develop an expression for the apparent viscosity.

$$\mu_{app} = \frac{\rho_s b^2 h^2 g \sin\alpha}{\dot{m}_s} F\left(\frac{h}{b}\right) \tag{3.41}$$

The parameter F(h/b) should be defined such that the apparent viscosity is constant with respect to mass flow, angle of inclination, and bed height. Experimental results have shown that the apparent viscosity is dependent on the mass flow.

Astarita, et al. [1] developed a model to account for slip velocity at the base. The authors define the solids velocity, u, as:

$$u_s = u_{slip} + \int_0^y \frac{du_s}{ds}\, ds \tag{3.42}$$

and the volume flow per width, Q, as:

$$Q = u_{slip} H + \int_0^H y \frac{du_s}{dy}\, dy \tag{3.43}$$

Equations 3.42 and 3.43 can be manipulated to yield the shear rate:

$$\gamma = \frac{Q}{h^2}\left(\frac{\partial(\ln Q)}{\partial(\ln h)}\right) - \frac{u_{slip} h}{Q}\left(1 - \frac{\partial(\ln u_{slip})}{\partial(\ln h)}\bigg|_{\alpha}\right) \tag{3.44a}$$

or, if the slip is zero:

$$\gamma = \frac{Q}{h^2}\left[\frac{\partial(\ln Q)}{\partial(\ln h)}\bigg|_{\alpha}\right] \tag{3.44b}$$

The value of the derivative at constant α must be determined experimentally from a logarithmic plot. The shear stress for this flow is given by Astarita, et al. [1], as:

$$\tau_b = \rho g h \sin\alpha \tag{3.45}$$

This model can be, and has been used, in a power law correlation for the shear stress to determine k′ and n′. Again, in doing so, it was found that the Fanning friction is inversely proportional to a generalized Reynolds number [1]:

$$f_f = \frac{16}{N'_{Re}} \tag{3.46}$$

3.3.3.2 *Woodcock and Mason's alternative approach*

Woodcock and Mason [32] began their modelling method with a momentum balance of an elemental section across steady uniform flow:

$$(2\tau_w h + \tau_b)\delta l - \rho g h b \delta l \sin\alpha = 0 \tag{3.47}$$

Equation 3.47 yields:

$$h = \frac{b\tau_b}{\rho g b \sin\alpha - 2\tau_w} \tag{3.48}$$

In order to develop the model further, we must relate τ_w and τ_b to actual flow parameters such as u_o, $\dot{m}$, and u_s. The authors kept u_o constant, but modeled the wall and base shear stresses as combinations of constant values and values proportional to solids flow velocity.

Case	τ_{wall}	τ_{base}
I	$K_w u_s$	Constant
II	$K_w u_s$	$K_b u_s$
III	Constant	$K_b u_s$

For Case I,

$$\dot{m} = \frac{\rho^2 g b^2 h \sin\alpha}{2K_w} - \frac{\rho b^2 \tau_b}{2K_w} \tag{3.49}$$

If total slip at the base occurs ($\tau_b = 0$), then:

$$\dot{m} = \frac{\rho^2 g b^2 h \sin\alpha}{2K_w} \tag{3.50}$$

The first equation for mass flow is a line having slope:

$$\frac{d\dot{m}}{dh} = \frac{\rho^2 g h \sin\alpha}{2k_w} \tag{3.51}$$

and intercept:

$$h|_{\dot{m}=0} = \frac{\tau_b}{\rho g \sin\alpha} \tag{3.52}$$

Using the above slope and intercept:

$$K_w = \frac{\rho^2 g b^2 \sin\alpha}{2} \frac{dh}{d\dot{m}} \tag{3.53}$$

and:

$$\tau_b = \rho g \sin\alpha \, (h_{\dot{m}=0}) \tag{3.54}$$

The experimental data for P.V.C. powder [32] show that the values of K_w and τ_b are very far from constant; unfortunately, the model of Case I presupposes K_w and τ_b to be constant. This model may only be applicable for very deep beds greater than 12 cm.

The model of Case II is very similar to the approach of Mori, et al. [21]. The mass flow rate becomes:

$$\dot{m} = \frac{\rho^2 g b^2 h^2 \sin\alpha}{2K_w h + K_b b} = F' \rho^2 g b h^2 \sin\alpha \tag{3.55}$$

where:

$$F' = \frac{1}{2K_w \frac{h}{b} + K_b} \tag{3.56}$$

F′ is a function of aspect ratio to account for an apparent viscosity. Mori, et al. [21] modeled the flow similarly and determined values for K_b and K_w by plotting experimental results of $(h \sin\alpha)/u_s$ versus (h/b). The parameters K_b and K_w in a model of Case II were found to be strongly dependent on superficial gas velocity. Rearranging Equation 3.55 gives:

$$\frac{h^2 \sin\alpha}{\dot{m}} = \frac{2K_w}{\rho^2 g b^2} h + \frac{K_b}{\rho^2 g b^2} \tag{3.57}$$

A plot of $(h^2 \sin\alpha)/\dot{m}$ versus h should yield a straight line. In actuality, a series of curves was found from data for h, $\dot{m}$, and α [32], complicating the process of determining an average value of K_w or K_b for the flow conditions.

For Case III, the relation for mass flow is:

$$\dot{m} = \frac{\rho^2 g b^2 h \sin\alpha}{K_b} \frac{h}{b} - \frac{2\rho h^2 \tau_w}{k_b} \tag{3.58}$$

Similarities of this model to those of other workers should be noted. Also bed depth seems to be less than proportionally sensitive to the mass flow (i.e., $h \propto \sqrt{\dot{m}}$).

Rearranging Equation 3.58 yields:

$$\frac{\dot{m}}{h^2} = \frac{\rho^2 g b}{K_b} \sin\alpha - \frac{2\rho \tau_w}{K_b} \tag{3.59}$$

Plotting $\dot{m}/h^2$ versus $\sin\alpha$ should yield a straight line. Actually, test data [32] yield a series of lines which are close enough to use average values of τ_w and K_b to predict behavior of P.V.C. powder.

3.4 Experimental findings in aerated open-channel flow

Several workers performed experiments with open-channel flow of aerated solids. Although most flows studied were fluidized, Ishida, et al. [12,13,14] also studied flows which were not fluidized. The first studies by Ishida, et al. had no assisting air and used very severe angles of inclination. In the later air-assisted flow studies, the angles were still quite steep, and the flow was generally not fluidized.

Ishida, et al. found five types of flow, as follows:

- Sliding flow
- Immature sliding flow
- Splashing flow
- Bubbling flow
- Gliding flow

Sliding, immature sliding, and splashing flows all occur with gas velocities below or at the minimum fluidization velocity. Bubbling and gliding flows occur with the gas flow above the minimum fluidization velocity. Sliding flow is laminar flow with a linear profile. Immature sliding flow is similar to sliding flow, but it occurs at lower angles of inclination, so that the bottom particles tend to remain stationary. Splashing flow shows repeated wave-like motion, especially at the free surface, and a more curved velocity profile near the top surface. Bubbling flow occurs above the minimum bubbling velocity at low inclination angles (low shear rates), and the velocity profile is

significantly curved. Finally, gliding flow is a fast, shallow flow in which no bubbles appear. High shear rates suppress the bubbles in gliding flow, and the flow probably has a low viscosity due to increased dense phase air flow. Gliding flow is the type of flow which occurs prior to a hydraulic jump. The main flow type of concern for coal cleaning is the bubbling flow, since the bubbling action is non-existent in the other flows.

The experimental regions of Ishida, et al. do not match the regions of interest for coal cleaning; the angle is much too steep, the fluidizing velocity ratio is too low, and the bed is very narrow (3.9 cm) and short (95.4 cm), all of which lead to very shallow bed depths (~ 0.5 to 1.0 cm).

3.4.1 *Variations in physical systems*

3.4.1.1 *Distributors*

All of the previous experimental investigators except Singh, et al. used a porous sintered medium distributor, and Singh, et al. used a unique distributor they called a Pneuslide. The Pneuslide is intended to be able to handle very hot solids. Woodcock and Mason [31] stated that the main disadvantage to fluidized solids conveying is associated with the method and quality of air distribution and type of distributor.

Based on visual observation and a minimum fluidization velocity calculation from pressure probes 11 cm above the air inlet at various positions along the length of the bed, the Pneuslide (see Figure 3.3) is supposed to have uniform air distribution. In contrast, a photograph in reference [6] shows large bubbles with an uneven distribution

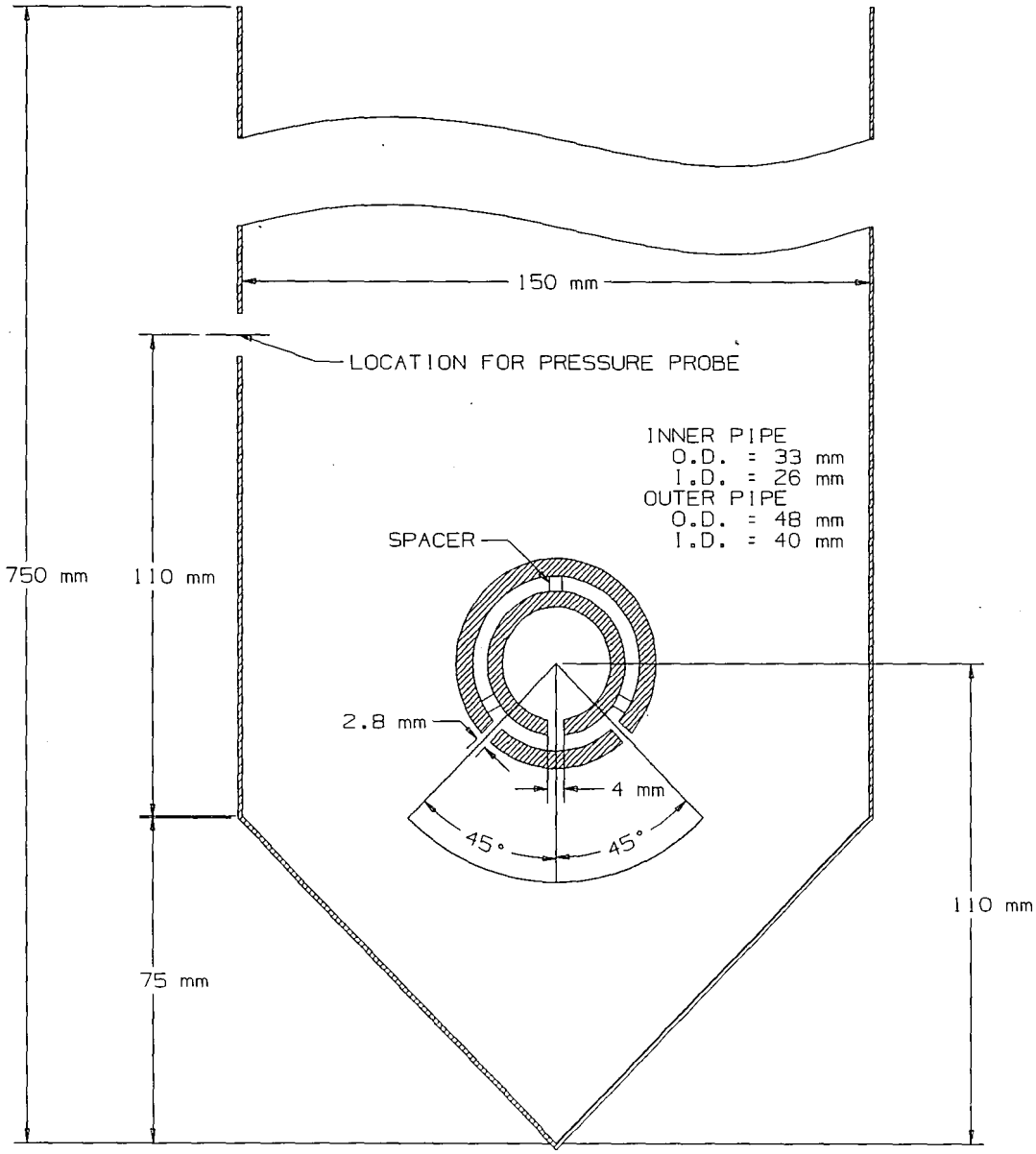

Figure 3.3
Pneuslide cross-section [27]

of bubbles being especially concentrated along the channel walls. The number of outlet holes per length of the air inlet pipe greatly affects the uniformity of the bubbling.

Singh, et al. argued that the assumption of no-slip at the distributor is more realistic than slip at the distributor. The defluidized particles on the surface of the distributor and on the bottom of the channel below the air inlet affect the ability for slip to occur. It is true that the base and air distributor of the Pneuslide are no-slip surfaces, but this is particular to only this design, and this appears to be the authors' basis for preferring the no-slip assumption when modelling. In an arbitrary open channel, the amount of slip is still undetermined, and seems to depend upon the shear rate. The Pneuslide distributor may be adequate for high bed height solids conveying, but it is certainly not adequate for the coal cleaning process.

Porous plate distributors used by most authors can be made of several sintered materials, such as plastic, steel, or glass and other ceramics. The porous plate offers the advantages of relatively uniform fluidization and the ability to use fine powders as small as 50 μm. The disadvantages are applicability to high temperature situations and the relatively high pressure drop across the plate.

3.4.1.2 *Solids mass feed methods*

Aerated solid conveying requires a strong understanding of the relationships of bed height and solids longitudinal velocity as functions of the mass flow rate, superficial gas velocity, and angle of inclination. Therefore, the mass flow rate should be as independent as possible of the air velocity and bed angle. Many workers rely on

a "flooded" feed to the upper end of the conveying channel, controlling the solids mass flow rate by adjusting a sluice gate. (See Figure 3.4.)

Singh, et al. [27] found that the material mass flow rate, $\dot{m}$, was dependent on the air velocity, u_o, until u_o was high enough for $\dot{m}$ to reach an asymptotic value. The asymptotic behavior should preferably not occur in an experimental apparatus, since any effect of u_o on $\dot{m}$ skews the actual flow behavior with respect to u_o. The bulk flow velocity, u_s, may be dependent on u_o, but $\dot{m}$ should be independent. In their experiments, Singh, et al. used a large feed chute, which increased u_s in the feed chute as u_o increased, thus causing $\dot{m}$ to increase with u_o due to its dependence on u_s. (See Figure 3.5 for a diagram of feed chute arrangement.)

Woodcock and Mason [31] stated that some reported experimental data has been obtained using flooded feed principles. This does appear to have caused misinterpretation of the resulting relations of $\dot{m}$ versus channel slope, α, and u_o. Figure 3.6 gives an anticipated form of this behavior. Woodcock and Mason reported that $\dot{m}$ should be independent of u_o and α, allowing study of the relations of bed height versus u_o, α, and $\dot{m}$.

3.4.2 *Experimental procedures of others*

3.4.2.1 *Bed height*

The height of the flowing fluidized bed can be measured either with linear scales along the side of the channel or by measuring the pressure drop through the bed.

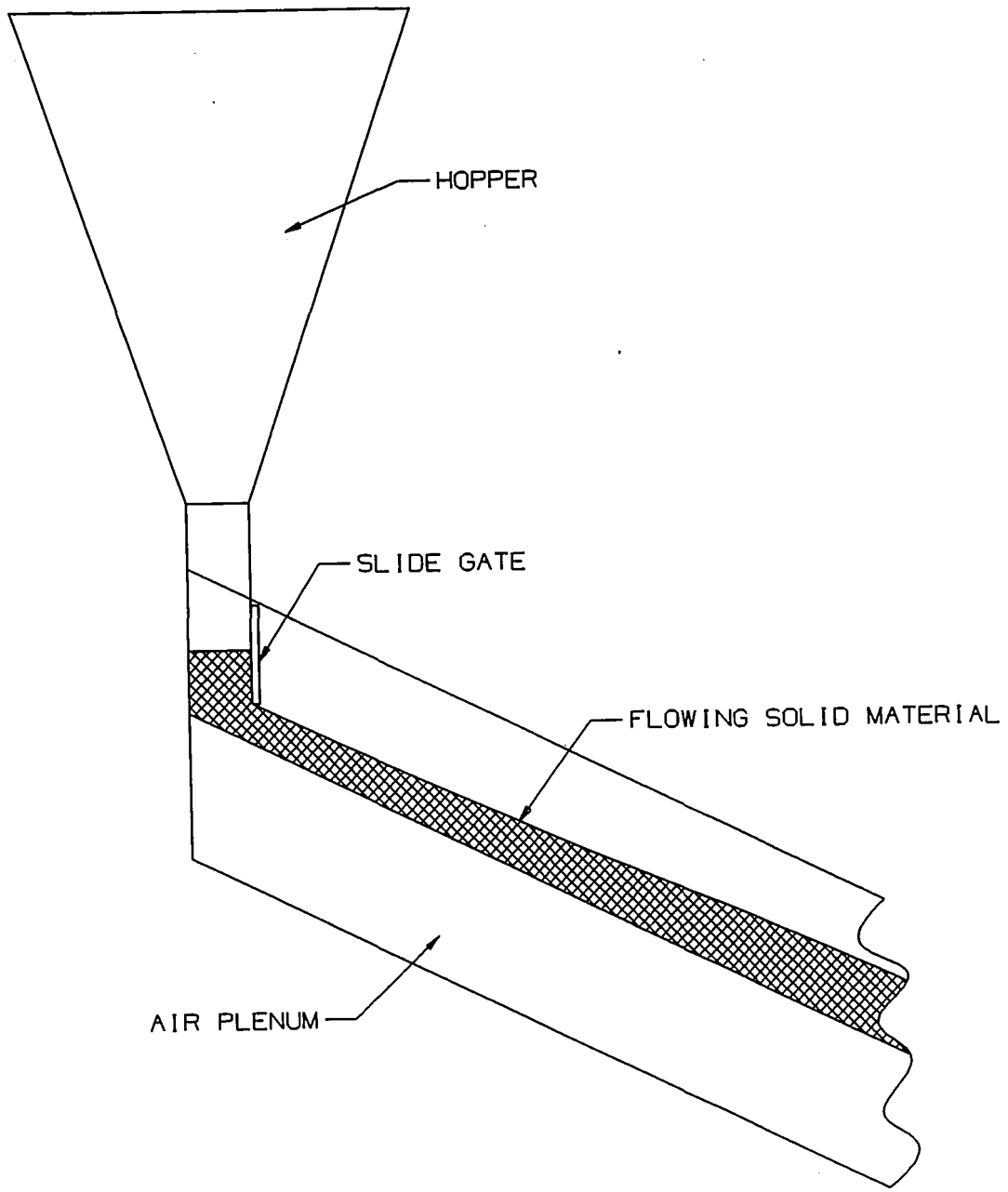

Figure 3.4
Flooded solids mass feed from hopper

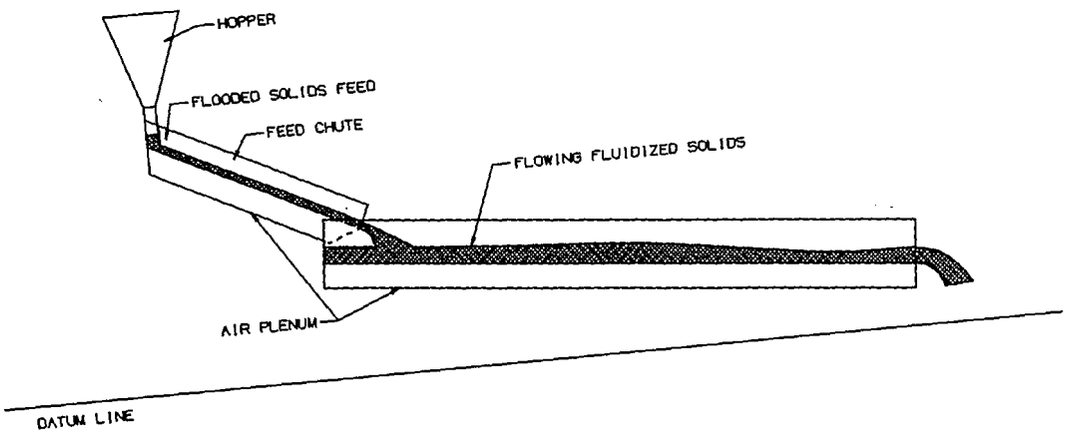

Figure 3.5
Feed chute mass flow to inclined open channel

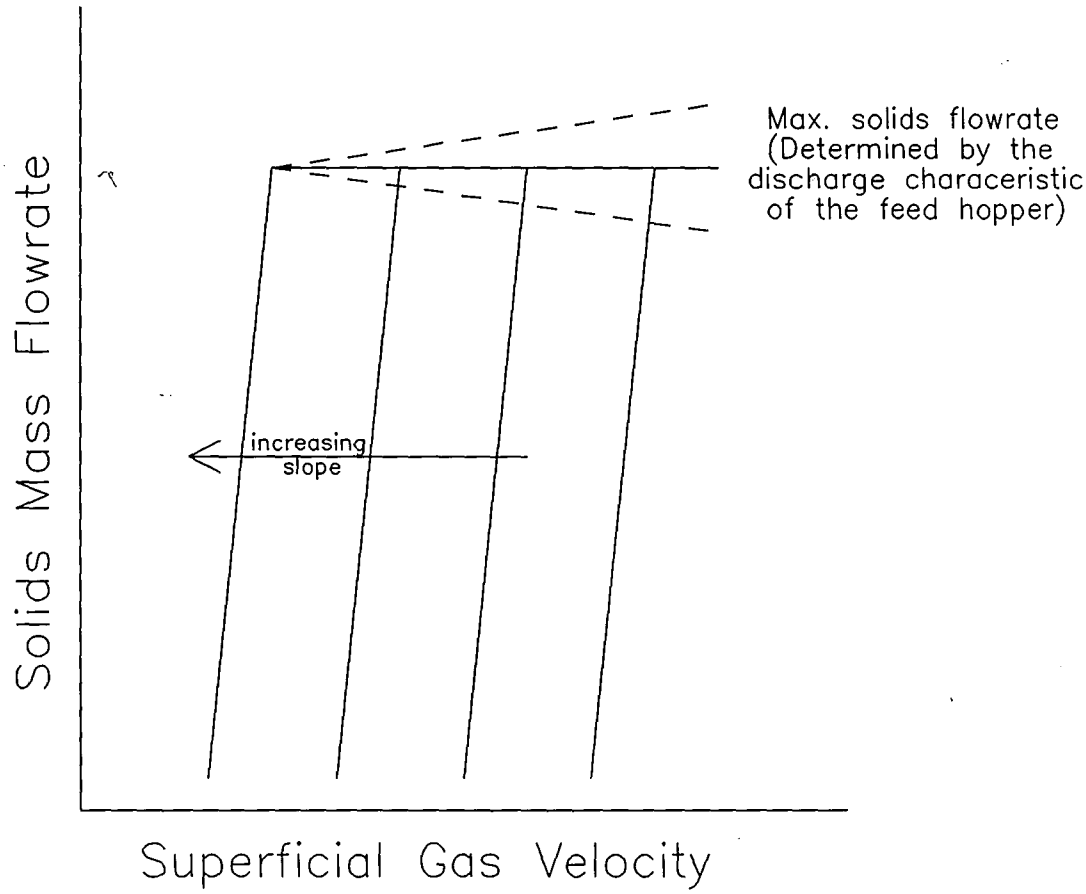

Figure 3.6
Anticipated form of mass feed from feed chute or flooded feed [31]

Singh, et al. [27] measured the pressure at a point a known distance above the air inlet. An alternative method would be to measure the pressure in the plenum, knowing the pressure drop across the distributor at the particular superficial air velocity. Knowing the pressure drop, the relation:

$$h = \frac{\Delta P}{\rho g}$$

determines the bed depth, h. The above determination of h depends greatly on an accurate knowledge of the density, usually determined in a stationary bed. Therefore, this procedure can only be used for conditions of very similar bed height and low bulk flow rates. Since the bubbles grow as they rise to the surface, the average density in a deep bed can be different in a shallow bed. Also, if the bulk flow rate is high, bubble suppression will increase the fluidized material's density. Woodcock and Mason [31] stated that when using ρ_b from a stationary bed, there was a very definite visual difference in a "smooth" flowing bed and a bubbling stationary bed at the same superficial gas velocity. Gliding flow, as defined by Ishida, et al. [14], must have a very high density, which is much different from a stationary bed at the same superficial gas velocity. Gliding flow shows an additional dependence of ρ_b on the shear rate of the flow. Due to the extrapolation from stationary to flowing beds, Woodcock and Mason [32] reported that there is no difference in accuracy between pressure drop methods and direct scale reading methods in bed height measurements.

3.4.2.2 *Velocity profiles*

In order to determine the amount of slip at the walls and distributor, several workers measured velocity profiles to determine the extent of the velocity gradient. Ishida, et al. measured profiles of aerated solid flow with an optical probe [12], and Botterill, et al. used a small turbine element [5]. Any velocity probe or element must be small, sensitive, and non-disturbing to the flow, but robust enough to withstand the buffeting of the bubbles. Botterill, et al. calibrated the turbine element in a small rotating annular bed, but noted some small discrepancies when integrating the velocity profile for the bulk flow rate. Botterill and Abdul-Halim [8] found the turbine element worked very well for sand (196 μm). However, a catalyst (77 μm) tended to jam the rotor bearing, and the turbine element simply did not work at all with coarse ash (380 μm).

3.4.2.3 *Shear stress and shear rate*

Using the model for shear stress, τ, and shear rate, γ, the apparent viscosity can be determined experimentally. Again:

$$\tau = \frac{\Delta P D_e'}{4L} \tag{3.60}$$

and:

$$\gamma = \frac{3n'+1}{4n'} \frac{8V}{D_e'} \tag{3.61}$$

The above relations and their corresponding coefficients are exact only for flow in circular pipes. However, the equivalent diameter model in Newtonian fluids has proven very useful. Calculating the shear stress - shear rate relations from experimental data requires knowing the height and width of the flow, the pressure drop along the length of a test-section in the flow, and the bulk flow velocity. After determining ΔP, D_e', and V, a logarithmic plot of $\frac{\Delta P D_e'}{4L}$ versus $\frac{8V}{D_e'}$ determines k′ and n′, and gives an indication of the apparent viscosity.

Botterill, et al. [8] measured the bulk flow velocity using a triangular float filled with ballast and submerged to a depth within ten percent of the total bed depth from the distributor. The authors stated that this "left much to be desired." However, they did state that they felt the velocity measurement had only a $\pm 5\%$ error. More than likely, this is a large underestimation of the error.

Since shear stress differed at the walls and the distributor, the equivalent diameter was altered using the modified hydraulic diameter, D_e', instead of D_e. Forces measured on a sliding wall with attached strain gauges gave an indication of the ratio of

stresses at the walls and at the distributor, τ_{wall} and τ_{dist}, respectively. The total pressure drop force is equal to the sum of the drag forces at the walls and distributor.

$$F_{\Delta P} = F_{wall} + F_{dist} \tag{3.62}$$

where:

$$\tau_{dist} = \frac{F_{\Delta P} - F_{wall}}{Lw} \tag{3.63}$$

$$\tau_{wall} = \frac{F_{wall}}{2hL} \tag{3.64}$$

$$\tau_{\Delta P} = \frac{\Delta P D_e'}{4L} \tag{3.65}$$

and:

$$F_{\Delta P} = \Delta P \times Flow\ Area = \Delta P h_{ave} w \tag{3.66}$$

Finally:

$$\frac{\tau_{dist}}{\tau_{wall}} = \frac{2h_{ave}}{wF_{wall}} \left(\Delta P w h_{ave} - F_{wall} \right) \tag{3.67}$$

Botterill used two versions of K in D_e'. The first is the ratio of drag force at the base to the total drag force, and the second is the ratio τ_{dist}/τ_{wall}. Since K is effectively multiplied by an area, the second representation of K is preferred. Therefore:

$$D_e' = \frac{4wh}{\frac{\tau_{dist}}{\tau_{wall}} w + 2h} \tag{3.68}$$

The above idea developed because, as the height becomes very large, the shear at the distributor is negligible, and the product $K \cdot w$ should approach zero [6].

Wall drag experiments and air slide experiments of Botterill et al. [6,8] gave information on the effect of the distributor. The wall drag measurements yielded τ_{dist}/τ_{wall} data, though bubbles caused some noise in the strain gauge signals. The very shallow bed depths (< 2.0 cm) and low aspect ratios in the air slide experiments resulted in no bubbling and very little wall drag interaction. The air slide experiments gave distributor drag information directly from pressure drop data.

3.4.3 *Flow behavior*

3.4.3.1 *Apparent viscosity*

In an aerated flow of solid particles, the air flow causes lubrication of the particles. As the air velocity increases, this lubrication increases until bubbles begin to form. The bubbling action begins to drain air from the dense phase, thus decreasing the

lubrication and increasing the apparent viscosity. Due to bubble growth, the bed height is the most important parameter affecting the apparent viscosity.

In bubbling flow, the bubbles tend to draw air from the dense phase. Also, as the bubble enlarges, the local region of defluidization around the bubble increases, thereby increasing the viscosity with increases in air velocity and bed height. When the bed height of fluidized bauxilite increased from 9.0 cm to 21.0 cm at a constant u_o, the viscosity increased by a factor of 5 [3]. Using sand in air slide experiments with low bed height (therefore, no bubbling) the viscosity decreased tenfold as the airflow increased from 1.25 u_{mf} to 2.5 u_{mf}, thereby increasing the amount of dense phase lubrication with u_o. There is a possible minimum apparent viscosity which occurs when the competing effects of increased dense-phase lubrication and increased bubble growth have a resultant maximum lubrication. For 200 μm sand, this point was found to occur at about 2.0 u_{mf} [6]. Table 3.1 summarizes the trends with respect to air velocity.

Table 3.1
Three viscosity regions of fluidized solids

1.	Decreasing viscosity with increasing u_o, which increases bed depth and decreases density (material dependent and $u_o < u_{mf}$).
2.	Steeply decreasing viscosity at the onset of fluidization.
3.	Increasing viscosity with increasing bubble size and air velocity.

Botterill and Bessant [5] found that μ_{app} decreased with particle size, d_p. Adding smaller particles or "fines" to coarser material may lower the viscosity of the coarser material. Changes in particle size distribution, which lead to changes in

viscosity, may actually be due to changes in the minimum fluidization velocity, u_{mf}, of the bed material. McGuigan and Pugh [18] repeated very little dependence of viscosity on d_p when comparing results at similar fluidizing air velocity ratios, u_o/u_{mf}.

3.4.3.2 *Bed height and transverse velocity*

The general trends of flowing aerated solids with no discrete resistance points, such as a defluidized area or an interface between channel sections, are summarized as follows:

General Trends

1. Bed height, h, decreases with increases in angle of inclination, α, and u_o/u_{mf}.
2. Bed height increases with an increase in $\dot{m}$.
3. Solids transverse velocity, u_s, increases as $\dot{m}$, α, and u_o/u_{mf} increase.
4. As α increases, u_o required for flow begins to decrease.

As described in Section 4, the findings of the present work agree with the above, with one exception. Due to methods of mass input, there was significant momentum flux into the flowing bed, and, due to defluidized areas between sections of the channel, discrete point resistances to the flow existed. In the present study, it was observed that increasing $\dot{m}$ increased the momentum influx and allowed easier flow past the resistances. Therefore, an increase in $\dot{m}$ at low $\dot{m}$ decreased h and, as in the above table, increased u_s.

Again, speaking in general terms of the work of others, Woodcock and Mason [32] found an increase in $\dot{m}$ at a constant u_o, giving a non-linear increase in h_{ave}

and u_s. Theoretical Case III [32] supports the non-linearity of $\dot{m}$, h, and u_s in the following equation:

$$\dot{m} = \frac{\rho^2 g b^2 h \sin\alpha}{K_b} \frac{h}{b} - \frac{2\rho h^2 \tau_w}{K_b} \qquad (3.69)$$

Equation 3.69 displays the dependence of $\dot{m}$ on h and α. The bed depth is less than linearly sensitive to $\dot{m}$ and linearly to α, since above:

$$h \propto \sqrt{\dot{m}}$$

and, for small angles, $\sin\alpha \approx \alpha$, so:

$$h \propto \alpha$$

Woodcock and Mason found a set of parallel knee-shaped curves at various solids mass flow rates, which indicate optimum values of inclination and air velocity for solids conveying.

Furthermore, Woodcock and Mason observed that P.V.C. flowed at a higher bed height than sand when both were at their optimum inclination and air velocity for a given mass flow. This is consistent with P.V.C.'s lower density and its need for a higher bed height to generate the driving force for flow. The flow of aerate solids is governed by the driving forces and resistances of the system.

3.4.4 *Electrostatic charging effects*

Woodcock and Mason [30,31,32] found electrostatic effects to be of great importance when conveying fluidized P.V.C. powder (dp $\simeq$ 140 μm, $\rho_b \simeq 0.5$ g/cm^3, and $u_{mf} \simeq 2.3$ cm/s). Due to the charging effects, the pressure drop across the bed material increased with time after start-up until reaching an equilibrium. This increase in pressure drop with time is very similar to behavior in two phase gas-solids flow in pipes, where it helps to keep the humidity high. Even when Woodcock and Mason kept the humidity high, the electrostatic effect was quite evident.

Experimentally, a great problem exists if the inter-particle forces vary with time. The charging changes the nature of the flowing bed (see Figure 3.7). Also, the charging greatly affects the minimum fluidization velocity. Woodcock followed the procedure below using P.V.C. powder [31]:

1. Slowly fluidize to and beyond u_{mf} (increasing u_o).
2. Bubble vigorously and allow to reach equilibrium electrostatic charge.
3. Reduce u_o to well below u_{mf}.
4. Increase u_o to beyond current u_{mf}.

After the bubbling, the u_{mf} point was much less distinct and fluidization was not as uniform as when first fluidized (see Figure 3.8).

In the flowing bed, the bed's physical appearance was markedly different from the first uncharged runs. After charging, a rough, fluffy texture replaced the previous smooth surface and little bubbling occurred. The material tended to "slide" down the channel and was not fully fluidized. Velocity profiles for this condition were

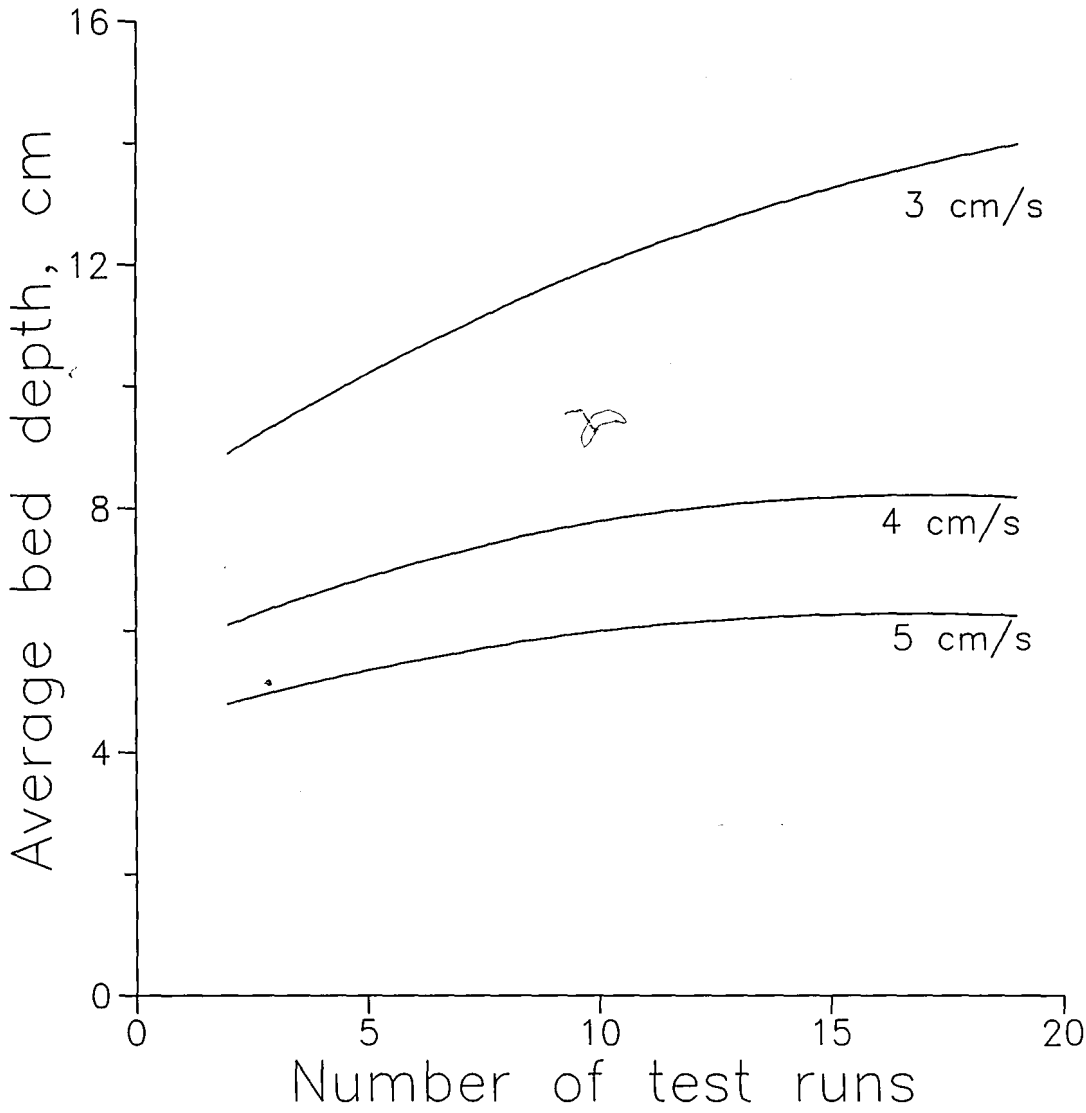

Figure 3.7
Trends of increasing bed depth with running time,
as a result of increased electrostatic forces [30]

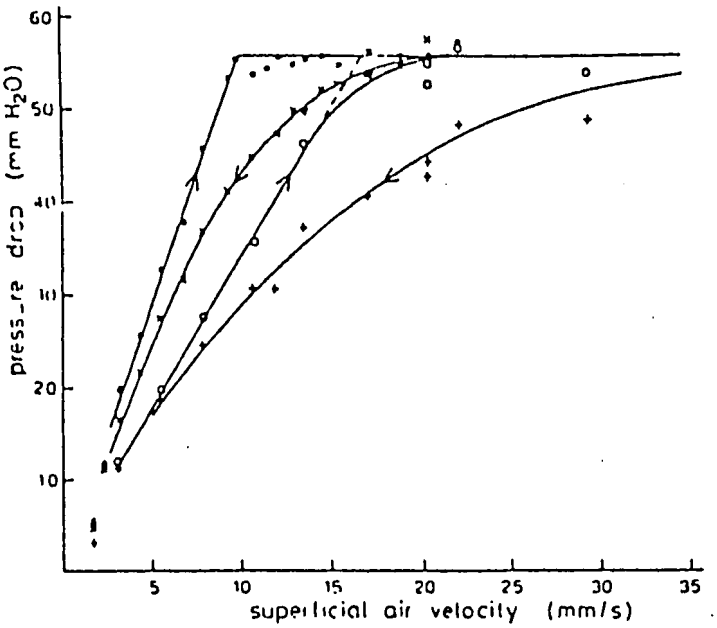

Figure 3.8
Variation of pressure drop across a stationary bed of P.V.C. powder with superficial gas velocity, showing the effect of charging [31]

not investigated.

3.4.5 *Velocity profile results*

Botterill, et al. [5,6,8] studied the velocity profiles of several materials, including an extensively studied 200 μm sand. They found the profiles to be slightly asymmetric in the horizontal plane due to air maldistribution. Most importantly, though, they found the sand to have a semi-plug velocity profile with varied slip depending on bed dimensions and fluidizing velocity. A semi-plug flow has a velocity profile that exhibits slip or partial slip along one or more surfaces, and has one or more other surfaces on which the flow has no slip (See Figure 3.9 and 3.10. Note that in Figure 3.10, unique symbols represent different bed depths.)

Large slip across the distributor seemed to occur, resulting in semi-plug flow. Small scale viscometer and wall drag measurements supported the semi-plug profile [5]. There exist two possible mechanisms allowing the slip at the distributor. First, semi-plug flow could indicate a possible air layer at the distributor. Secondly, the semi-plug flow could indicate a more complex dense-phase slip mechanism similar to that in solid-liquid dispersions [5]. This second slip mechanism would be sensitive to u_o and bed width. To support this idea, it has been seen that $\tau_{\Delta P}$ is a function of width and the slip factor in the D_e' correlation is a function of the distributor dimensions and parameters.

By using a power-law model for a pseudo-plastic, shear curve data can determine values for the power law constants, k′ and n′. Applying the finite difference approach of Wheeler and Wissler [29] for flow in rectangular ducts, Botterill and Bessant

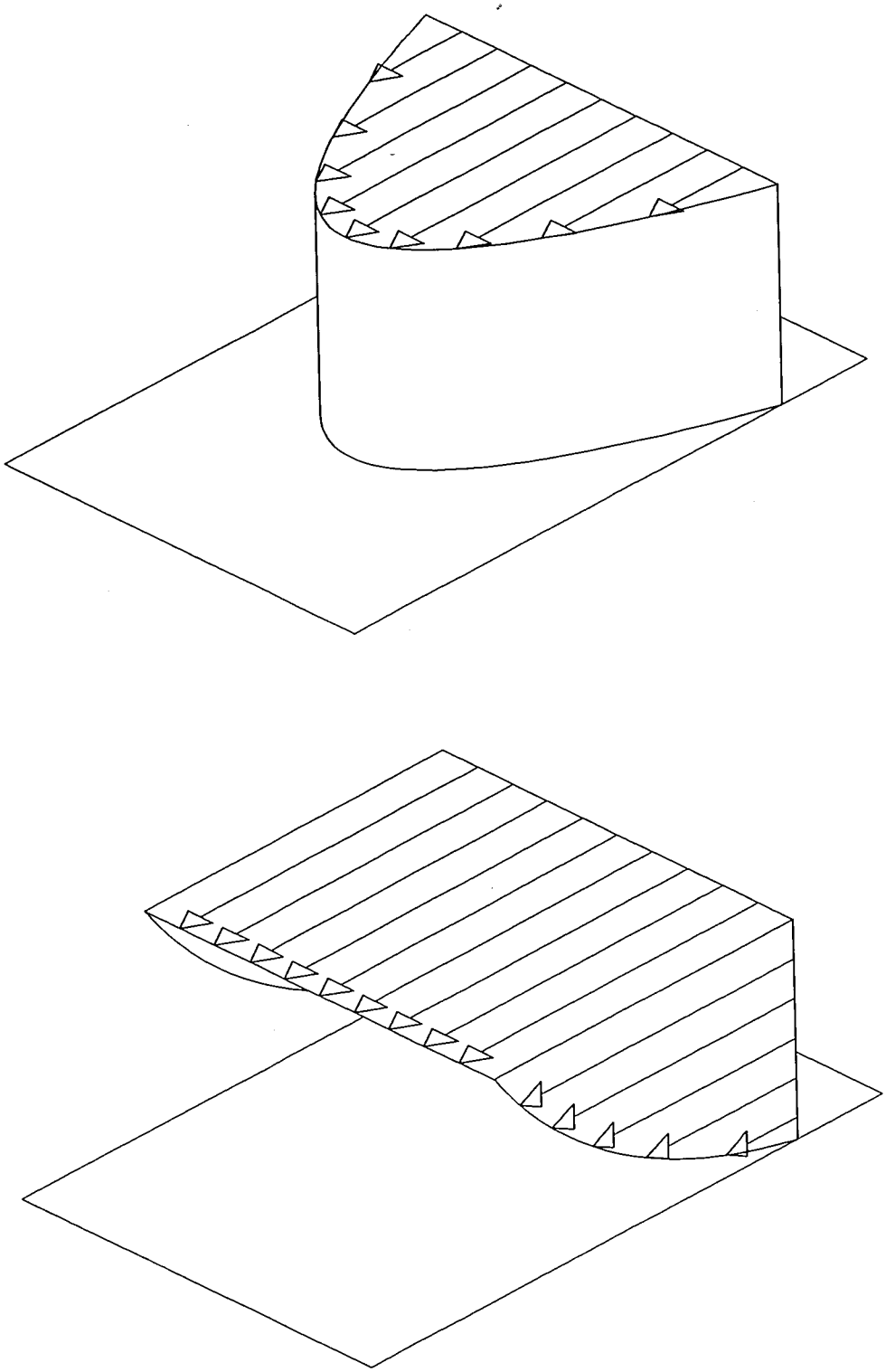

Figure 3.9
Semi-plug velocity profiles

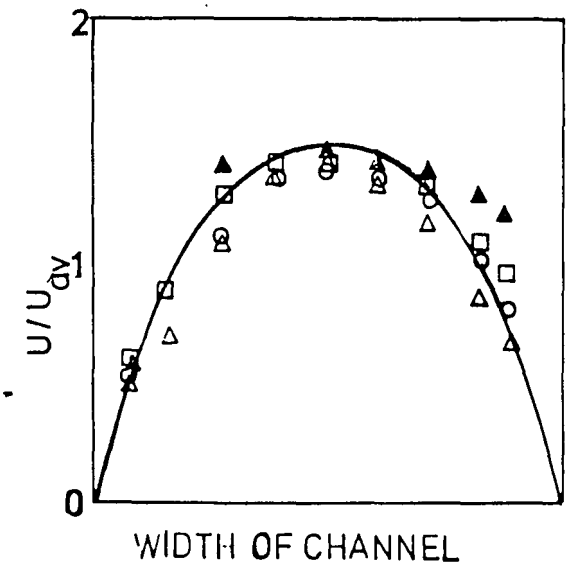

Figure 3.10
Typical measured velocity profiles, with slip at the distributor [7]
Bed height 11.8 cm; width = 18.0 cm
$u_o = 2.0\ u_{mf}$

[5] predicted a velocity profile, which matches well with the actual measured values. (See Figure 3.11. Note that in Figure 3.11, unique symbols represent different bed depths.)

Later, the authors [6] stated that the above approach worked well if the drag at the wall and the distributor were of the same magnitude. Poorer agreement to experimental measurements exists, however, when the aspect ratio becomes high and the distributor drag is negligible compared to the wall drag. Controlling the slip factor appears to be more important than controlling the power-law indices, again, until a bed has a very high aspect ratio. (See Table 3.2.)

Table 3.2
The calculated effect of aspect ratio and slip on the total flow rate [6]

	V_{max}/V_{ave} (dimensionless)			
	$n' = 1.0$		$n' = 0.65$	
Channel Aspect Ratio	No Slip	50% Base Slip	No Slip	50% Base Slip
0.430	2.13	1.76	1.91	1.61
0.655	2.11	1.76	1.90	1.62
0.840	2.07	1.75	1.88	1.62
25.0	1.57	1.57	1.45	1.45
Parallel Plates	1.51	1.51	1.48*	1.48*

* For an n value of 0.9

From flow experiments, Botterill, et al. [6] found that at low u_o/u_{mf} and low bulk flow rates, the profiles suggest drag of similar magnitude at the distributor and walls. However, at high u_o/u_{mf} and high solids shear rates, there appeared to be a negligible velocity gradient in the vertical direction, suggesting negligible drag at the base

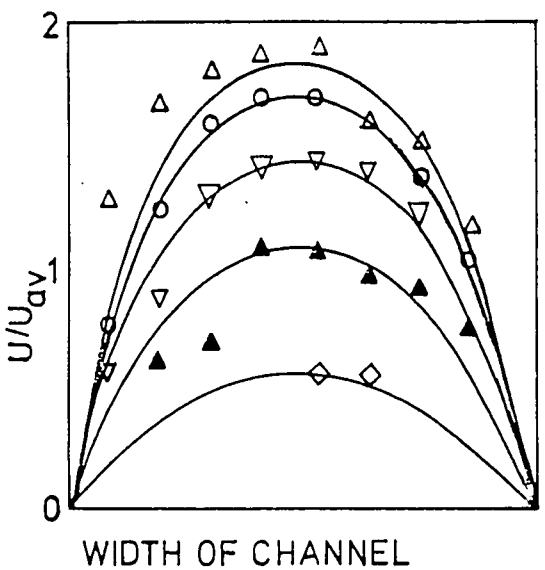

Figure 3.11
Typical measured and predicted velocity profiles with negligible slip at the distributor [7]
Bed height 11.8 cm; width 18.0 cm
$u_o = 1.75\ u_{mf}$

or distributor. In air slide experiments (low height, no bubbling), the base slip was lowest for low u_o and had a maximum slip velocity at about 2 u_{mf}. This air velocity corresponds to a minimum viscosity found prior to this experiment with the same sand.

Judging from the predicted profiles, the authors felt the profiles to be relatively flat. The parameter V_{max}/V_{ave} was between 1.5 and 1.8, where V_{ave} is calculated from the condition of zero slip at the base. Prediction of velocity profiles agrees best with experimental results at low shear rates, which is consistent with the finding of greater slip at higher shear rates. The velocity profile prediction is quite sensitive to the slip prediction.

Ishida, et al. [12,13,14] studied velocity profiles for aerated solids at conditions generally inappropriate for coal cleaning, although several of their results are rather interesting. They studied flowing solids at high inclination with no fluidizing air and found nearly linear profiles. Also at high angles ($\sim$ 14° and 24°), they studied aerated glass beads at low fluidizing velocities. The bed depths were between 0.5 and 1.0 cm and virtually no slip was seen at the distributor.

Also, as $\dot{m}$ increased at constant u_o and α, the profile followed the same path and shape, but the bed depth increased (see Figure 3.12.) The profile, again, was nearly linear at the bottom, but became curved at the top as bed depth increased. When u_o

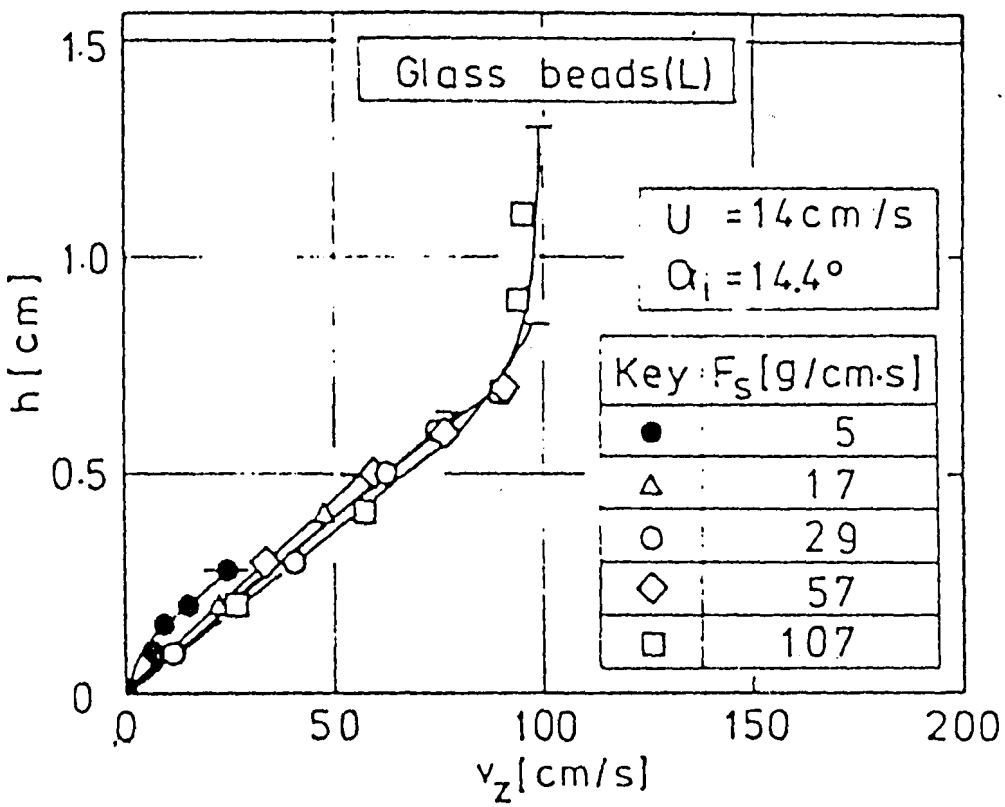

Figure 3.12
Effect of feed rate of particles on the velocity profile [13]

increased and α was lower ($\simeq$ 14°), bubbling occurred and the profile was much more curved (see Figure 3.13). For sliding flow, their theory predicted the profile as:

$$v_s = \frac{\rho g \sin\alpha_i - k_\tau}{k_n} h \qquad for\ \alpha_i \geq \alpha_{ic}, \tag{3.70}$$

which supports the linear velocity profile, and the gradient is independent of bed height. Unfortunately, these conditions are not suitable for coal cleaning, but the results can be qualitatively extrapolated to other conditions.

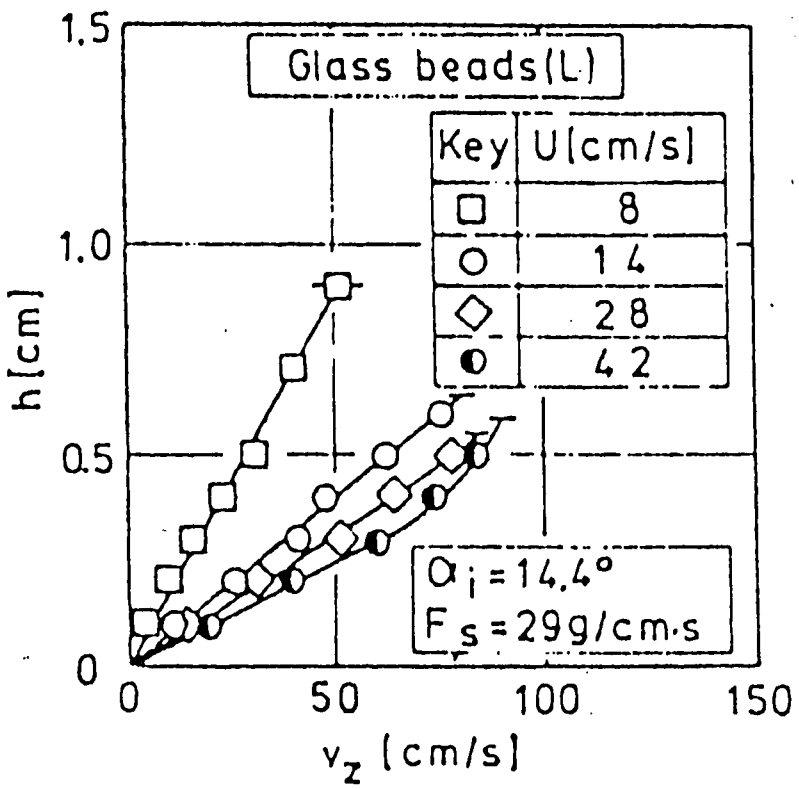

Figure 3.13
Curved velocity profile of bubbling flow [13]

4 Continuous coal cleaning

4.1 Introduction

Previous coal cleaning tests performed by Sahan [23] and others were carried out in a batch fluidized bed. Since a batch bed system is not feasible for commercial, large-scale application, a small-scale, inclined open-channel fluidized bed was developed by Latkovic, which was used in the present study to clean coal in a continuous operating mode [17]. Theoretical predictions of inclined bubbling fluidized flow have so far not been well developed, and the difficulties in prediction are even greater for a binary mixture of coal and magnetite. The mixture's large density variation causes exceptionally large inhomogeneity, for which no theoretical model of binary mixtures of solids is known. In developing the ability to remove impurities from coal in an inclined bed, a thorough knowledge of the flow behavior of the bed is needed. This investigation emphasized flow experiments and coal cleaning tests in the inclined bed.

Latkovic studied the flow behavior of 139 μm magnetite in the 1.3 m section of the inclined fluidized bed. He determined the effects of channel inclination and superficial gas velocity on the bed height profile, the average bed height, and the float residence time in the 1.3 m section of the open channel. In order to extend the residence time, Latkovic added the 1.0 m section to the end of system. This enabled placing a separator gap in between the two bed sections. During the present study, the added

0.3 m section enabled the residence time to be increased to values closer to the desired processing times of the cleaning process.

The flow studies and continuous coal cleaning experiments were performed in a 2.6 m long by 10 cm wide inclined fluidized open channel using feed hoppers to supply material to the bed. (See Figure 4.1.) Magnetite flow regime experiments yielded information on average bed height, bed height variation along the length of the channel, and residence time of a surface float, all of which depend on variations in angle of inclination, solids mass flow rate, and superficial gas velocity. To further understand the relation between residence time of a surface float and the average processing time of the coal, float tests were performed using floats positioned at various depths. Information on the flow characteristics of the separator gap, which separated the refuse and product portions of the fluidized mixture, was also needed for the continuous coal tests. Using information obtained from the above work, continuous coal cleaning tests were performed and compared with batch bed results at the same processing conditions.

4.2 Experimental apparatus

The inclined bed apparatus is shown in Figure 4.1. It consists of three sections (1.3 m, 1.0 m, and 0.3 m), each with an air plenum supplying air to the bed material via a sintered glass porous plate distributor (see Figure 4.2). The porous plate has a relatively high pressure drop, which allows uniform air distribution. Also, the pores are approximately 15 μm, which allows use of fine particles.

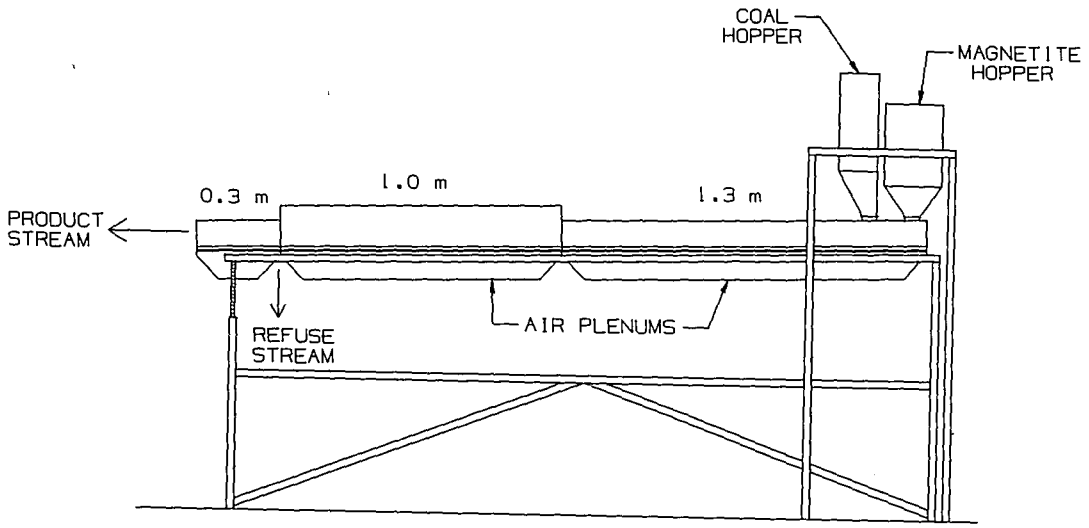

Figure 4.1
Open-channel inclined fluidized bed used for continuous coal cleaning

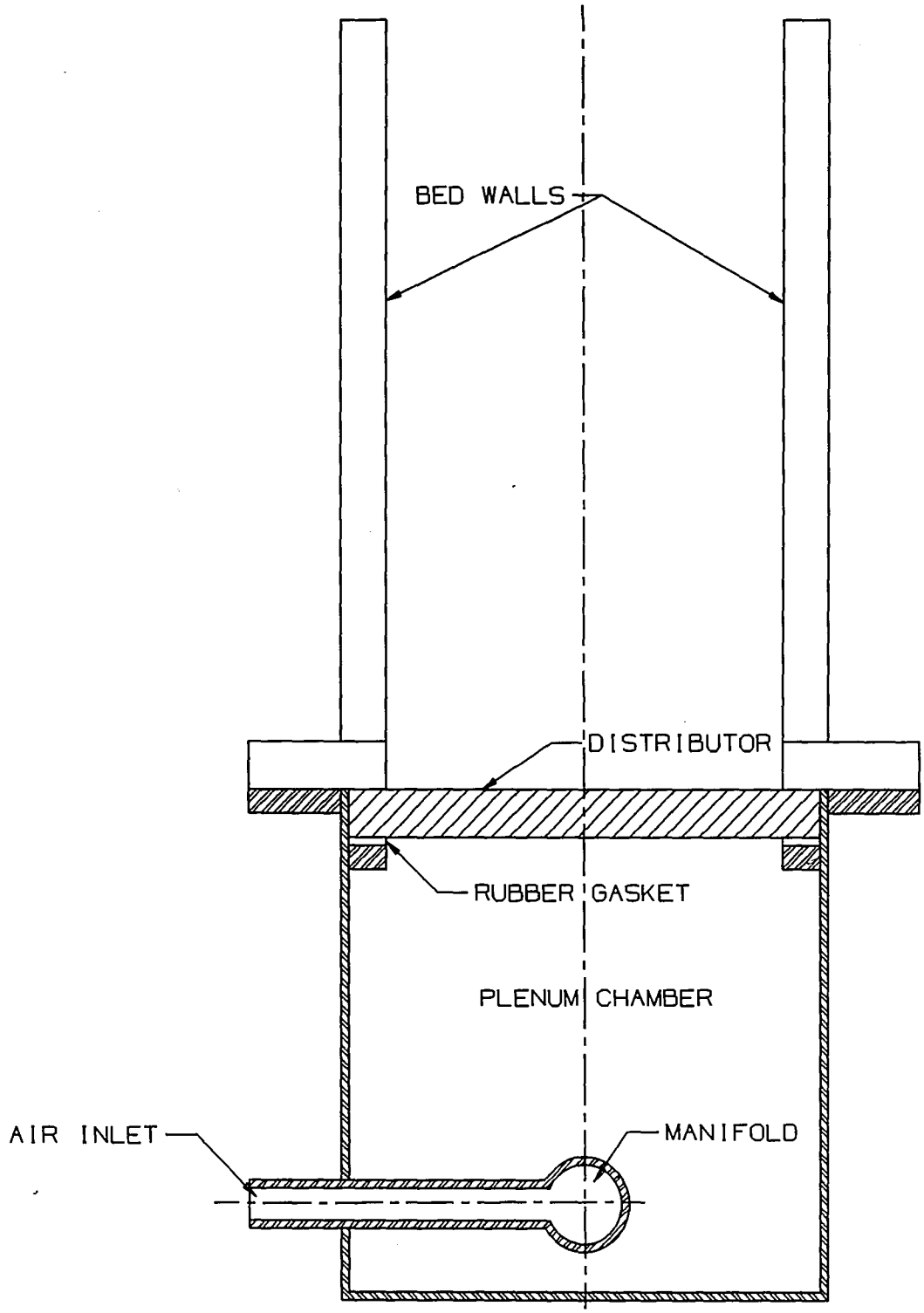

Figure 4.2
Cross-sectional view of open channel, showing air plenum and porous sintered glass air distributor

The air supplied to the bed material originated from an Ingersoll-Rand compressor delivering up to 14 m^3/min at 6 bar. A Moore model 42 pressure regulator was used to eliminate pressure fluctuations. The flow was metered using the following Ametek, Inc. (Schutte & Koerting Division) rotameters and floats:

Bed Section	Flow Meter	Float
0.3 m	4 - HCF	44 - J
1.0 m	5 - HCF	54 - J
1.3 m	6 - HCF	64 - J

For flow correction, the pressure at the outlet was measured using a mercury U-tube manometer and the air temperature was taken to be the ambient air temperature.

Two hoppers (one each for coal and magnetite) supplied the solids mass flows and calibrated slide gates controlled the mass flow rates. Fluctuations of up to ten percent in solids flow rate due to the slip-stick motion of the bulk material in the hopper were observed. Once in the open channel, the material flowed toward the separator gap, which allowed removal of a certain amount of material from the bottom of the bed, depending on the separator aperture. The aperture could be as small as 1.0 mm and had a positioning error of $\pm$ 0.25 mm. The remaining solids fell off the end of the bed, either to be collected in a bucket or, if the material was solely magnetite, a conveyor belt returned the magnetite to the hopper.

4.3 Flow regime experiments

4.3.1 *Flow regime experimental procedure*

Magnetite with a wide size distribution (approximately -100 +140 mesh, $\bar{d}_{vsm}$ $\approx$ 114 μm, u_{mfm} = 2.1 cm/s, and u_{mb} = 2.8 cm/s) was used to study the flow regimes under various bed conditions. The experiments began by setting the inclination angle, selecting the appropriate air flow rate in each bed to give the desired superficial gas velocity, and opening the slide gate on the magnetite hopper to start the mass flow. The open-channel flow was allowed to reach steady state, i.e., no change in average bed height at a point with respect to time, after which the bed heights were measured at eleven positions along the bed. (See Table 4.1.) The bed height measurements were made using linear scales at each of the positions. Next, the time required for a surface float to travel from position three (coal inlet) to the separator gap determined the residence time. For each solids flow rate, this procedure was repeated at seven different fluidizing velocities (see below). Later, the solids mass flow rate was changed for a total of five mass flows per angle of inclination, while repeating the measurements and u_o variations. The above procedure was completed for angles of inclination of 0° and 1°, and was partially done for an angle of 1.25°. (By convention, a positive angle of inclination is downhill.) A summary of the testing conditions follows:

$$\alpha = 0°, 1°, \text{ and } 1.25°$$
$$u_o = 4.64, 5.15, 5.58, 5.99, 6.48, 6.99, \text{ and } 7.50 \text{ cm/s}$$
$$\dot{m} = 0.12, 0.32, 0.53, 0.86, 1.18 \text{ kg/s}$$

Table 4.1
Height measurement positions along the open channel

	Distance	
Position 1	19.05 cm	(Magnetite inlet)
Position 2	31.75 cm	
Position 3	44.45 cm	(Coal inlet)
Position 4	57.15 cm	
Position 5	69.85 cm	
Position 6	95.25 cm	
Position 7	120.65 cm	
Position 8	146.05 cm	
Position 9	185.42 cm	
Position 10	223.52 cm	
	232.41 cm	(Distributor Gap)
Position 11	241.30 cm	

4.3.2 *Results of flow tests with magnetite*

The important aspect of a flow regime study when applied to coal cleaning is to find a relatively constant bed depth, a float residence time which allows adequate processing time for cleaning, and an appropriate fluidized bed height. Figures 4.3 to 4.37 show the bed height profiles. These profiles consistently show lower bed heights at higher angles of inclination. Also, some flow conditions gave a fairly uniform bed height profile, while others show a strongly decreasing bed height along the bed length. Interestingly, the flow seemed to be more unsteady at low solids mass flow rates when the profile was more constant.

Figures 4.38 to 4.44 show the average bed height versus the solids mass flow at constant superficial gas velocity. The maximum and minimum of any fluctuation in bed height were measured at positions along the bed. The average bed height was calculated as the average of the midpoint of the maximum and minimum bed height at

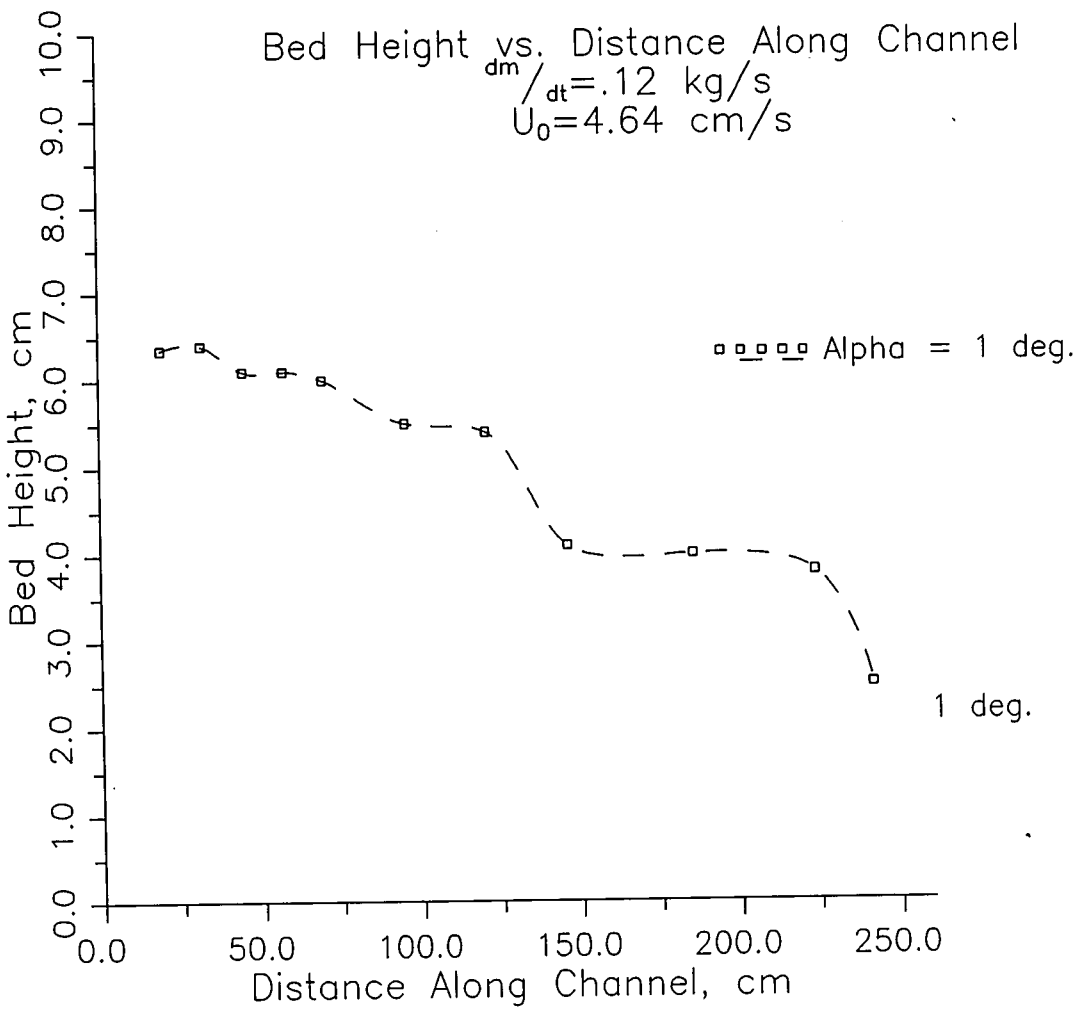

Figure 4.3
Bed height profile for -100 +140 magnetite
$\dot{m}$ = 0.12 kg/s
u_o = 4.64 cm/s

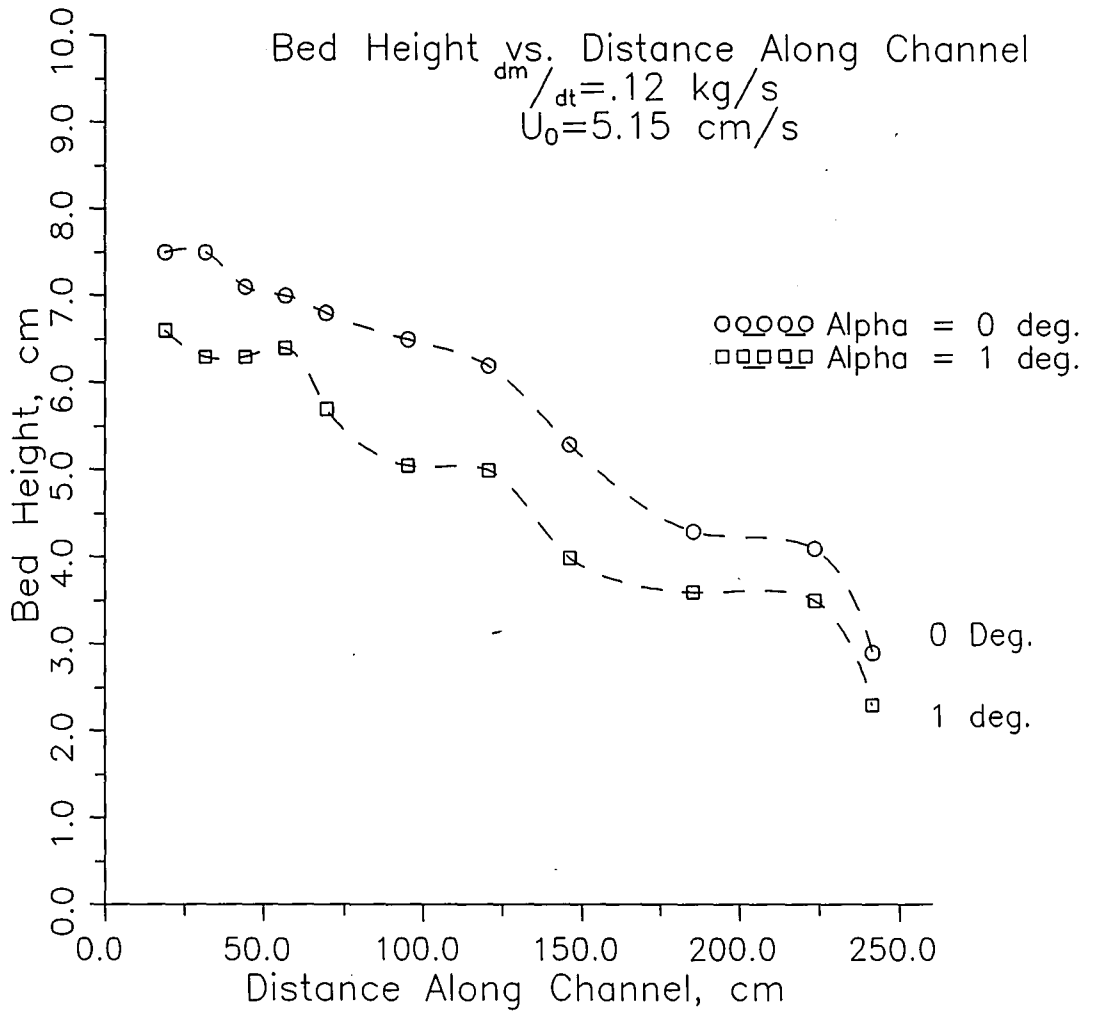

Figure 4.4
Bed height profile for -100 +140 magnetite
$\dot{m}$ = 0.12 kg/s
u_o = 5.15 cm/s

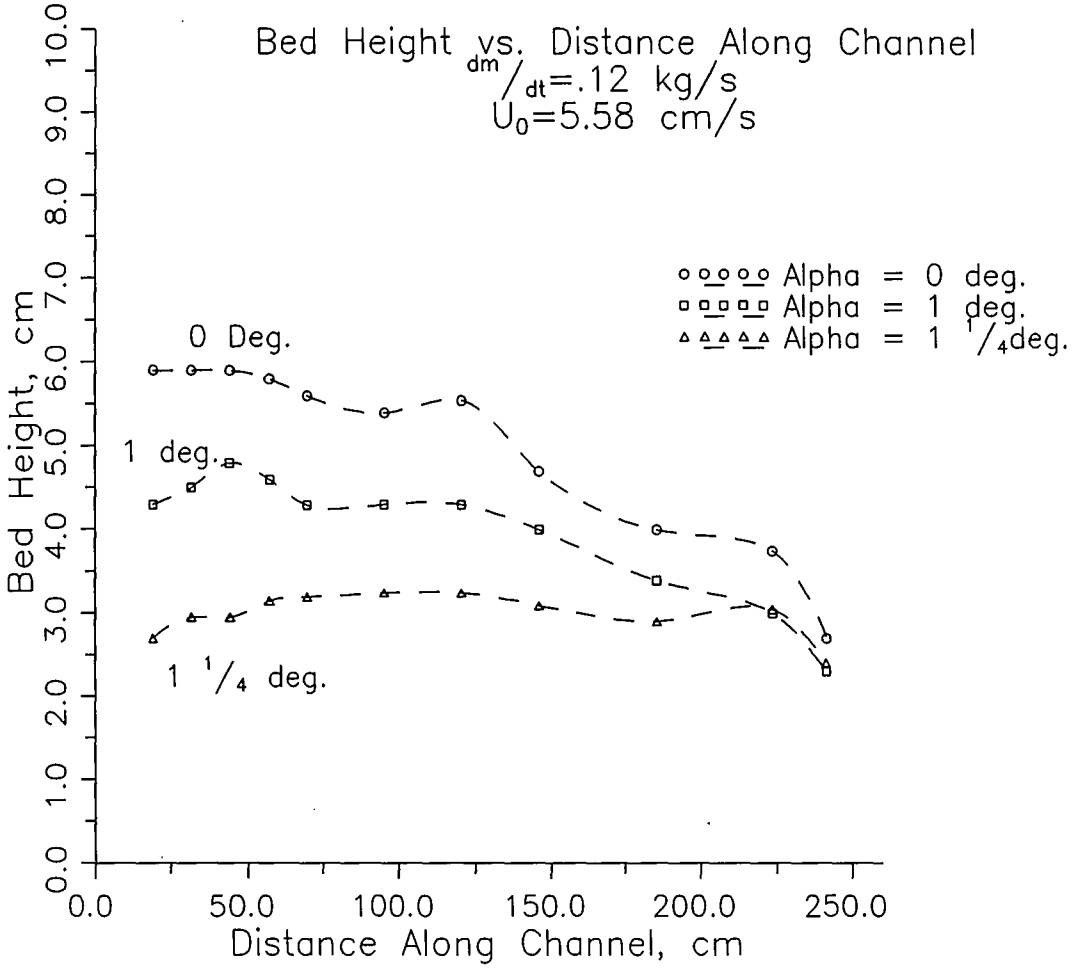

Figure 4.5
Bed height profile for -100 +140 magnetite
$\dot{m}$ = 0.12 kg/s
u_o = 5.58 cm/s

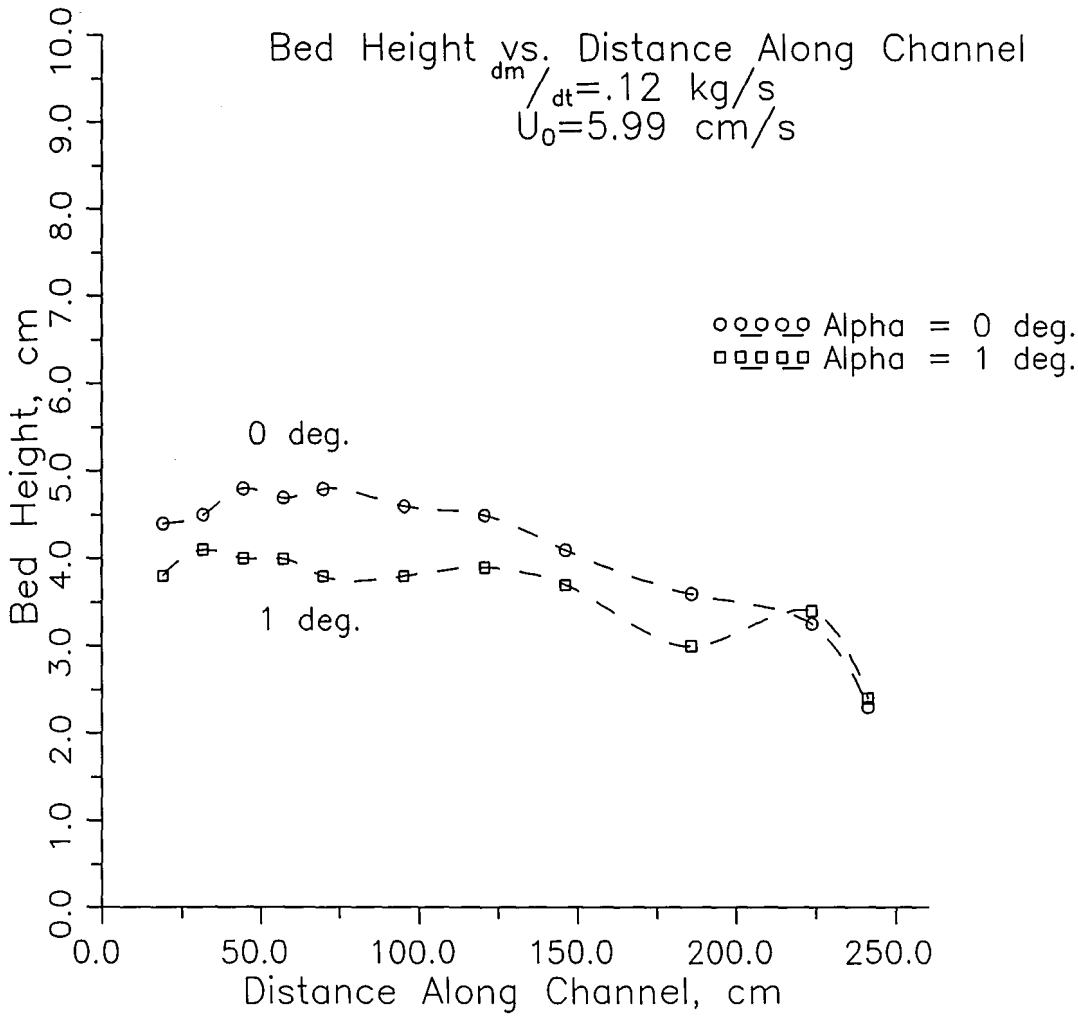

Figure 4.6
Bed height profile for -100 +140 magnetite
$\dot{m}$ = 0.12 kg/s
u_o = 5.99 cm/s

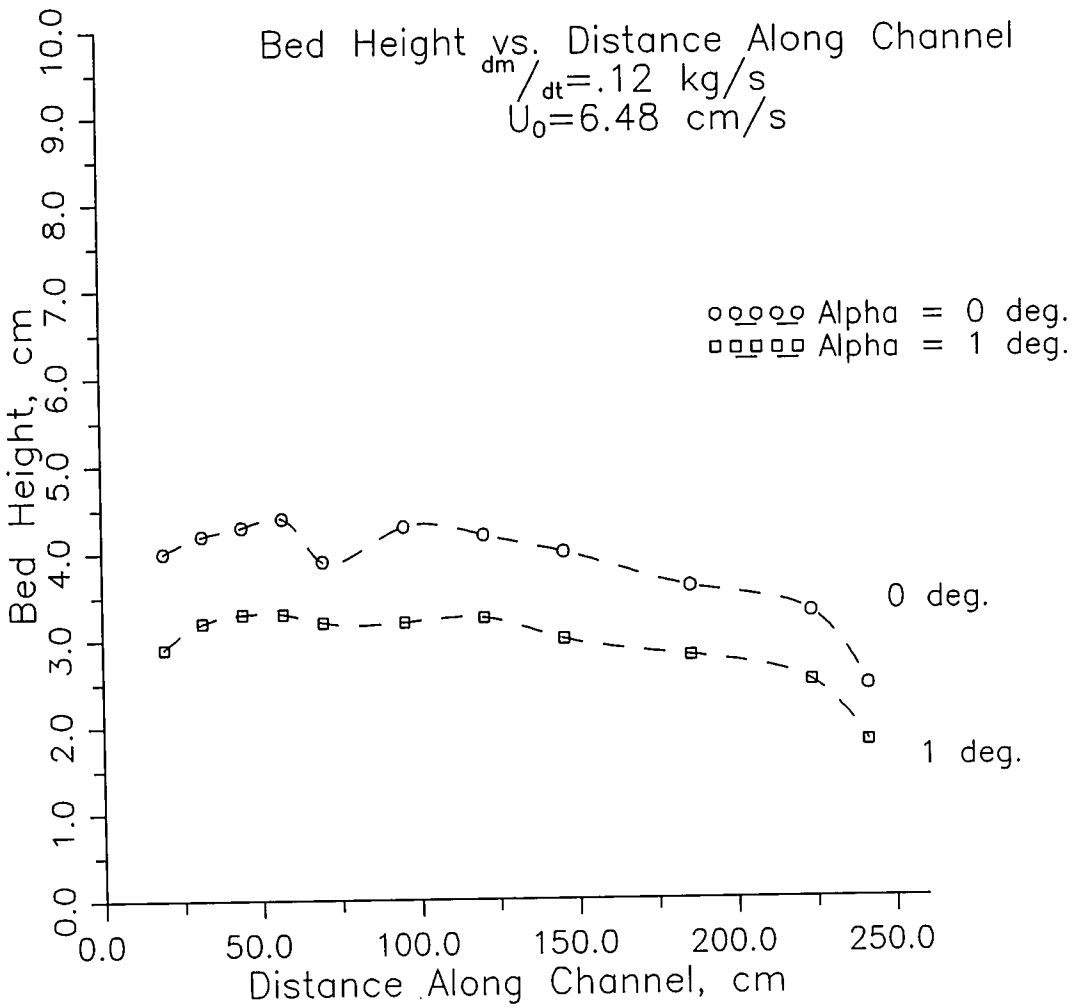

Figure 4.7
Bed height profile for -100 +140 magnetite
$\dot{m}$ = 0.12 kg/s
u_o = 6.48 cm/s

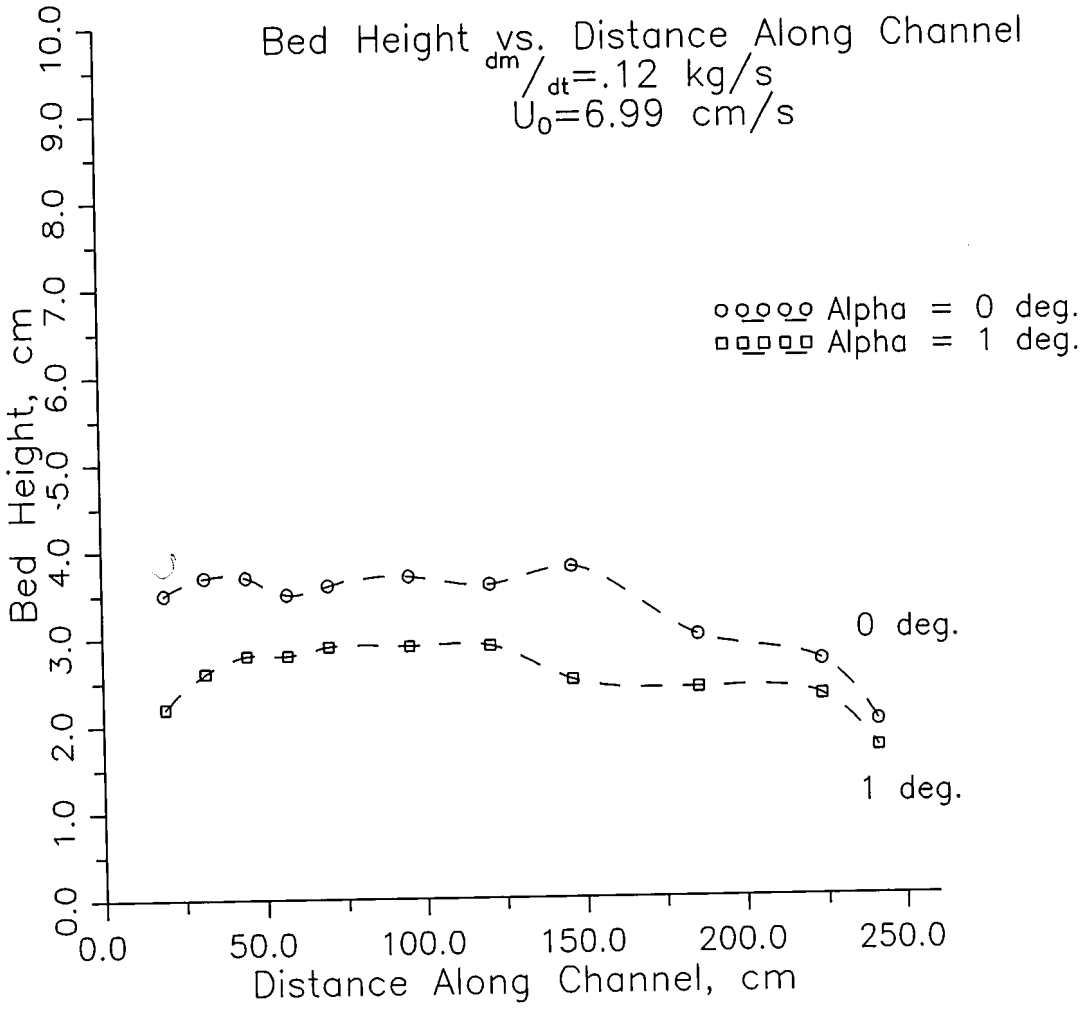

Figure 4.8
Bed height profile for -100 +140 magnetite
$\dot{m}$ = 0.12 kg/s
u_o = 6.99 cm/s

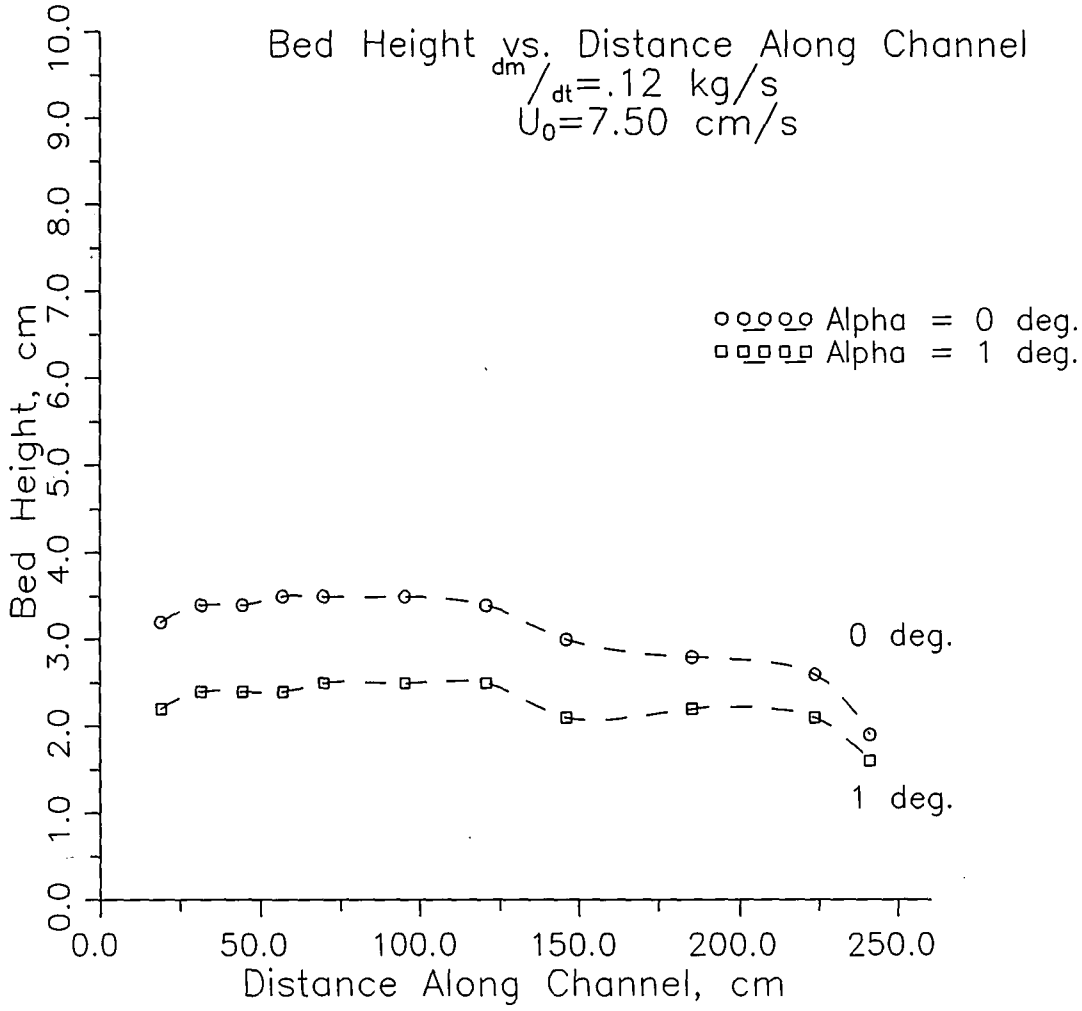

Figure 4.9
Bed height profile for -100 +140 magnetite
$\dot{m}$ = 0.12 kg/s
u_o = 7.50 cm/s

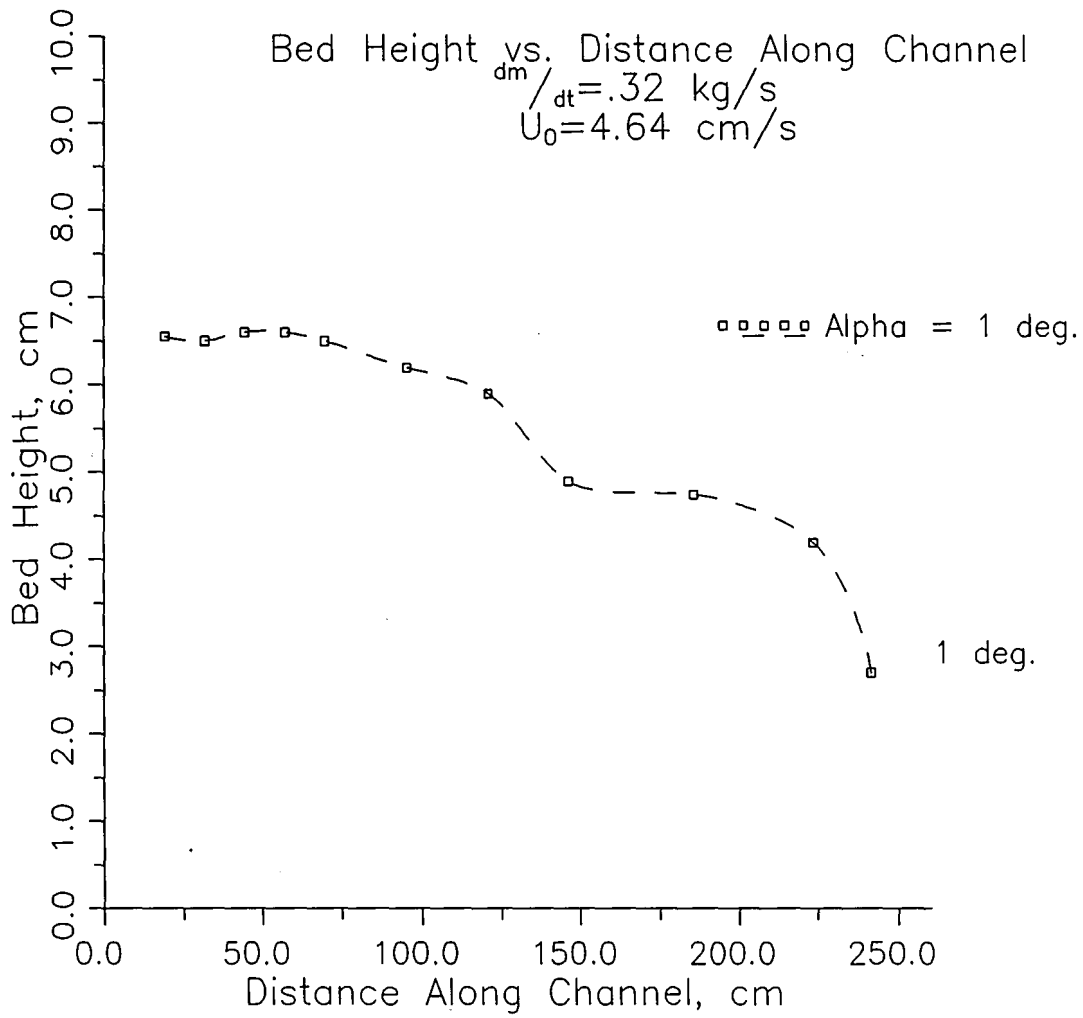

Figure 4.10
Bed height profile for -100 +140 magnetite
$\dot{m}$ = 0.32 kg/s
u_o = 4.64 cm/s

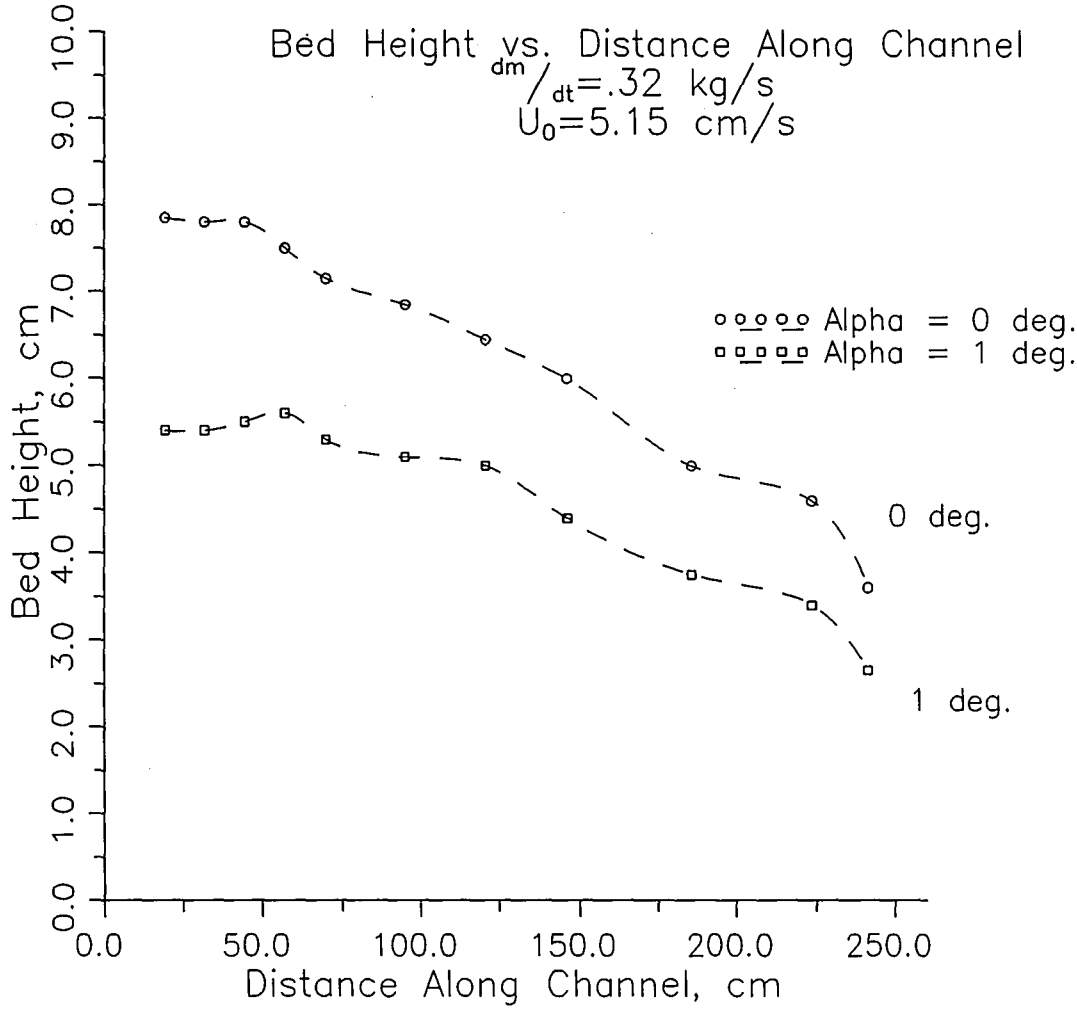

Figure 4.11
Bed height profile for -100 +140 magnetite
$\dot{m}$ = 0.32 kg/s
u_o = 5.15 cm/s

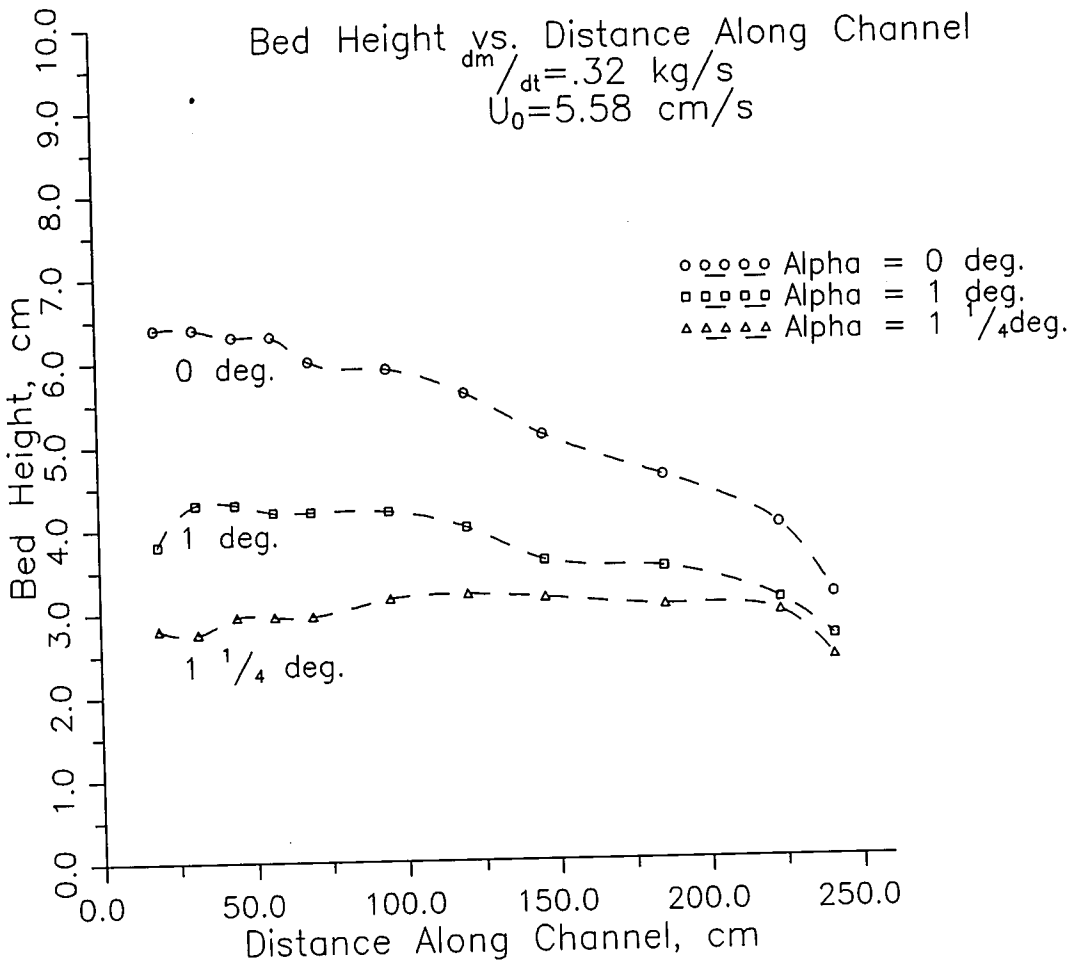

Figure 4.12
Bed height profile for -100 +140 magnetite
$\dot{m}$ = 0.32 kg/s
u_o = 5.58 cm/s

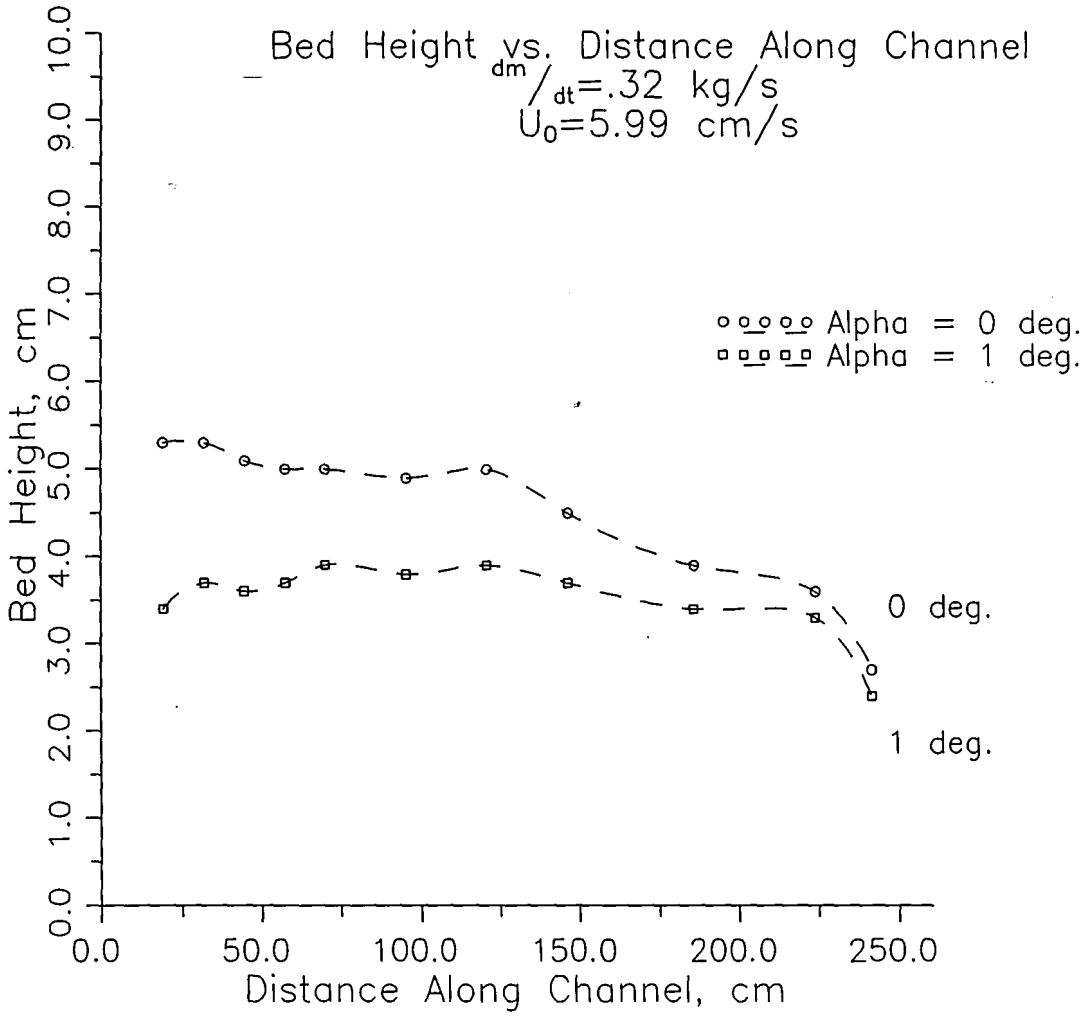

Figure 4.13
Bed height profile for -100 +140 magnetite
$\dot{m}$ = 0.32 kg/s
u_o = 5.99 cm/s

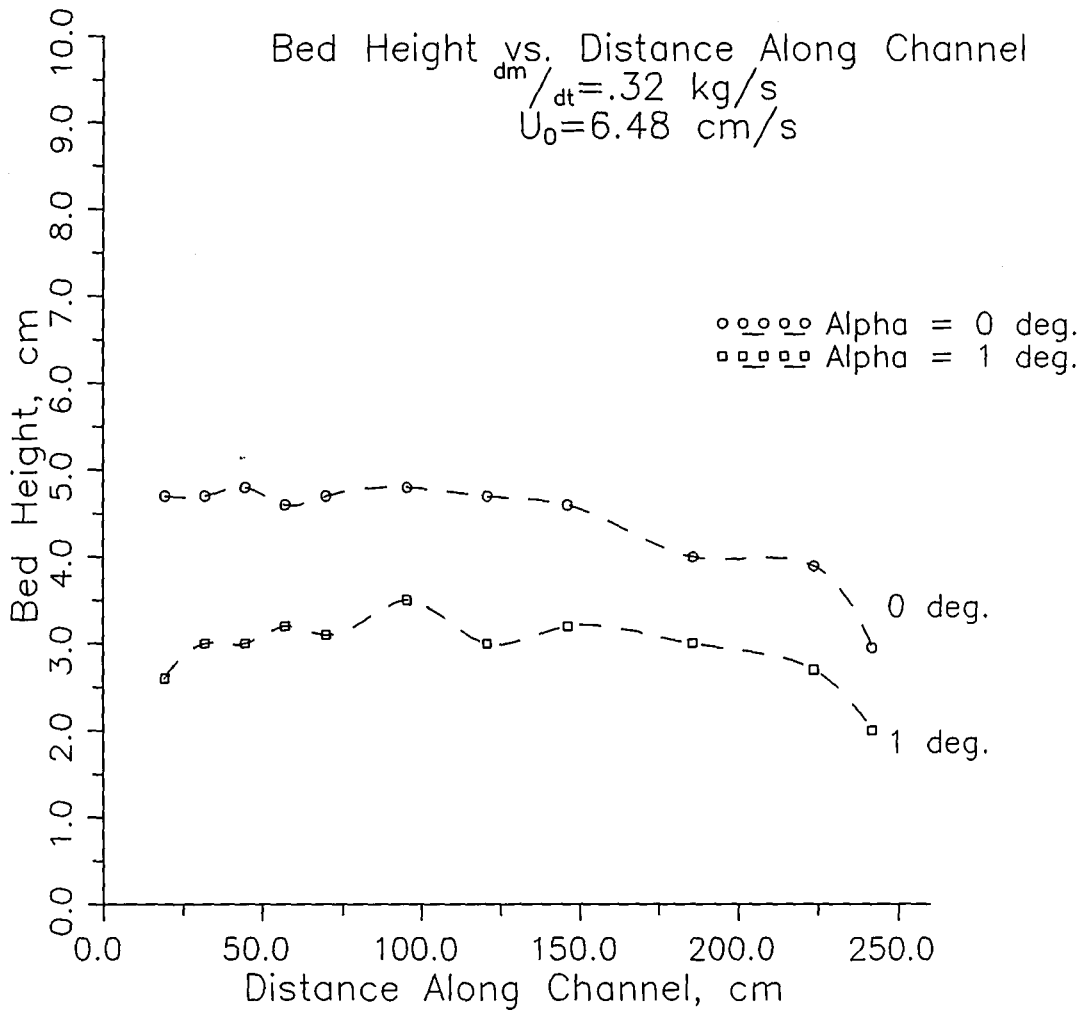

Figure 4.14
Bed height profile for -100 +140 magnetite
$\dot{m}$ = 0.32 kg/s
u_o = 6.48 cm/s

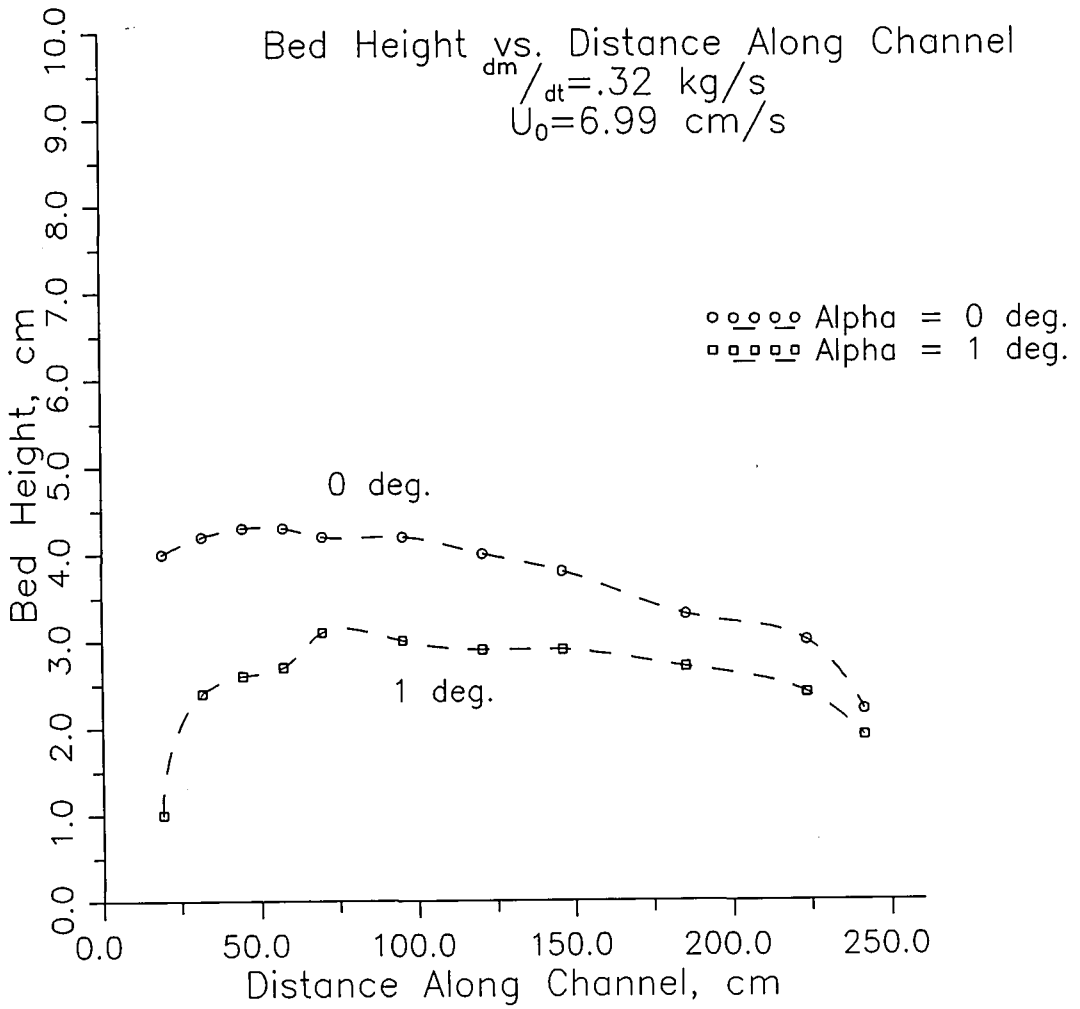

Figure 4.15
Bed height profile for -100 +140 magnetite
$\dot{m}$ = 0.32 kg/s
u_o = 6.99 cm/s

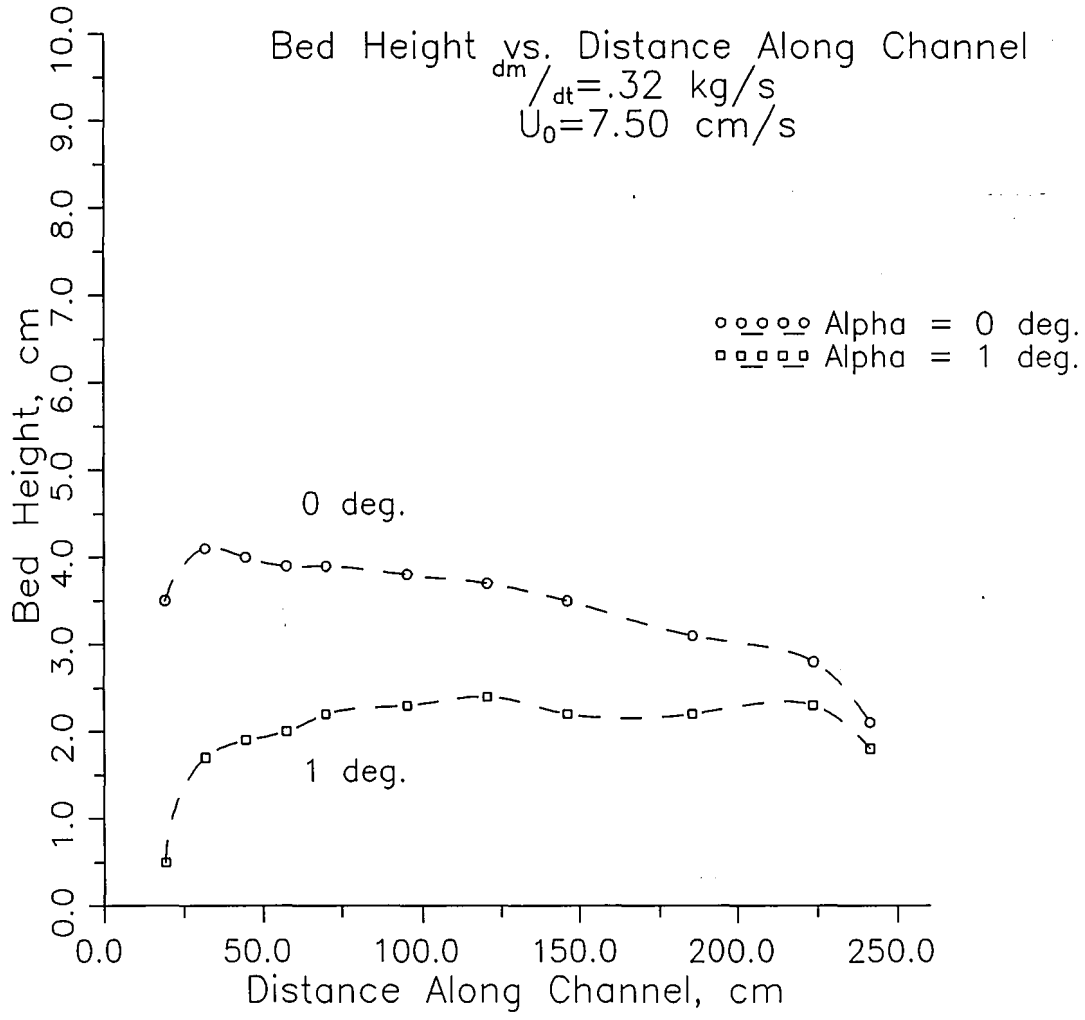

Figure 4.16
Bed height profile for -100 +140 magnetite
$\dot{m}$ = 0.32 kg/s
u_o = 7.50 cm/s

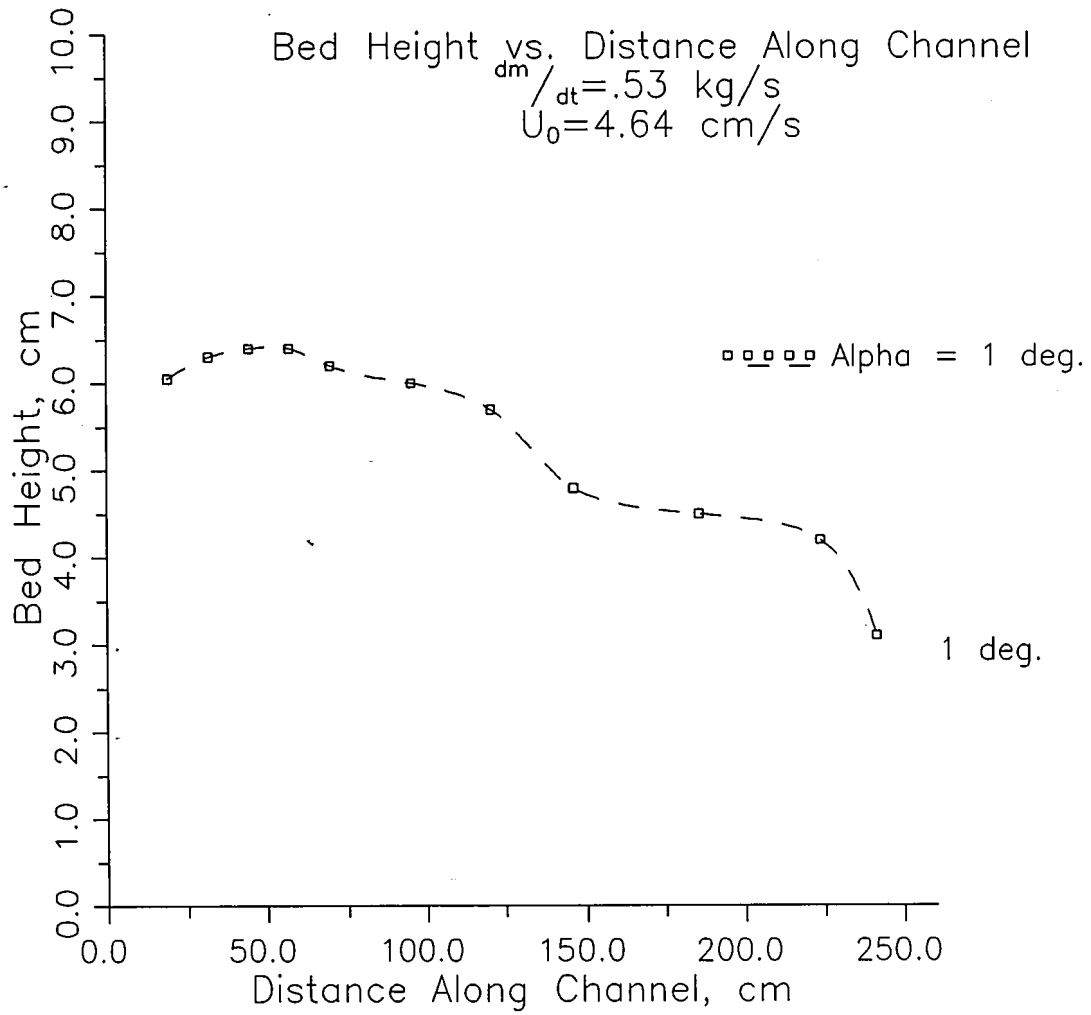

Figure 4.17
Bed height profile for -100 +140 magnetite
$\dot{m}$ = 0.53 kg/s
u_o = 4.64 cm/s

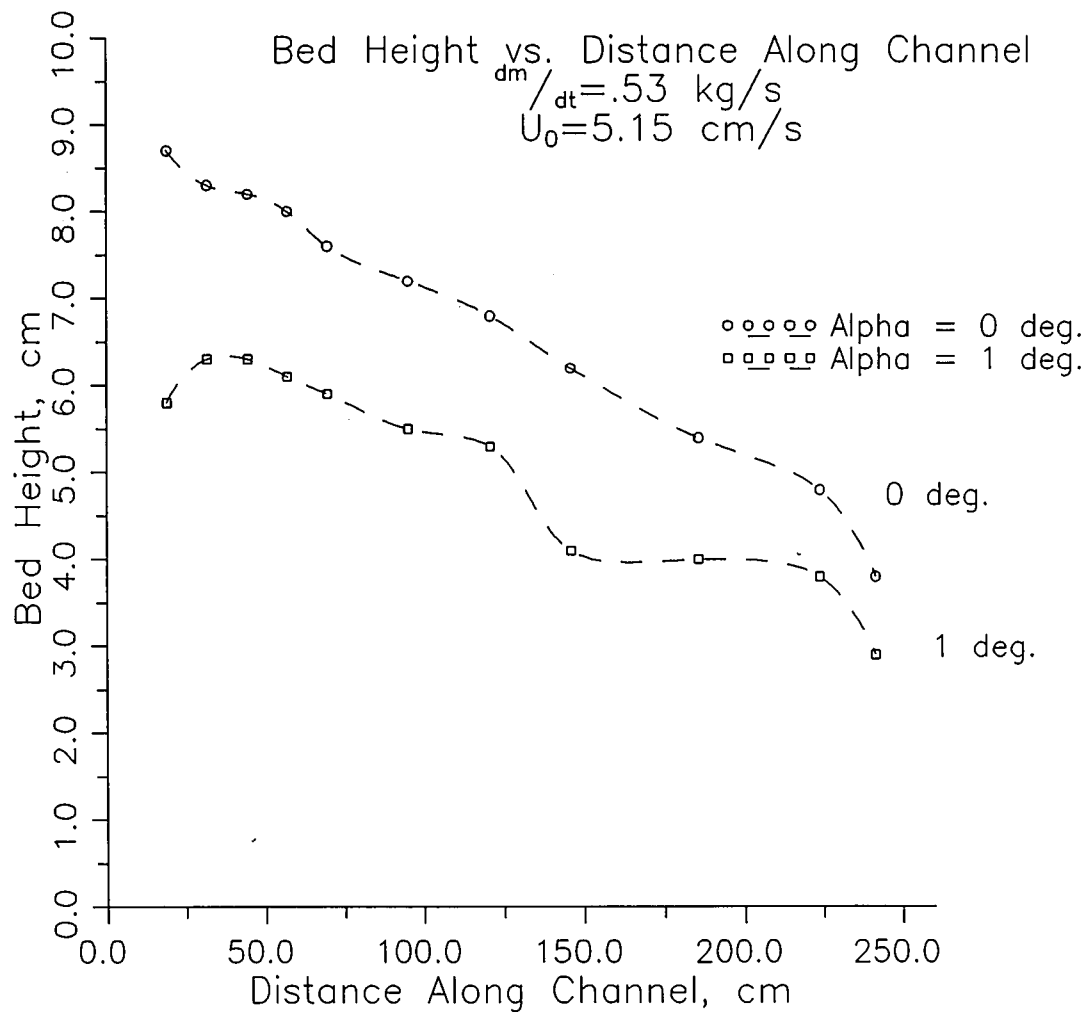

Figure 4.18
Bed height profile for -100 +140 magnetite
$\dot{m}$ = 0.53 kg/s
u_o = 5.15 cm/s

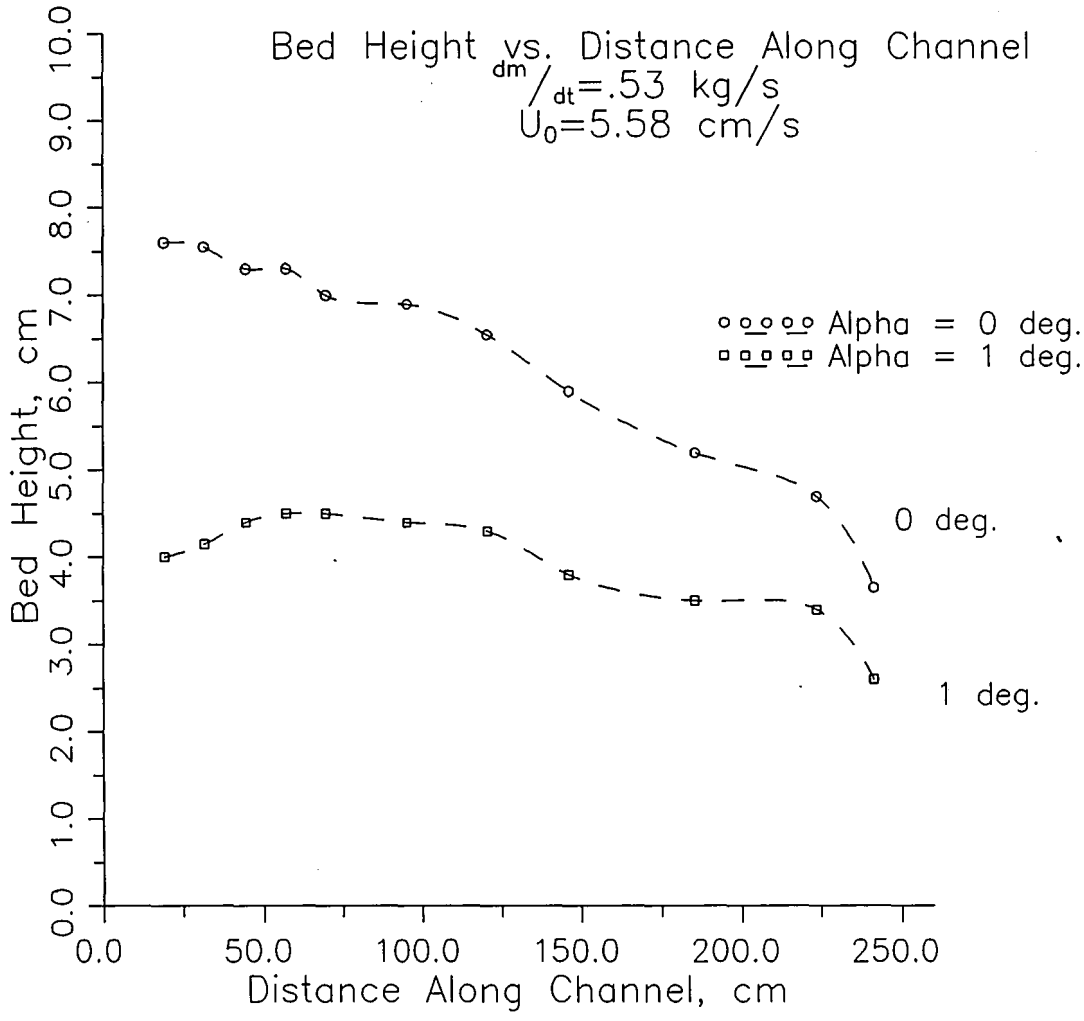

Figure 4.19
Bed height profile for -100 +140 magnetite
$\dot{m}$ = 0.53 kg/s
u_o = 5.58 cm/s

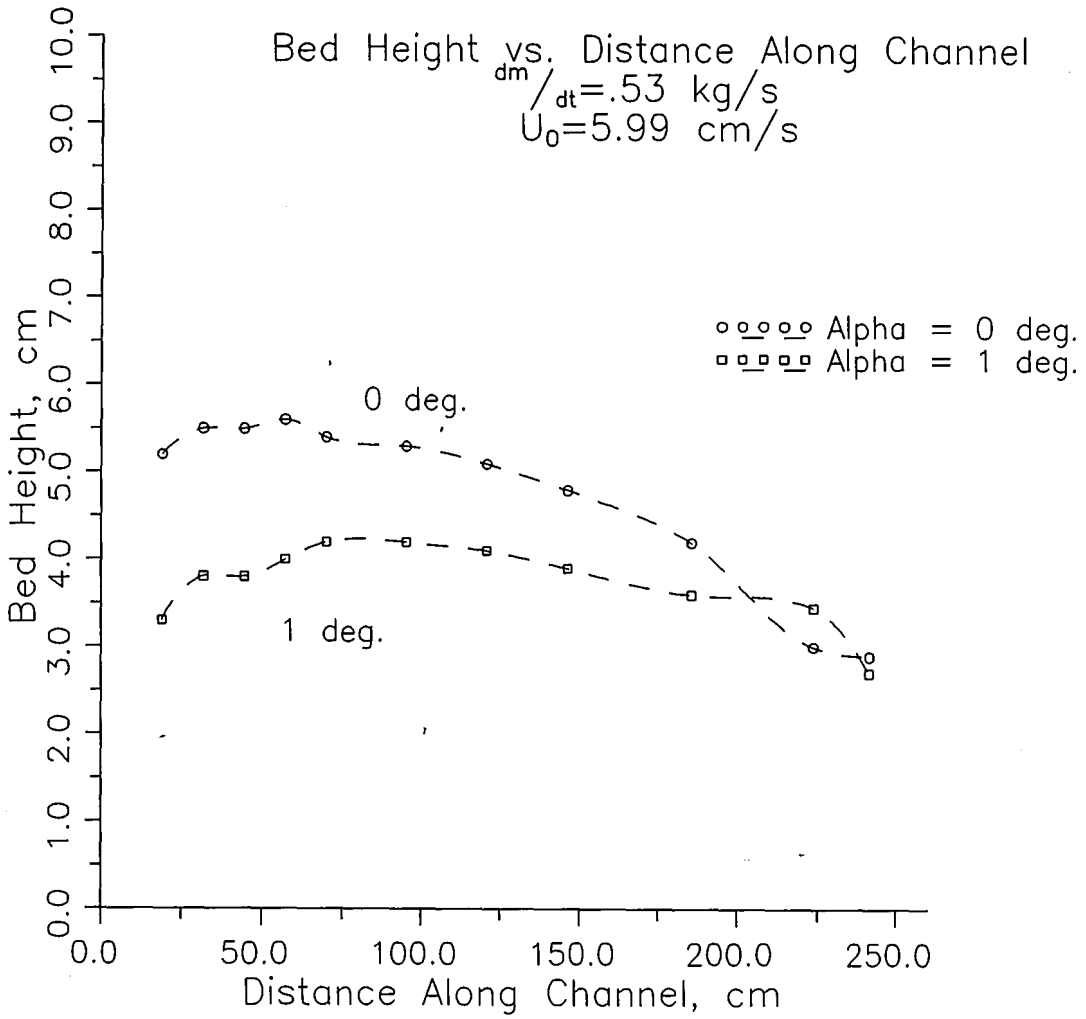

Figure 4.20
Bed height profile for -100 +140 magnetite
$\dot{m}$ = 0.53 kg/s
u_o = 5.99 cm/s

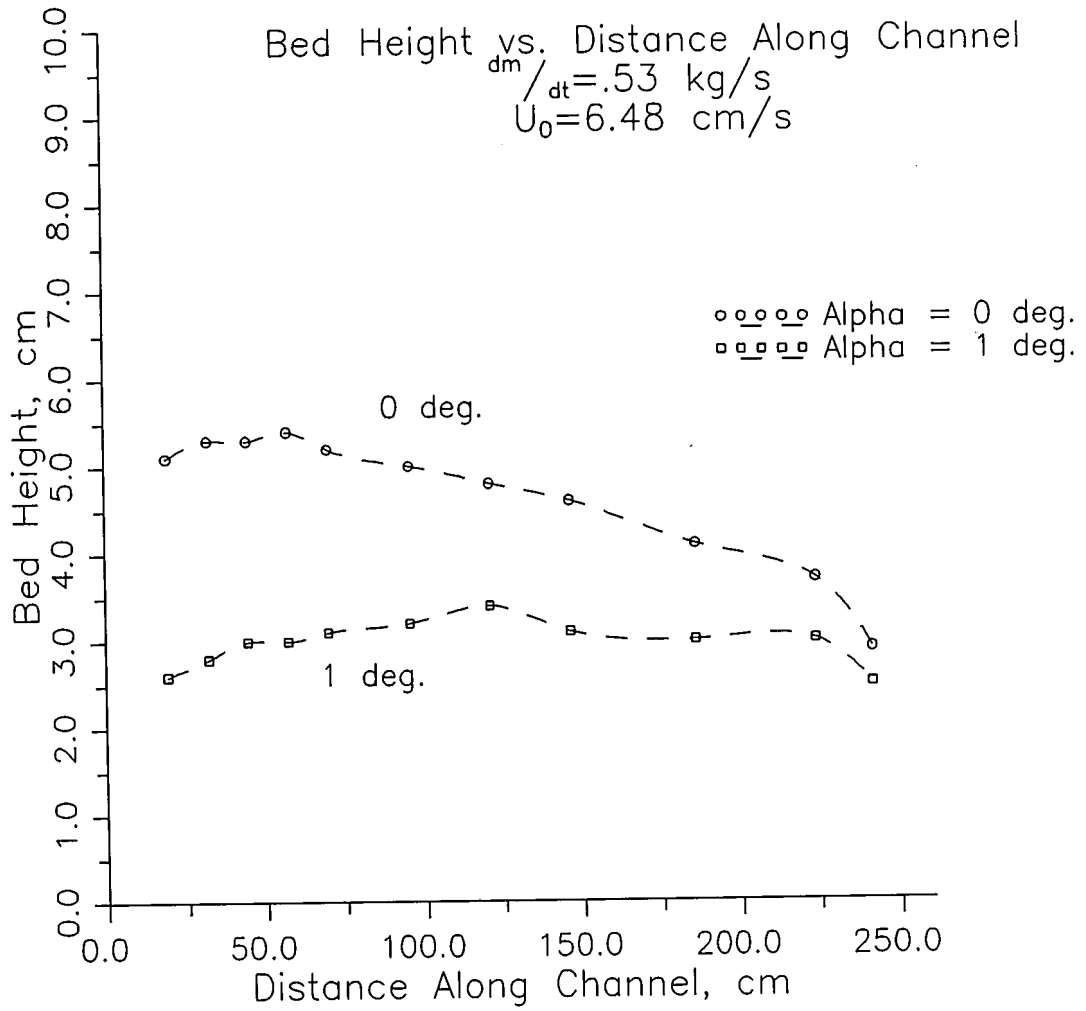

Figure 4.21
Bed height profile for -100 +140 magnetite
$\dot{m}$ = 0.53 kg/s
u_o = 6.48 cm/s

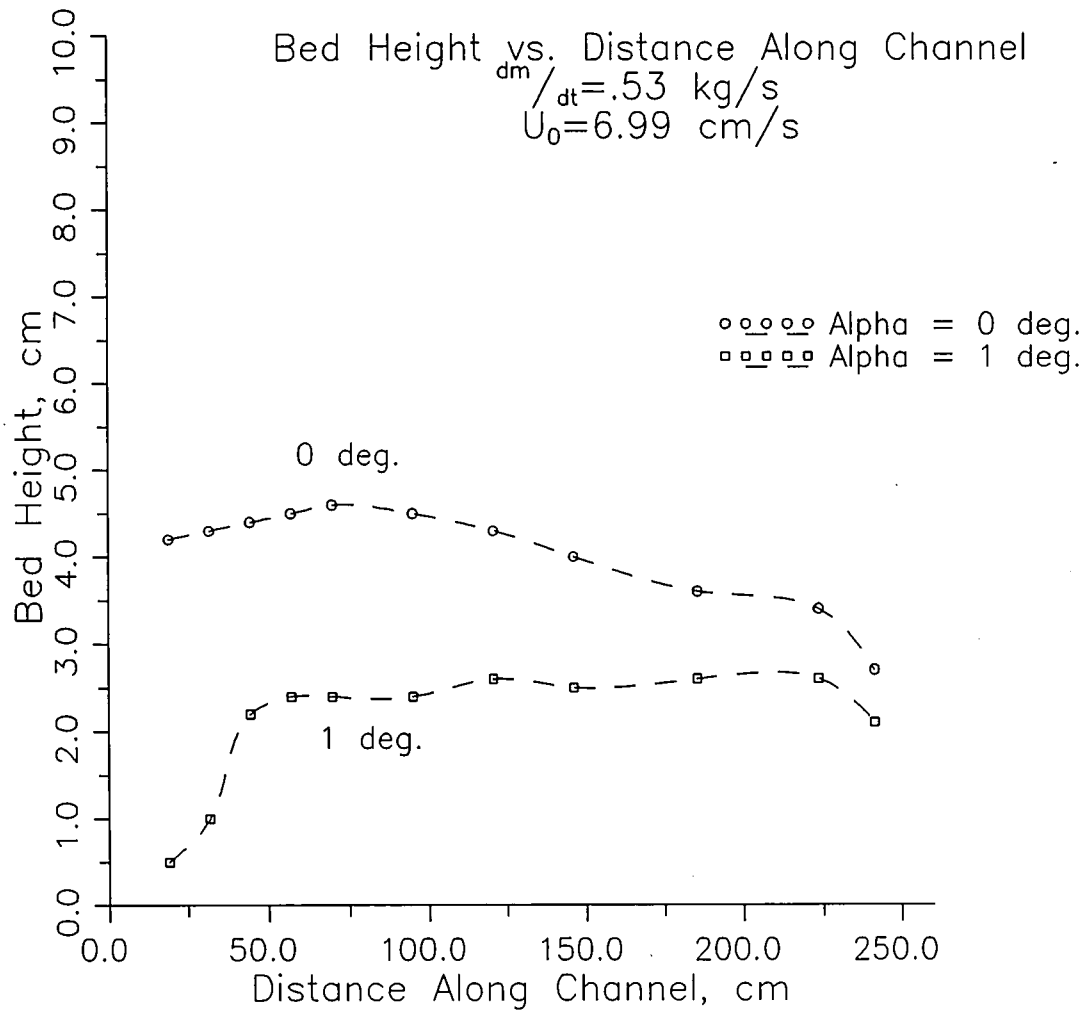

Figure 4.22
Bed height profile for -100 +140 magnetite
$\dot{m}$ = 0.53 kg/s
u_o = 6.99 cm/s

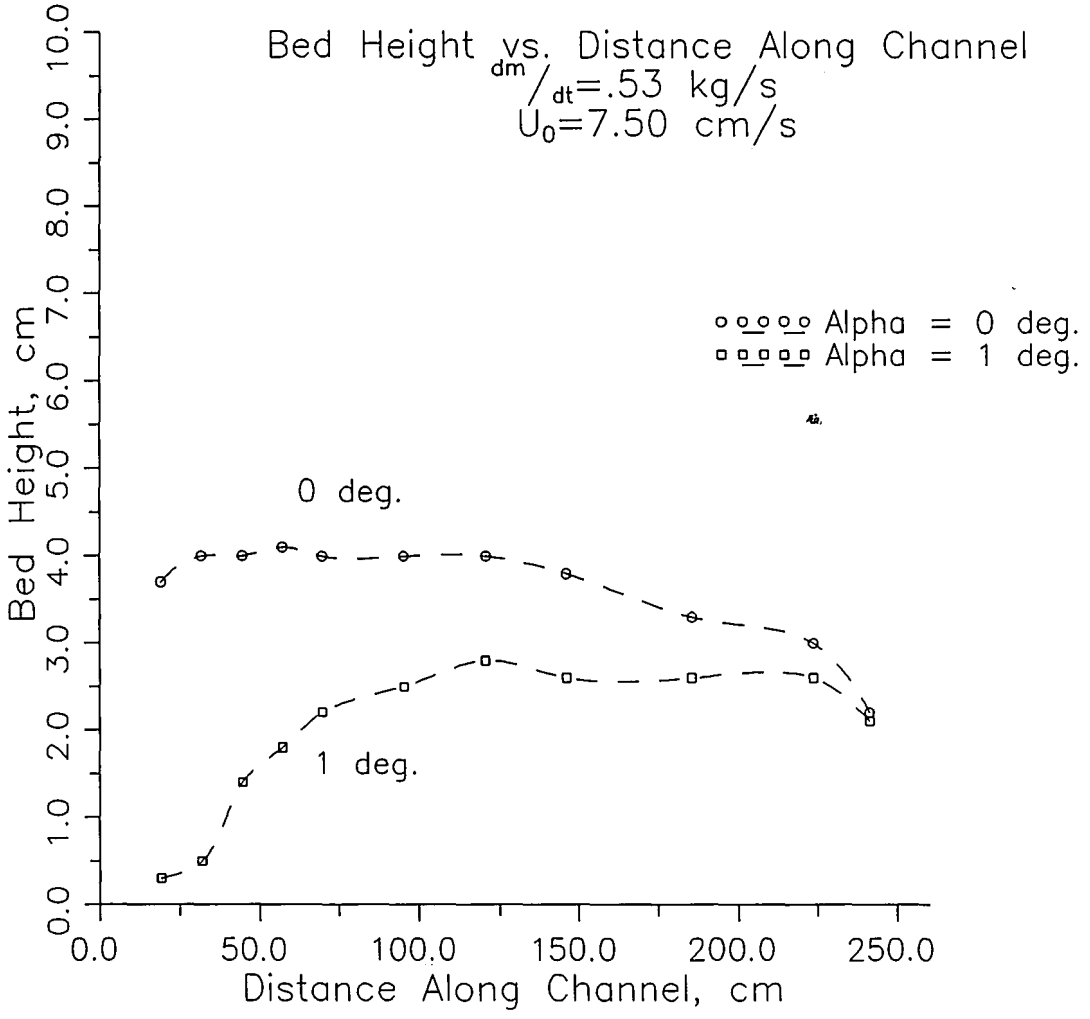

Figure 4.23
Bed height profile for -100 +140 magnetite
$\dot{m}$ = 0.53 kg/s
$\bar{u}_o$ = 7.50 cm/s

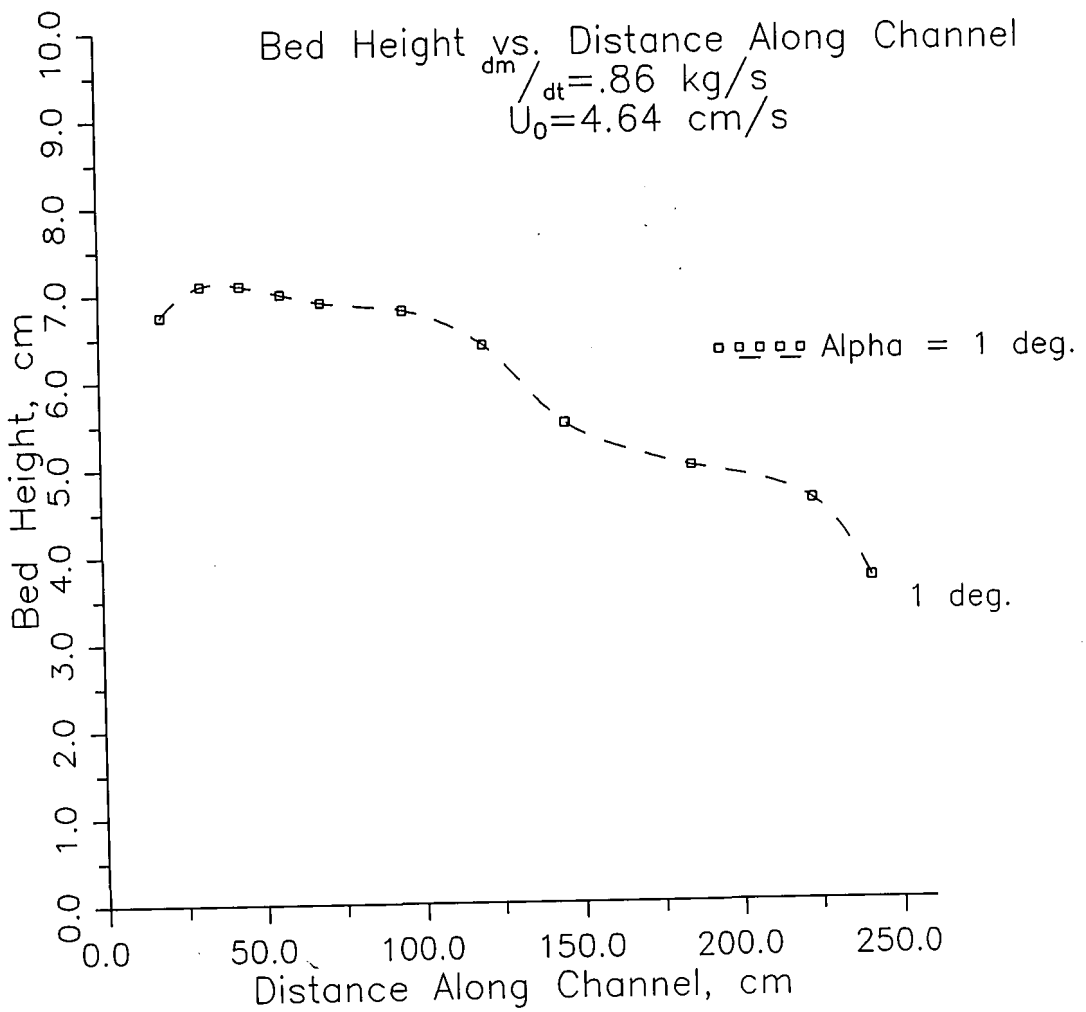

Figure 4.24
Bed height profile for -100 +140 magnetite
$\dot{m}$ = 0.86 kg/s
u_o = 4.64 cm/s

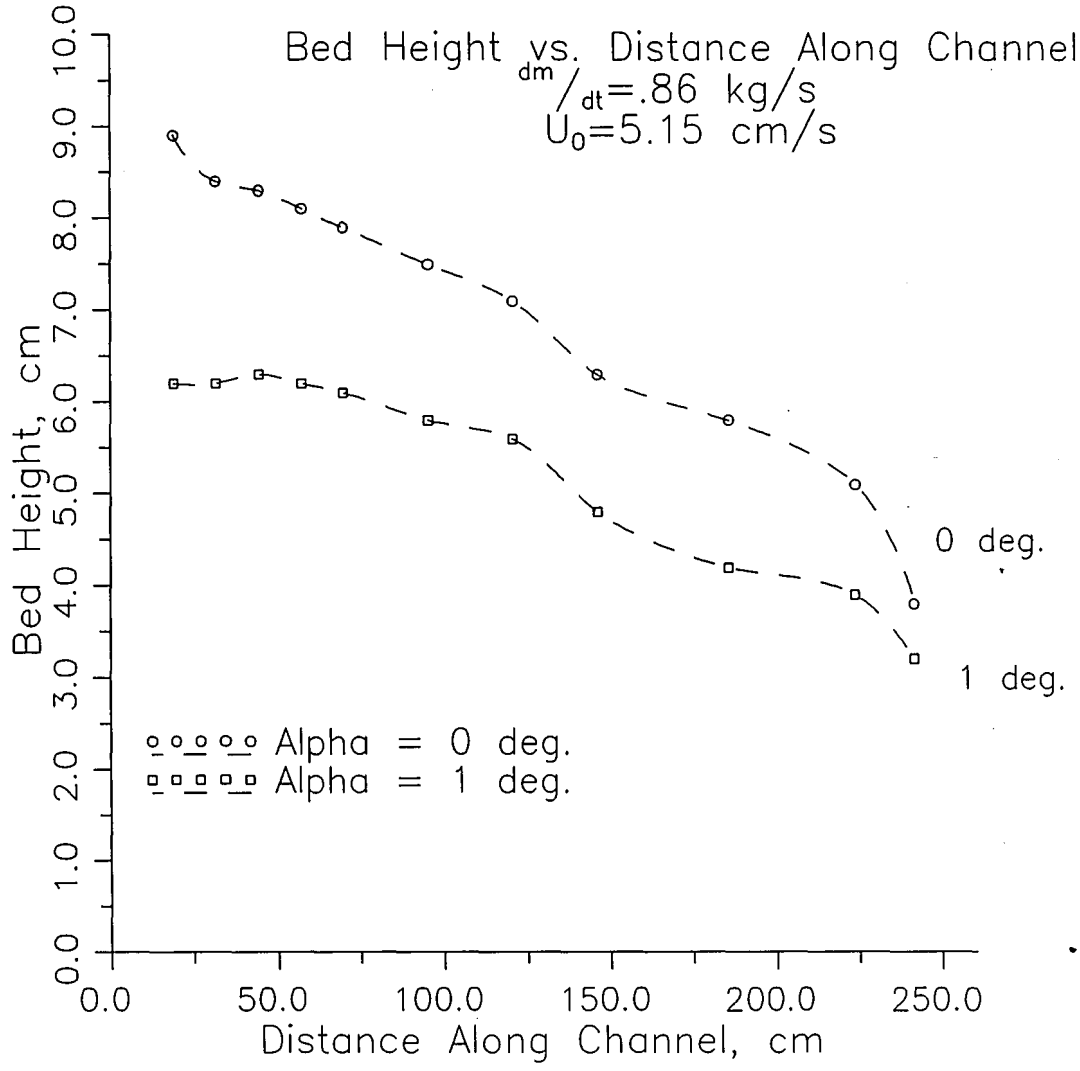

Figure 4.25
Bed height profile for -100 +140 magnetite
$\dot{m}$ = 0.86 kg/s
u_o = 5.15 cm/s

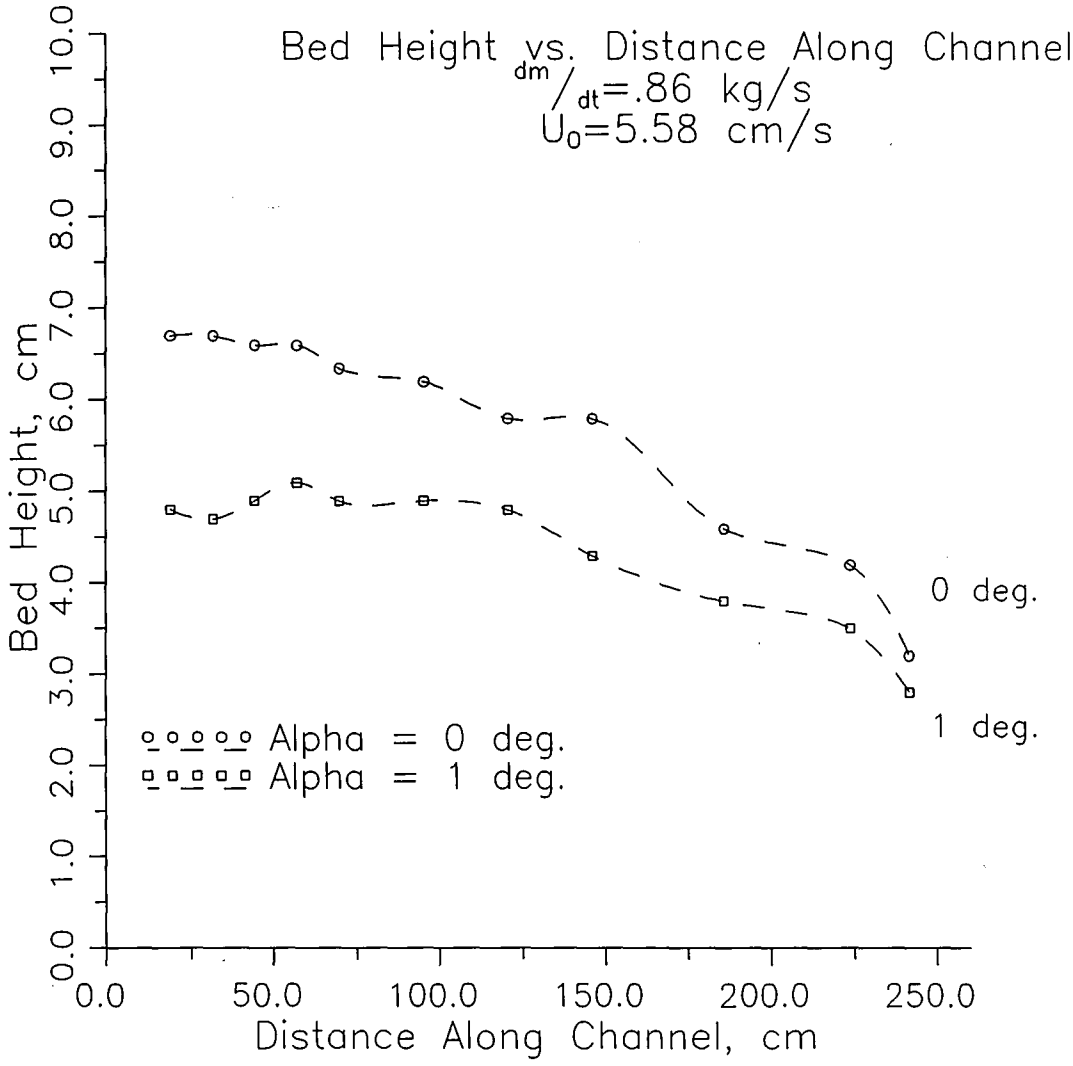

Figure 4.26
Bed height profile for -100 +140 magnetite
$\dot{m}$ = 0.86 kg/s
u_o = 5.58 cm/s

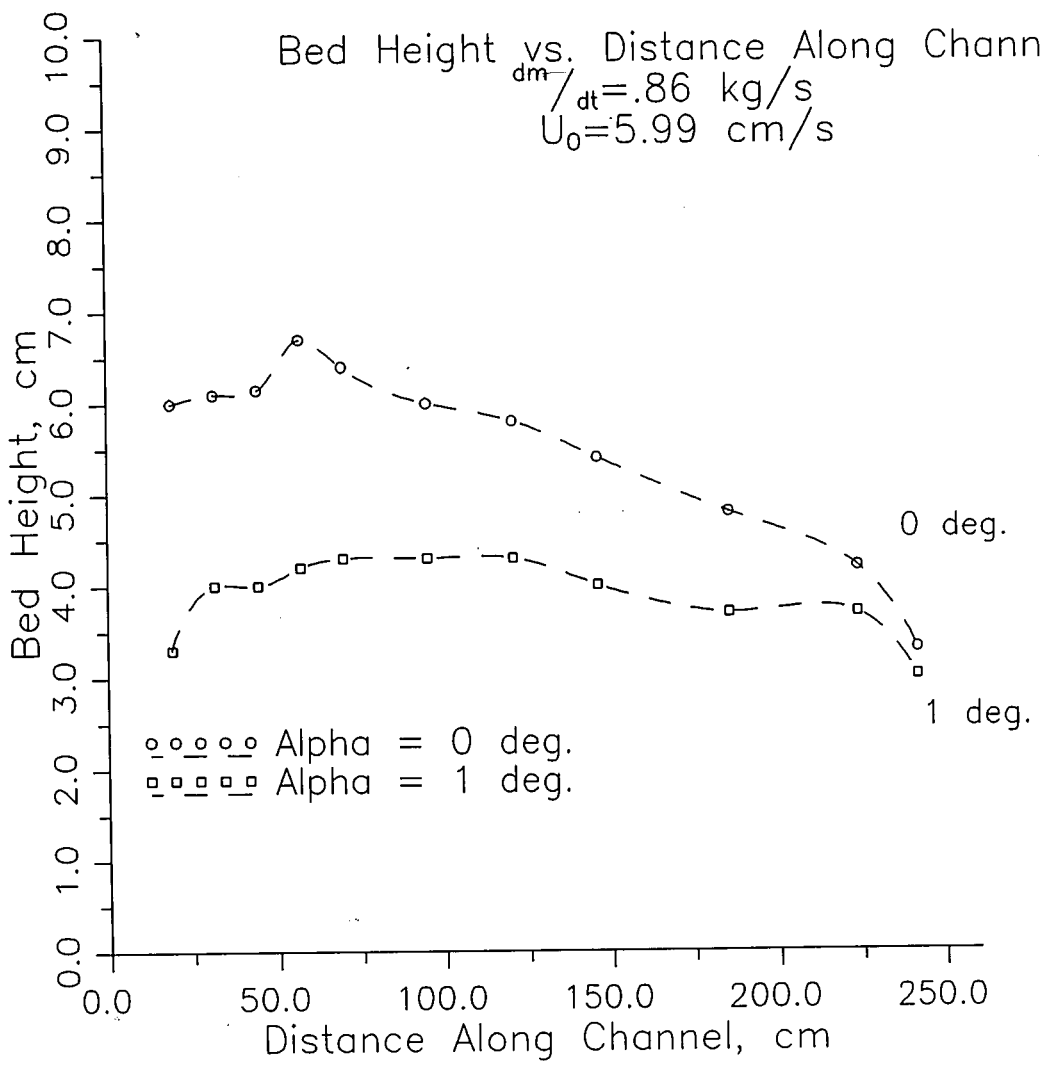

Figure 4.27
Bed height profile for -100 +140 magnetite
$\dot{m}$ = 0.86 kg/s
u_o = 5.99 cm/s

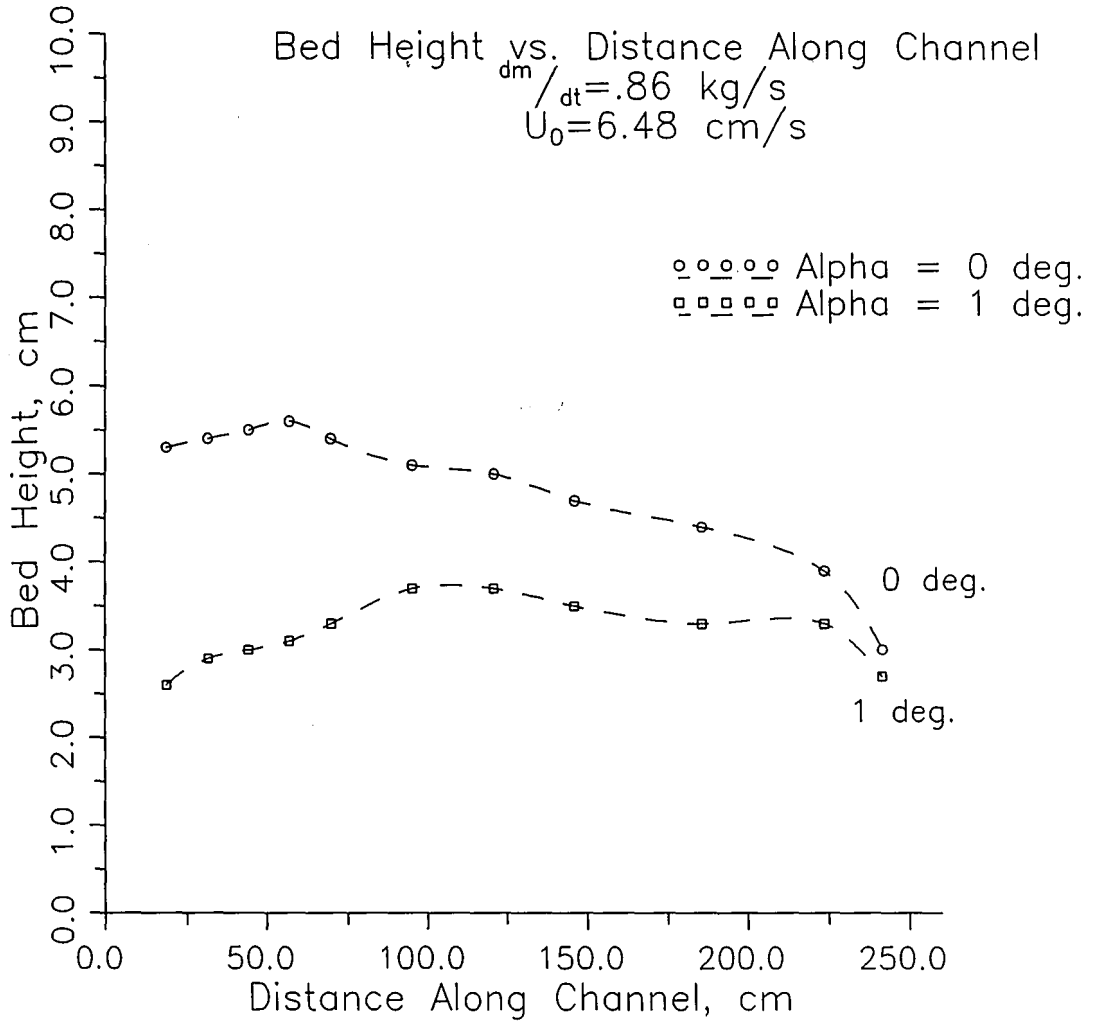

Figure 4.28
Bed height profile for -100 +140 magnetite
$\dot{m}$ = 0.86 kg/s
u_o = 6.48 cm/s

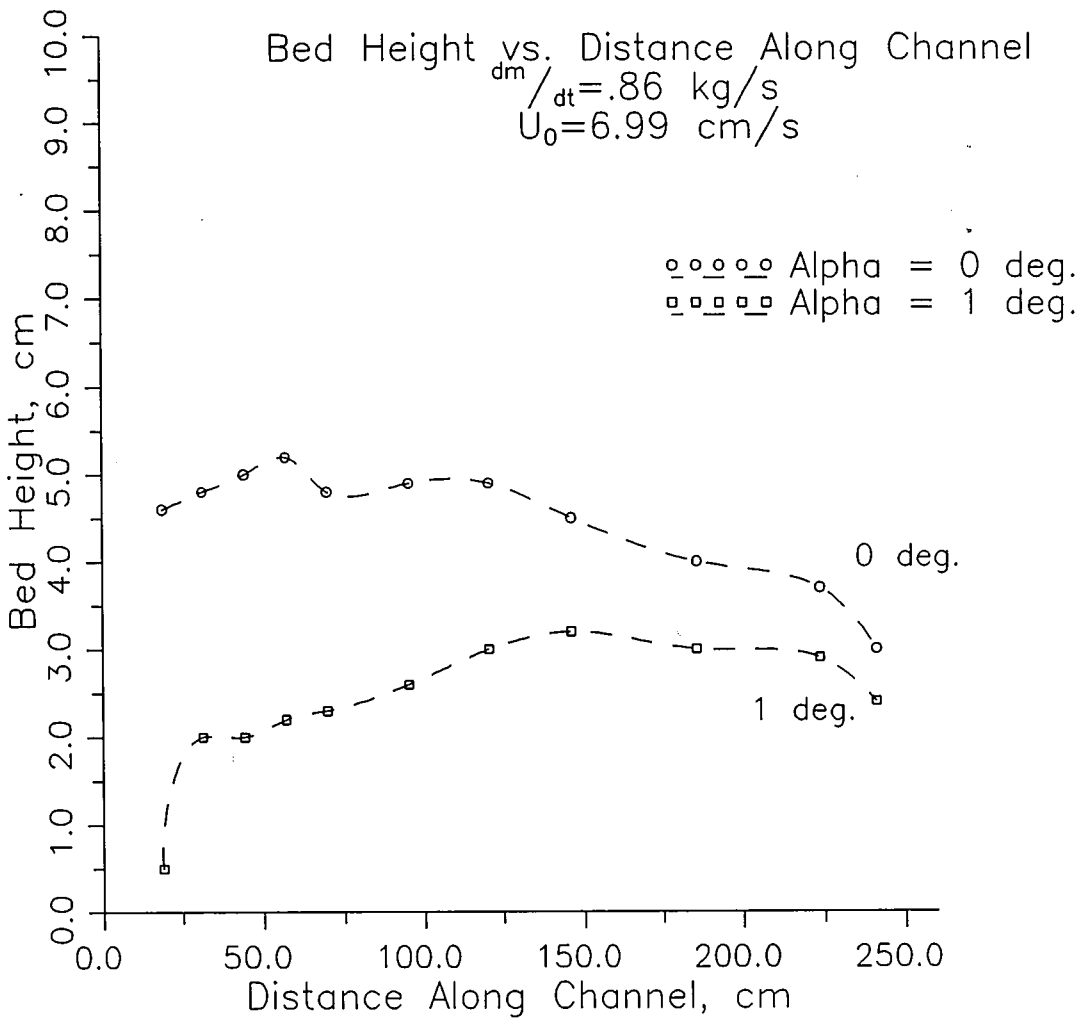

Figure 4.29
Bed height profile for -100 +140 magnetite
$\dot{m}$ = 0.86 kg/s
u_o = 6.99 cm/s

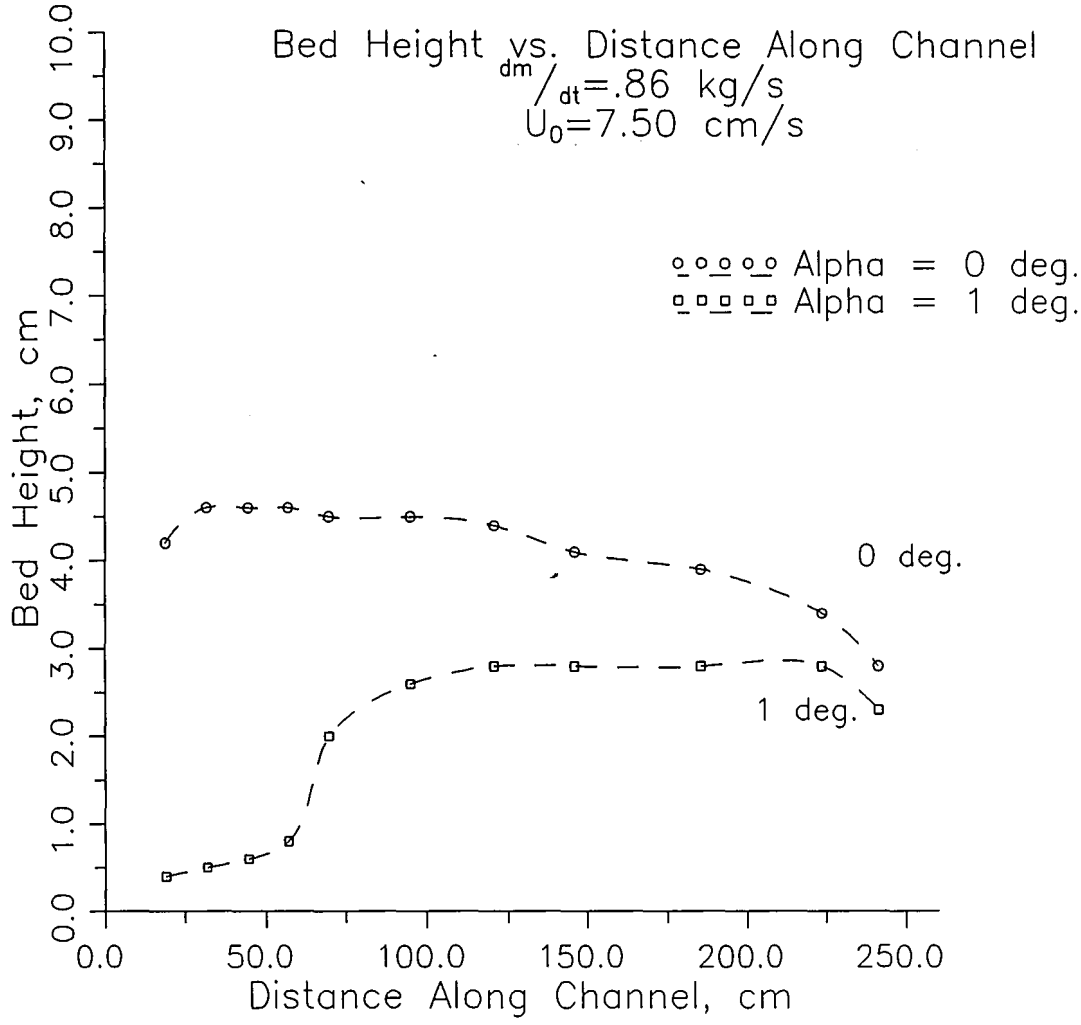

Figure 4.30
Bed height profile for -100 +140 magnetite
$\dot{m}$ = 0.86 kg/s
u_o = 7.50 cm/s

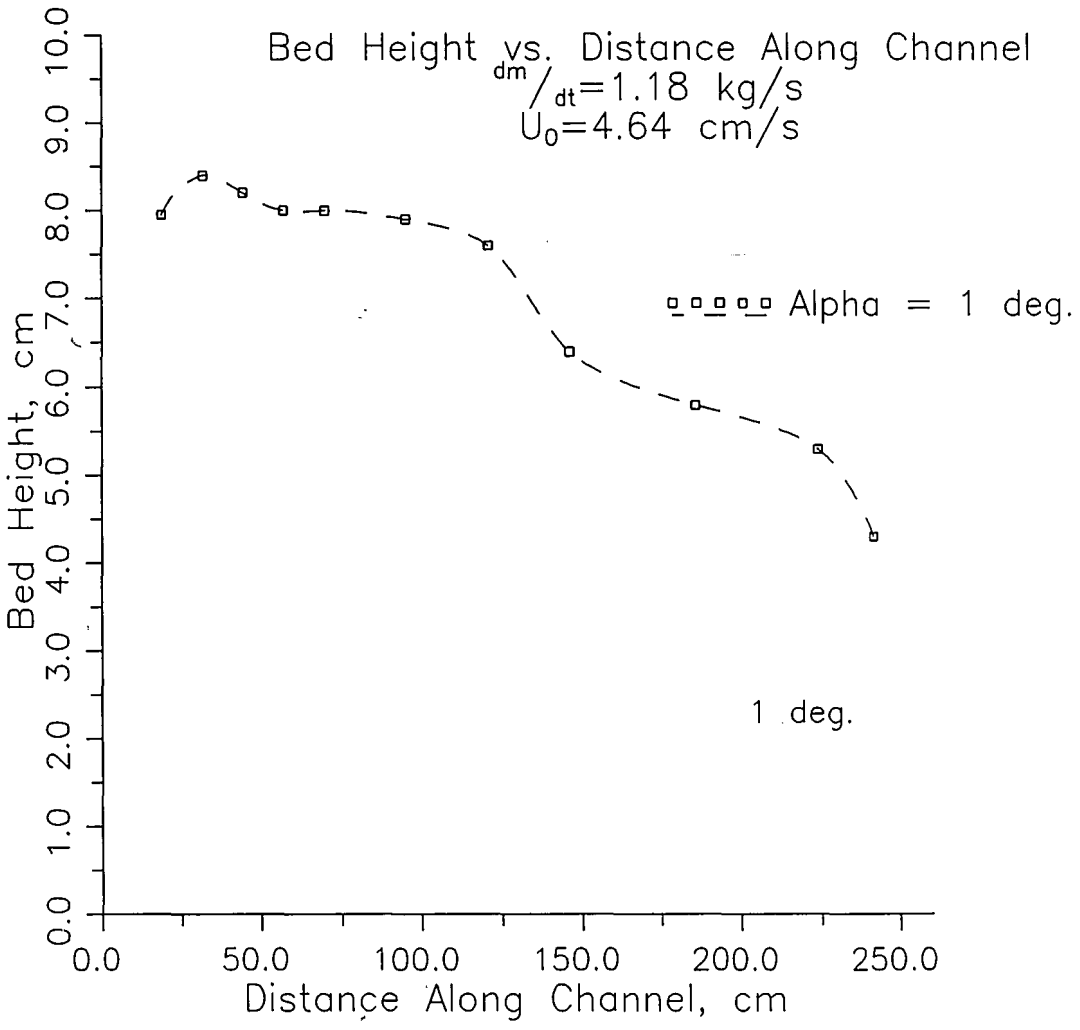

Figure 4.31
Bed height profile for -100 +140 magnetite
$\dot{m}$ = 1.18 kg/s
u_o = 4.64 cm/s

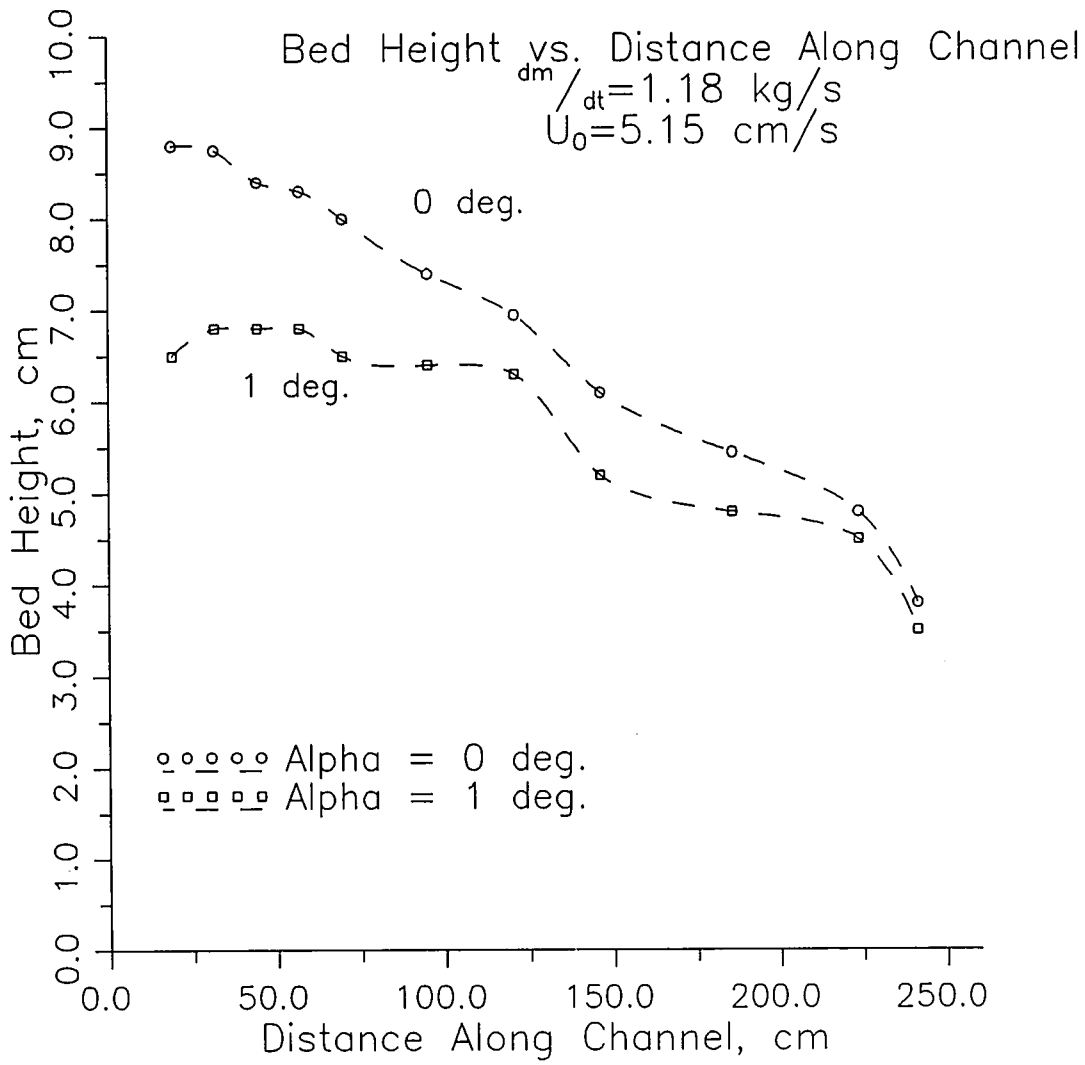

Figure 4.32
Bed height profile for -100 +140 magnetite
$\dot{m}$ = 1.18 kg/s
u_o = 5.15 cm/s

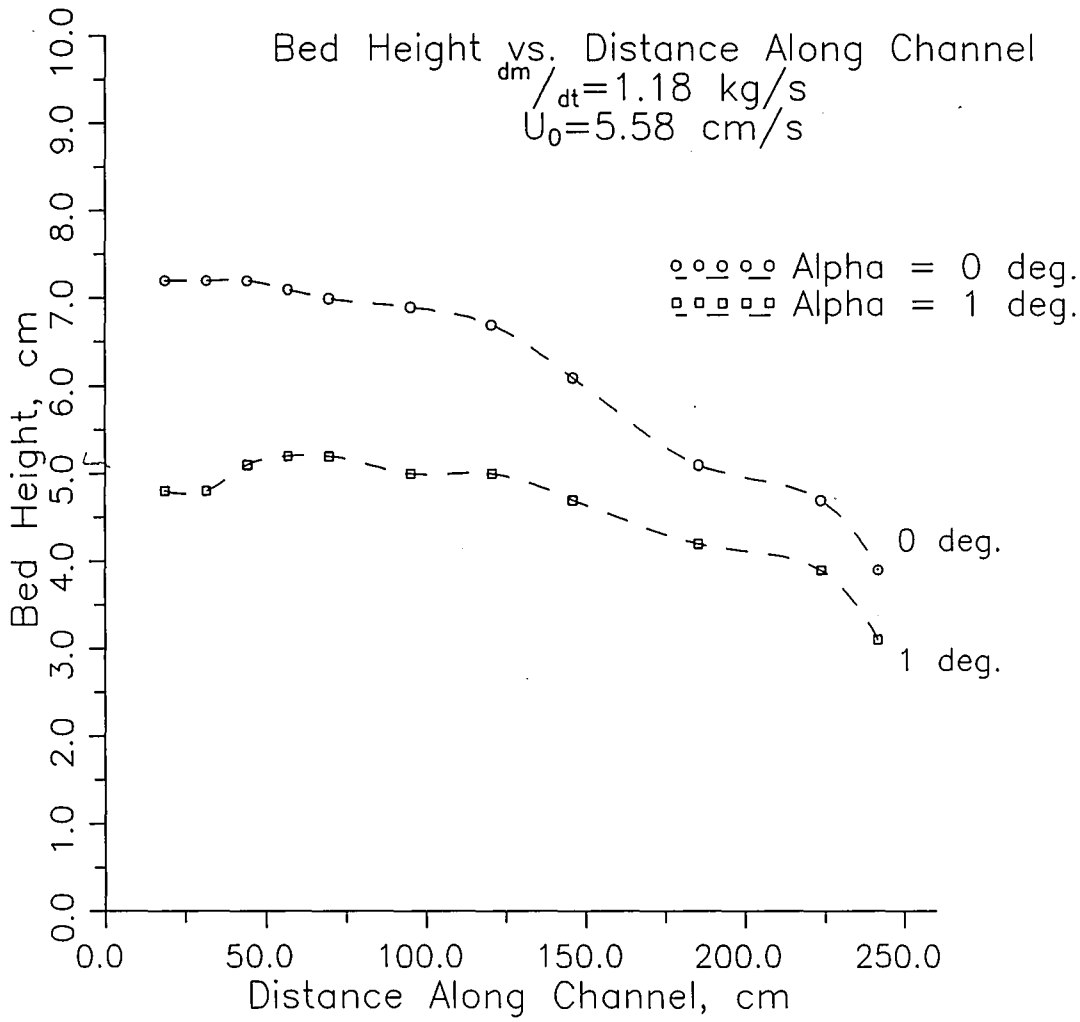

Figure 4.33
Bed height profile for -100 +140 magnetite
$\dot{m}$ = 1.18 kg/s
u_o = 5.58 cm/s

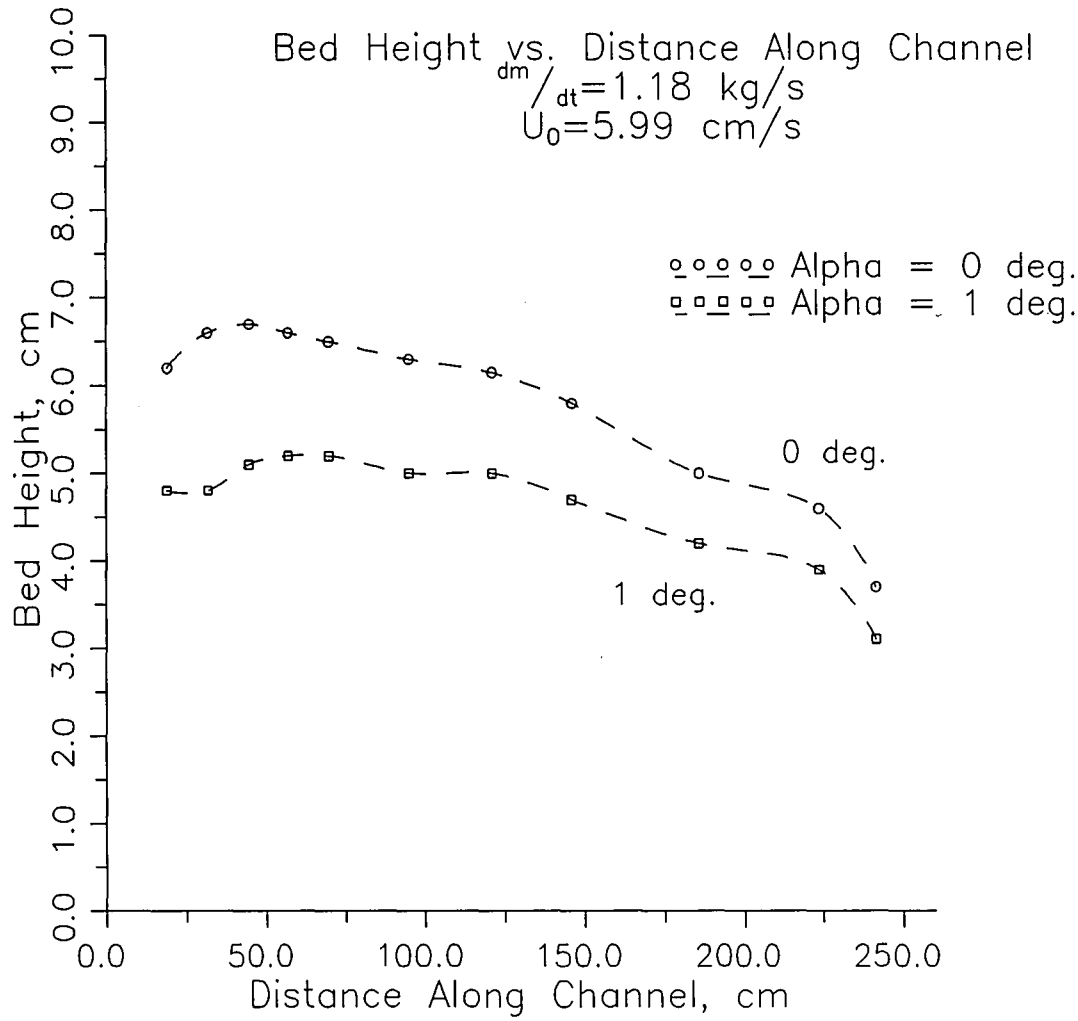

Figure 4.34
Bed height profile for -100 +140 magnetite
$\dot{m}$ = 1.18 kg/s
u_o = 5.99 cm/s

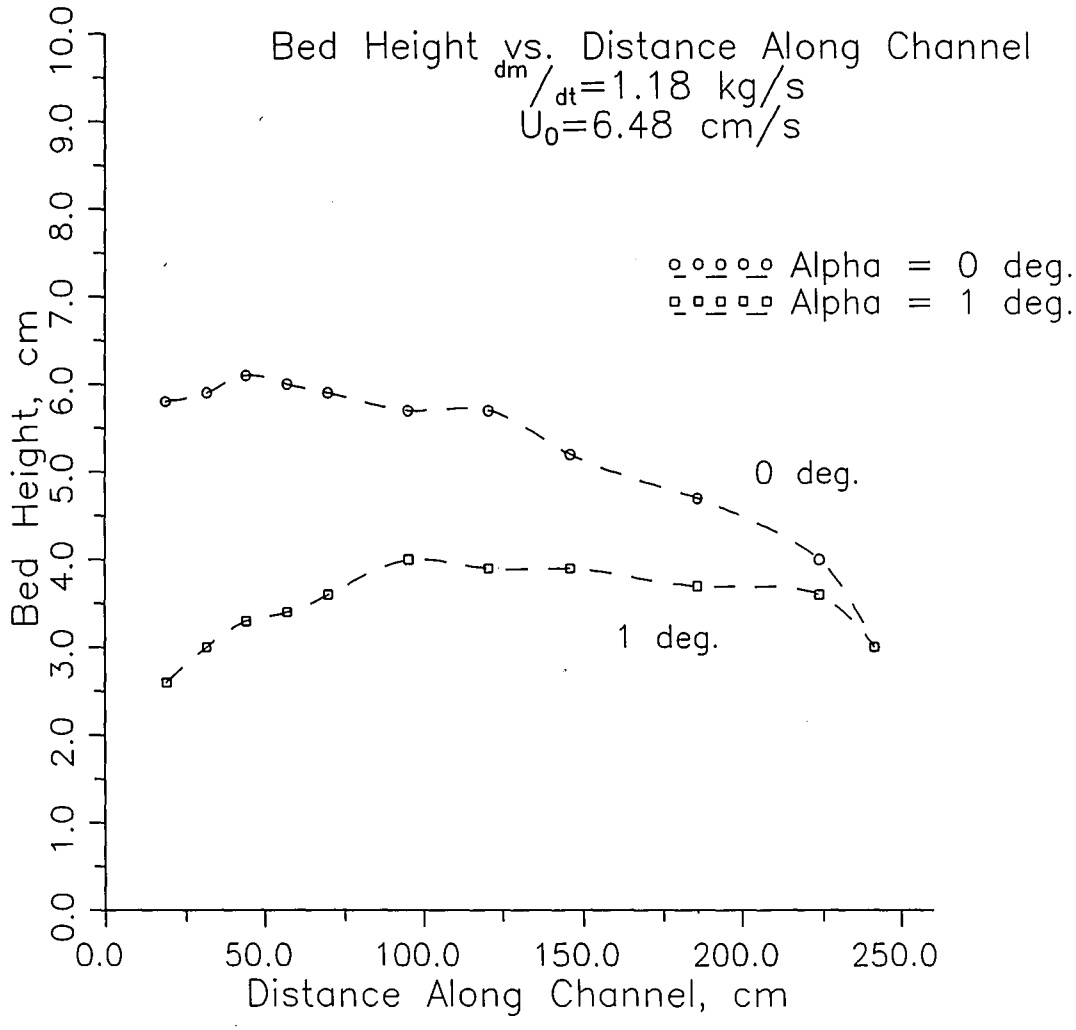

Figure 4.35
Bed height profile for -100 +140 magnetite
$\dot{m}$ = 1.18 kg/s
u_o = 6.48 cm/s

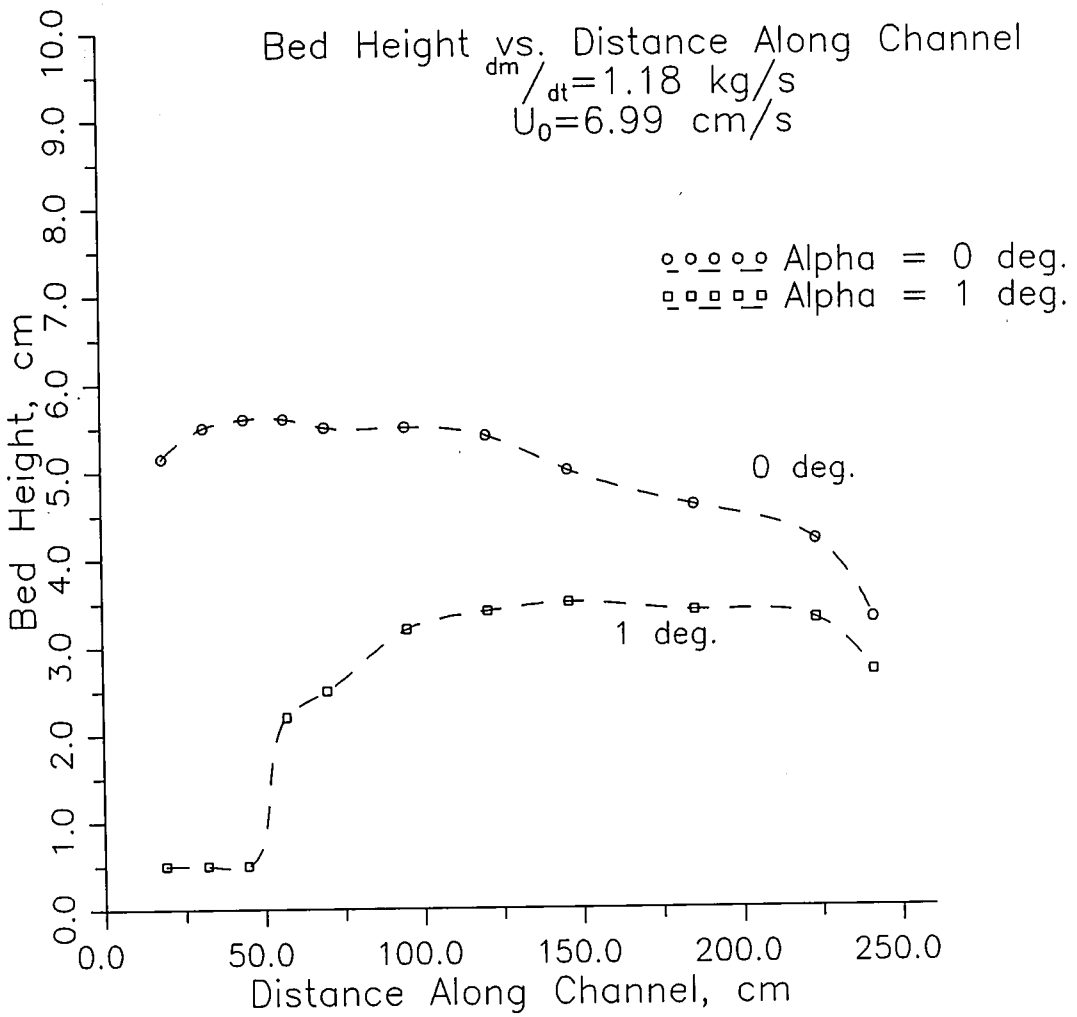

Figure 4.36
Bed height profile for -100 +140 magnetite
$\dot{m}$ = 1.18 kg/s
u_o = 6.99 cm/s

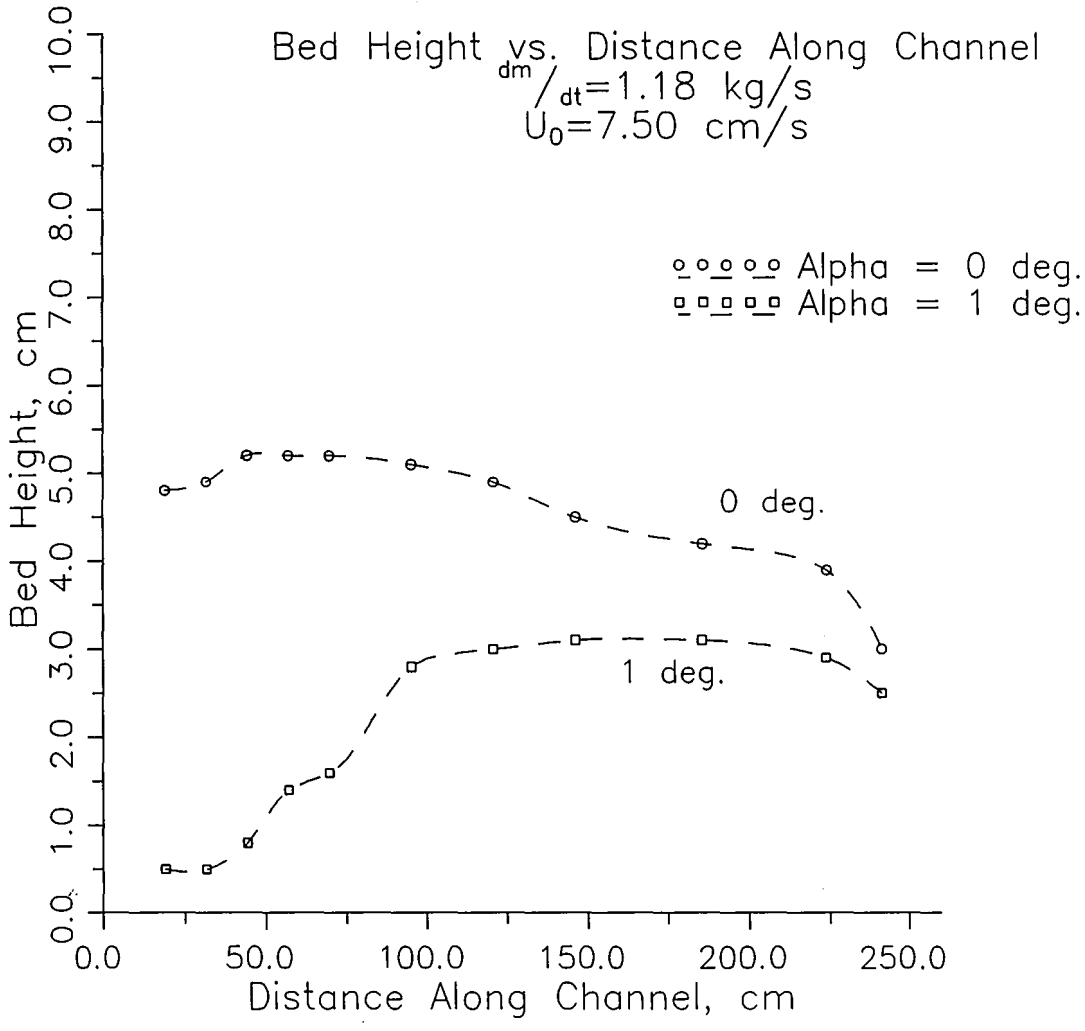

Figure 4.37
Bed height profile for -100 +140 magnetite
$\dot{m}$ = 1.18 kg/s
u_o = 7.50 cm/s

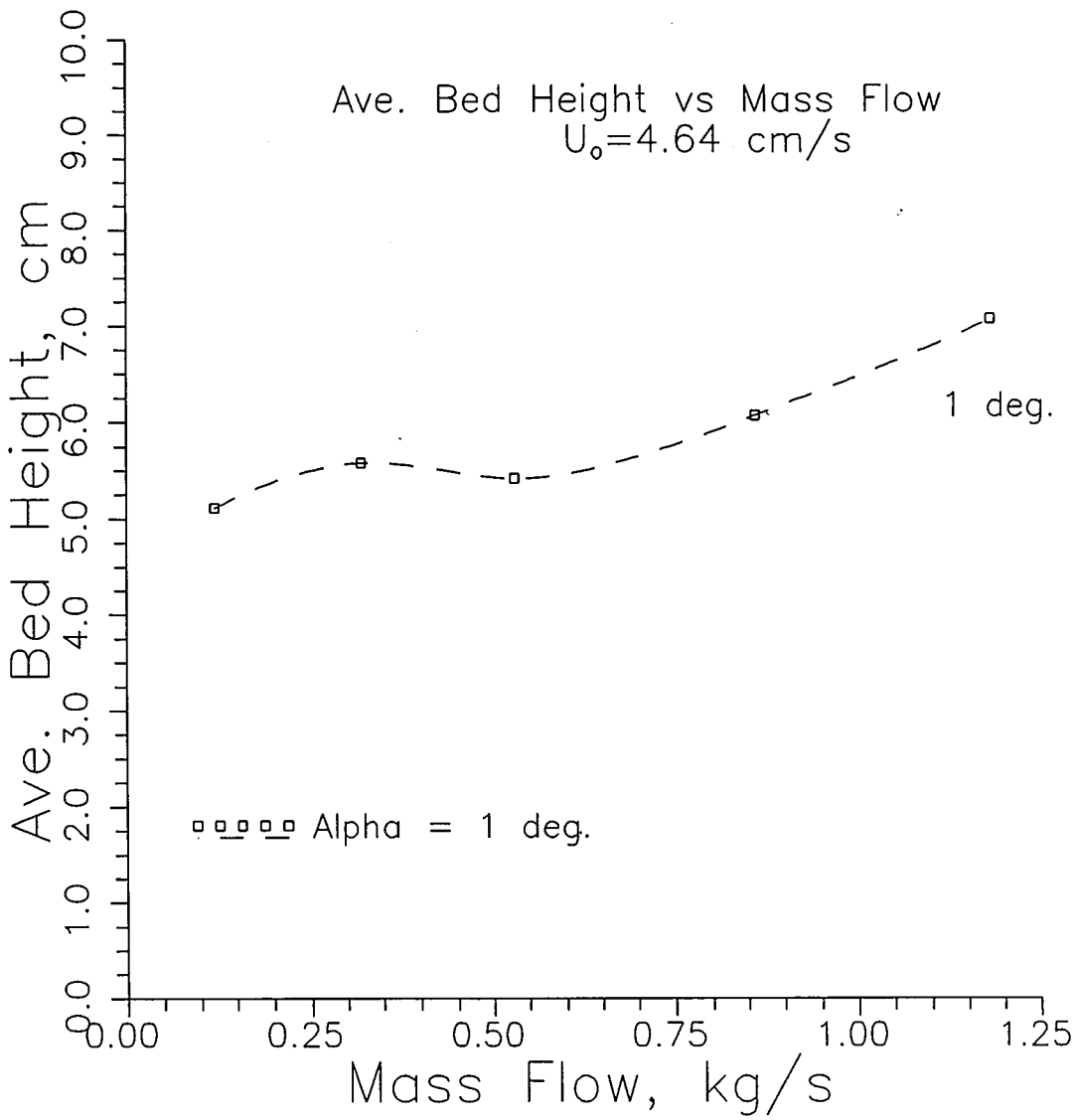

Figure 4.38
Average bed height variation with mass flow for -100 +140 magnetite
u_o = 4.64 cm/s

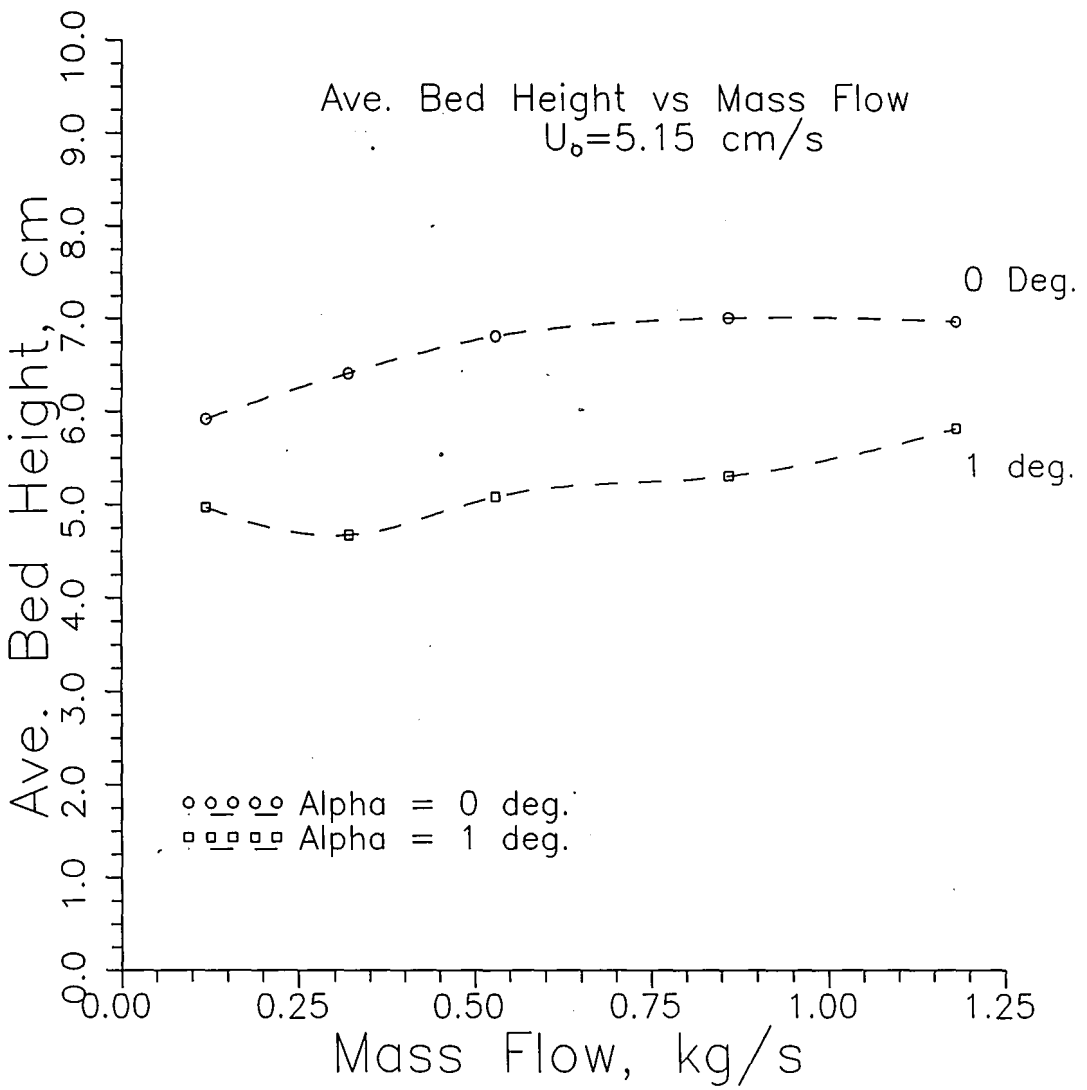

Figure 4.39
Average bed height variation with mass flow for -100 +140 magnetite
u_o = 5.15 cm/s

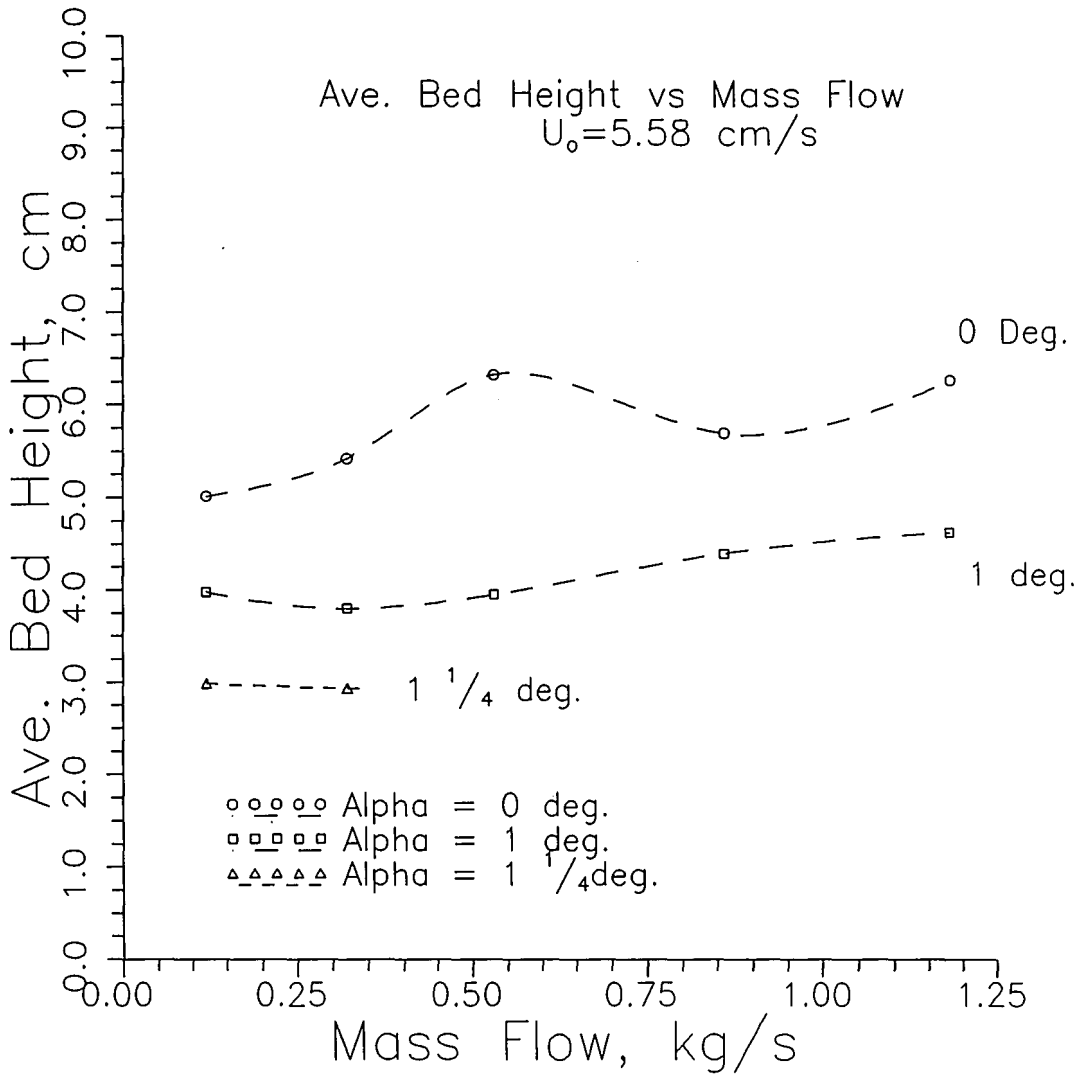

Figure 4.40
Average bed height variation with mass flow for -100 +140 magnetite
u_o = 5.58 cm/s

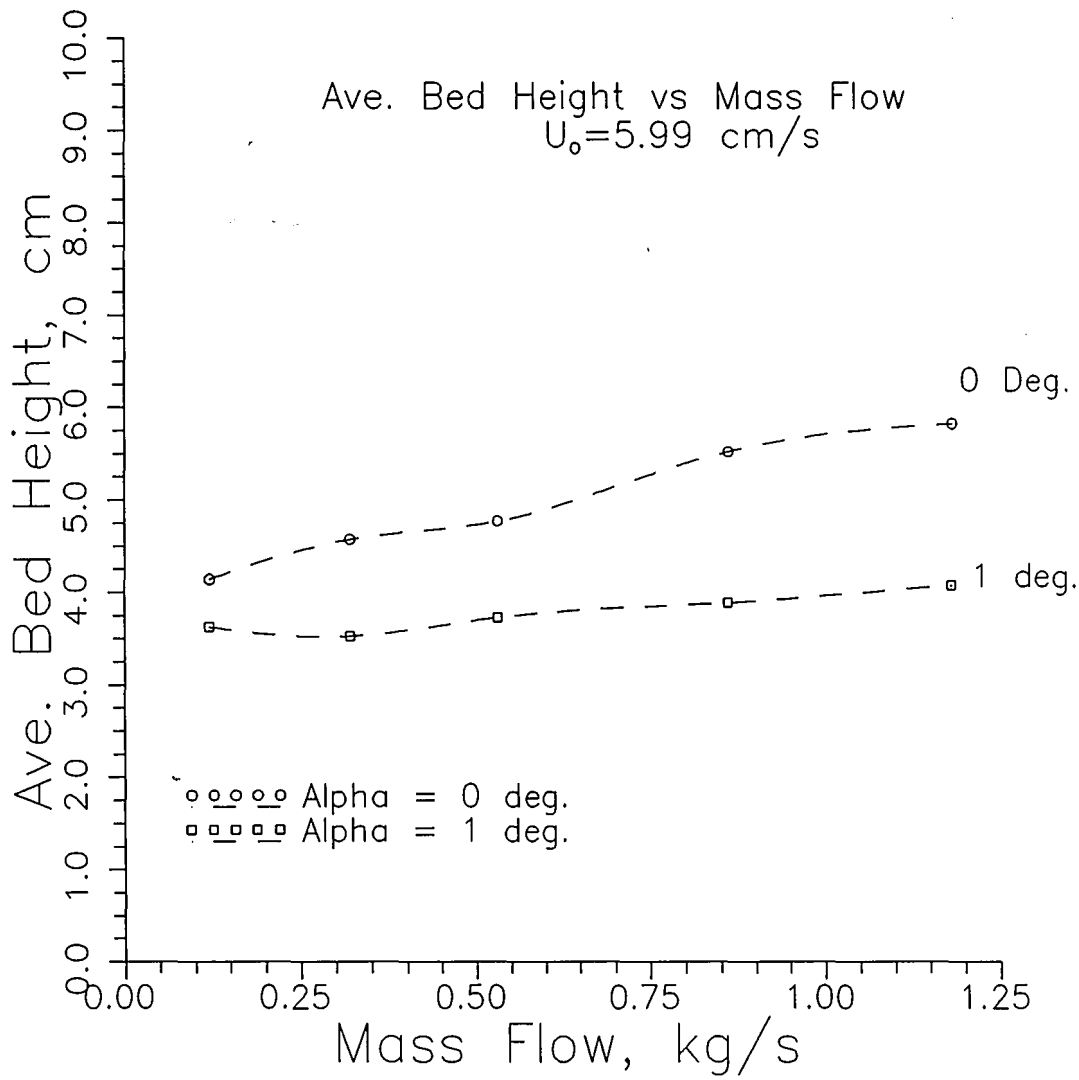

Figure 4.41
Average bed height variation with mass flow for -100 +140 magnetite
u_o = 5.99 cm/s

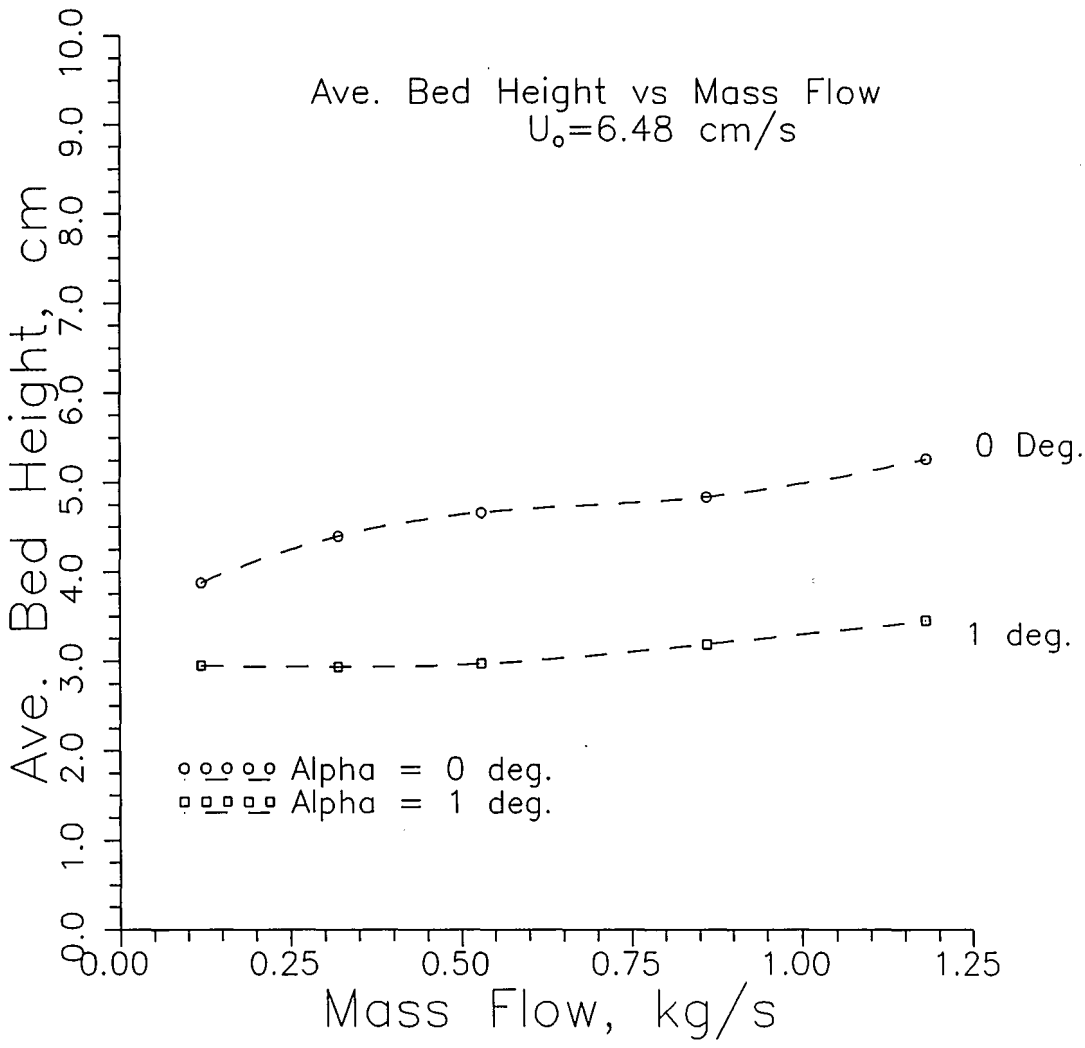

Figure 4.42
Average bed height variation with mass flow for -100 +140 magnetite
u_o = 6.48 cm/s

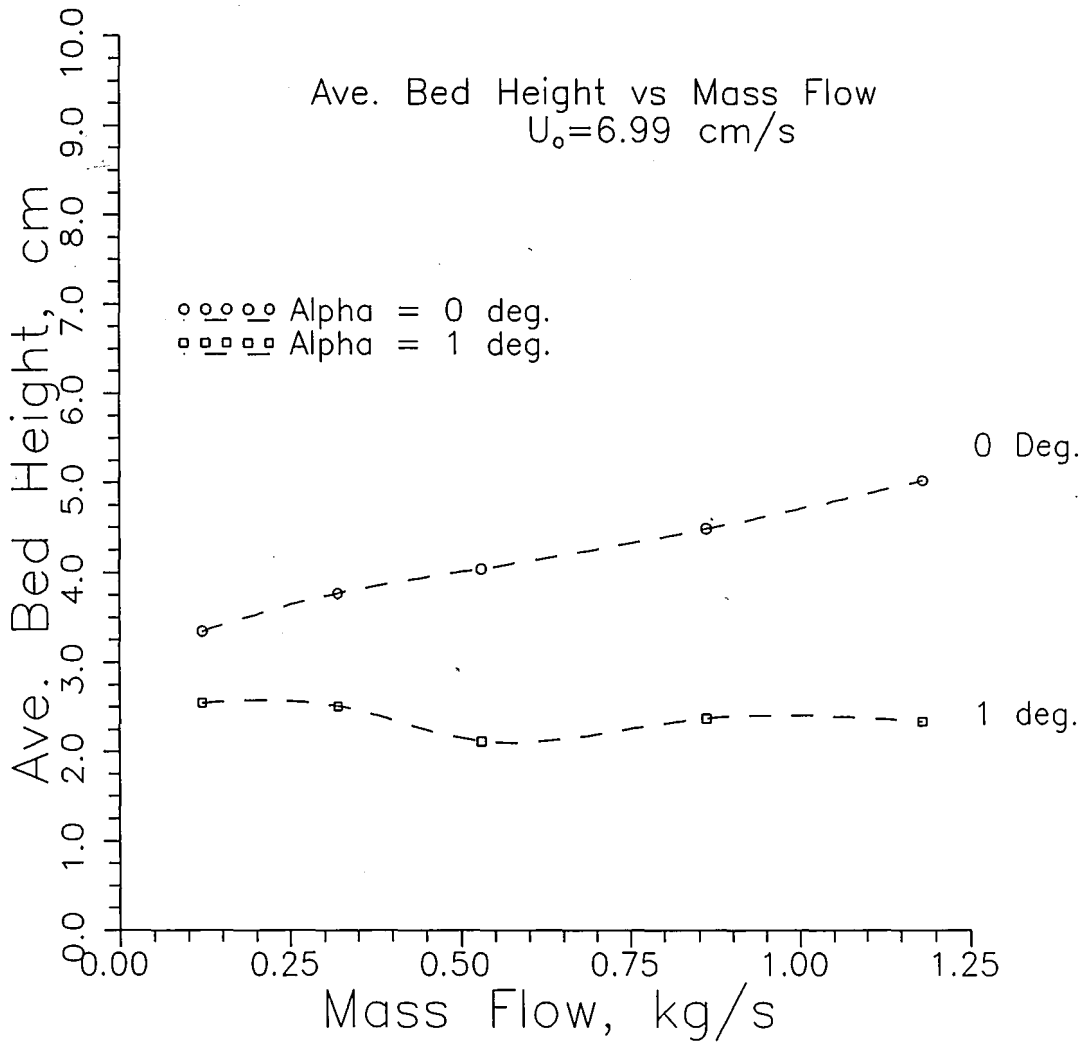

Figure 4.43
Average bed height variation with mass flow for -100 +140 magnetite
u_o = 6.99 cm/s

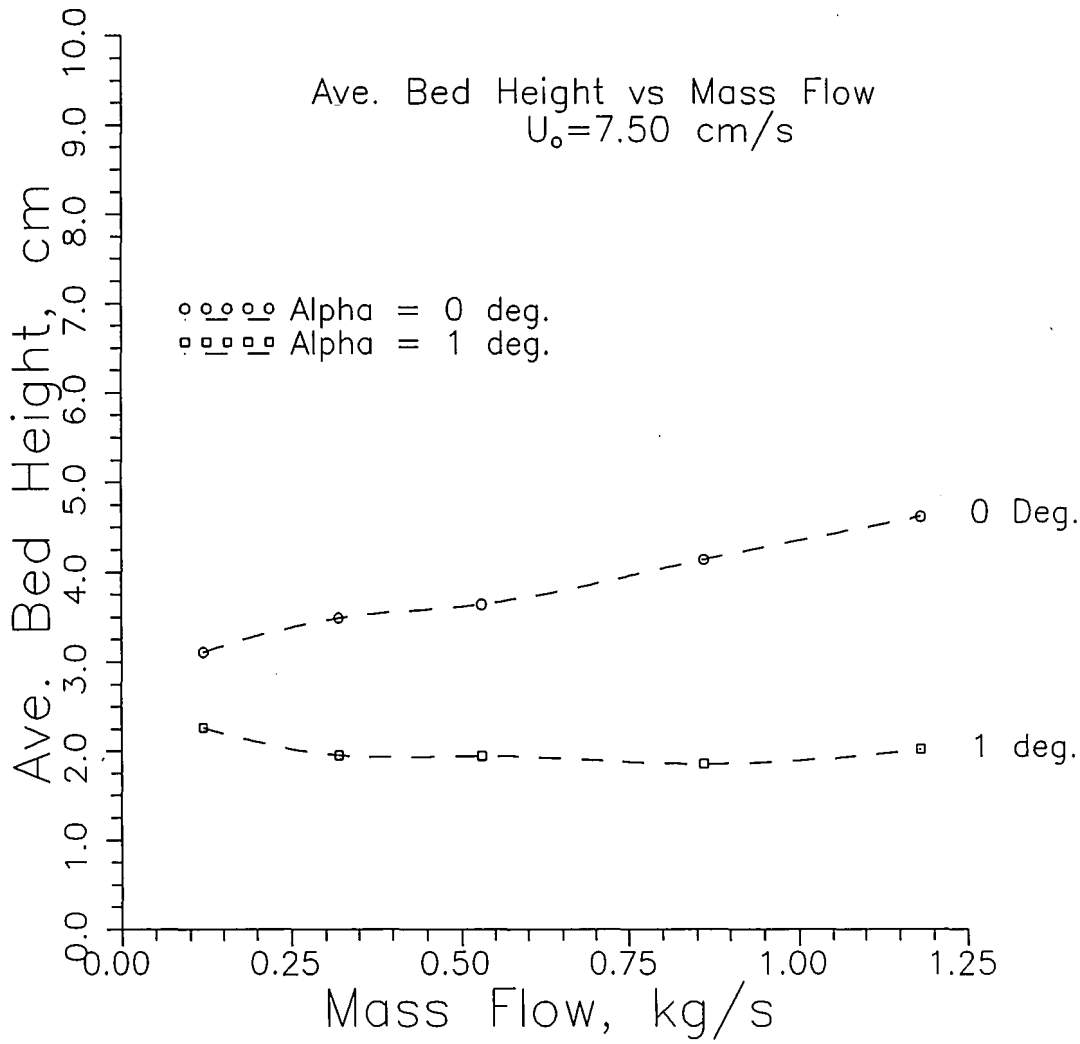

Figure 4.44
Average bed height variation with mass flow for -100 +140 magnetite
u_o = 7.50 cm/s

all eleven positions. These above mentioned figures show the bed height to increase with mass flow, except under certain conditions. During some conditions, usually at low $\dot{m}$, increased mass flow allowed greater momentum influx, allowing a larger average flow velocity and a lower bed height.

Figures 4.45 to 4.49 show the effect of superficial gas velocity on the average bed height at constant solids mass influx. At higher u_o, the average bed height is lower. Furthermore, the effect of the increased air flow and of increased inclination are greater at higher mass flow rates.

Figures 4.50 to 4.56 show the relationship of residence time of a surface float versus mass flow at constant superficial gas velocity. The residence time decreases, seemingly to an asymptotic value for each air flow. As the air velocity increases, the angle of inclination has less effect. Also, at higher gas velocities, the flow reaches its asymptotic transverse velocity at lower $\dot{m}$. In Figures 4.57 to 4.61, the residence time versus u_o at constant $\dot{m}$, show the same trends as above, reaching an asymptotic value more quickly at higher $\dot{m}$.

In order to check consistency and repeatability, as well as to find a level height profile, measurements were also made at $\alpha = 1¼°$. The data at $\alpha = 1¼°$ fit the trends of Figures 4.40, 4.45, 4.46, 4.52, 4.57, and Figure 4.58, while Figures 4.5 and 4.12 show a rather level bed profile.

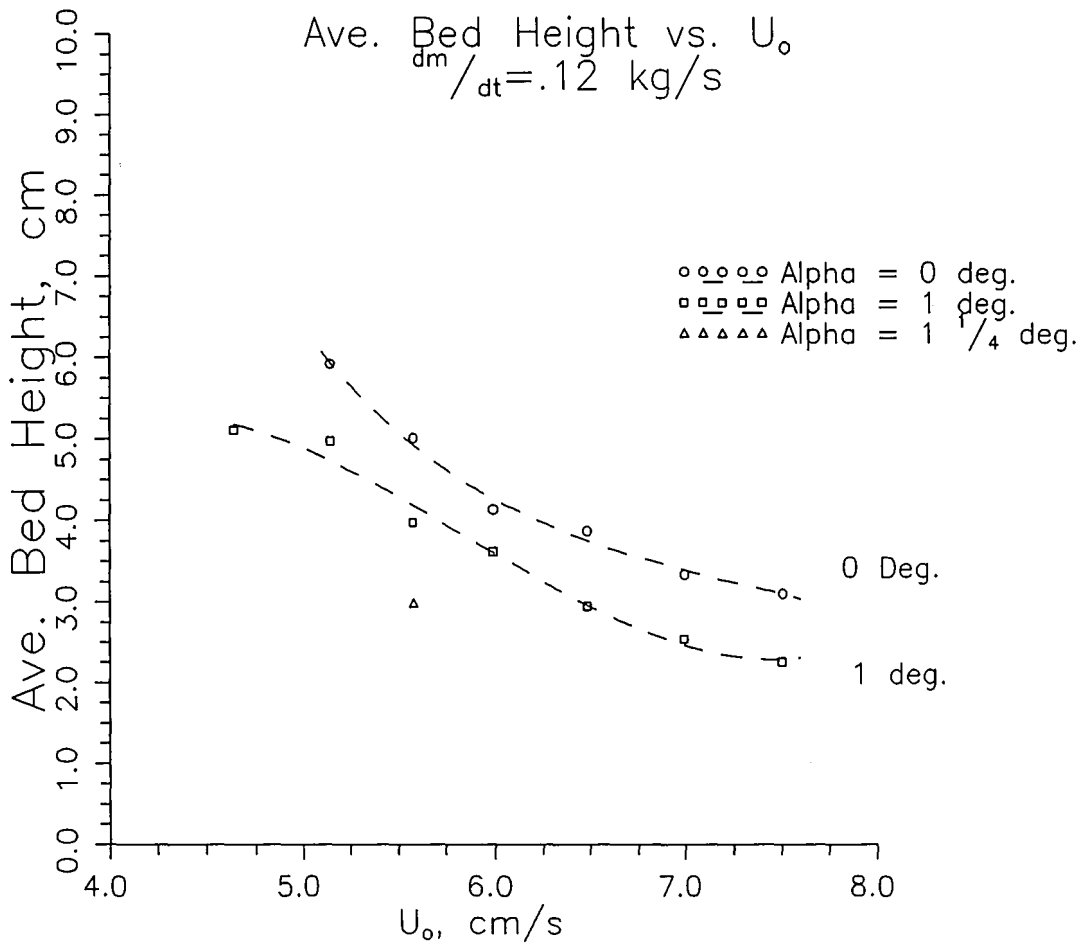

Figure 4.45
Average bed height variation with superficial gas velocity for -100 +140 magnetite
$\dot{m}$ = 0.12 kg/s

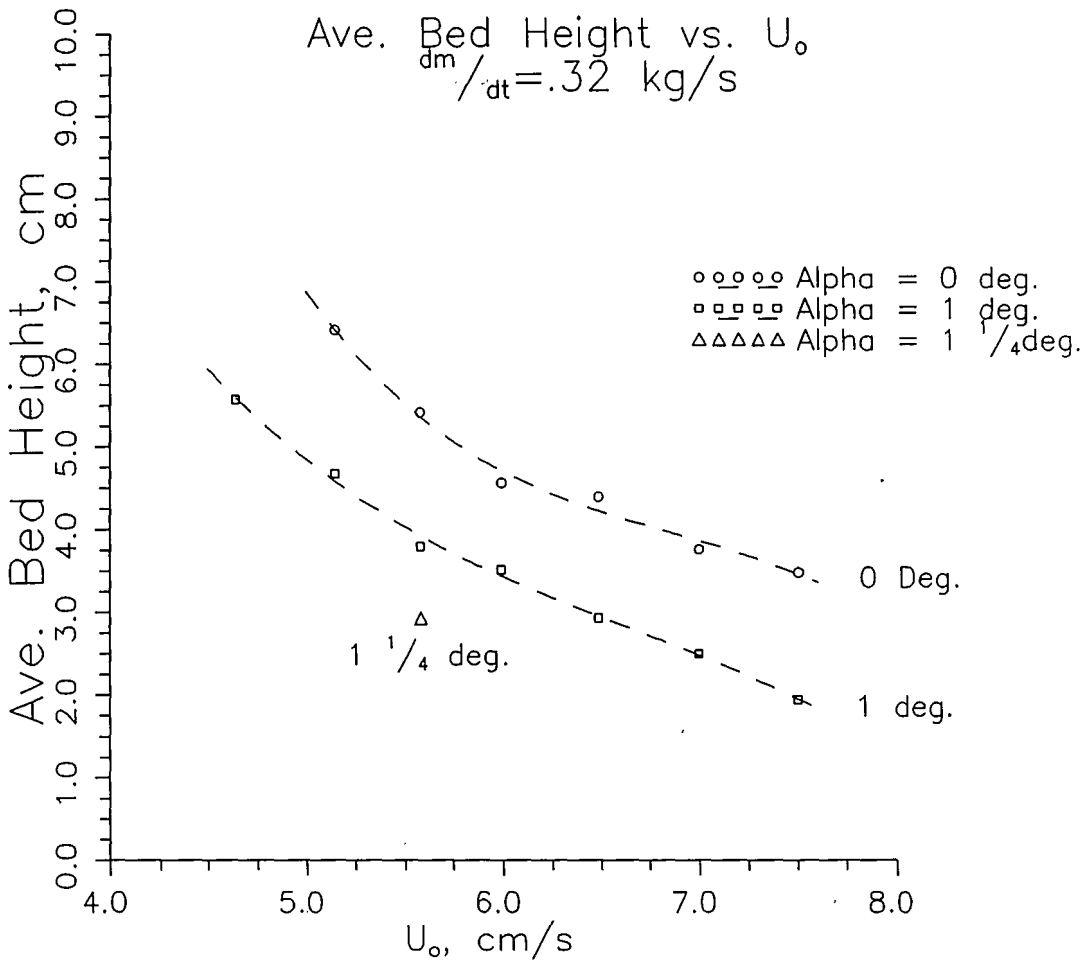

Figure 4.46
Average bed height variation with superficial gas velocity for -100 +140 magnetite
$\dot{m}$ = 0.32 kg/s

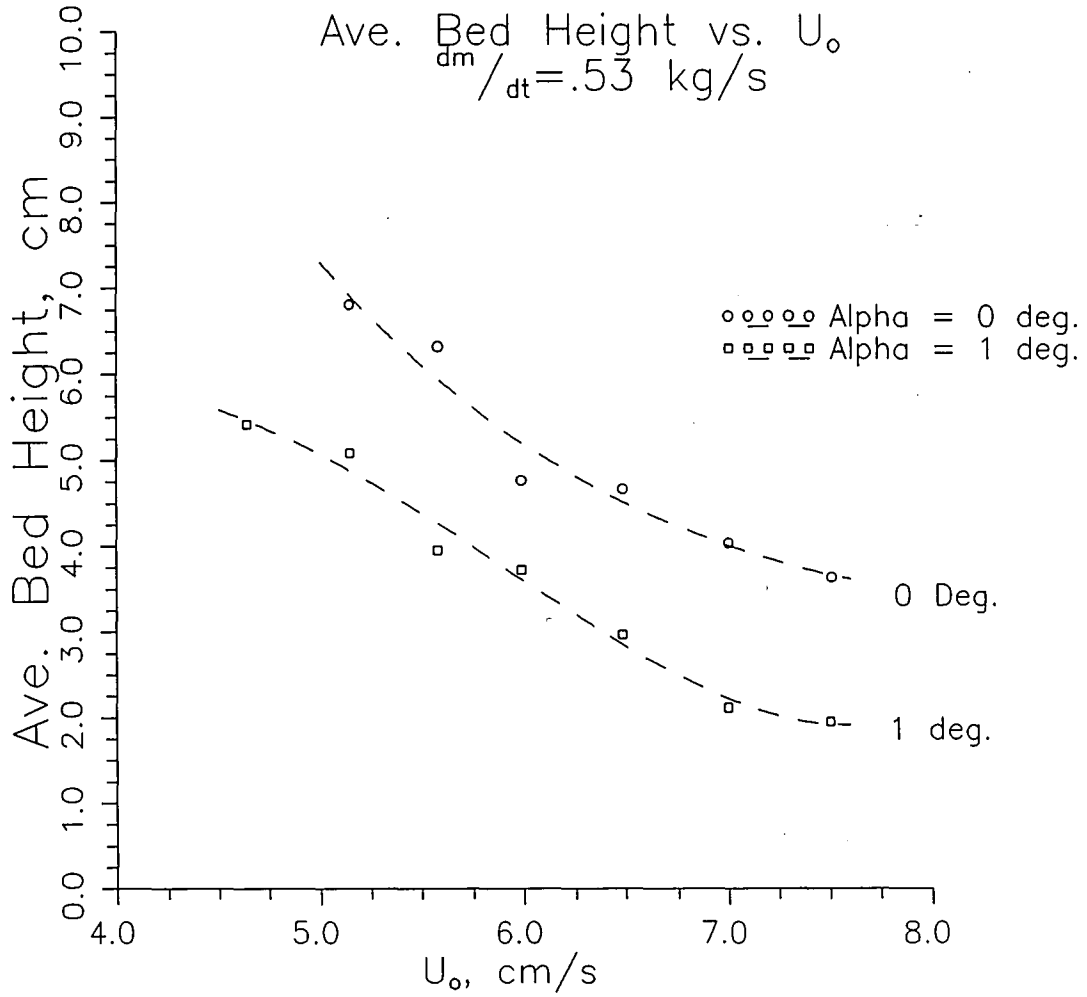

Figure 4.47
Average bed height variation with superficial gas velocity for -100 +140 magnetite
$\dot{m}$ = 0.53 kg/s

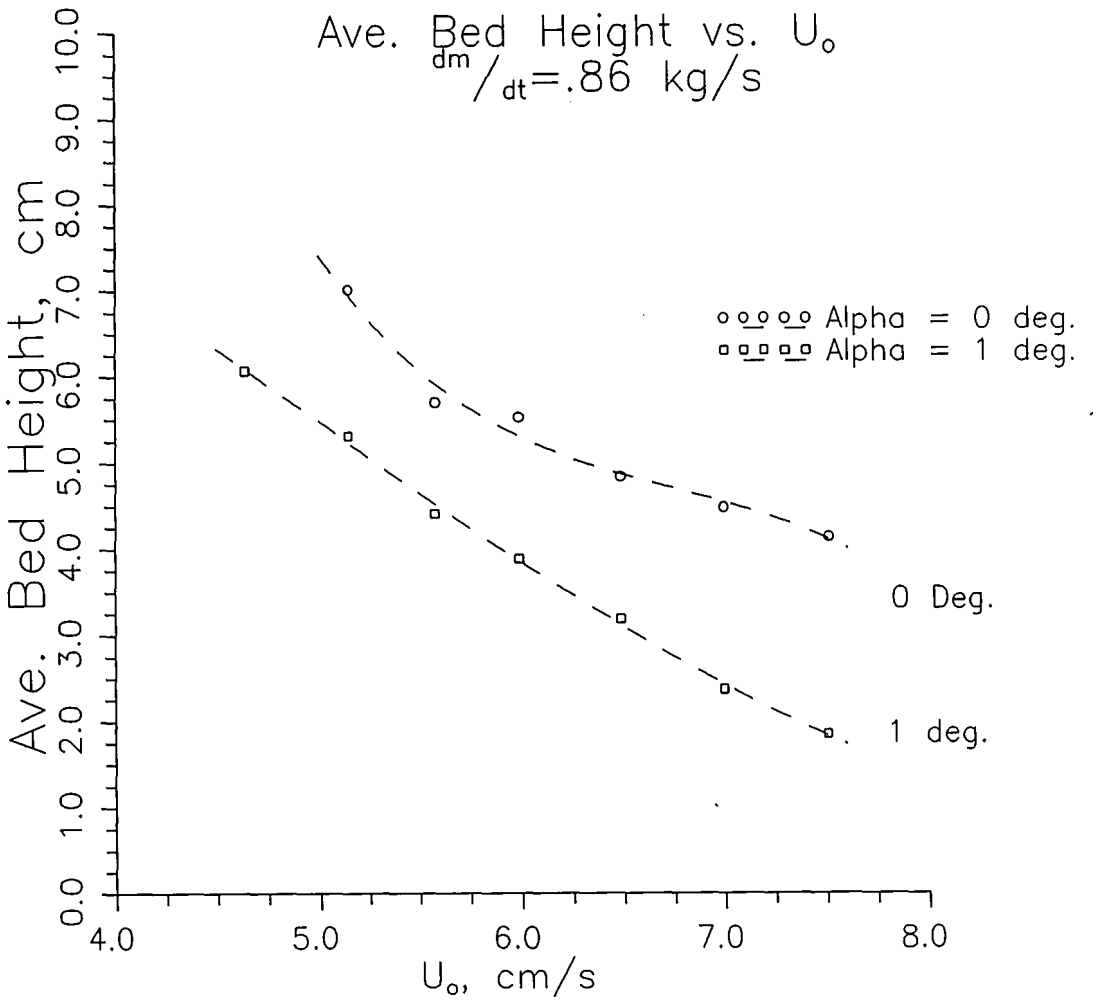

Figure 4.48
Average bed height variation with superficial gas velocity for -100 +140 magnetite
$\dot{m}$ = 0.86 kg/s

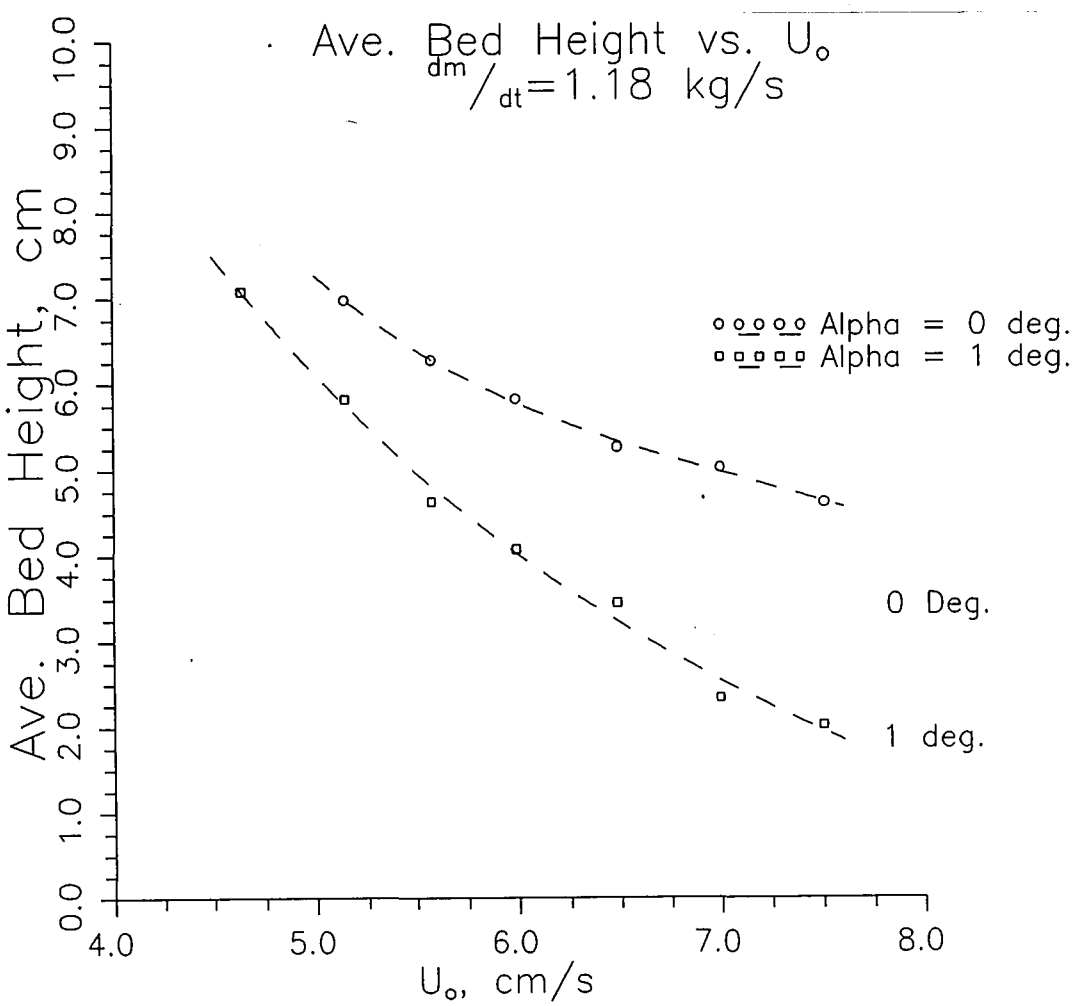

Figure 4.49
Average bed height variation with superficial gas velocity for -100 +140 magnetite
$\dot{m}$ = 1.18 kg/s

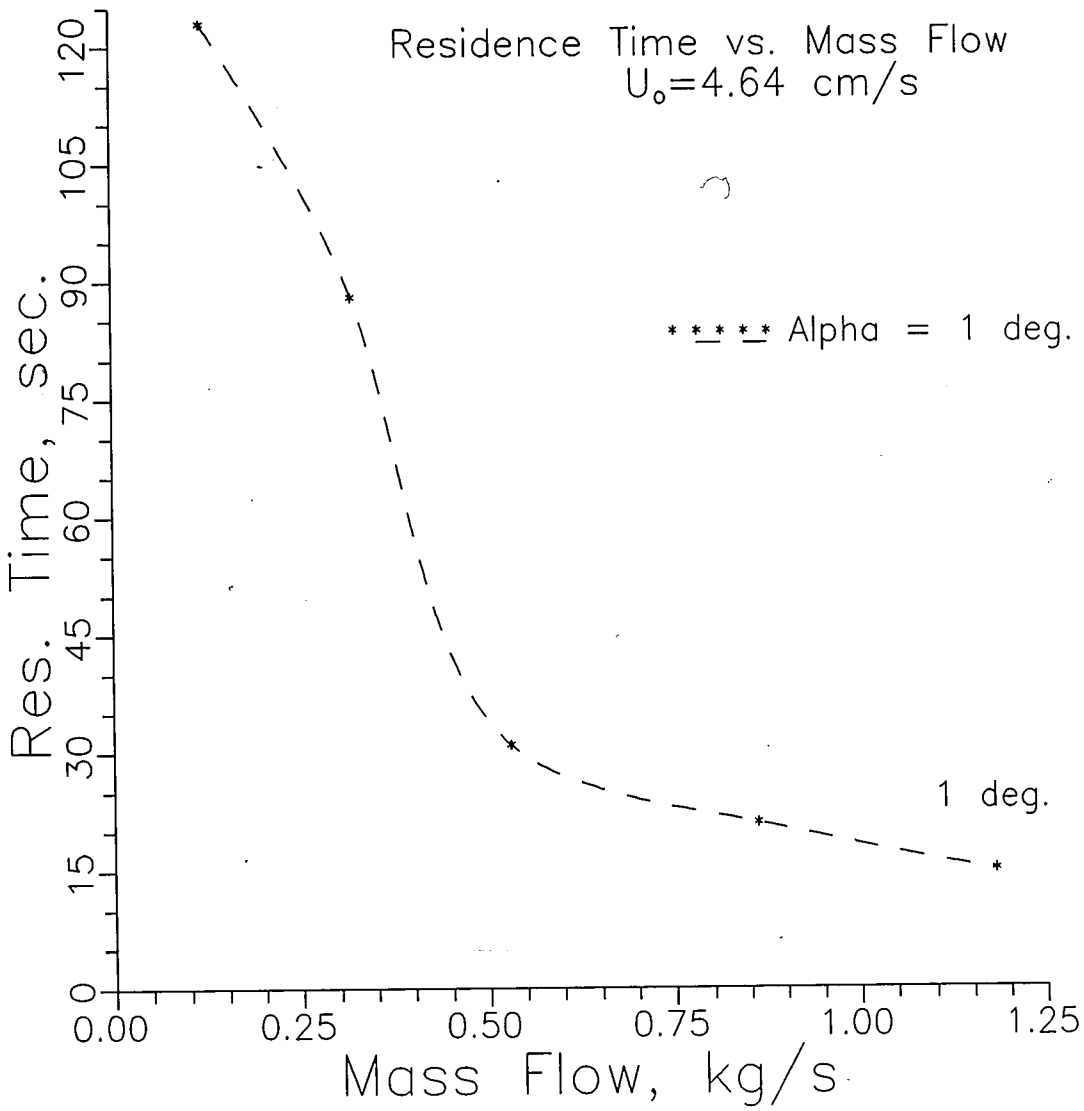

Figure 4.50
Float residence time variation with mass flow for -100 +140 magnetite
u_o = 4.64 cm/s

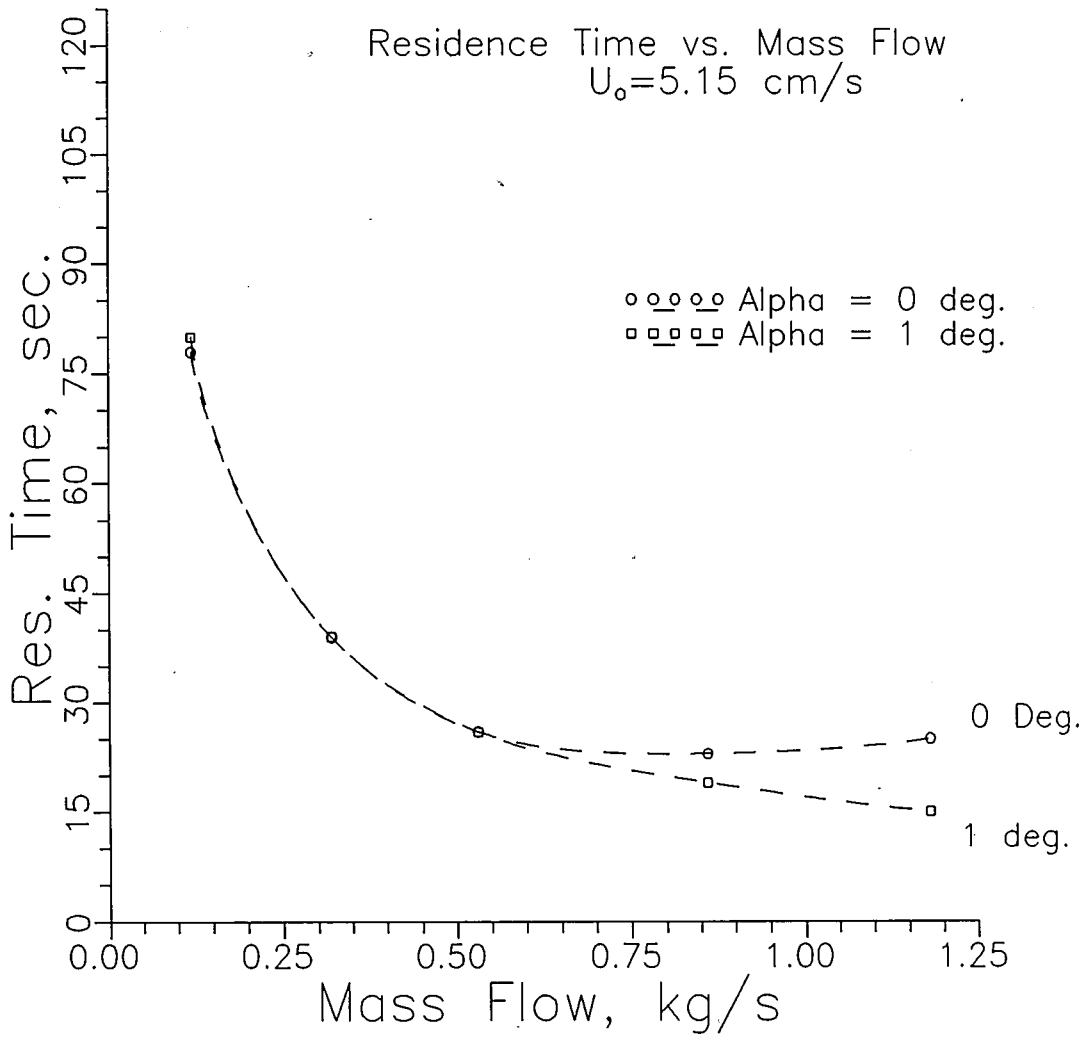

Figure 4.51
Float residence time variation with mass flow for -100 +140 magnetite
u_o = 5.15 cm/s

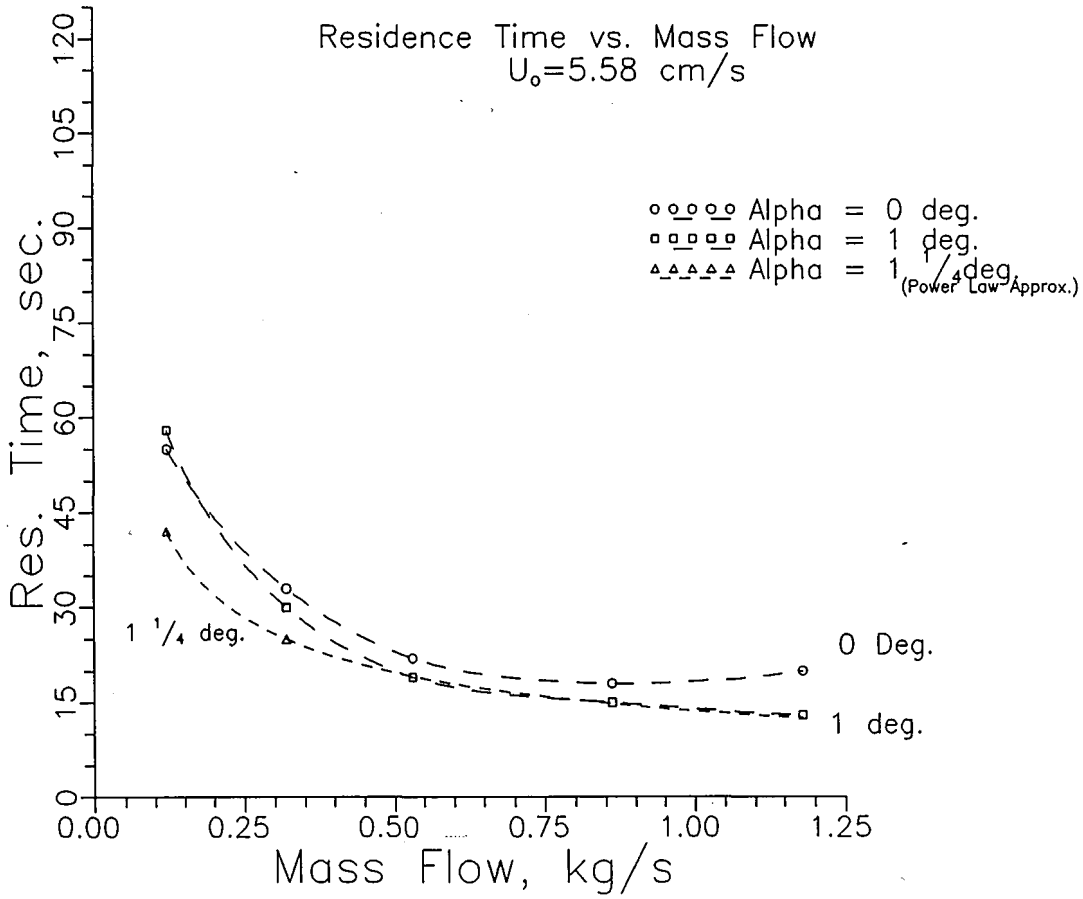

Figure 4.52
Float residence time variation with mass flow for -100 +140 magnetite
u_o = 5.58 cm/s

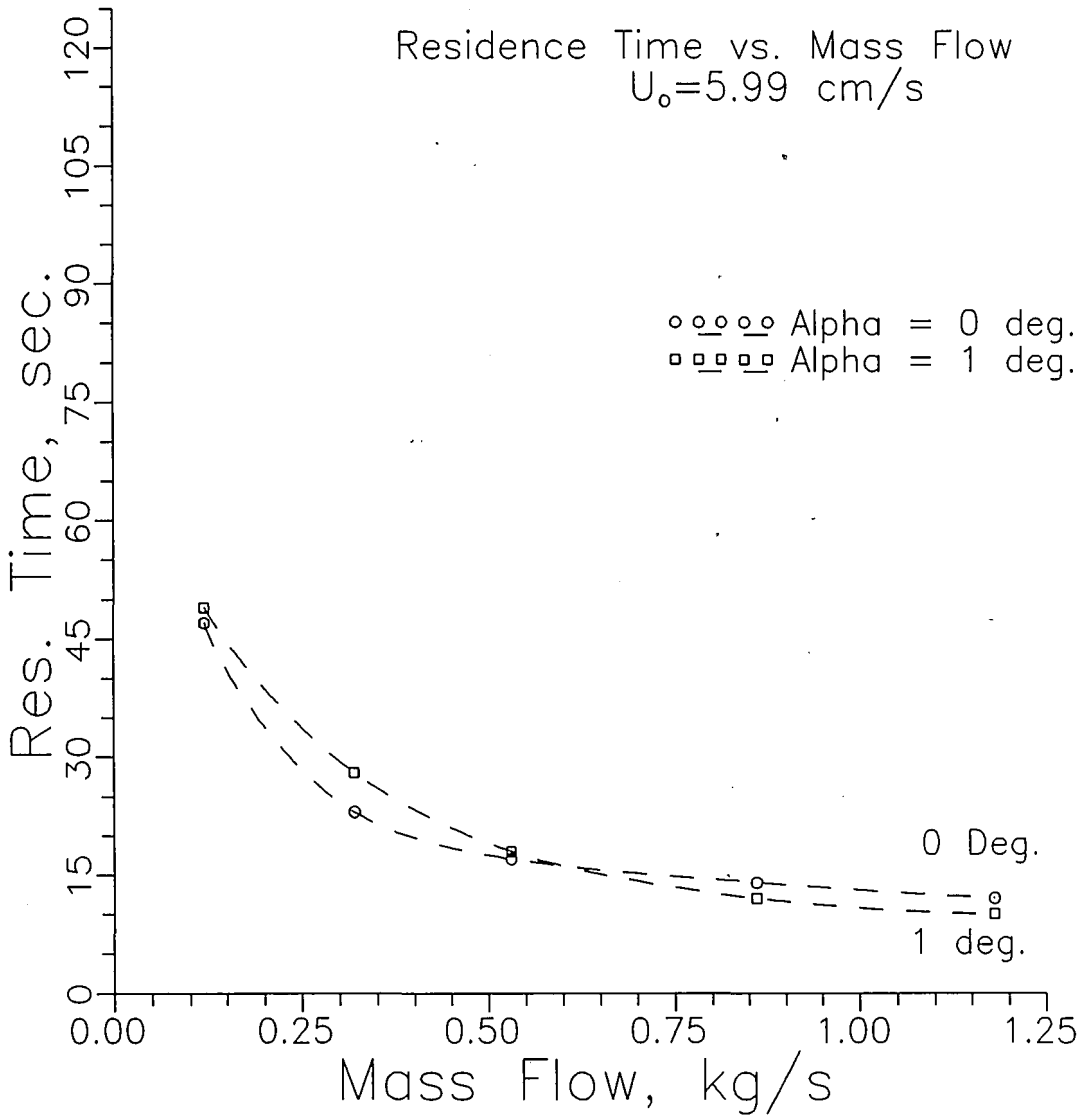

Figure 4.53
Float residence time variation with mass flow for -100 +140 magnetite
u_o = 5.99 cm/s

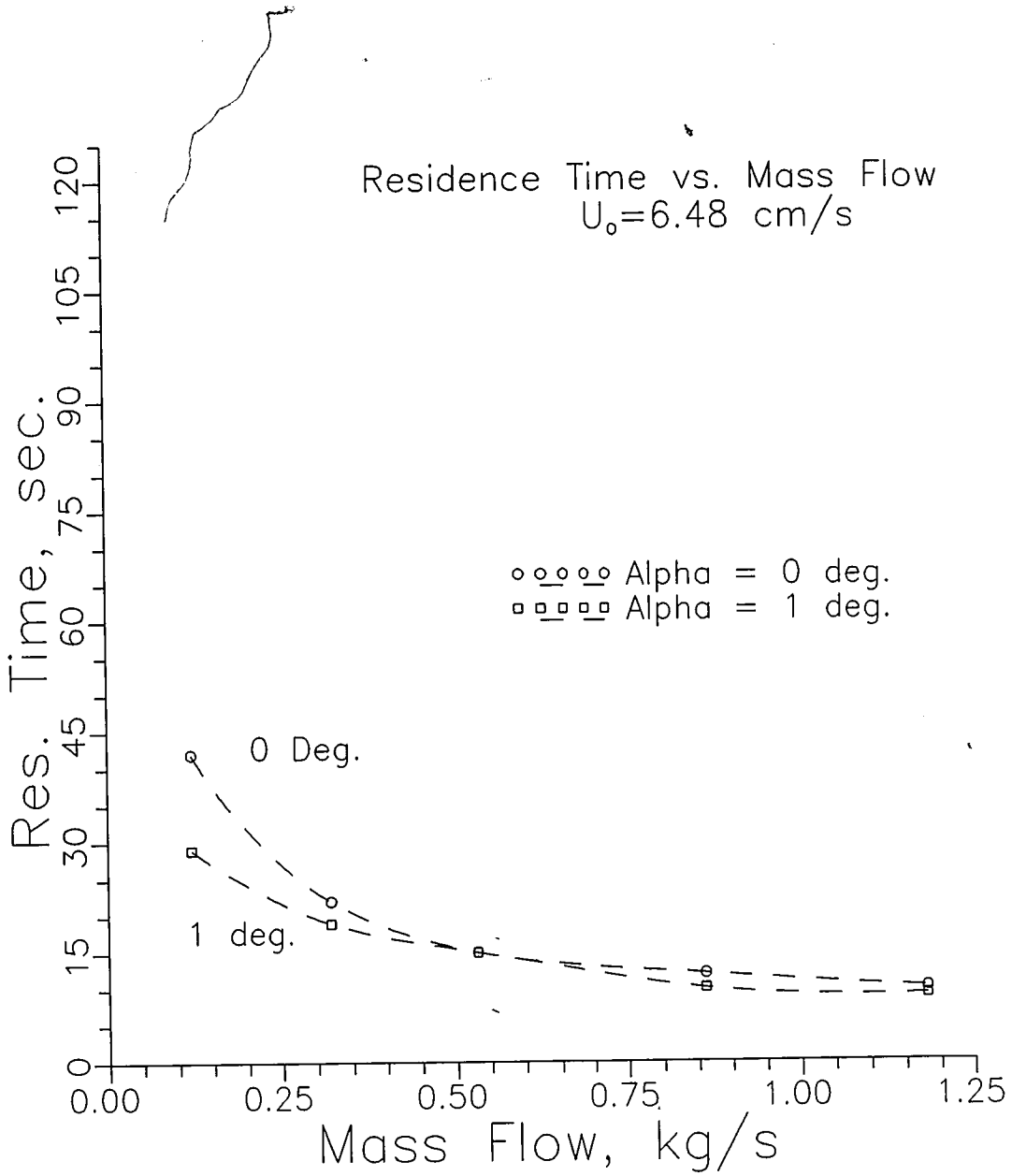

Figure 4.54
Float residence time variation with mass flow for -100 +140 magnetite
u_o = 6.48 cm/s

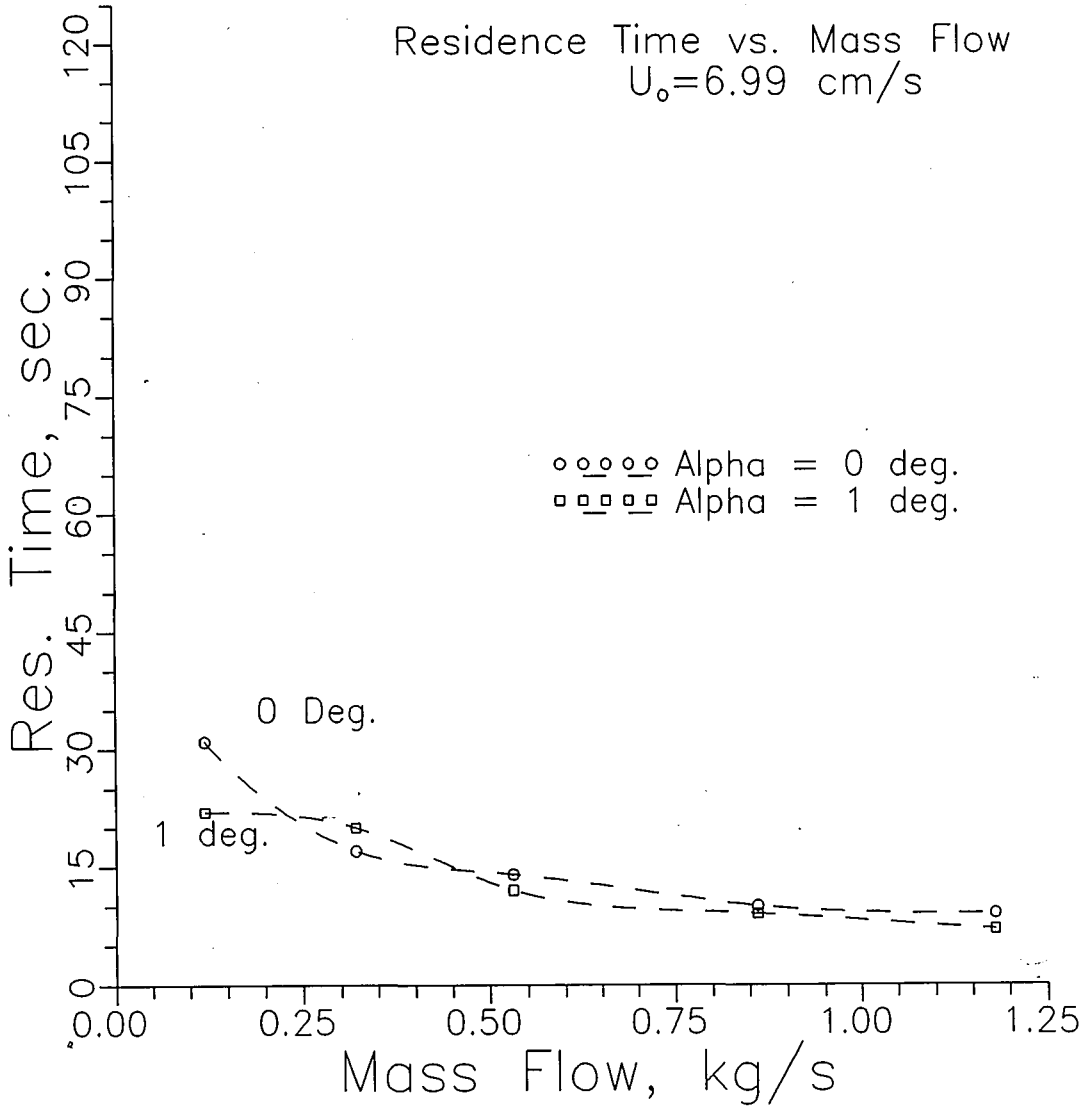

Figure 4.55
Float residence time variation with mass flow for -100 +140 magnetite
u_o = 6.99 cm/s

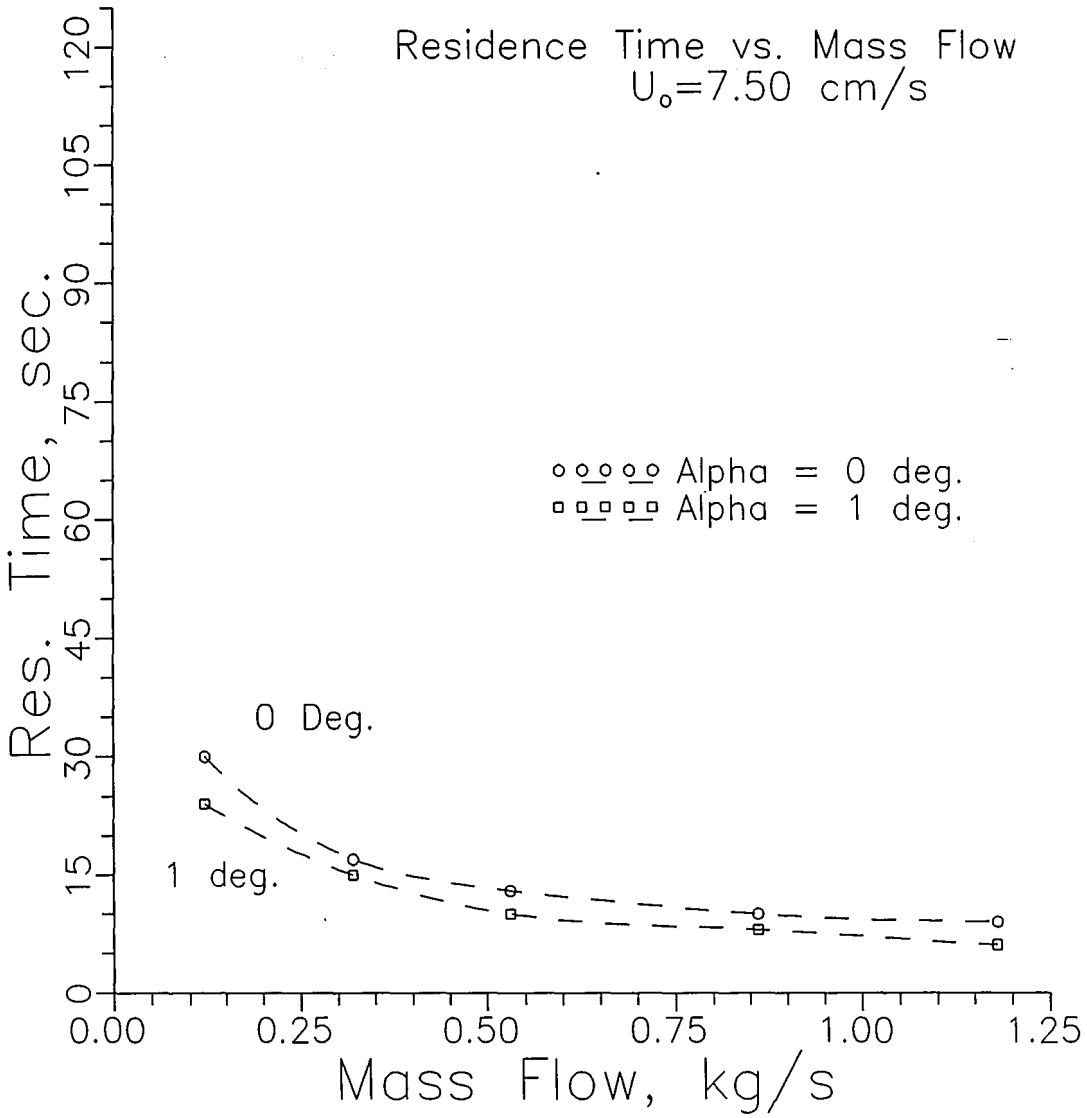

Figure 4.56
Float residence time variation with mass flow for -100 +140 magnetite
u_o = 7.50 cm/s

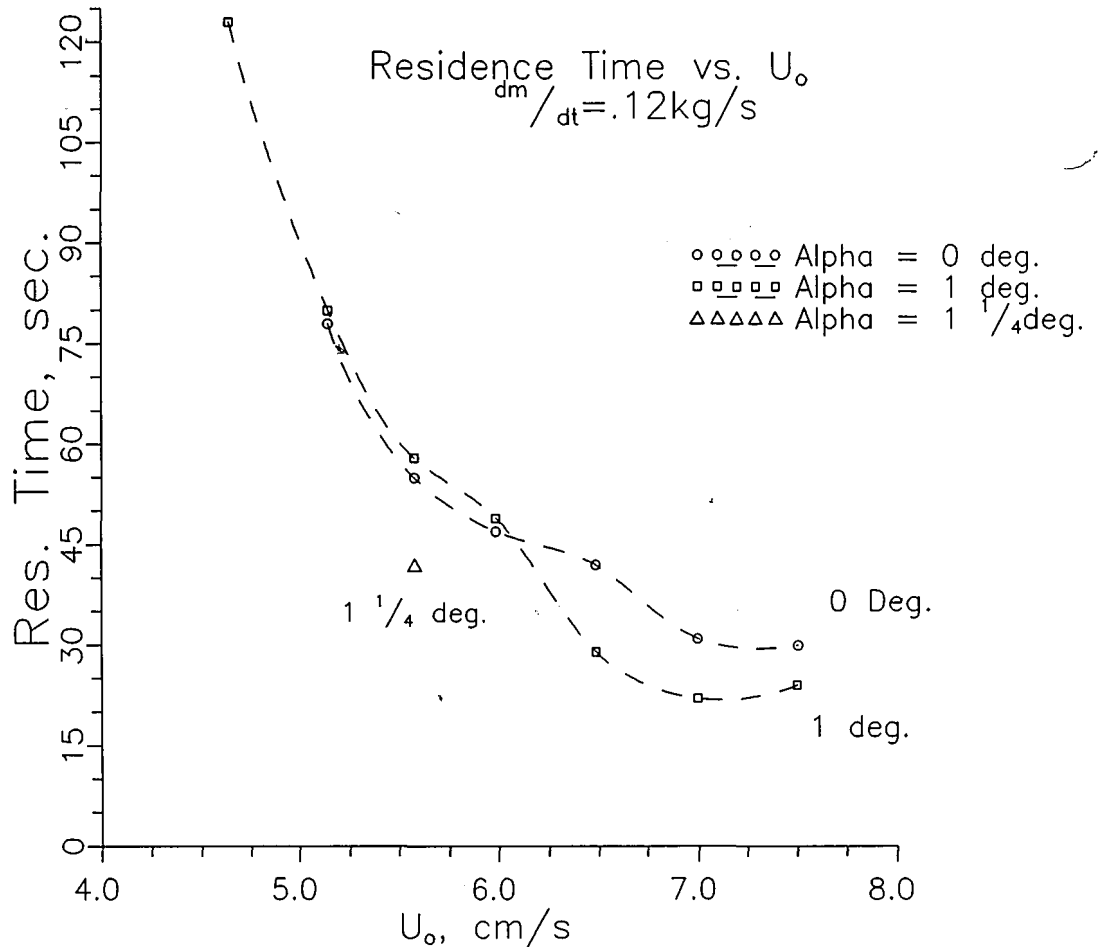

Figure 4.57
Float residence time variation with superficial gas velocity for -100 +140 magnetite
$\dot{m}$ = 0.12 kg/s

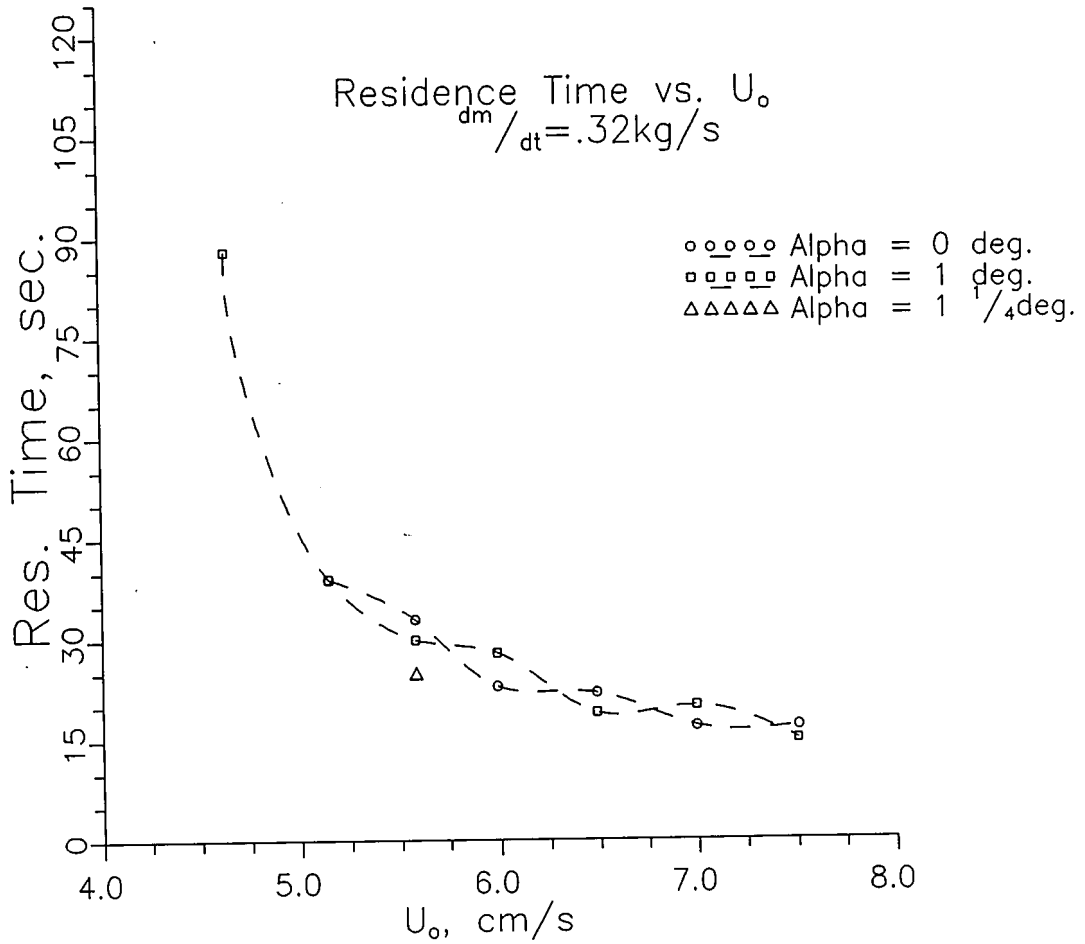

Figure 4.58
Float residence time variation with superficial gas velocity for -100 +140 magnetite
$\dot{m}$ = 0.32 kg/s

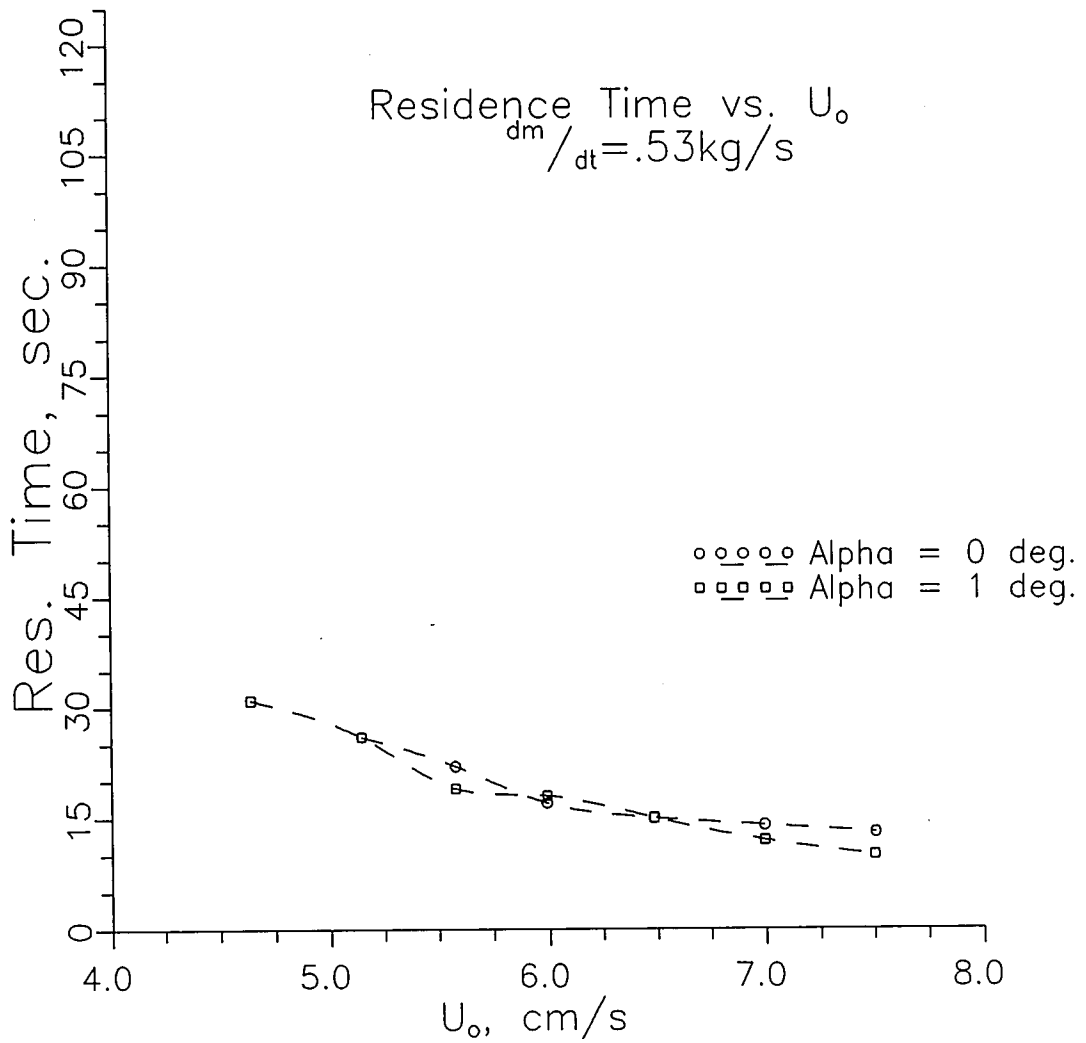

Figure 4.59
Float residence time variation with superficial gas velocity for -100 +140 magnetite
$\dot{m}$ = 0.53 kg/s

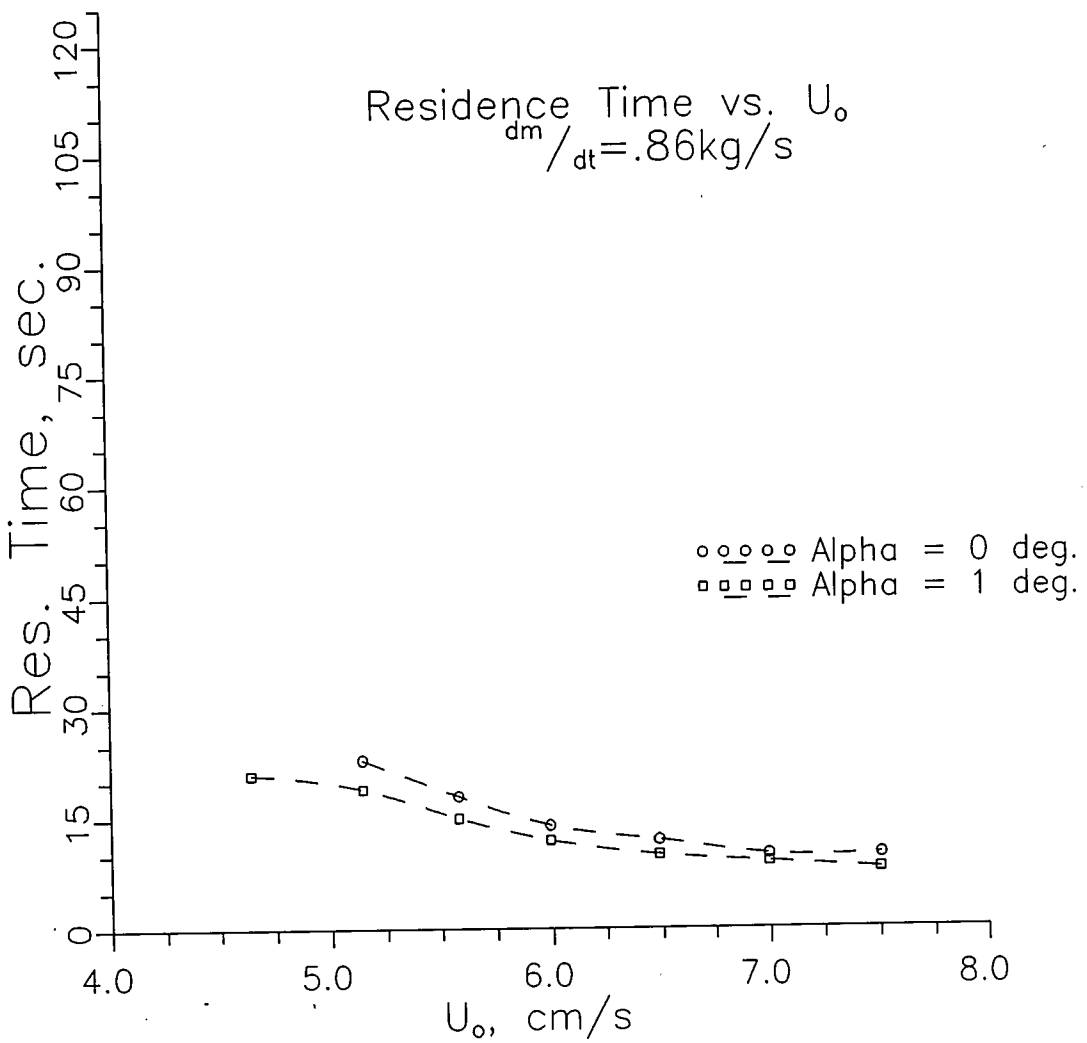

Figure 4.60
Float residence time variation with superficial gas velocity for -100 +140 magnetite
$\dot{m}$ = 0.86 kg/s

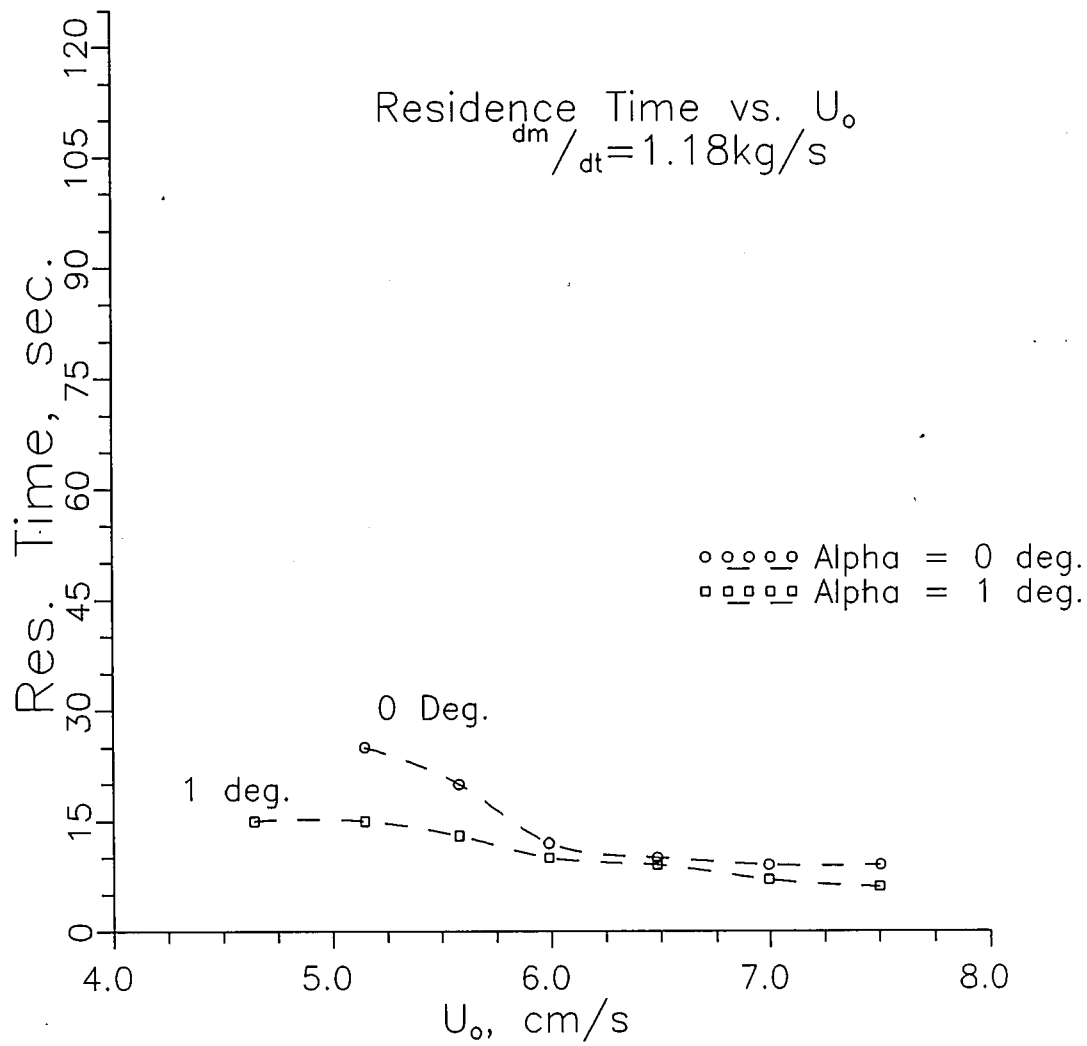

Figure 4.61
Float residence time variation with superficial gas velocity for -100 +140 magnetite
$\dot{m}$ = 1.18 kg/s

4.4 Float tests with co-flowing coal and magnetite

All the flow data shown in Section 4.3 were obtained using pure magnetite. When magnetite and coal were added to the bed together, the flow characteristics changed, causing a reduction in the residence time of the solids on the bed. In addition, a flowing bed of magnetite at low mass feed rates required a relatively high bed height to drive the flow against the resistance of the system. When the coal flow was added, the magnetite efflux from the bed surged, because the added coal on top of the magnetite added pressure, which pushed the magnetite. Eventually, the magnetite flow steadied at a lower bed height than prior to the addition of the coal. The overall bed height of the co-flowing mixture was also lower than for only the magnetite at a low mass feed rate.

This flowing binary mixture appeared to have a velocity gradient in the vertical direction, or, in other words, it was a boundary layer flow. This boundary layer may look something like the two-part boundary layer shown in Figure 4.62, and is believed to occur because the coal flows on top of the magnetite much faster than the magnetite flows alone. To complicate the situation further, the dense coal particles settled towards the bottom, and magnetite diffused to the upper portion of the bed as the cleaning process proceeded. Float tests, performed with floats containing various amounts of ballast to indicate solids mass flow velocities at different depths, gave insight to, and qualitatively proved the existence of, a boundary layer.

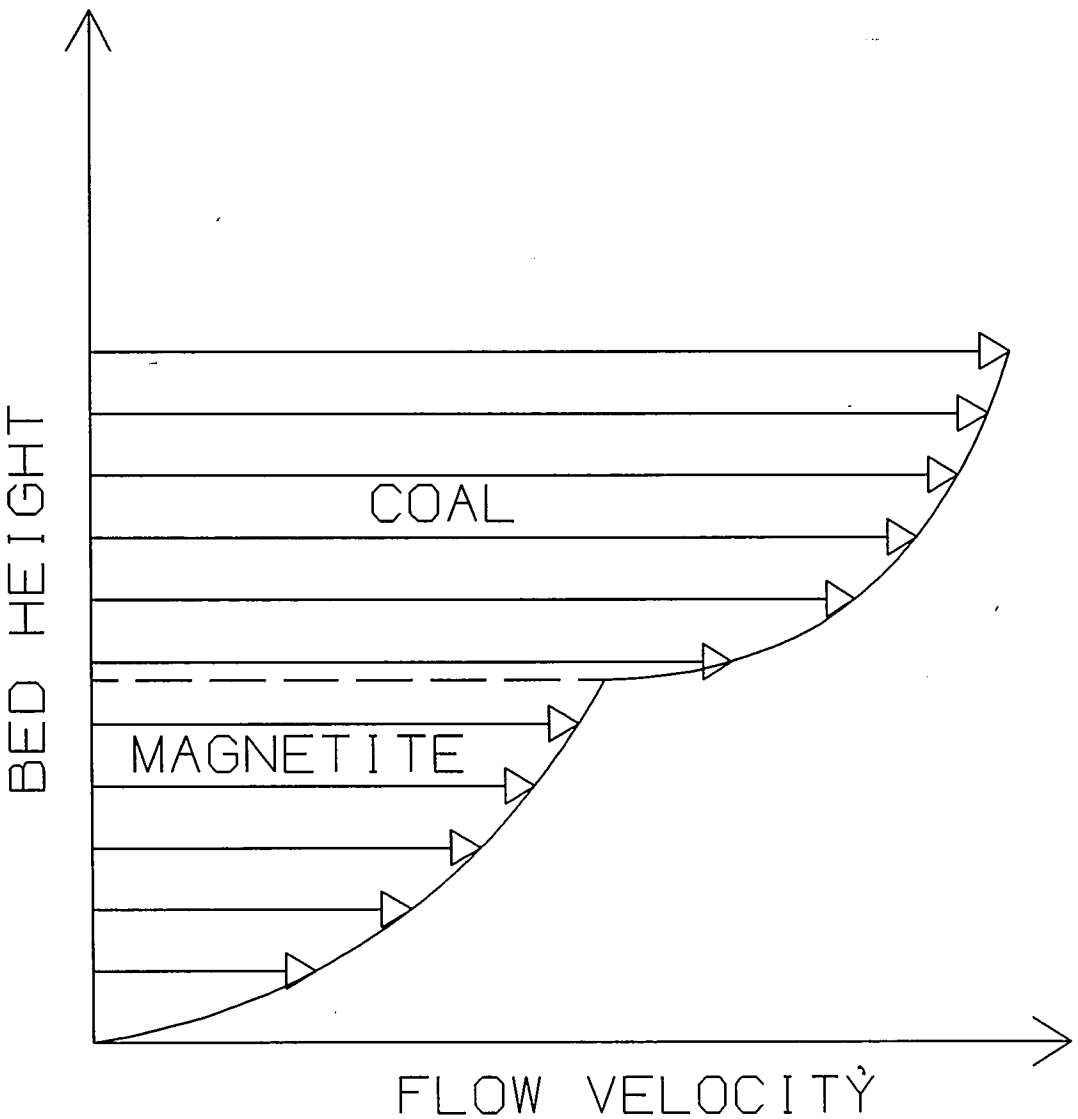

Figure 4.62
Two-part velocity boundary layer in binary solids fluidized open-channel flow

4.4.1 *Float test experimental procedure*

Two floats constructed of light cardboard tubes and balsa wood conical end caps (see Figure 4.63) were calibrated and tested in a batch bed. The first float was 2.7 cm long and the second was 5.9 cm long. Using a ruler to measure the exposed height of the float, the submerged length of the floats in the batch bed were found for different amounts of ballast. This procedure was followed in a bed of magnetite only and also in a bed of coal and magnetite. The bed heights, mass ratios, and fluidizing velocities were comparable to those to be used in the flowing inclined bed float tests.

The purpose of the residence time test was to measure the residence time of the coal under the same flow conditions which occurred during a coal cleaning test performed with a -28 +50 mesh coal ($\bar{d}_p \approx 450\ \mu m$, $u_{mf} \approx 6.6$ cm/s) and a -80 +100 mesh magnetite ($\bar{d}_p \approx 165\ \mu m$, $u_{mfm} \approx 3.5$ cm/s). The flow conditions in Table 4.2 are the same as those used in the cleaning trial. The coal and magnetite float test was allowed a start-up time of one minute. In similar tests with only magnetite, the same fluidizing conditions were used, and the magnetite mass flow rates were 0.125 kg/s and 0.31 kg/s. The lower mass flow rate corresponds to the flow rate of magnetite used in the cleaning experiments, and the higher mass flow rate represents the combined mass flow rate of magnetite and coal. Set at the appropriate operating conditions, bed heights and float times for several float masses were measured. The float residence time was measured along the entire bed length and also along the timing section of the bed used in the continuous cleaning experiments. The bed length sections in the magnetite-only tests were from positions 11.4 cm and 12.7 cm downstream of position 1 to the separator

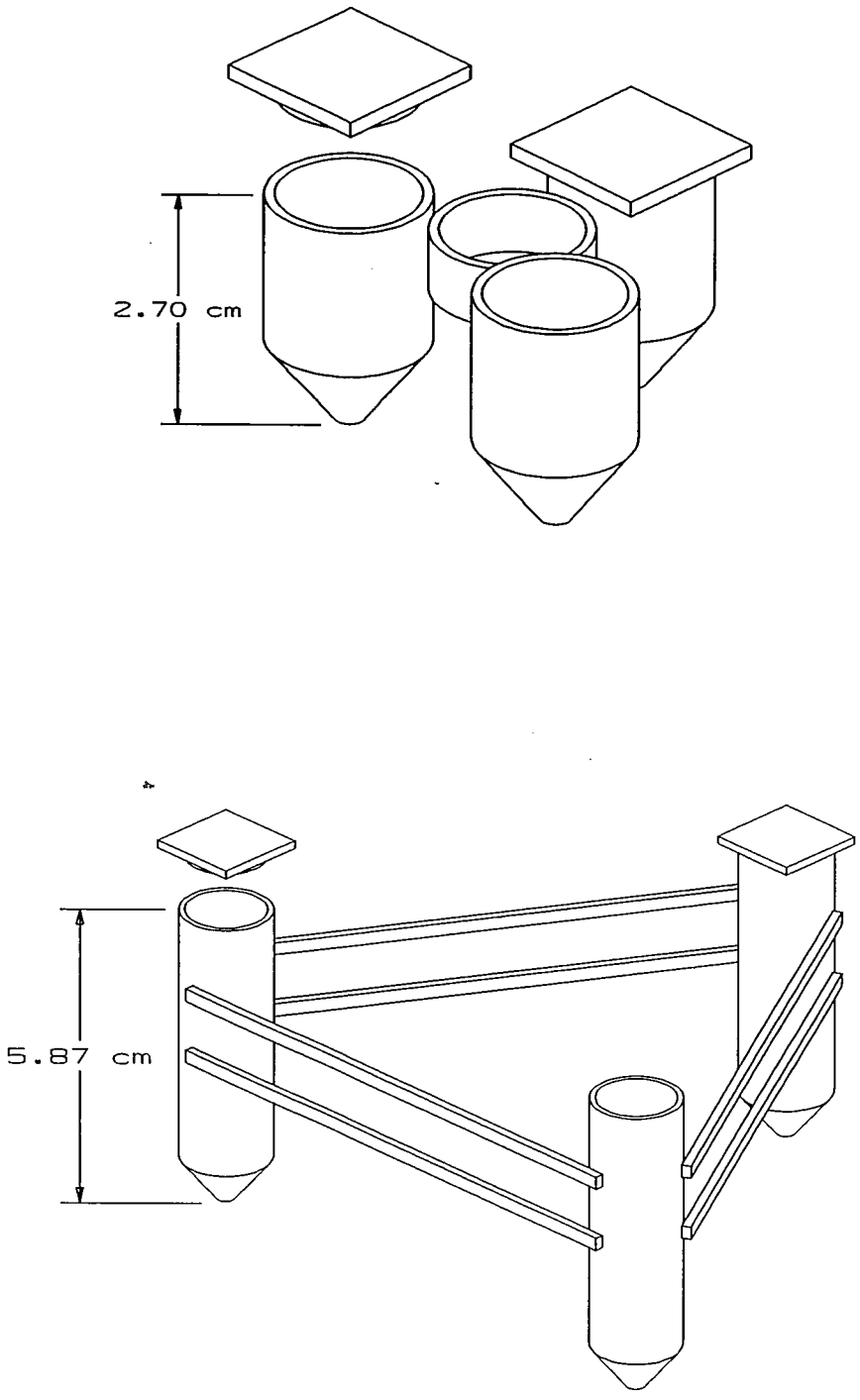

Figure 4.63
Small float and large float used in float experiments

gap for magnetite mass flow settings of $\dot{m}$ = 0.125 kg/s and $\dot{m}$ = 0.31 kg/s, respectively. The bed length section in the coal and magnetite float test was from position 3 to the separator gap. The timing section was always from position 6 to position 8. The parameter $x_{B.L.}$ is the bed length, and $x_{T.S.}$ is the timing section length used in the continuous coal cleaning experiments. The various lengths used are summarized in Table 4.3. The parameters $v_{B.L.}$ and $v_{T.S.}$ are the average float velocities over the bed length and the timing section, respectively. The parameter $v_{B.L.}/v_{T.S.}$ is the ratio of the above two velocities. During the continuous trials, the float was timed as it passed through the timing section, position 6 to position 8. The parameter $v_{B.L.}/v_{T.S.}$ is important, since it indicates how well the residence time measurement during the cleaning trials represents a float residence time over the entire bed length.

Table 4.2
Flow conditions for coal and magnetite float tests

Coal: -28 +50 mesh Emerald Pittsburgh #8
Magnetite: -80 +100 mesh
u_o = 9.63 cm/s = 2.75 u_{mfm}
$\dot{m}_c$ = 0.09 kg/s
$\dot{m}_m$ = 0.09 kg/s
α = -0.75°

4.4.2 *Float test results*

The calibration of the depth of the floats for a magnetite-only bed and a coal-and-magnetite mixture bed is given in Tables 4.4 and 4.5. The characteristic depth is

Table 4.3
Float test section lengths

Magnetite only:

$\dot{m}$ = 0.125 kg/s
$x_{B.L.}$ = 201.9 cm
$x_{T.S.}$ = 50.8 cm

$\dot{m}$ = 0.31 kg/s
$x_{B.L.}$ = 200.7 cm
$x_{T.S.}$ = 50.8 cm

Magnetite and coal:

$x_{B.L.}$ = 188.0 cm
$x_{T.S.}$ = 50.8 cm

defined as the midpoint between the free surface of the bed and the float bottom. All depth measurements have an error of $\pm$ 0.160 cm.

Float tests were performed in the continuous inclined fluidized bed for pure magnetite for two solids mass flow rates (0.125 kg/s and 0.31 kg/s) and for a coal and magnetite mixture.

For the magnetite-only trials, the average fluidized bed heights for low and high solids mass flows were 4.54 cm and 4.38 cm, respectively. The average velocity of the float was simply the distance of float travel per the residence time in the appropriate section. Table 4.6 summarizes the magnetite-only results, which are plotted in Figures 4.64 and 4.65. The above float data do seem to indicate qualitatively a velocity gradient, since the float velocity consistently decreases with depth of immersion of the float.

Table 4.4
Float depth measurements in batch bed
Fluidized -80 +100 magnetite only
u_o = 9.63 cm/s = 2.75 u_{mfm}
h_{fl} = 5.5 cm

Small Float

Total Ballast	Distance Exposed	Depth
0.0 g	2.06 cm	0.64 cm
1.0 g	1.43 cm	1.27 cm
2.0 g	1.11 cm	1.59 cm
3.0 g	0.64 cm	2.06 cm

Large Float

Total Ballast	Distance Exposed	Depth
0.0 g	4.76 cm	1.11 cm
6.0 g	3.81 cm	2.06 cm
12.0 g	3.18 cm	2.70 cm
18.0 g	2.22 cm	3.65 cm
24.0 g	0.95 cm	4.92 cm

The float experiment with coal and magnetite had an average fluidized bed height of 5.4 cm. The tabular data are given in Table 4.7. The mass ratio of coal to magnetite remaining in the channel at the end of the test was m_c/m_m = 0.798 and the ratio of the total mass flows out of the channel was $\dot{m}_c/\dot{m}_m$ = 0.867. Since the mass efflux ratio and mass ratio of the coal to magnetite were almost equal, the coal flowed at approximately the same velocity as the magnetite. Again, Figure 4.66 shows qualitatively the existence of a velocity gradient. Figure 4.67 compares the curve fits of all the float experiments; and the coal and magnetite flow velocity is faster and the profile is steeper than the profiles of the magnetite-only float test results.

Table 4.5

Float depth measurements in batch bed
Fluidized -80 +100 magnetite and -28 +50 Emerald Raw coal
u_o = 9.63 cm/s = 2.75 u_{mfm}; h_{fl} = 5.0 cm; mm = 5

Small Float

Total Ballast	Distance Exposed	Depth
0.0 g	1.43 cm	1.27 cm
1.0 g	0.95 cm	1.75 cm
2.0 g	0.48 cm	2.22 cm

Large Float

Total Ballast	Distance Exposed	Depth
0.0 g	3.65 cm	2.22 cm
3.0 g	2.70 cm	3.18 cm
6.0 g	1.98 cm	3.89 cm
9.0 g	1.11 cm	4.76 cm

There are serious difficulties with attempting to use an immersed float to find a velocity profile, and thus the data should be viewed qualitatively only. Inaccuracies arise in the repeatability of the ballast mass and the determination of the characteristic bed depth. Most importantly, the use of a characteristic bed depth is of limited value since the drag force on the float varies with local flow velocity. In addition, the area at the bottom of the float (nose of the float) is different than on the cylindrical portion. However, even when considering all the above problems, the results still indicate a velocity gradient, since the average float velocity consistently decreased with depth of immersion. Also, the float velocity of the co-flowing mixture at a characteristic depth of 1.5 cm was used as an upper bound prediction of the processing time of the -28 +50

Table 4.6
Magnetite-only float velocity results

$\dot{m}$ = 0.125 kg/s

Float Bottom Depth	Characteristic Depth	$v_{B.L.}$	$v_{T.S.}$	$v_{B.L.}/v_{T.S.}$
0.64 cm	0.320 cm	3.37 cm/s	2.88 cm/s	1.17
1.27	0.635	3.25	2.65	1.23
1.59	0.795	3.18	2.42	1.31
1.11	0.555	2.87	2.89	0.99
2.06	1.030	2.77	2.69	1.03
2.70	1.350	2.40	2.36	1.02
3.65	1.825	2.26	2.14	1.06

average $v_{B.L.}/v_{T.S.}$ = 1.12

$\dot{m}$ = 0.310 kg/s

Float Bottom Depth	Characteristic Depth	$v_{B.L.}$	$v_{T.S.}$	$v_{B.L.}/v_{T.S.}$
0.64 cm	0.320 cm	6.20 cm/s	6.44 cm/s	0.96
1.27	0.635	5.95	6.54	0.91
1.59	0.795	6.17	6.97	0.89
1.11	0.555	6.34	6.55	0.97
2.06	1.030	6.15	6.62	0.93
2.70	1.350	5.89	6.04	0.98
3.65	1.825	5.55	5.78	0.96

average $v_{B.L.}/v_{T.S.}$ = 0.94

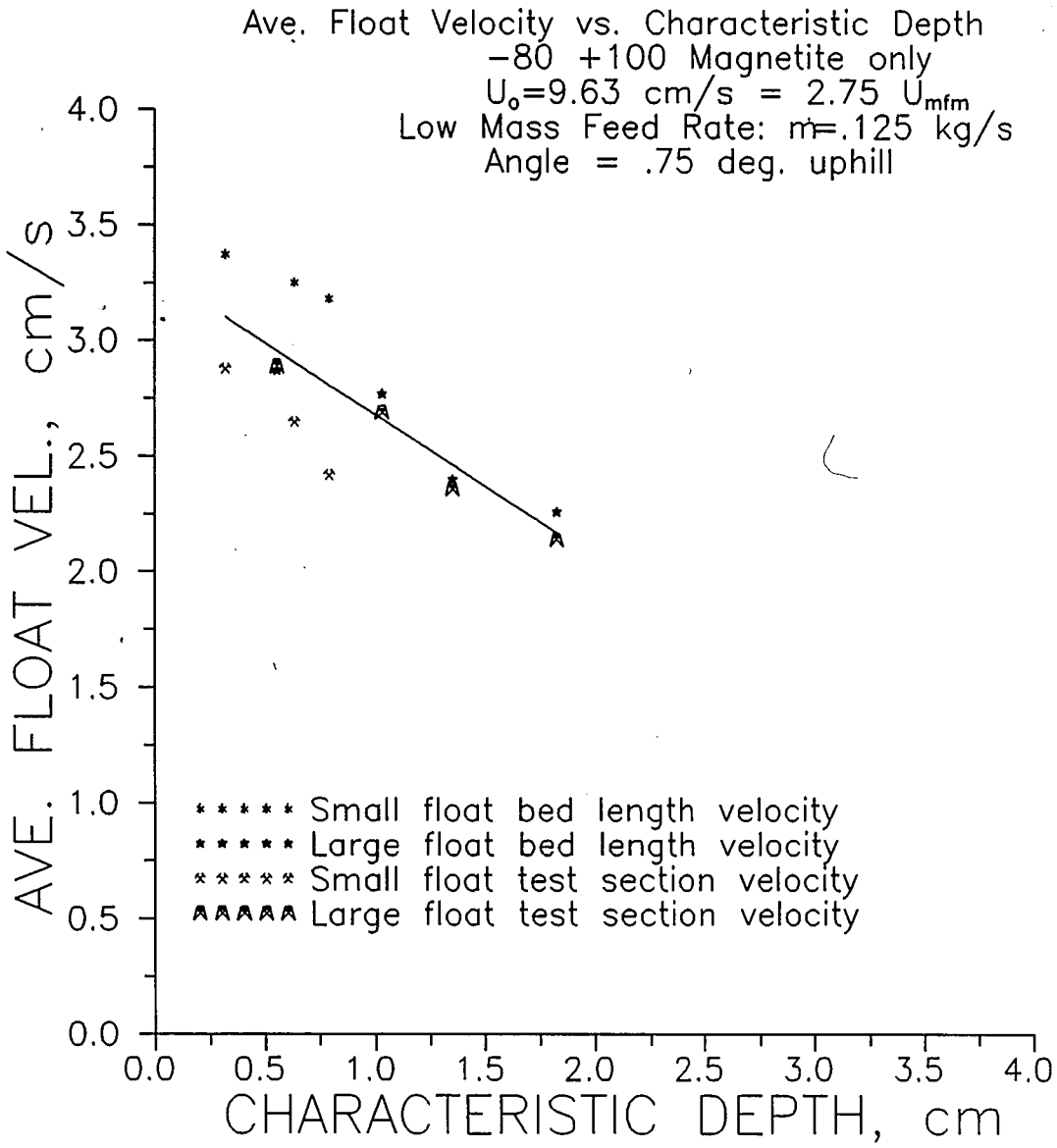

Figure 4.64
Magnetite-only float test profile results
$\dot{m}$ = 0.12 kg/s

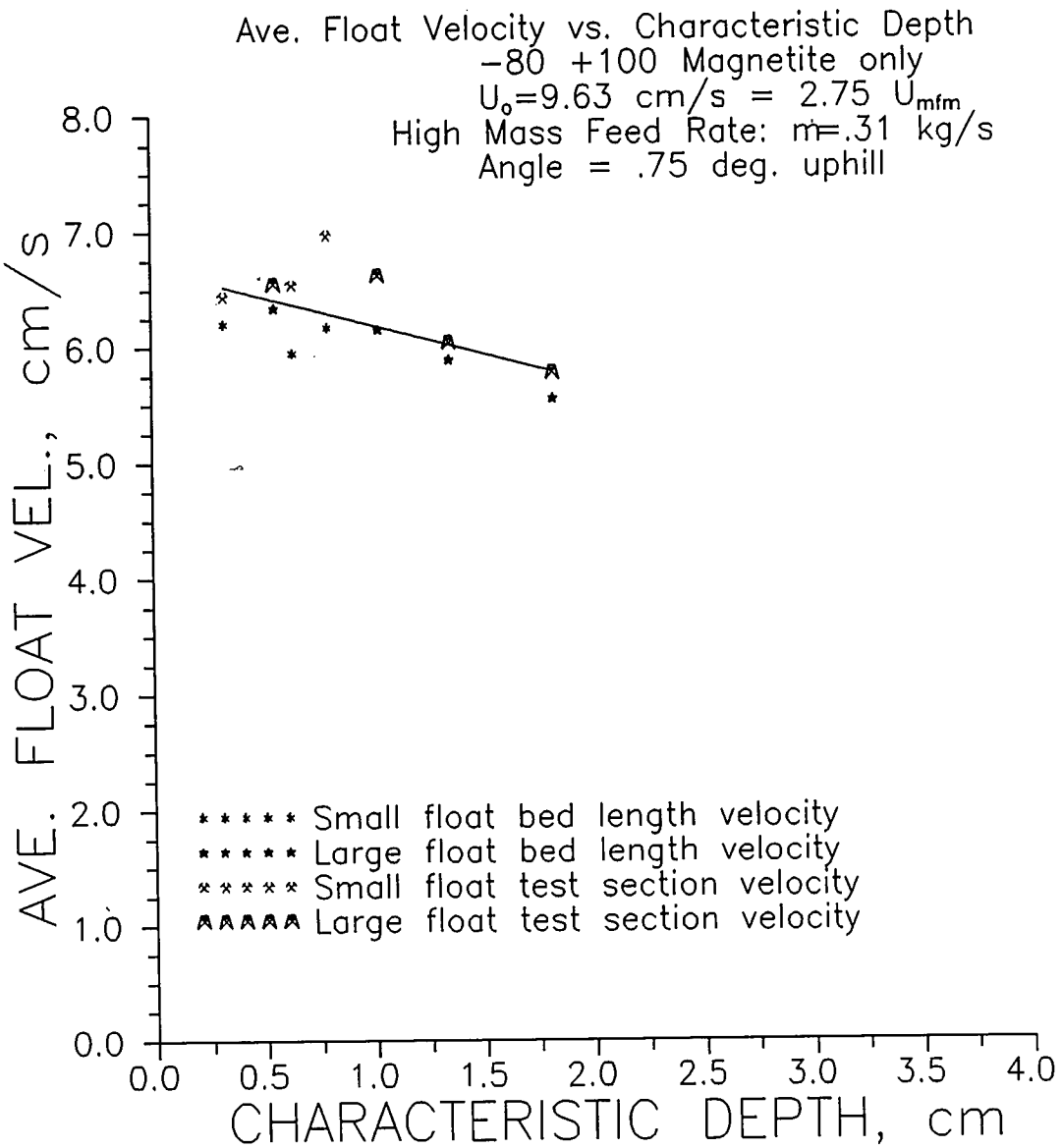

Figure 4.65
Magnetite-only float test profile results
$\dot{m}$ = 0.32 kg/s

Table 4.7
Magnetite-and-coal float velocity results

Float Bottom Depth	Characteristic Depth	$v_{B.L.}$	$v_{T.S.}$	$v_{B.L.}/v_{T.S.}$
0.00 cm	0.000 cm	7.39 cm/s	6.77 cm/s	1.09
1.27	0.635	9.27	8.47	1.09
1.75	0.875	10.48	9.14	1.15
1.75	0.875	9.14	8.33	1.10
2.22	1.110	9.53	9.48	1.01
3.18	1.590	8.31	7.20	1.15
3.18	1.590	8.92	8.04	1.11
3.89	1.950	7.26	7.41	0.98
3.89	1.950	7.12	6.80	1.05

average $v_{B.L.}/v_{T.S.} = 1.08$

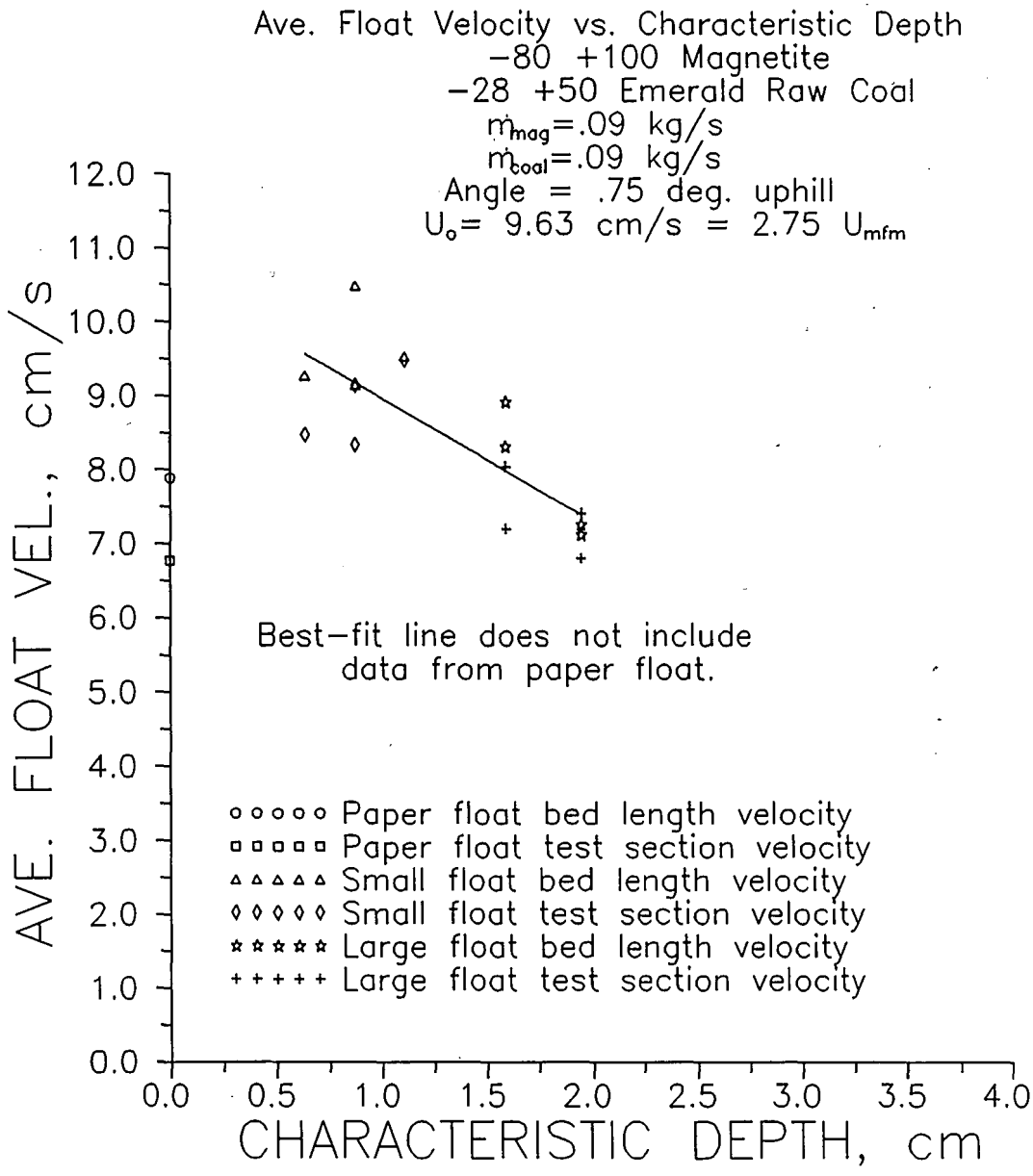

Figure 4.66
Coal-and-magnetite float test profile results
$\dot{m}_{coal}$ = 0.09 kg/s
$\dot{m}_{mag}$ = 0.09 kg/s

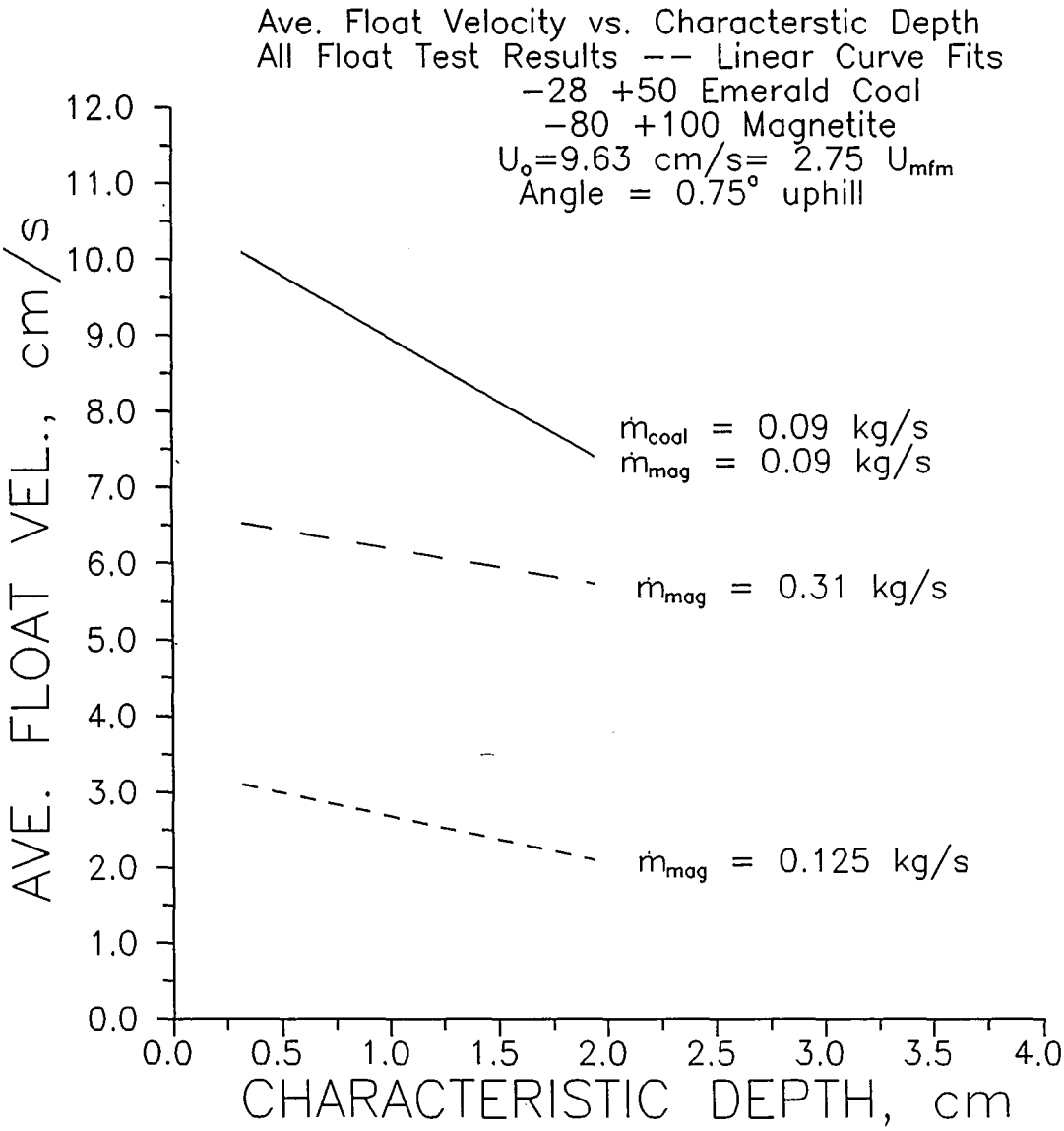

Figure 4.67
Linear curve fits of all float test results

Rushton coal continuous cleaning trials.

4.5 Continuous coal cleaning trials

The preliminary flow experiments in the inclined bed were used to determine the best combinations of bed inclination angle and mass flow rates. The flow data with magnetite indicated that a combined coal and magnetite flow rate of approximately 0.15 to 0.20 kg/s was needed to obtain the desired bed height and solids residence time. However, these mass feed rates resulted in an oscillation in the flow. In order to stop the oscillations and achieve the best combination of residence time and bed height, the bed was inclined at an uphill (negative α) angle. Based on these results, coal cleaning experiments were then performed at the desired values of u_o, α, $\dot{m}_c$, and $\dot{m}_m$.

4.5.1 *Experimental procedure*

The cleaning trials required the use of a six-person team, with each person performing a specific task during the rapidly progressing test. The experiment began by setting the inclination angle air flow rate and separator gap, and beginning the magnetite mass flow. The magnetite was allowed to reach a quasi-steady flow, which, in some cases, had oscillations, due to the relatively low magnetite mass flow rates. The oscillations in the magnetite flow stopped once the coal flow began. The coal added sufficient momentum to induce steady, non-oscillatory flow. While only magnetite

flowed, time was not a constraining factor, since the magnetite could be recycled indefinitely to the feed hopper via the conveyor.

After quasi-steady flow was established with the magnetite, the coal feed was initiated and time then became very critical. Prior to the coal flow reaching the separator gap, the flow to the conveyor was re-routed to a "trash mixture" bucket, and the sample at the separator gap was also switched to a "trash mixture" bucket. A "trash mixture" is a mixture of coal and magnetite obtained during both start-up and between the samplings. A start-up time of thirty seconds began when the coal had almost reached the separator gap. At this time, buckets were switched to prevent coal from entering the magnetite hopper via the conveyor belt and to recycle the magnetite which fell through the separator gap during the magnetite-only start-up time. After the start-up time had elapsed, four 12-second samples were obtained at the product and refuse outlets. The time between starting each sample collection sequence was thirty seconds. During each sampling, one person timed a float as it moved along the bed from position 6 to position 8, and another read the bed heights at positions 4, 7, 9, and 10. The residence time and bed height readings had to be made very quickly, and a substantial possibility for error in the readings certainly existed. During the test, a steady solids mass flow was critical, so one person monitored the solids' levels in the hoppers and added coal or magnetite as needed. At the end of a test, a material hold-up experiment was performed to determine the coal-to-magnetite mass ratio on the bed.

Finally, the samples were weighed, magnetically separated, and the coal fraction was weighed. The coal samples were chemically analyzed for ash, sulfur, and

energy content. These results led to values of sulfur reduction (S.R.) and ash reduction (A.R.) for a given energy recovery (BTUR).

The continuous test results were compared to batch bed tests to judge the ability of the continuous cleaning system to perform similarly to the batch bed. To accomplish this, batch bed experiments were performed at the same conditions as those in the continuous test for the following processing times:

8, 14, 20, and 26 seconds (-50 +80 Upper Freeport coal)
8, 14, 20, 26, 40 and 60 seconds (-28 +50 Rushton coal)

(See Section 2.3.5 for description of batch bed cleaning experimental procedure.)

4.5.2 *Experimental data analysis procedure*

4.5.2.1 *Prediction of processing time*

For conditions of uniform bubbling, uniform bed depth and constant float velocity, the total processing time for the coal is:

$$t_{proc} = \frac{t_{float}}{x_{float}} x_{bed} \qquad \textbf{(4.1)}$$

However, due to air maldistribution over a the length, x_{dz}, one part of the bed had a relatively low superficial gas velocity. Assuming that negligible coal cleaning occurred within the defluidized zone, the actual processing time was found to be:

$$t_{proc} = \frac{t_{float}}{x_{float}} \left(x_{bed} - x_{dz} \right) \tag{4.2}$$

It was also noted that the average float velocity over the short measurement section differs from the average float velocity over the entire bed length. Magnetite flow studies performed at the same fluidizing conditions as those in the -50 +80 Upper Freeport coal cleaning trials showed the velocity ratio, c_f, to be approximately 1.09. The parameter c_f is defined as:

$$c_f = \frac{1}{n} \sum_{i=1}^{n} \frac{v_{B.L.}}{v_{T.S.}} \tag{4.3}$$

where $v_{B.L.}$ is the float velocity over the entire bed section, and $v_{T.S.}$ is the float velocity over the timing section (position 6 to 8).

It is very interesting that float tests with -28 +50 Emerald Raw coal showed values of c_f to be almost identical (see Tables 4.6 and 4.7, above). Data for these empirical studies are shown in Table 4.8. This yields:

$$t_{proc} = \frac{t_{float}}{c_f \, x_{float}} \left(x_{bed} - x_{dz} \right) \tag{4.4}$$

Table 4.8
Empirical data for c_f

Float Velocity -100 +200 magnetite only	
Over Entire Bed	Over Test Section
7.85 cm/s	7.22 cm/s
8.05 cm/s	7.52 cm/s
8.02 cm/s	7.18 cm/s

The final correction accounts for the vertical gradient in the solids flow velocity. The correction factor followed from the observation that the average bulk flow velocity of the -100 +200 magnetite (used in the -50 +80 Upper Freeport coal cleaning trials) was approximately half of the free surface velocity (float velocity). The average bulk flow velocity calculation is based on a known mass flux and a mass in a sample over a known length in what is termed a hold-up test.

Since the coal is, in general terms, on the top of the magnetite, the bulk flow velocity of the coal was estimated as the average of the float velocity and the bulk flow velocity of the entire bed. This assumes a linear velocity profile with respect to a direction normal to the bed surface (see Figure 4.68). Therefore:

$$\bar{v}_{coal} = \frac{1}{2}(v_{float} + \bar{v}_{bed}) \qquad (4.5)$$

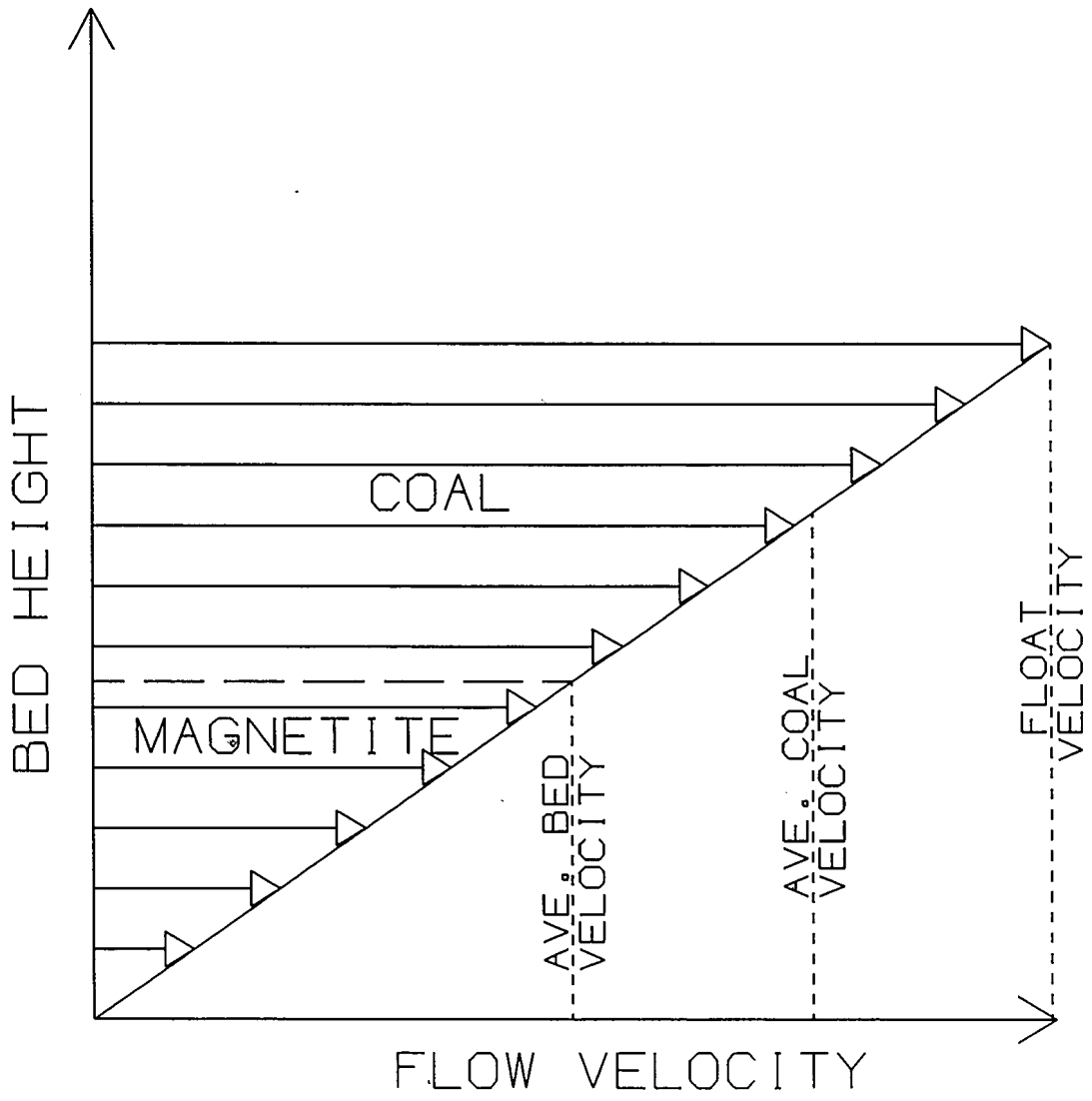

Figure 4.68
Schematic of linear velocity profile of coal and magnetite mixture

and, using the magnetite flow observation, $\bar{v}_{coal}$ is predicted as:

$$\bar{v}_{bed} = \frac{1}{2} v_{float} \tag{4.6}$$

so:

$$\bar{v}_{coal} = \frac{3}{4} v_{float} \tag{4.7}$$

Using the above result to make a correction from the average velocity calculation, the processing time finally becomes:

$$t_{proc} = \frac{4}{3} \frac{t_{float}}{c_f x_{float}} \left(x_{bed} - x_{dz} \right) \tag{4.8}$$

After determining various definitions of processing times, a range must be found to predict the true processing time. The best estimate of the processing time was assumed to be that which uses the correction for the boundary layer. The lower bound for the processing time is taken to be the residence time of the surface float, corrected for the defluidized zone. The upper bound was estimated assuming a binary slug flow of the coal and magnetite, and calculated using data from a hold-up test (see Figure 4.69).

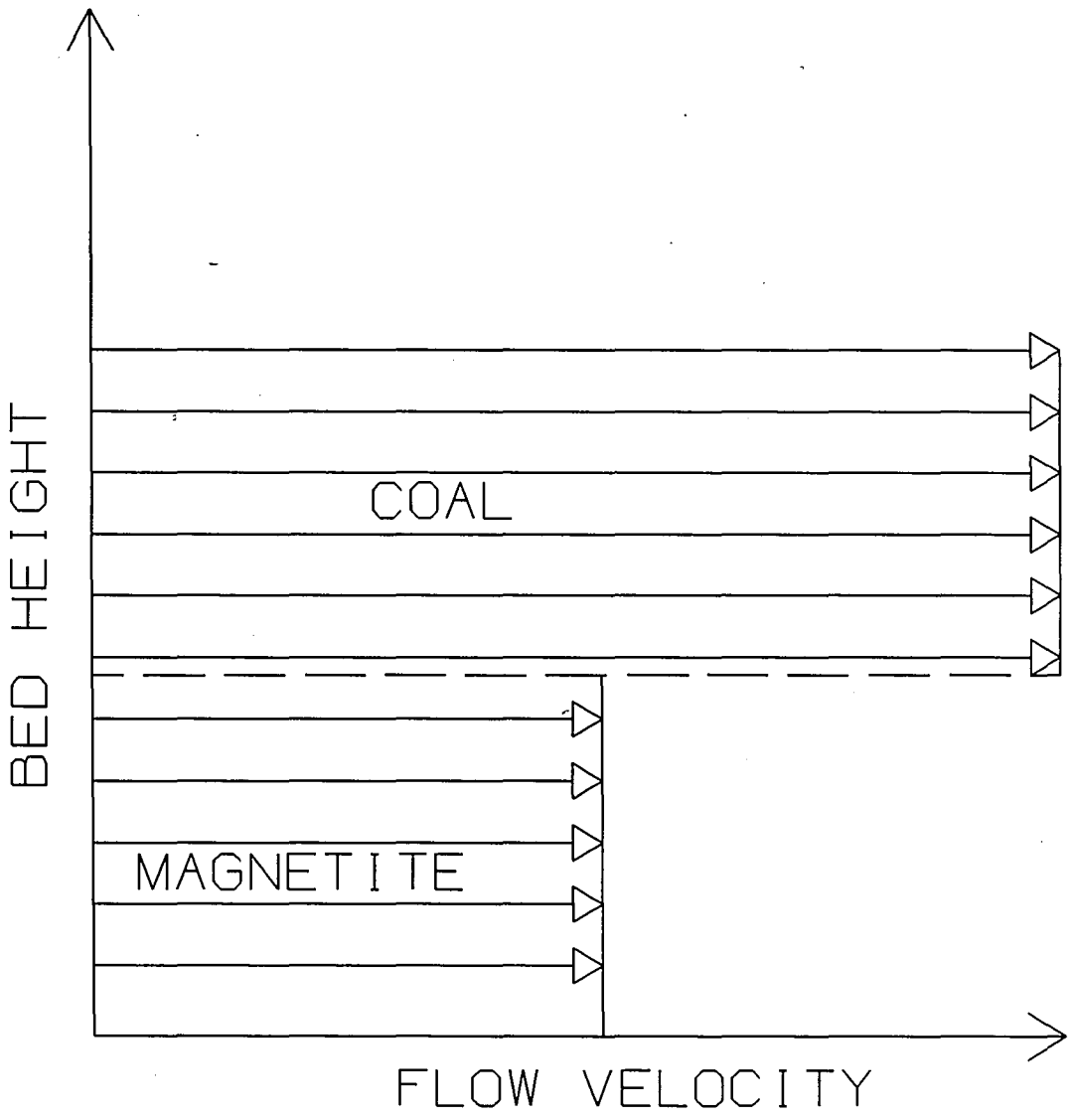

Figure 4.69
Binary slug flow profile schematic

The average coal velocity calculated from a hold-up test is:

$$\bar{v}_{coal,\ h.u.} = \frac{\dot{m}_{coal}}{m_{s,\ coal}} l_s \tag{4.9}$$

and,

$$t_{proc_{coal,\ h.u.}} = \frac{(x_{bed} - x_{dz})}{\bar{v}_{coal,\ h.u.}} \tag{4.10}$$

It should be noted that this processing time provides an upper bound, because the coal which moves slowly at the bottom of the bed is weighted disproportionately high. This distortion causes the calculated processing time to be unrealistically high, and renders this prediction unusable if some coal collects at the distributor and either does not move or moves very slowly. This collection could occur if the dense fractions segregated quickly, and then did not fluidize.

4.5.2.2 *Hold-up test analysis*

A hold-up test results in data, which can be used to approximate the mean velocity of a flow. The necessary data are the solids mass flow through a control volume, $\dot{m}$, the length of the sample control volume, l_s, and the total mass in the control volume, m_s. The sample is obtained by suddenly blocking the flow at two positions and isolating a section of the flowing bed material.

The analysis is based on the relationship of mass flow of a steady, incompressible flow to velocity, density, and cross-sectional flow area, where:

$$\dot{m} = \rho \bar{v} A \tag{4.11}$$

The density is the mass per volume, so:

$$\rho = \frac{m_s}{A\, l_s} \tag{4.12}$$

Combining the above equations,

$$\bar{v} = \frac{\dot{m}}{m_s} l_s \tag{4.13}$$

A slug flow profile of the average flow velocity gives an equivalent mass flow as the profile of the actual flow. If the binary mixture flow profile is modeled with a binary slug profile, above, in Figure 4.69, the average flow velocity of the coal can be estimated as:

$$\bar{v}_{coal,\ h.u.} = \frac{\dot{m}_{coal}}{m_{s,\ coal}} l_s \tag{4.14}$$

4.5.3 *Experimental results*

4.5.3.1 *-50 +80 Upper Freeport coal*

The -50 +80 Upper Freeport coal ($\bar{d}_p \approx 240\ \mu m$, $u_{mf} \approx 1.8$ cm/s, $u_{mb} \approx 2.4$ cm/s) had the composition given in Table 4.9. It had an overall sulfur concentration of 2.66 percent and an ash concentration of 23.14 percent. Figure 2.10 shows cleaning performance with ideal segregation. Results follow for the continuous trials and comparisons are given to actual and computer-simulated batch bed tests at matching conditions. The -50 +80 Upper Freeport coal was cleaned in a co-flowing mixture with -100 +200 magnetite ($\bar{d}_{vsm} \approx 109\ \mu m$, $u_{mfm} \approx 2.55$ cm/s, $u_{mb} \approx 3.4$ cm/s).

Table 4.9
-50 +80 Upper Freeport coal composition

Specific Gravity Range	Wt %	Wt % S	Wt % Ash	Energy Content [Btu/lb_m]
Float - 1.3	38.04	0.78	2.20	15340
1.3 - 1.4	23.29	1.25	8.53	14257
1.4 - 1.6	12.65	1.80	18.38	12525
1.6 - 1.8	3.99	3.18	30.50	10214
1.8 - 2.0	1.89	4.78	44.90	7655
2.0 - 2.45	2.59	7.11	60.19	5058
2.45 - 2.9	11.87	2.06	86.23	638
2.9 - Sink	5.67	21.11	72.81	2275

The bed behavior results are summarized in Table 4.10. It is seen that the values for bed height, $\dot{m}_c/\dot{m}_m$, and float time appear to have approached steady state

values. Also, the final magnetite and coal mass flow rates existing from the bed were very close to those desired from the hopper slide-gate setting.

Interestingly, the magnetite total mass flow was high at the first sampling and it decreased during the test. The cause of this higher initial magnetite flow was the increased head to the channel when the coal flow was suddenly begun. Prior to starting the coal flow, the magnetite flow was unsteady with a high bed height. The added coal head eliminated the need for a high bed height to generate steady flow, and the excess volume of magnetite surged out of the channel. Thus, the magnetite mass flow rate discharging from the bed eventually reached the steady state value of the magnetite mass influx.

The results of the chemical analysis of trials In-10-3-11 to 14 are given in Table 4.11a, and the associated S.R., A.R., and BTUR are given in Table 4.11b. The suffix "ref" represents a refuse sample and "cle" represents a product sample. The final or asymptotic energy recovery was 0.83. As clearly seen in Figure 4.70, the S.R. and A.R. tended toward an asymptotic value with respect to increasing time. At 0.83 BTUR, the S.R. tended to 0.440 and the A.R. tended to 0.423.

Table 4.10

-50 +80 Upper Freeport coal and -100 +200 magnetite inclined bed flow behavior

Trial	Time Since Start-Up	Fluidized Bed Heights (mm) Pos 4	Pos 7	Pos 9	Pos 10	Float Time	Test Time
11	36 s	69	60	45	35	3.99 s	12.00 s
12	66	66	58	42	33	3.61	11.94
13	96	66	57	41	30	3.54	11.94
14	126	66	57	39	29	3.42	12.06

Trial	Time Since Start-Up	Total Mass Efflux Rate $\dot{m}_c/\dot{m}_m$	$\dot{m}_c$	$\dot{m}_m$	Weight Recovery (WTR) Mag. & Coal	Coal Only
11	36 s	0.436	0.075 kg/s	0.173 kg/s	0.502	0.810
12	66	0.512	0.077	0.151	0.497	0.784
13	96	0.596	0.082	0.137	0.505	0.785
14	126	0.600	0.077	0.129	0.484	0.770

Desired Mass Influx

Coal: 0.081 kg/s
Magnetite: 0.125 kg/s
$\dot{m}_c/\dot{m}_m = 0.648$

Operating Conditions

$u_o = 5.10$ cm/s $= 2.0\ u_{mfm}$
$\alpha = -½°$ (½° uphill)
$a_g = 4.0$ mm

Hold-Up Test

$m_{s,\,coal} = 1.193$ kg
$m_{s,\,mag} = 9.121$ kg
$l_s = 137.5$ cm

Table 4.11a

Composition of coal in product and refuse samples in cleaning trials In-10-3-11 to 14

Sample	Time Since Start-Up	Coal mass	Wt % S	Wt % Ash	Energy Content [Btu/lb_m]
In-10-3-11-cle	36 s	732.51 g	1.78	18.67	12401
In-10-3-11-ref	36	172.53	3.56	34.60	9549
In-10-3-12-cle	66	724.37	1.67	16.90	12583
In-10-3-12-ref	66	199.98	3.81	36.15	9310
In-10-3-13-cle	96	764.12	1.70	17.07	12534
In-10-3-13-ref	96	209.48	3.68	36.27	9234
In-10-3-14-cle	126	716.47	1.66	16.37	12770
In-10-3-14-ref	126	214.97	4.23	36.79	8875

Table 4.11b

Sulfur reduction, ash reduction, and energy recovery of cleaning trials In-10-3-11 to 14

Trial	BTUR	S.R.	A.R.	Time After Start-Up
In-11	0.846	0.320	0.304	36
In-12	0.830	0.386	0.371	66
In-13	0.834	0.372	0.368	96
In-14	0.826	0.433	0.403	126

In addition to the inclined bed experiments described above, computer-simulations and actual batch bed experiments were performed at the same fluidizing conditions used for the continuous trials. The batch bed experiments had conditions of a packed bed height of 5.0 cm, u_o = 5.1 cm/s = 2.0 u_{mfm}. When the batch bed fluidized and expanded, its height corresponded to the average fluidized bed height of the Upper Freeport coal continuous cleaning trials. This value was used to perform batch bed tests and computer calculations to verify cleaning ability with the wider size range -100 +200

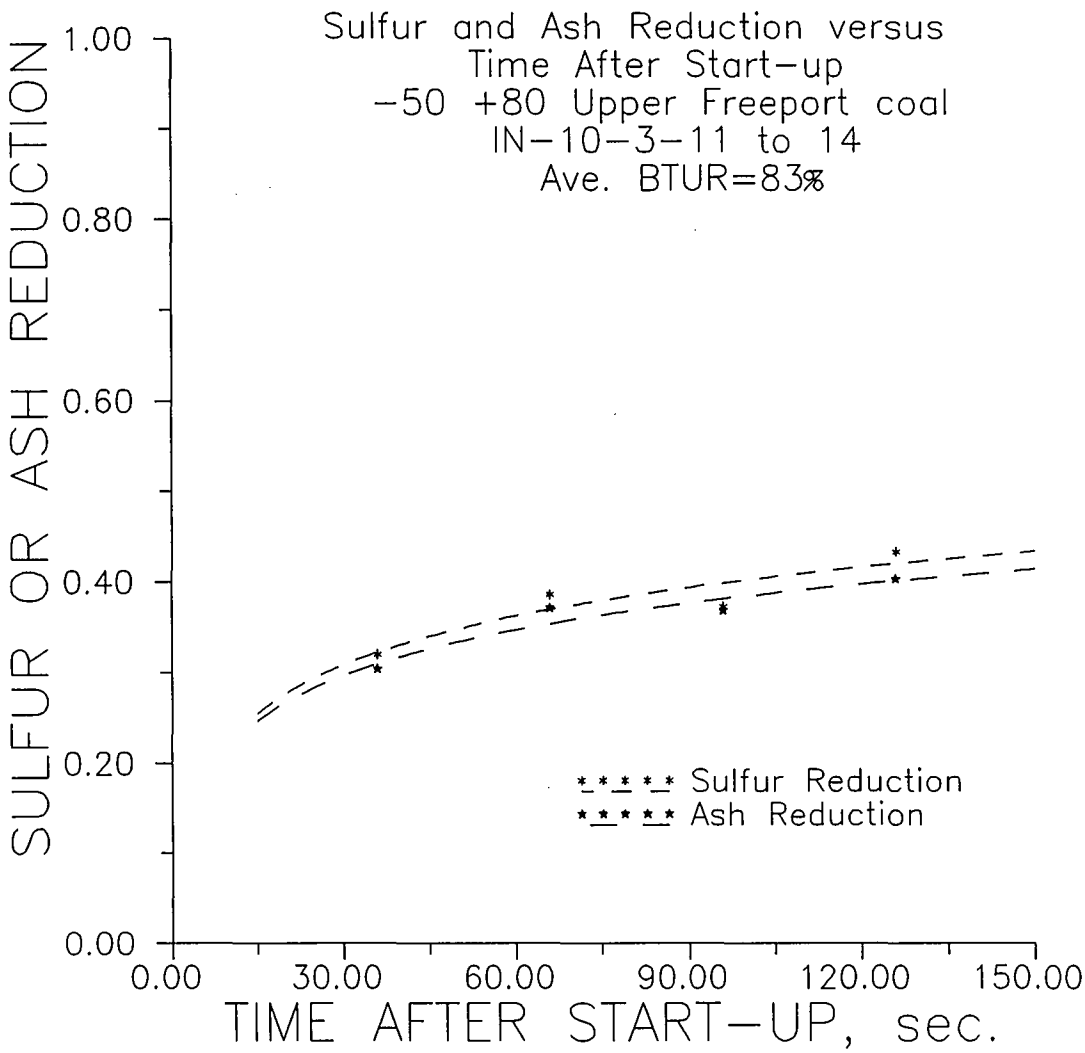

Figure 4.70
-50 +80 Upper Freeport coal continuous cleaning trials
S.R. and A.R. versus time after start-up

mesh magnetite. This predicted value closely matched the average bed height of the continuous cleaning trials. The actual experiments had processing times of 8, 14, 20, and 26 seconds, and the processing time in the computer simulations went to 30 seconds. The experiments had a mass ratio, m_c/m_m, of approximately 0.6, corresponding to a volumetric ratio mm = 6.44. Similarly, the computer simulation had mm = 6, since the volumetric ratio in the computer code must be an integer.

The results for S.R. and A.R. versus BTUR of the actual experiments are shown graphically in Figures 4.71 and 4.72. Experiment 9-10-91-77 differs from the others in that all six sample layers were individually chemically analyzed. Because of the small size of the samples, the bottom two layers in each of the other tests were analyzed together. This difference in analysis procedure caused an inconsistency in cleaning performance with respect to processing time. However, agreement was found when the bottom two layers of Experiment #77 were treated as one layer, when calculating the S.R. and A.R. versus BTUR.

Since the effective energy recovery in the continuous trials was 83%, the batch bed performance at 83% BTUR was evaluated versus processing time. (See Table 4.12 and Figures 4.73 and 4.74.) The simulated results are better than the actual, because the actual batch experiments used a wide size range magnetite (-100 +200 mesh), but the computer code only recognizes an average size.

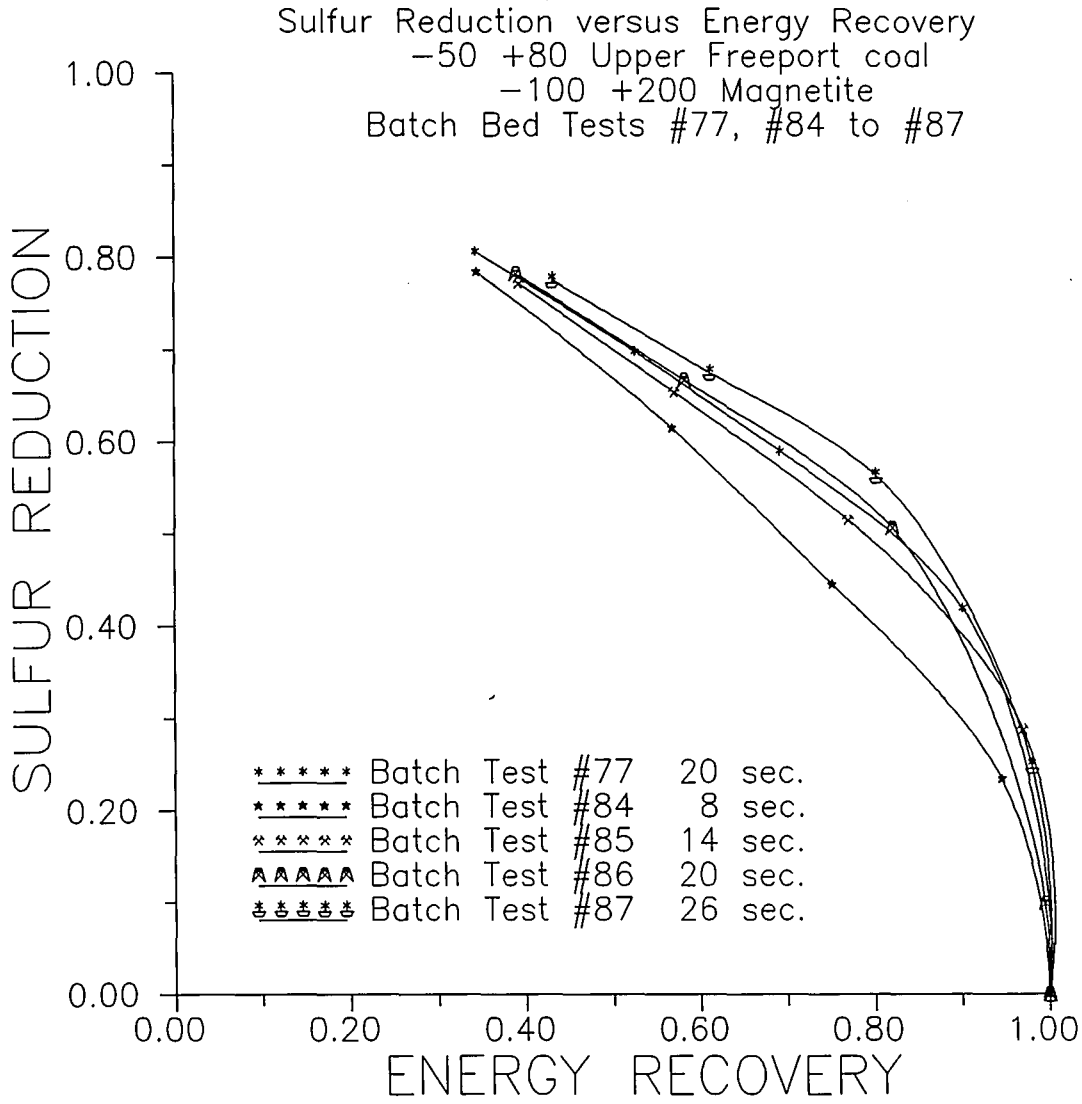

Figure 4.71
-50 +80 Upper Freeport coal
Batch bed experiments #77 and #84 to #87
Sulfur reduction versus energy recovery

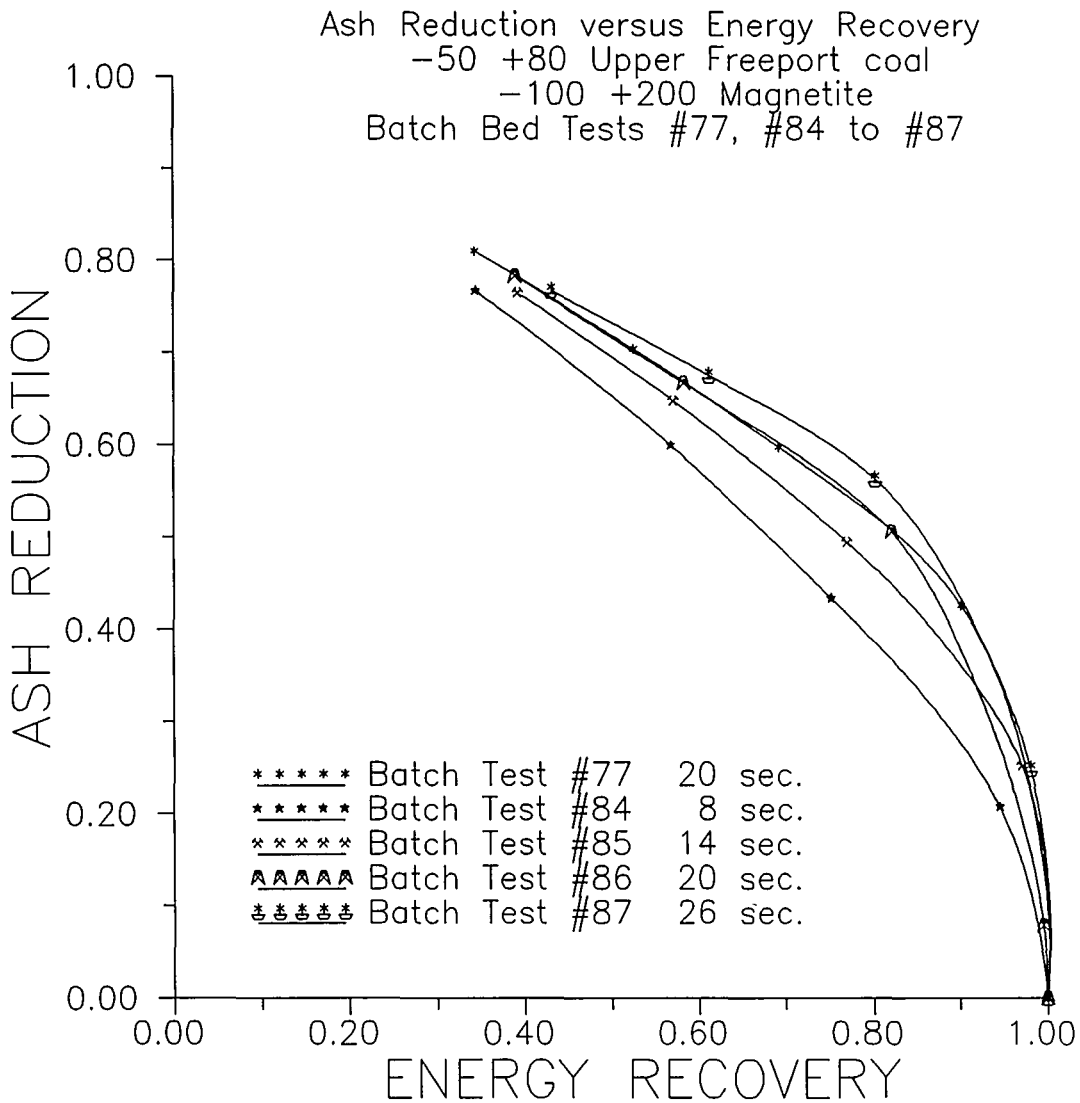

Figure 4.72
-50 +80 Upper Freeport coal
Batch bed experiments #77 and #84 to #87
Ash reduction versus energy recovery

Table 4.12

Sulfur and ash reduction at 83% energy recovery
for batch experiments #77, and #84 to #87, and for computer simulation results

Actual Experiments at 83% BTUR:

Experiment	Processing Time	S.R.	A.R.
84	8	0.370	0.353
85	14	0.463	0.438
86	20	0.497	0.500
77	20	0.495	0.499
87	26	0.537	0.530

Computer Simulation:

Processing Time	S.R.	A.R.
8	0.483	0.495
14	0.570	0.597
20	0.598	0.629
26	0.615	0.650
30	0.637	0.685

The final comparison follows from predictions of the processing time of the continuous cleaning system as outlined in Section 4.5.2.1. The range of processing times is as follows:

Lower bound: 9.85 sec
Best estimate: 13.1 sec
Upper bound: 18.4 sec

This range is based on the information in Table 4.13.

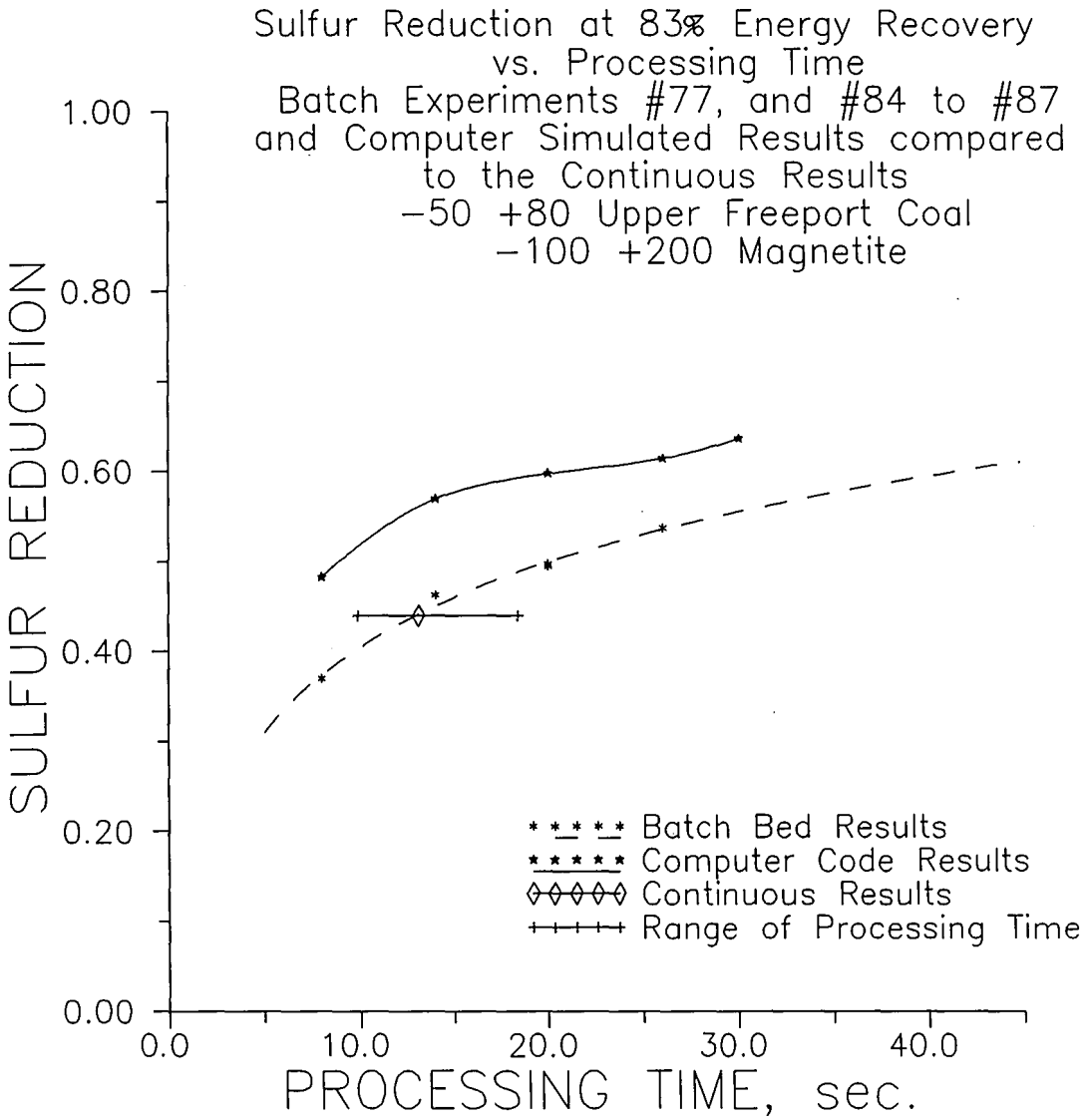

Figure 4.73
-50 +80 Upper Freeport coal
Sulfur reduction at 83% BTUR versus processing time
Comparison between continuous operation and batch operation

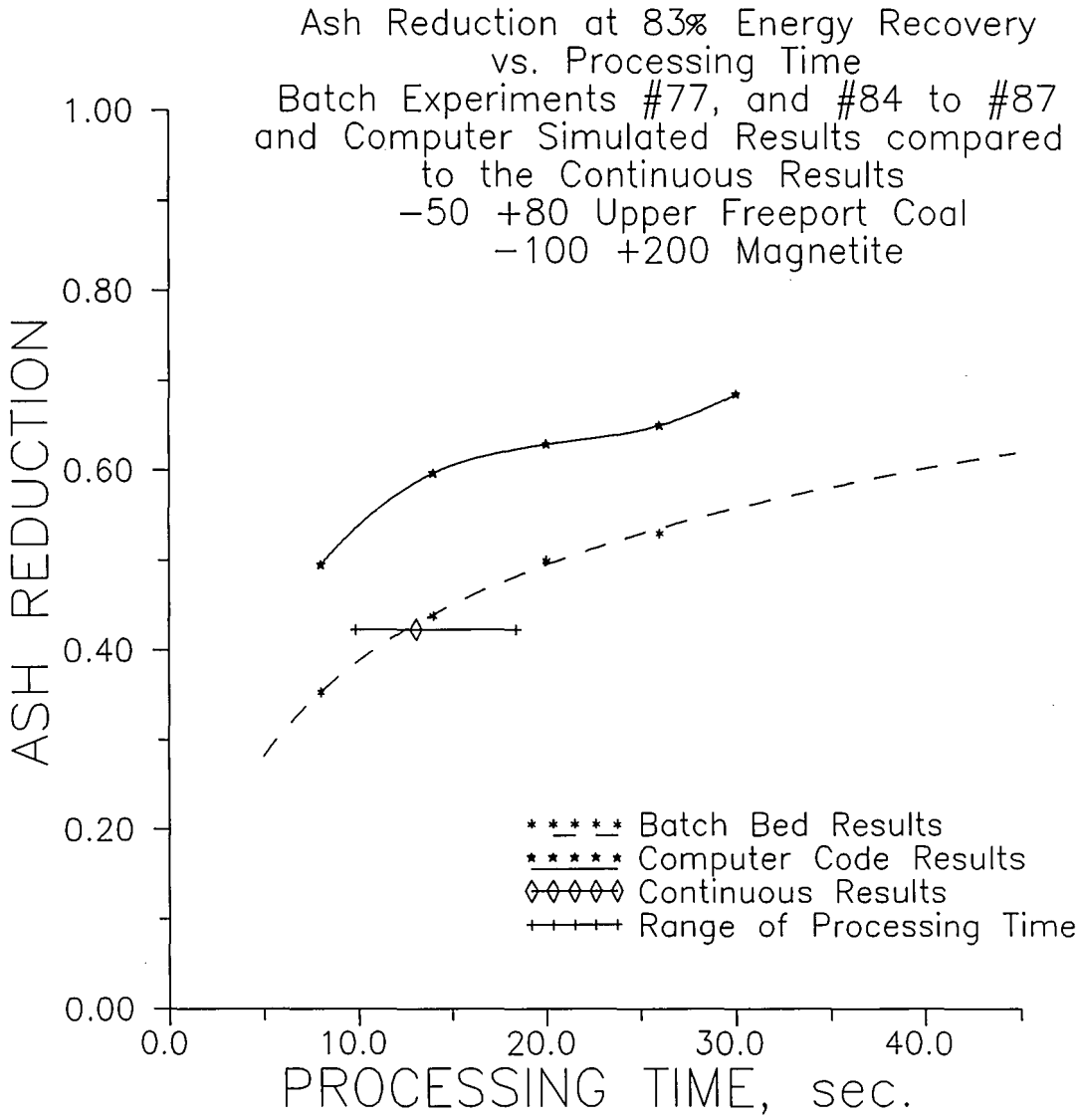

Figure 4.74
-50 +80 Upper Freeport coal
Ash reduction at 83% BTUR versus processing time
Comparison between continuous operation and batch operation

Table 4.13
Data for the computation of the range of processing time
for the -50 +80 Upper Freeport coal cleaning trials

Float data:

$t_{float} = 3.42$ sec
$x_{float} = 52$ cm
$x_{bed} = 188$ cm
$x_{dz} = 25$ cm

Hold-up test:

$\dot{m}_m = 0.129$ kg/s
$\dot{m}_c = 0.077$ kg/s
$m_{m,\,sample} = 9.121$ kg
$m_{c,\,sample} = 1.193$ kg
$l_{sample} = 137.5$ cm

A sample calculation of the predicted range of processing times follows from equations 4.4, 4.8, and 4.10 for the lower bound, best estimate, and upper bound prediction of the processing time, respectively.

Lower Bound:

$$t_{proc} = \frac{3.42 \text{ sec}}{(1.09)(52\ cm)}(188\ cm - 25\ cm) = 9.85 \text{ sec}$$

Best Estimate:

$$t_{proc} = \frac{4}{3}\frac{3.42 \text{ sec}}{(1.09)(52\ cm)}(188\ cm - 25\ cm) = 13.1 \text{ sec}$$

Upper Bound:

$$\bar{v}_{coal,\ h.u.} = \left(\frac{0.077\ \frac{kg}{s}}{1.193\ kg}\right)(137.5\ cm) = 8.873\ \frac{cm}{s}$$

$$t_{proc} = \frac{(188\ cm - 25cm)}{8.873\ \frac{cm}{s}} = 18.4 \text{ sec}$$

The S.R. and A.R. for the continuous test are also plotted on the curves of batch bed data versus processing time (Figures 4.73 and 4.74, above), and the data fit well into the range. The best estimate for the processing time matches within one second of the processing times where the performance is equal. (t_{proc} = 12.8 seconds for S.R. and 12.4 seconds for A.R.)

4.5.3.2 *-28 +50 Rushton Raw coal*

Continuous coal cleaning experiments using -28 +50 mesh Rushton coal ($\bar{d}_p \approx 450\ \mu m$, $u_{mf} \approx 6.6$ cm/s) and -80 +100 magnetite ($\bar{d}_p \approx 165\ \mu m$, $u_{mfm} \approx 3.5$ cm/s) were performed at two energy recoveries. The -28 +50 Rushton coal has a composition similar to that given in Table 4.14, obtained from an earlier batch of Rushton coal. Figure 2.11 showed the ideal segregation results based on the washability of the earlier Rushton coal. As in the previous section, results follow for the bed behavior, cleaning results, comparisons to batch bed tests, and, unlike before, the sulfur and ash concentrations.

The flow behavior results for the two cleaning experiments at different energy recoveries are listed in Tables 4.15 and 4.16. These data show that the bed heights further downstream tended to reach an asymptotic value; however, the bed heights upstream seemed to be continually increasing. In addition, the float times seemed to be continually decreasing, except for the last float time of the first energy recovery (In-11-21-18). Also, the magnetite mass flow approached an expected value, but the coal flow was consistently much lower than anticipated. Finally, the coal mass in the hold-up test

Table 4.14
-30 +50 Rushton coal composition

Specific Gravity Range	Wt %	Wt % S	Wt % Ash	Energy Content [Btu/lb_m]
Float - 1.3	26.33	1.14	3.14	15362
1.3 - 1.4	17.27	1.55	9.74	14122
1.4 - 1.6	9.76	2.01	24.40	11450
1.6 - 1.8	6.59	2.09	43.70	8153
1.8 - 2.0	5.52	2.30	56.48	5961
2.0 - 2.45	10.08	2.60	73.69	2926
2.45 - 2.9	18.78	3.19	86.87	722
2.9 - Sink	5.77	38.42	63.79	2760

was much higher than that of the magnetite, even though the mass effluxes are close in magnitude. With the coal flowing on top of the magnetite, it was expected that the average velocity of the coal would be higher than the average velocity of the magnetite. A higher coal velocity would give a coal-to-magnetite mass ratio in the hold-up test, which is lower than the ratio based on the mass efflux.

The tabulated data from the -28 +50 Rushton coal cleaning test are opposite from the expected result. The inconsistency in the hold-up data, the increase in bed height with time, and the mass imbalance seem to indicate that the bed was storing coal. If this actually occurred, it may have been due to the densest fractions settling onto the distributor, beginning at the coal solids inlet and moving down the bed with time. A storage of the dense fractions would also explain the results obtained for chemical composition.

The results of the chemical analysis of the Rushton coal cleaning experiments are given in Table 4.17a (In-11-19-15 to 18) and Table 4.18a (In-11-21-19 to 22). The

Table 4.15
-28 +50 Rushton coal cleaning experiments' flow behavior
First energy recovery, 73%

Trial	Time Since Start-Up	Fluidized Bed Heights (mm) Pos 4	Pos 7	Pos 9	Pos 10	Float Time	Test Time
15	36 s	56	50	40	32	4.13 s	12.00 s
16	66 s	55	48	38	30	3.77 s	12.00 s
17	96 s	62	45	36	28	3.02 s	12.00 s
18	126 s	70	46	35	28	3.81 s	12.00 s

Trial	Time Since Start-Up	Total Mass Efflux Rate $\dot{m}_c/\dot{m}_m$	$\dot{m}_c$	$\dot{m}_m$	Weight Recovery (WTR) Mag. & Coal	Coal Only
15	36 s	0.774	0.103 kg/s	0.133 kg/s	0.692	0.765
16	66 s	0.895	0.102 kg/s	0.114 kg/s	0.634	0.690
17	96 s	0.967	0.088 kg/s	0.091 kg/s	0.616	0.671
18	126 s	0.905	0.076 kg/s	0.084 kg/s	0.562	0.620

Desired Mass Influx

Coal: 0.133 kg/s
Magnetite: 0.088 kg/s
$\dot{m}_c/\dot{m}_m = 1.51$

Operating Conditions

$u_o = 9.63$ cm/s $= 2.75\ u_{mfm}$
$\alpha = -¾°$ (¾° uphill)
$a_g = 3.0$ mm

Hold-Up Test:

$m_{s,\,coal} = 6.069$ kg
$m_{s,\,mag} = 2.923$ kg
$l_s = 150.5$ cm

Table 4.16
-28 +50 Rushton coal cleaning experiments' flow behavior
Second energy recovery, 89%

Trial	Time Since Start-Up	Fluidized Bed Heights (mm) Pos 4	Pos 7	Pos 9	Pos 10	Float Time	Test Time
19	36 s	53	48	39	30	5.23 s	11.97 s
20	66 s	54	48	38	29	4.24 s	12.03 s
21	96 s	62	49	38	30	3.50 s	11.94 s
22	126 s	71	50	38	29	2.50 s	12.06 s

Trial	Time Since Start-Up	Total Mass Efflux Rate $\dot{m}_c/\dot{m}_m$	$\dot{m}_c$	$\dot{m}_m$	Weight Recovery (WTR) Mag. & Coal	Coal Only
19	36 s	0.593	0.096 kg/s	0.162 kg/s	0.825	0.879
20	66 s	0.990	0.097 kg/s	0.098 kg/s	0.779	0.833
21	96 s	1.000	0.091 kg/s	0.091 kg/s	0.760	0.812
22	126 s	0.989	0.088 kg/s	0.089 kg/s	0.758	0.811

Desired Mass Influx	Operating Conditions	Hold-Up Test:
Coal: 0.133 kg/s	u_o = 9.63 cm/s = 2.75 u_{mfm}	$m_{s,\,coal}$ = 5.711 kg
Magnetite: 0.088 kg/s	α = -¾° (¾° uphill)	$m_{s,\,mag}$ = 3.031 kg
$\dot{m}_c/\dot{m}_m$ = 1.51	a_g = 2.0 mm	l_s = 149.9 cm

associated S.R., A.R., and BTUR are given in Tables 4.17b and 4.18b. Again, the energy recoveries, S.R.'s and A.R.'s do tend towards asymptotic values, but they seem to approach these values more slowly than the -50 +80 Upper Freeport coal had shown. (See Figures 4.75, 4.76, and 4.77.) The energy recoveries were 73% and 89% for the first and second Rushton coal cleaning experiments, respectively. The apparent cleaning results were as follows:

BTUR:	0.730	0.890
S.R.:	0.498	0.317
A.R.:	0.601	0.446

Table 4.17a

Composition of coal in product and refuse samples in cleaning trials In-19-15 to 18

Sample	Time Since Start-Up	Coal mass	Wt % S	Wt % Ash	Energy Content [Btu/lb_m]
In-11-19-15-cle	36 s	942.42 g	2.00	23.70	11620
In-11-19-15-ref	36	289.11	2.76	41.76	18331
In-11-19-16-cle	66	841.27	1.89	22.13	11762
In-11-19-16-ref	66	378.13	2.94	48.21	7450
In-11-19-17-cle	96	708.90	1.87	22.88	11766
In-11-19-17-ref	96	347.66	2.86	47.67	7395
In-11-19-18-cle	126	566.31	1.78	20.37	12214
In-11-19-18-ref	126	346.98	2.51	43.19	8361

Table 4.17b

Sulfur reduction, ash reduction, and energy recovery of cleaning trials In-11-19-15 to 18

Trial	BTUR	S.R.	A.R.	Time Since Start-Up
In-15	0.8197	0.2974	0.3509	36
In-16	0.7784	0.4115	0.4947	66
In-17	0.7644	0.4286	0.5054	96
In-18	0.7045	0.4635	0.5650	126

Table 4.18a

Composition of coal in product and refuse samples in cleaning trials In-21-19 to 22

Sample	Time Since Start-Up	Coal mass	Wt % S	Wt % Ash	Energy Content [Btu/lb_m]
In-11-21-19-cle	36 s	1004.67 g	2.09	25.19	11458
In-11-21-19-ref	36	139.11	2.98	45.26	7881
In-11-21-20-cle	66	971.43	1.93	21.45	12009
In-11-21-20-ref	66	195.80	3.06	47.03	7285
In-11-21-21-cle	96	885.56	1.92	19.69	12256
In-11-21-21-ref	96	205.60	3.33	52.04	6391
In-11-21-22-cle	126	862.44	1.93	20.33	12154
In-11-21-22-ref	126	201.89	3.28	54.06	6284

Table 4.18b

Sulfur reduction, ash reduction, and energy recovery of cleaning trials In-11-21-19 to 22

Trial	BTUR	S.R.	A.R.	Time Since Start-Up
In-19	0.9130	0.1649	0.1992	36
In-20	0.8911	0.2422	0.3065	66
In-21	0.8920	0.2871	0.3803	96
In-22	0.8920	0.2846	0.3837	126

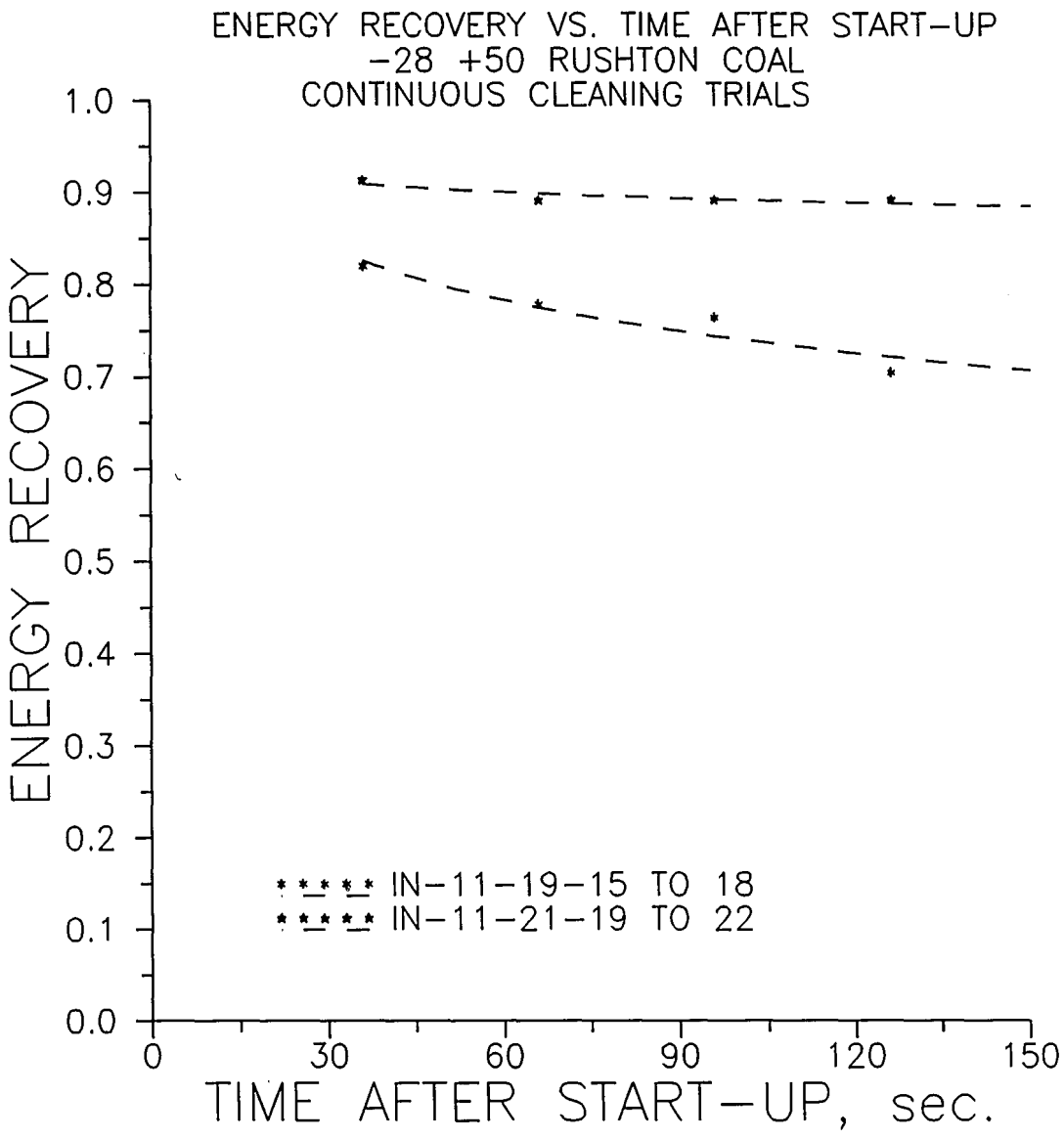

Figure 4.75
-28 +50 Rushton coal continuous cleaning trials
Energy recovery versus time after start-up

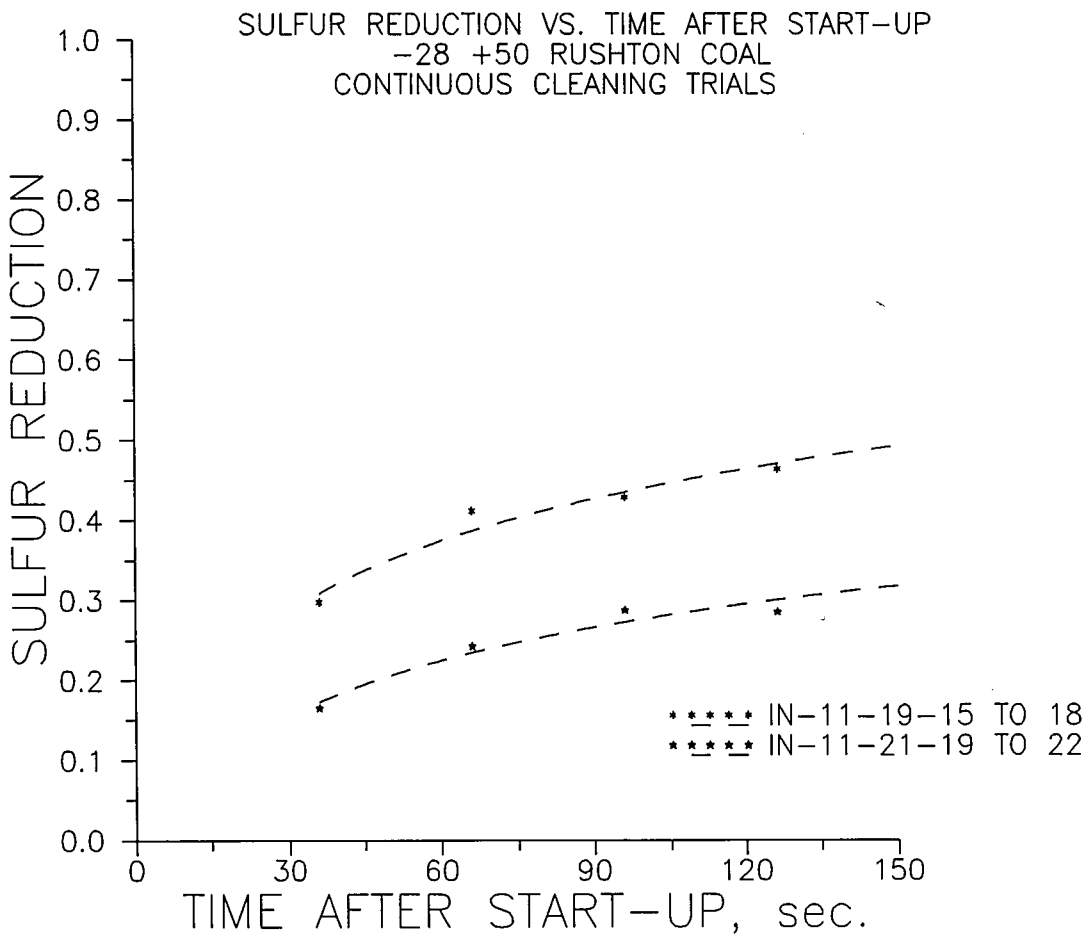

Figure 4.76
-28 +50 Rushton coal continuous cleaning trials
Sulfur reduction versus time after start-up

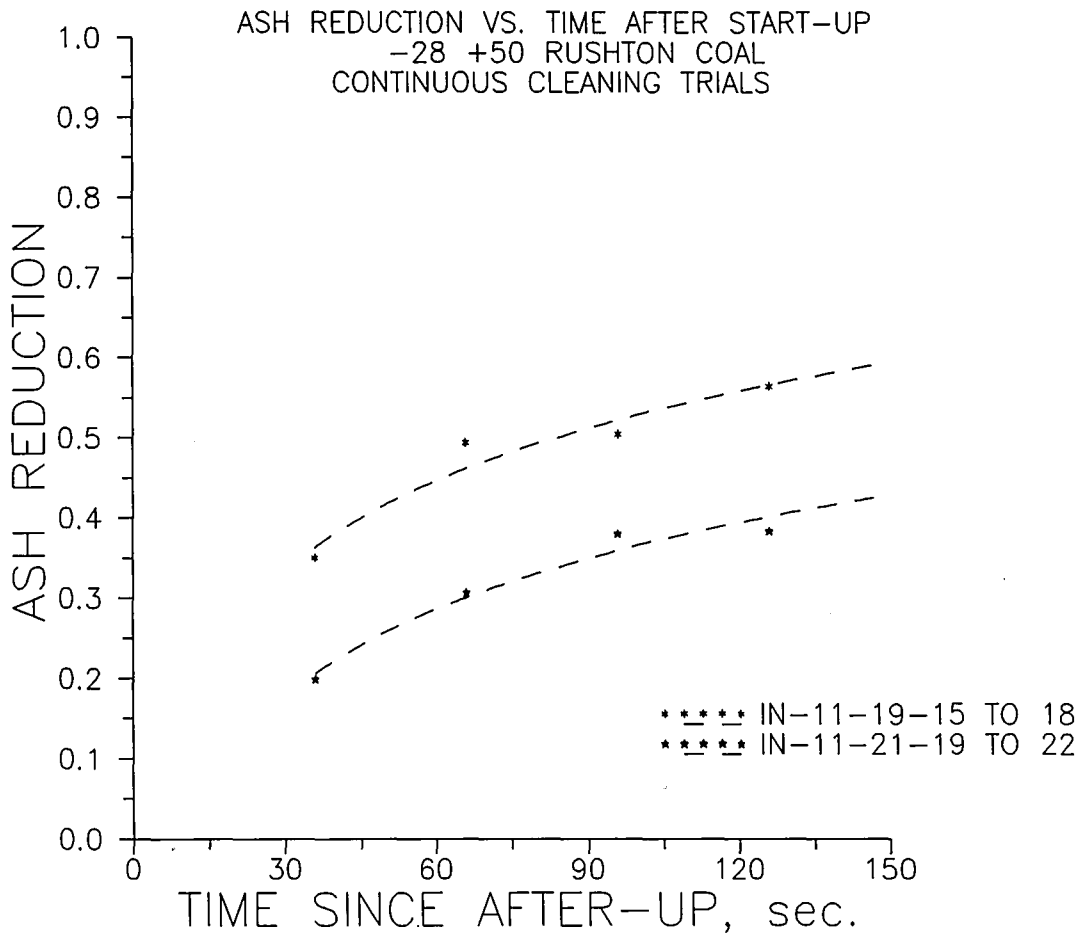

Figure 4.77
-28 +50 Rushton coal continuous cleaning trials
Ash reduction versus time after start-up

Again, to correlate the continuous results to batch bed data and to the computer-simulations, batch bed experiments and analyses were performed according to the following:

-28 +50 Rushton coal
-80 +100 magnetite
u_o = 9.63 cm/s = 2.75 u_{mfm}
h_o = 4.3 cm
mm = 4.9 (5 for computer simulations)
Processing times: 8, 14, 20, 26, 40, and 60 seconds

The listed processing times were for the actual experiments; the computer-simulation was executed up to a cleaning time of 60 seconds.

The resulting S.R. and A.R. versus BTUR for the actual batch bed experiments are shown graphically in Figure 4.78 through 4.83.

The batch bed performance is plotted versus processing time for the energy recovery values of the continuous cleaning trials (73% and 89%) in Figures 4.84 to 4.87 and tabulated in Table 4.19. The cleaning performance in the batch bed showed extremely strong segregation of the fractions high in sulfur and ash and it reached a maximum level of cleaning performance in a very short processing time. At 73% BTUR, the maximum S.R. is approximately 74%, and the maximum A.R. is 80%. At 89% BTUR, the maximum S.R. is 65%, and the A.R. is 70%. The difference in performance between the batch bed experiments and the computer calculations is probably due to the small differences in coal composition between that in the actual coal and that used as input to the computer code.

To correlate the batch bed results to the continuous results, the processing time must be determined. The lower bound and the best estimate are processing times

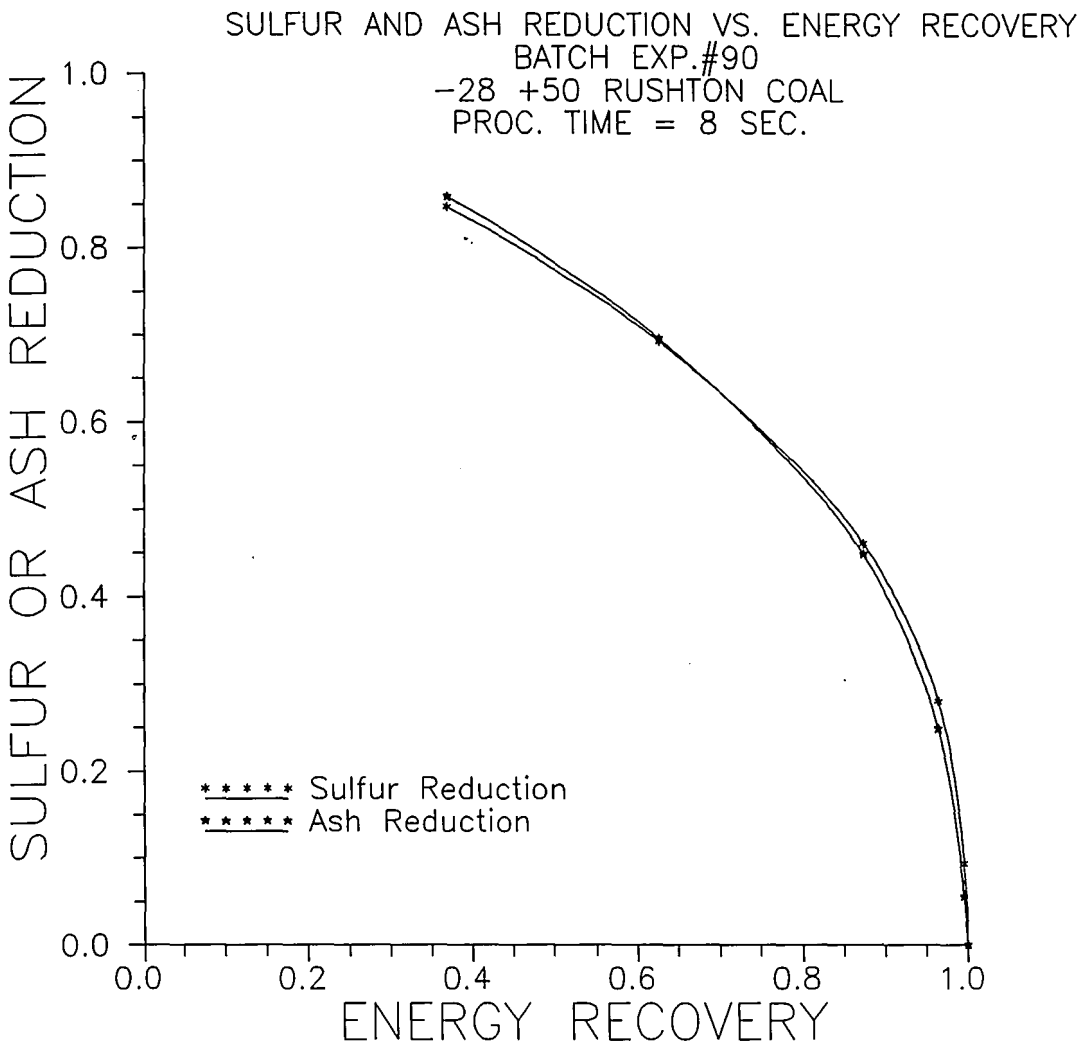

Figure 4.78
-28 +50 Rushton coal batch bed cleaning test #90
S.R. and A.R. versus BTUR
t_{proc} = 8 seconds

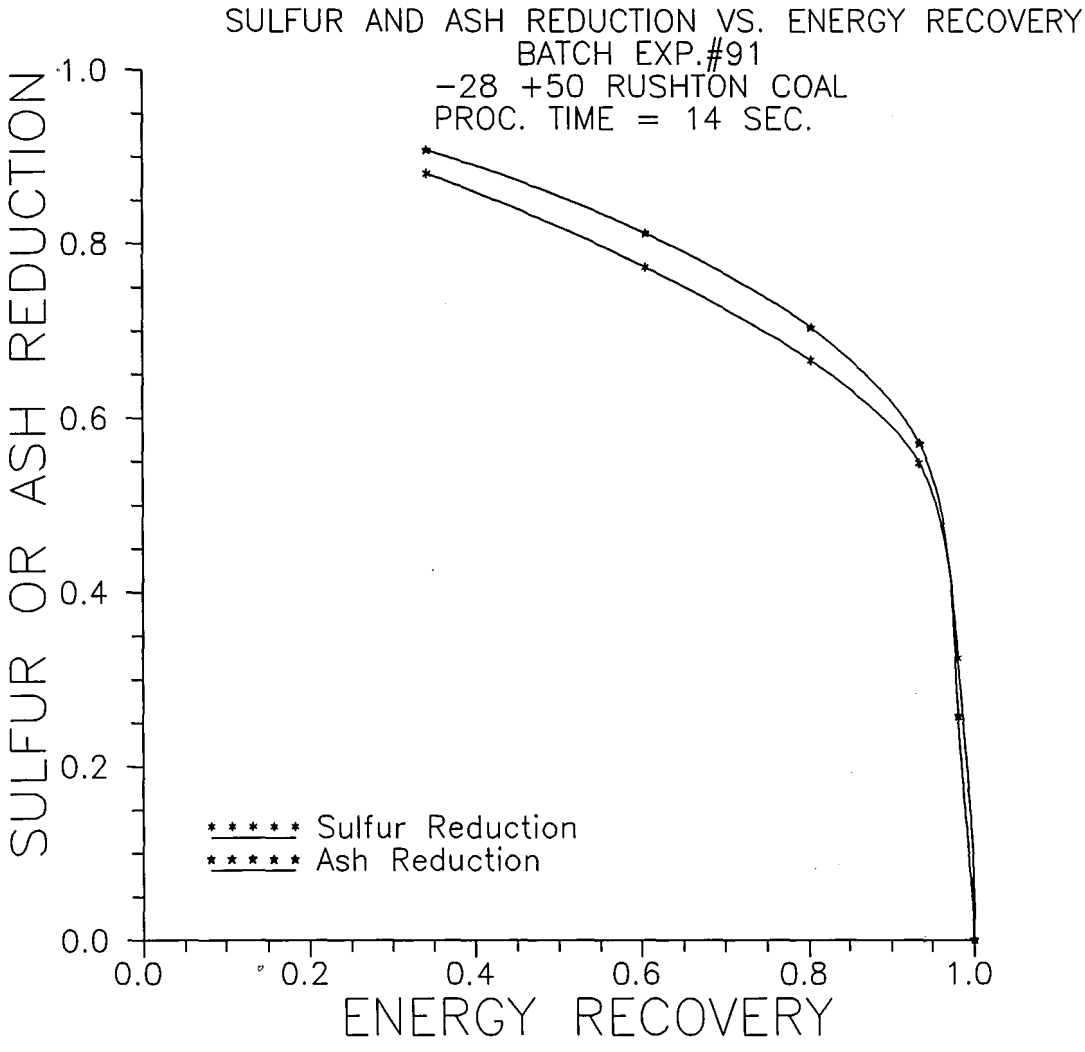

Figure 4.79
-28 +50 Rushton coal batch bed cleaning test #91
S.R. and A.R. versus BTUR
t_{proc} = 14 seconds

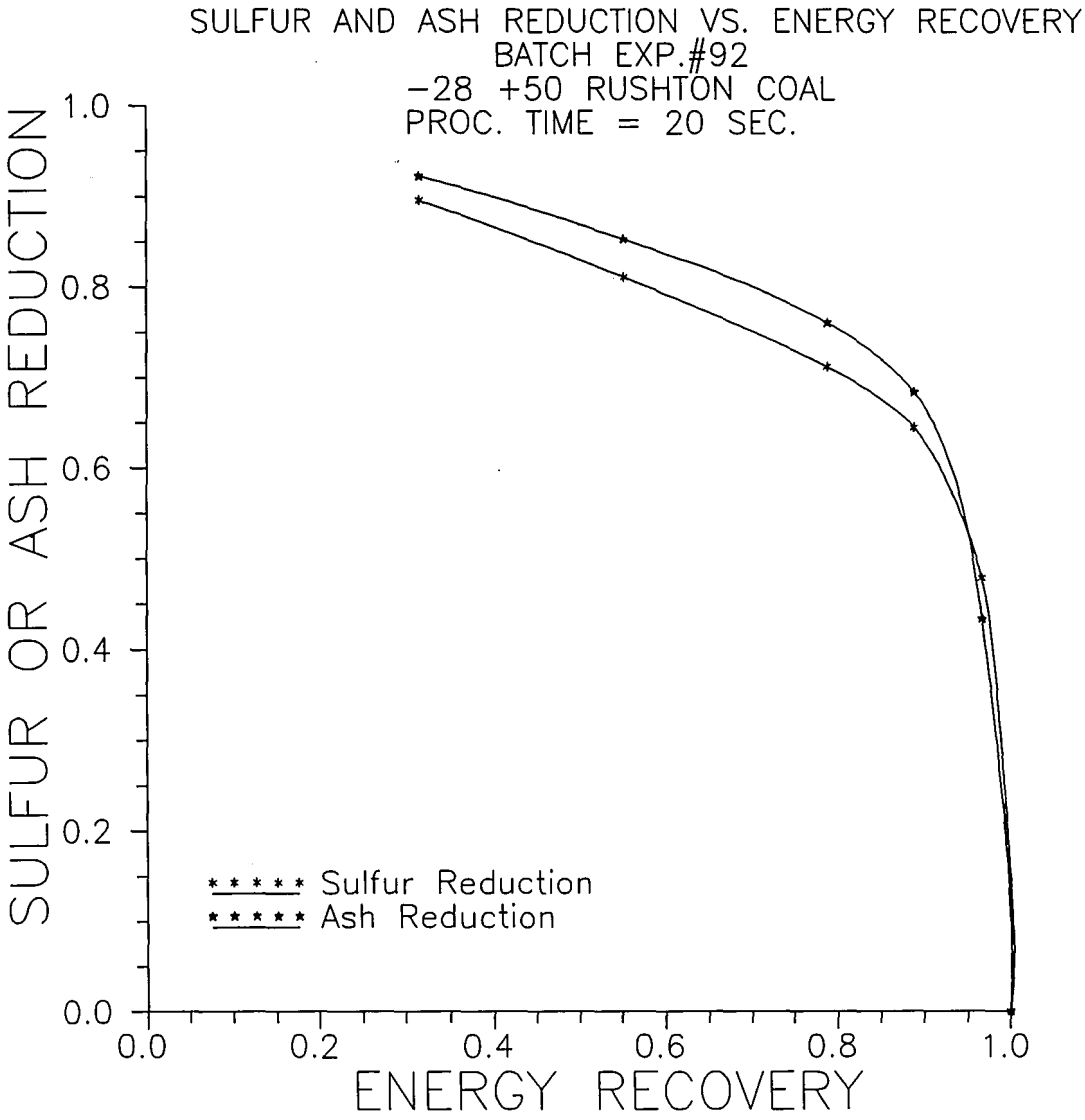

Figure 4.80
-28 +50 Rushton coal batch bed cleaning test #92
S.R. and A.R. versus BTUR
t_{proc} = 20 seconds

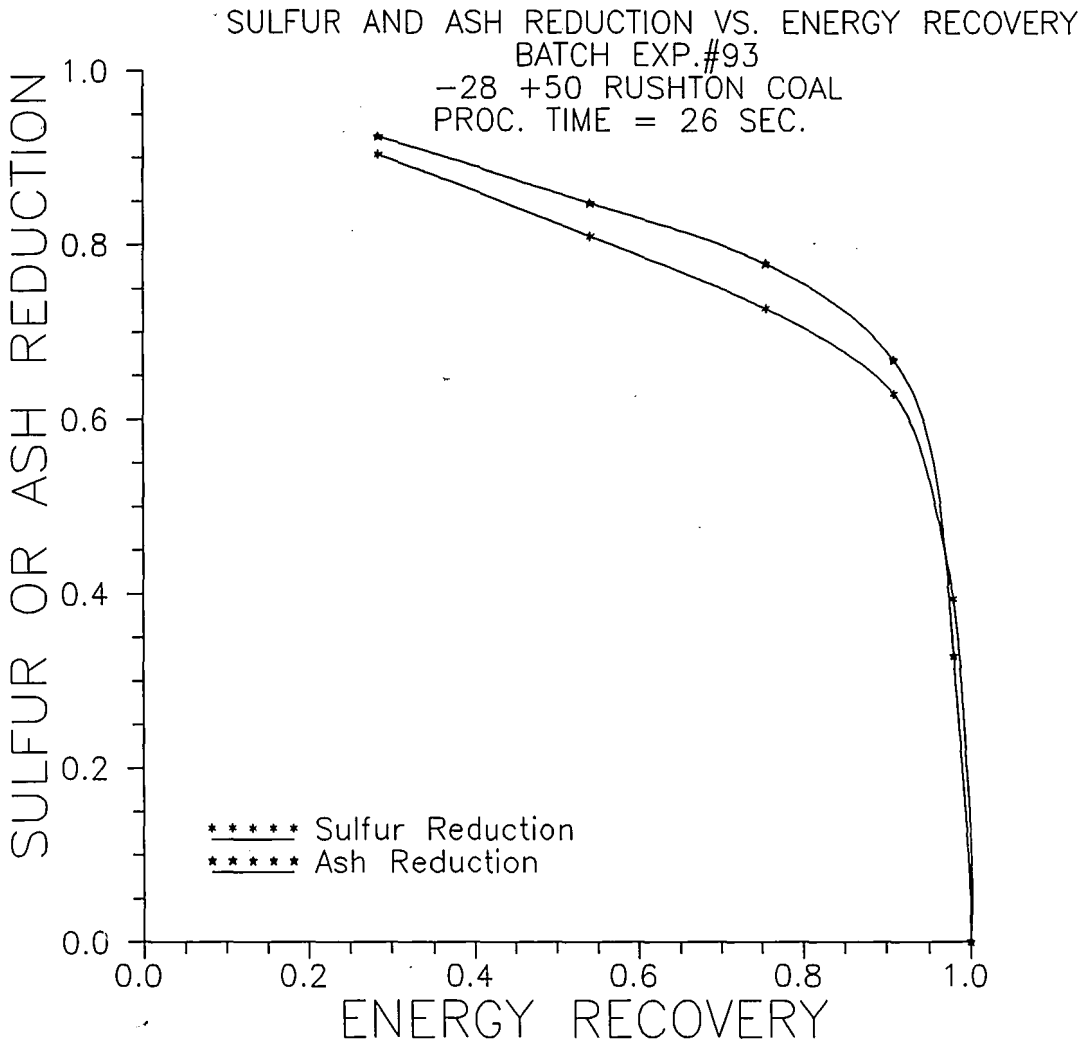

Figure 4.81
-28 +50 Rushton coal batch bed cleaning test #93
S.R. and A.R. versus BTUR
t_{proc} = 26 seconds

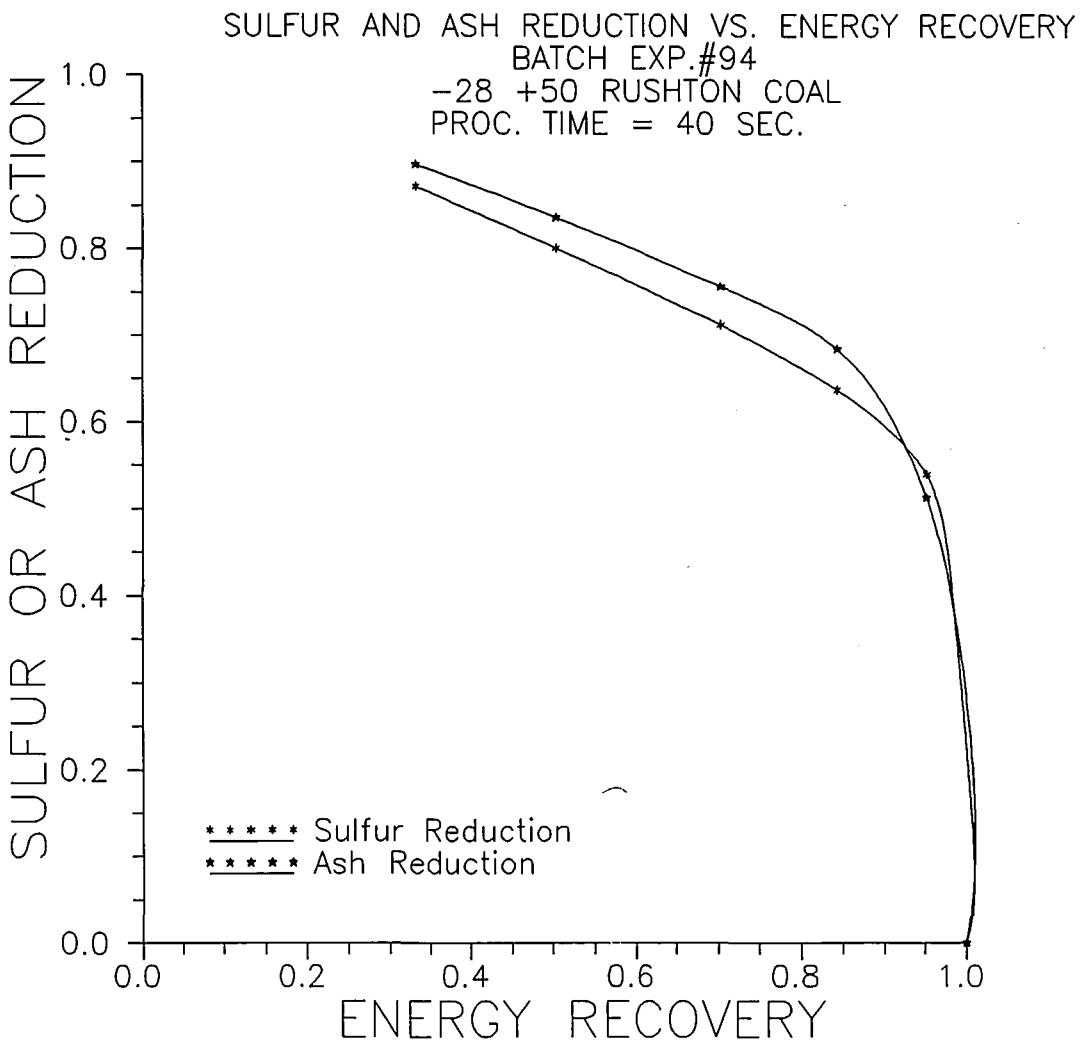

Figure 4.82
-28 +50 Rushton coal batch bed cleaning test #94
S.R. and A.R. versus BTUR
t_{proc} = 40 seconds

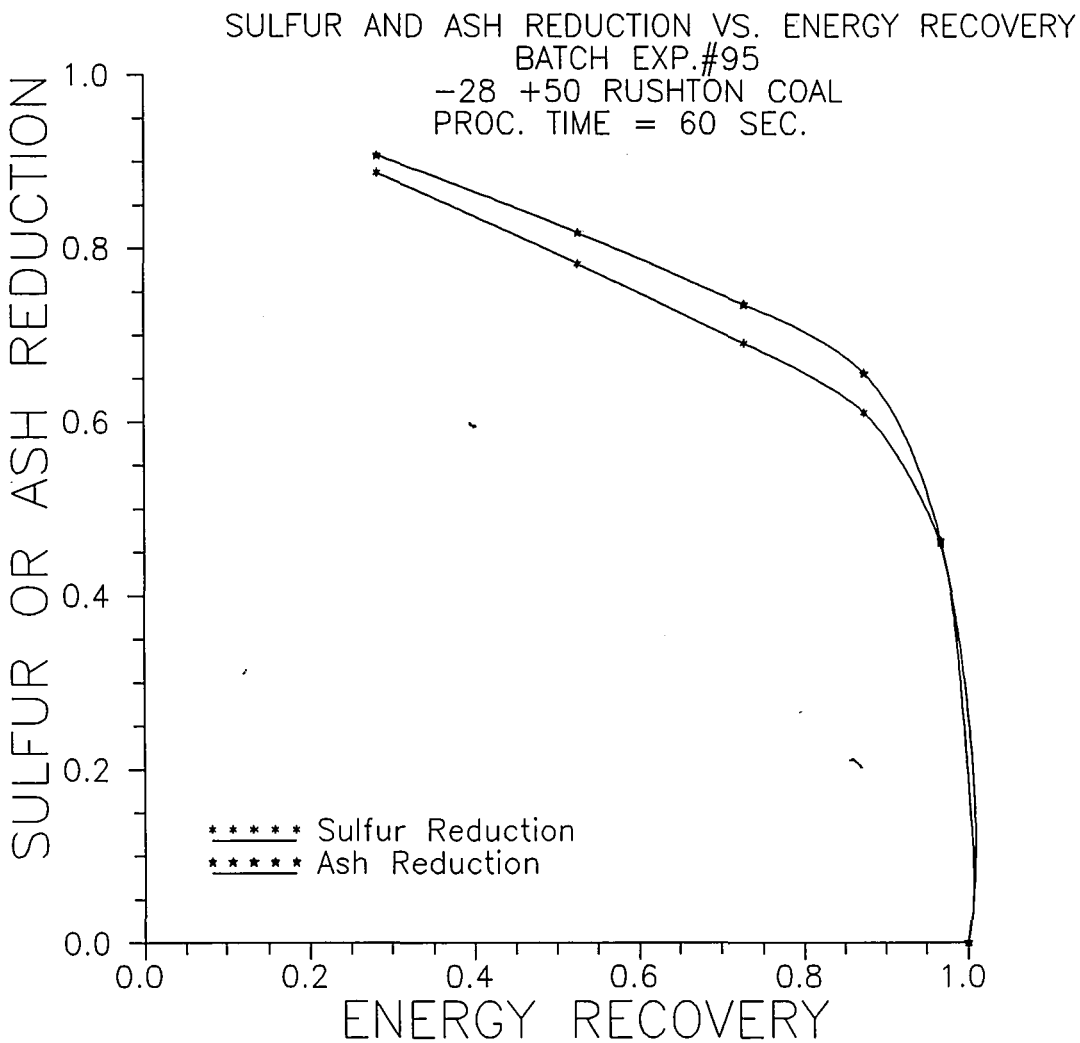

Figure 4.83
-28 +50 Rushton coal batch bed cleaning test #95
S.R. and A.R. versus BTUR
t_{proc} = 60 seconds

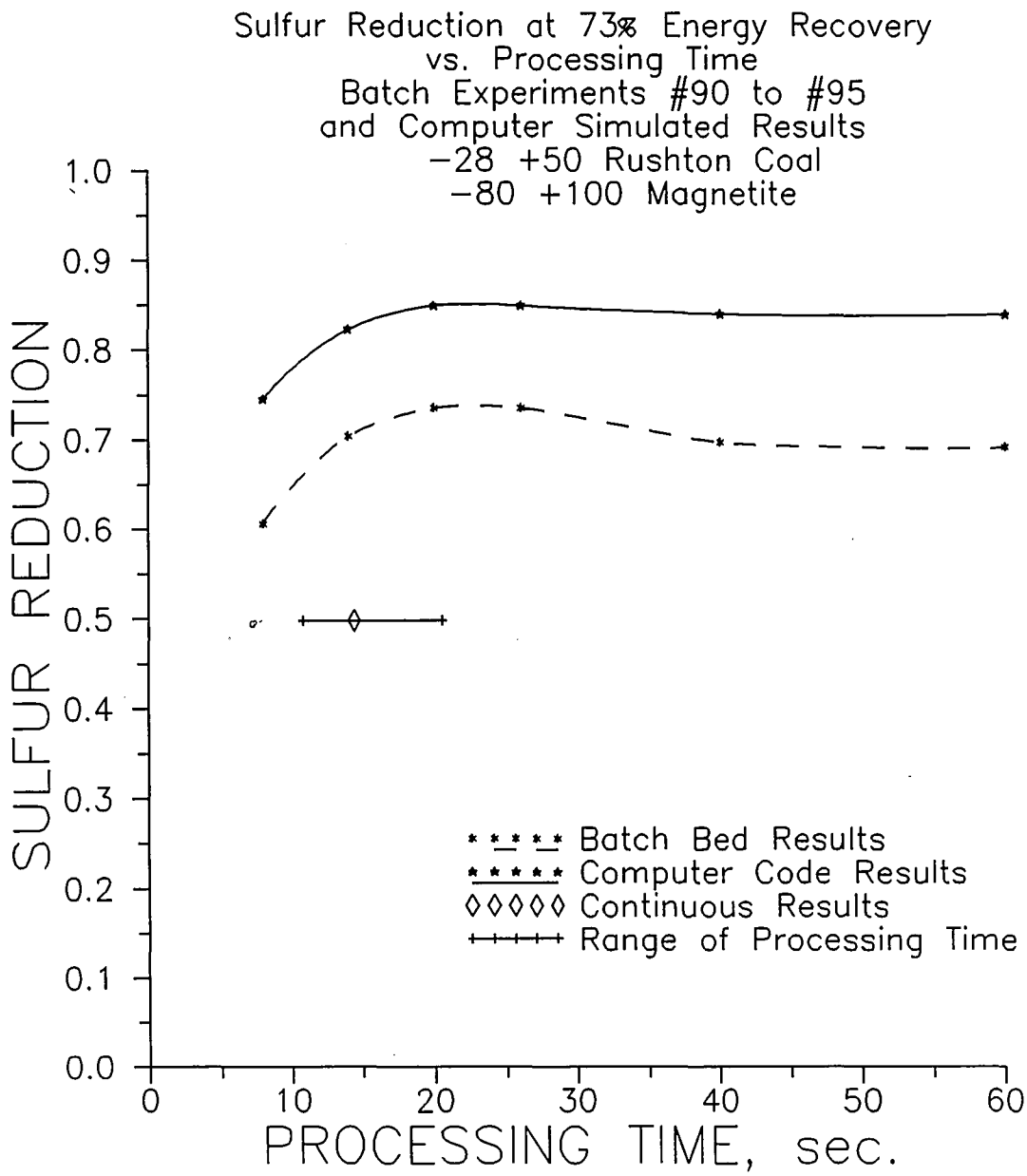

Figure 4.84
-28 +50 Rushton coal cleaning trials
S.R. at 73% BTUR versus processing time
Comparison between continuous and batch operation

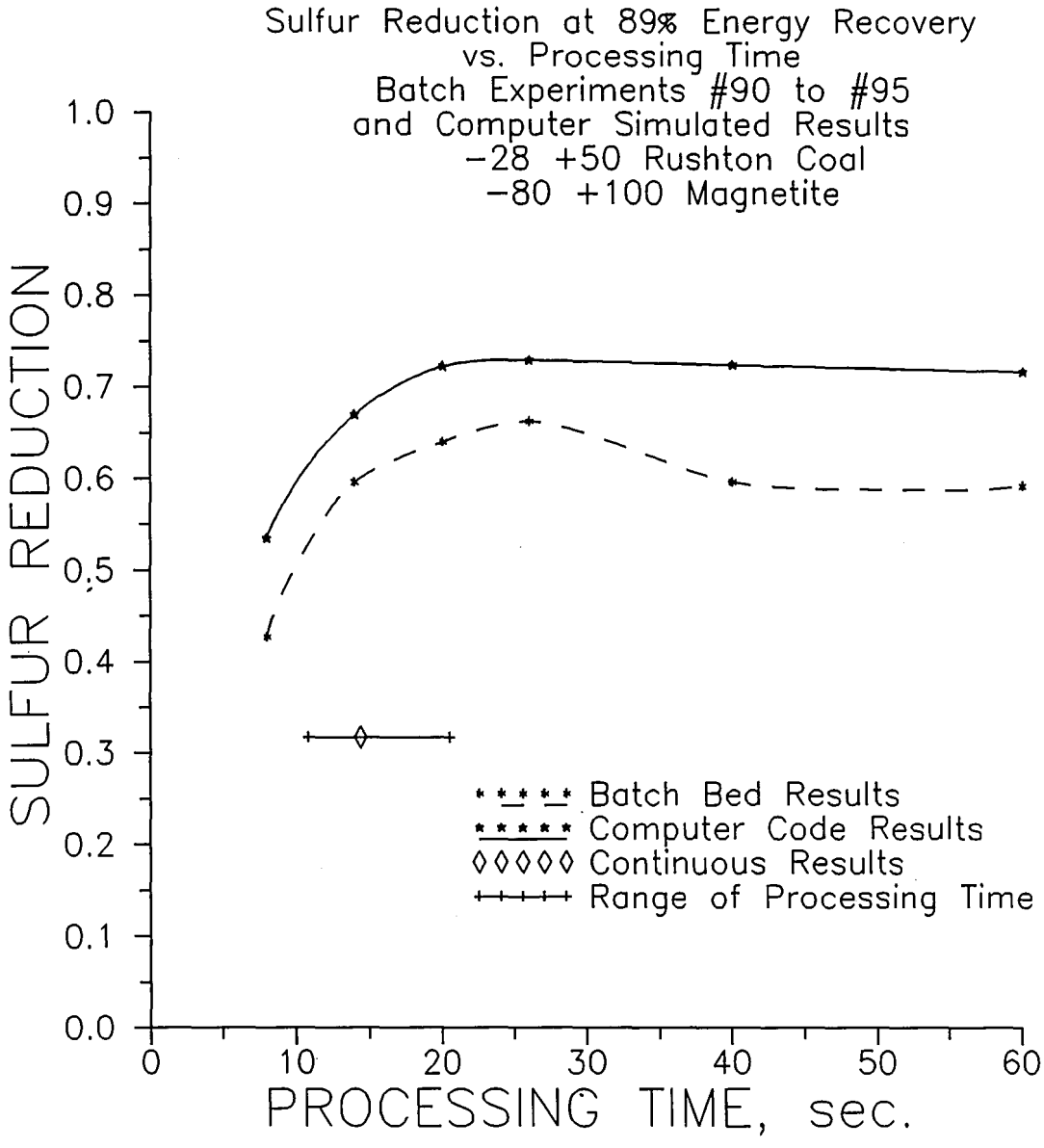

Figure 4.85
-28 +50 Rushton coal cleaning trials
S.R. at 89% BTUR versus processing time
Comparison between continuous and batch operation

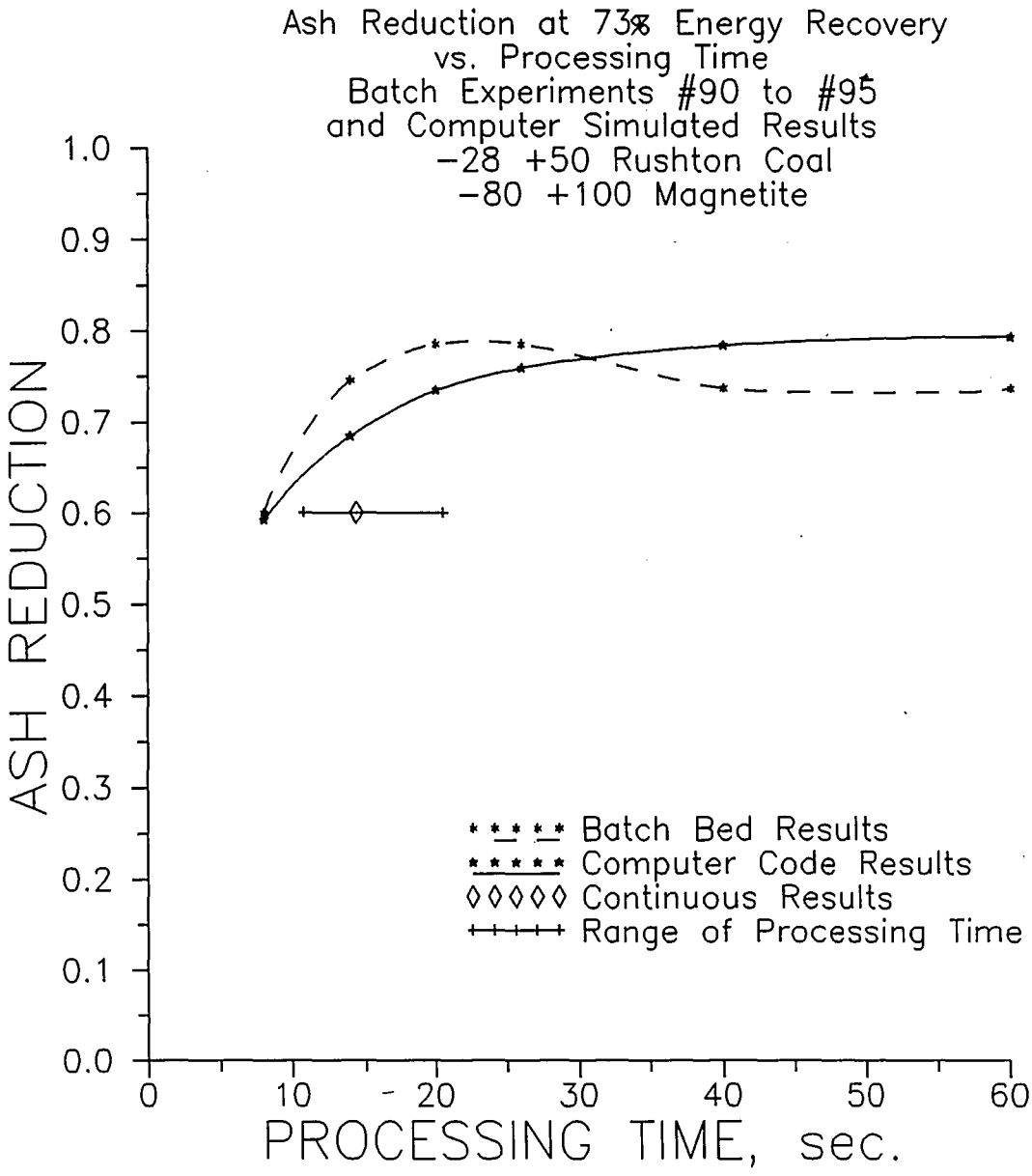

Figure 4.86
-28 +50 Rushton coal cleaning trials
A.R. at 73% BTUR versus processing time
Comparison between continuous and batch operation

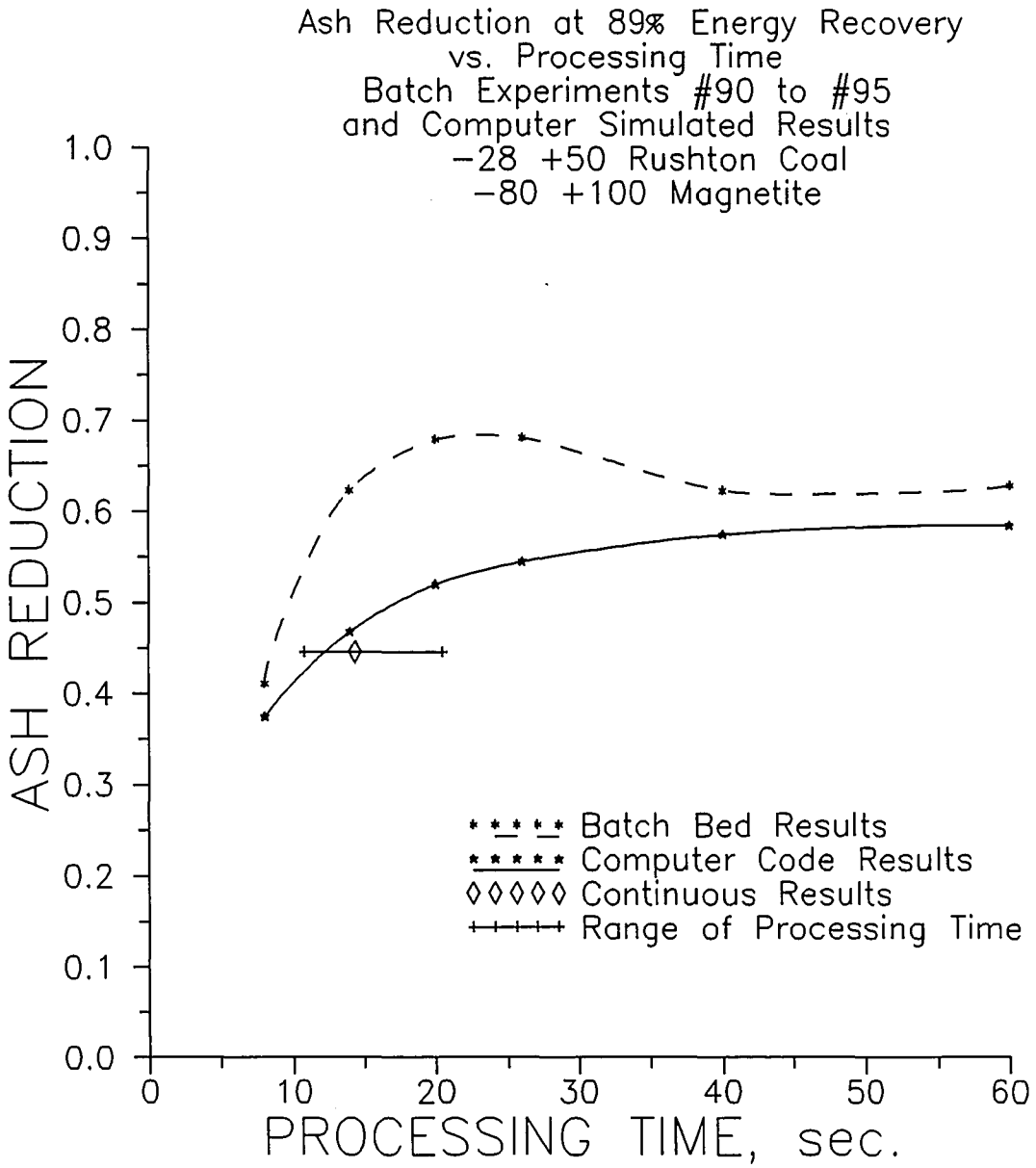

Figure 4.87
-28 +50 Rushton coal cleaning trials
A.R. at 89% BTUR versus processing time
Comparison between continuous and batch operations

Table 4.19
Sulfur reduction and ash reduction at 73% and 89% energy recovery for batch experiments #90 to #95

Batch Experiment	At 73% BTUR		At 89% BTUR	
	S.R.	A.R.	S.R.	A.R.
90	0.606	0.600	0.427	0.411
91	0.704	0.746	0.596	0.623
92	0.736	0.786	0.641	0.679
93	0.736	0.786	0.663	0.681
94	03698	0.738	0.597	0.623
95	03693	0.738	0.593	0.629

based on float times without and with corrections for the velocity gradient, according to the data which follows. The float times are the averages of the last three float times for each energy recovery. The prediction and range also follows:

Float time: 3.53 seconds (73% BTUR)
Float time: 3.41 seconds (89% BTUR)

x_{float} = 50.8 cm
x_{bed} = 188 cm
x_{dz} = 20 cm

73% BTUR experiments:

Lower bound: 10.8 seconds
Best estimate: 14.4 seconds
Upper bound: 20.5 seconds

89% BTUR experiments:

Lower bound: 10.5 seconds
Best estimate: 14.0 seconds
Upper bound: 20.5 seconds

In this case, the upper bound was not based on the average coal velocity determined from the hold-up tests, because the unusually high quantity of coal in the

hold-up test gives an unrealistically large processing time. Instead, the upper bound processing time was based on a velocity from the float tests with -28 +50 Emerald Raw coal. The coal velocity was taken to be the average float velocity at 1.5 cm below the surface; this velocity was 8.15 cm/s. (See float experiments.) This yields a processing time of 20.5 seconds.

Those ranges of processing times shown above in Figures 4.84 to 4.87 indicate relatively poor agreement between the continuous and batch cleaning trials. One possibility for the above disagreement is a difference in composition between the continuous test coal efflux and the composition of the coal in the batch tests. Table 4.20 shows a comparison between total sulfur and total ash content in the continuous test coal output and the coal used in the batch bed tests. The sulfur concentrations are distinctly different, while the ash concentrations agree to within twenty percent. This helps to explain the better agreement between the continuous test and the batch tests for A.R. than for S.R.

The difference in the total sulfur concentrations and total ash concentrations of the coal efflux of the Rushton continuous coal cleaning experiments and the associated batch bed tests can be explained two ways. First, due to random variations caused by material handling procedures, the coal used in the continuous tests could simply have had a different composition than the coal used in the batch bed experiments. Second, the coal flowing in the open channel had dense fractions, which segregated very quickly and defluidized. Once the dense fractions defluidized, they either did not flow or they flowed very slowly along the distributor. The dense fractions would then begin to be stored in

Table 4.20
Total sulfur and ash composition of coal efflux of
Rushton continuous cleaning experiments and Rushton coal
used in the associated batch tests

Continuous Tests:

Test	Total % S	Total % Ash
In-11-19-15	2.19	28.13
In-11-19-16	2.23	30.42
In-11-19-17	2.21	31.26
In-11-19-18	2.07	29.25
In-11-21-19	2.22	27.85
In-11-21-20	2.13	25.93
In-11-21-21	2.20	25.99
In-11-21-22	2.21	26.94
average:	2.18	28.25

Batch Tests:

Test	Total % S	Total % Ash
11-27-91-90	3.64	35.68
11-28-91-91	3.73	37.10
11-28-91-92	3.83	37.33
11-29-91-93	3.82	37.21
11-29-91-94	3.62	36.77
11-30-91-95	3.55	36.39
average:	3.70	36.75

the bed, while the lighter fractions would continue to flow as expected.

Several facts support the possibility of a storage of the dense fractions of coal within the channel. First, the minimum fluidization velocity of the coal is higher than that of the magnetite [2], and the dense fractions have even higher minimum fluidization velocities. The u_{mf} of the densest fractions could even be greater than the 2.75 u_{mfm} used

in the coal cleaning experiments. The excellent cleaning performance in the batch bed in very little processing time shows that the "dirtier" or denser fractions are segregating very quickly. The hold-up test data also indicate that the coal is being stored within the channel, since the coal-to-magnetite mass ratio on the bed was much larger than the mass efflux ratio. Again, this is the opposite of the expected result in which the coal flows on top of the magnetite and is not accumulating in the channel. The increasing bed heights with time are also consistent with an accumulation of coal, especially since the rate of increase is greater closer to the coal inlet. Finally, subsequent to the tests reported here, the experiments were repeated by Salmento and Sahan, but with all the coal being thoroughly mixed prior to experimentation. The results of the repeated experiments showed virtually identical trends in sulfur and ash concentration [24].

5 Conclusions and recommendations

Previous work has shown that physical coal cleaning can be performed in a batch fluidized bed of coal and magnetite with high sulfur and ash removal efficiencies. The further development of the process required the development of a continuous system, which would duplicate the cleaning processes occurring in the batch bed. Using the inclined open-channel fluidized bed described in this study for continuous operations, the denser and dirtier fractions of the coal separated from the lighter and cleaner fractions, producing a product coal with a low sulfur and ash concentrations and a high energy content per mass.

To convert from a batch to a continuous system, many design questions needed to be answered. First, the flow behavior in an inclined open-channel fluidized bed needed to be better understood. Though many theoretical models exist for the flow of aerated solids in an open channel, none provide the information on bed depth and solids flow rate required in this application. Furthermore, no theory exists for describing a binary mixture of solids, such as the coal and magnetite mixture used in coal cleaning. To more fully understand the flow behavior, fluidized magnetite flow was studied as an extension to the work of Latkovic [17]. The results showed that a relatively level bed height profile could be attained at bed heights associated with efficient coal cleaning. In addition, the above flow exhibited no undesirable flow phenomena such as pulsations or

hydraulic jumps. Unfortunately, the flow did have a very low residence time, once the coal was added.

After understanding the characteristics of a flow of pure magnetite, the next step was to find operating conditions which allowed the best fluidizing conditions for coal cleaning with the largest practical processing time. The best operating conditions for achieving a higher residence time involved using a low solids mass feed rate. At these low feed rates, the oscillations in the flow were avoided by inclining the open channel uphill. This resulted in an increase in bed depth beyond the optimal 3 cm value, but it also resulted in an increase in residence time.

At uphill inclinations, the kinetic energy of the flow and the gravity potential energy of the solids above the distributor (i.e., bed height potential energy) are traded for increased gravity potential energy of the solids flow. The decrease in kinetic energy causes an increase in bed height in order to conserve mass flow. The decrease in gravity potential energy of solids above the distributor causes a decrease in the bed height. The major drawback to an uphill inclination at the present operating conditions is the associated decreasing bed height along the length of the channel. If a longer open channel could be used, a higher solids feed rate at a lesser uphill inclination would create a more level bed height profile and a lower, more desirable, bed height. Even though the solids flow velocity would be higher at a lesser uphill inclination and a higher solids mass feed rate, the longer bed would still allow the co-flowing mixture to have an adequate processing time.

Using the best combination of operating conditions available in the present inclined fluidized bed, -50 +80 Upper Freeport coal and -28 +50 Rushton coal were cleaned, and the cleaning performance in the continuous system was compared to the batch bed results at comparable fluidizing conditions. The -50 +80 Upper Freeport coal showed very good agreement, once the asymptotic performance and the effective processing time were determined. The results for the -28 +50 Rushton coal did not agree as well, and this poor agreement is believed to be associated with defluidization of the densest fractions of the coal onto the distributor. At a superficial gas velocity of 2.75 u_{mfm} for the -80 +100 magnetite and the -28 +50 Rushton coal, the dense fractions appear to be segregating very quickly and settling out onto the distributor. Further work is needed to determine if the use of a coarser magnetite and a higher superficial air velocity will solve the problem encountered with the -28 +50 mesh coal.

There are also changes to the equipment which should be considered for improved performance. The most important improvements to the existing system would involve better control of the solids mass flow from the hoppers and the development of a longer open channel. The longer length would increase the transient start-up time of the continuous system, but it would also increase the processing time to the desired 30 seconds.

Research is needed on the nature of the velocity variations in the co-flowing mixture of coal and magnetite. A technique for measuring the longitudinal velocities also needs to be developed.

Finally, it is known that the longitudinal flow has an associated shear stress which suppresses bubble growth. The extent of the suppression and its effect on the bubbling mechanism which drives solids segregation needs to be understood.

Nomenclature

A.R.	Ash Reduction
A_t	Distributor area of fluidized bed
b	Width of open-channel
BTUR	Energy recovery
c	Factor of modified equivalent diameter and flow index
c_f	Correction factor for the difference in float velocity over the entire cleaning length and over the timing section
D	Flow diameter of pipe
D	Divergence
D_B	Average bubble diameter
D_{BM}	Maximum bubble diameter
D_{BO}	Initial bubble diameter
D_e	Equivalent hydraulic diameter
D'_e	Modified equivalent diameter
d_i	Average diameter of size fraction
$\overline{d}_{vsm}$	Weighted volume surface mean diameter
$\overline{d}_{wm}$	Weighted average of average diameter
E_p	Eckhart probability
F	External reaction force

F	Correction factor for mass flow as a function of aspect ratio
F_{dist}	Shear force at distributor
f_f	Fanning friction factor
F_{wall}	Shear force at wall
$F_{\Delta P}$	Force on flow control volume caused by pressure drop
g	Gravitational acceleration
GE_p	Generalized Eckhart probability
H	Overall bed height
h	Bed height coordinate
h_{ave}	Average fluidized bed height
h/b	Aspect ratio
J	Energy in open-channel flow
K	Correction factor to account for different shear stress at the walls and the distributor
K	Constant correction factor for the mass flow as a function of the aspect ratio
k	Consistency factor
k'	Modified consistency factor
K_b	Constant relating u_s to τ_b
K_w	Constant relating u_s to τ_w
k_μ	Characteristic constant of flow in Ishida's energy equation
k_τ	Characteristic constant of flow in Ishida's energy equation

L	Distance of flow between two points
L_{mf}	Height of bed at incipient fluidization
l_s	Length of hold-up test sample
$\dot{m}$	Mass flow rate of solids
m_c	Mass of coal in fluidized bed
$\dot{m}_c$	Mass efflux rate of coal
m_c/m_m	Mass ratio of coal to magnetite
$\dot{m}_c/\dot{m}_m$	Mass efflux rate ratio of coal to magnetite
m_f	Mass of fluid
m_m	Mass of magnetite in fluidized bed
$\dot{m}_m$	Mass efflux rate of magnetite
mm	Number of layers of magnetite in a total of 15 layers
m_p	Mass of particles only
m_s	Mass of sample from hold-up test
$\dot{m}_s$	Mass flow rate of solids
$m_{s,\,coal}$	Mass of coal in hold-up test sample
n	Flow index
n'	Modified flow index
N'_{Re}	Generalized Reynolds number
P	Pressure
Q	Volumetric flow rate of fluidized solids

S.G.S.	Specific gravity of separation
S.R.	Sulfur reduction
t_{proc}	Processing time
$t_{proc,\ coal,\ h.u.}$	Predicted processing time from hold-up test
u	Solids flow velocity
U_m	Bulk flow velocity
u_{mb}	Minimum bubbling velocity
u_{mf}	Minimum fluidization velocity
u_{mfm}	Minimum fluidization velocity of magnetite
u_o	Superficial gas velocity
u_o/u_{mf}	Fluidization velocity ratio
u_o/u_{mfm}	Fluidization velocity ratio of magnetite in coal cleaning fluidized bed
u_s	Solids bulk flow velocity
u_{slip}	Slip velocity of solids at distributor
V	Bulk flow velocity
$\bar{v}$	Bulk flow velocity
V_{ave}	Bulk flow velocity
v_{bed}	Bulk flow velocity of coal and magnetite in inclined fluidized bed
$v_{B.L.}$	Average float velocity over entire bed length
$\bar{v}_{coal}$	Average flow velocity of coal
$\bar{v}_{coal,\ h.u.}$	Average flow velocity of coal predicted form hold-up test

v_f	Volume of fluid
v_{float}	Velocity of surface float
V_{max}	Maximum flow velocity of the solids flow profile
v_p	Volume of particles only
$v_{T.S.}$	Average float velocity over timing section
v_z	Solids flow velocity
W	Weight of particles in fluidized bed
w	Width of channel
W_f	Work forces
WTR	Weight recovery
x_{bed}	Length of cleaning section in inclined fluidized bed
$x_{B.L.}$	Length of entire bed length section of open-channel
x_{dz}	Length of defluidized zone in open-channel
x_{float}	Distance float travels in continuous coal cleaning experiments
x_i	Weight fraction of a size fraction of particles
$x_{T.S.}$	Length of timing section of open-channel
y	Coordinate normal to flow
α	Angle of inclination
α_{ic}	Critical angle of inclination for flow of solids
β	Kinetic energy correction factor
γ	Shear rate

ΔP	Pressure drop
ΔP_b	Pressure drop across bed material only
ϵ	Void fraction
ϵ_{mf}	Void fraction at minimum fluidization
μ	Dynamic viscosity
μ_{app}	Apparent viscosity
ρ	Bulk flow density
ρ_b	Bulk density
ρ_c	Bulk density of coal
ρ_{fl}	Fluidized density of bed material
ρ_m	Bulk density of magnetite
ρ_p	Particle density
ρ_s	Bulk Flow density of solids flow
τ	Shear stress
τ_b	Shear stress at base or distributor
τ_{dist}	Shear stress at base or distributor
τ_w	Shear stress at wall
$\tau_{\Delta p}$	Shear stress associated with overall pressure drop
ϕ	Sphericity

References

1. Astarita, G., Marrucci, G., Palumbo, G., "Non-Newtonian Gravity Flow Along Inclined Plane Surfaces," *Ind. Eng. Fundam.*, **3**, (4), (1964), pp. 333-339

2. Basesme, E., "Mechanical Cleaning of Coal in an Air Fluidized Bed prior to Combustion," Energy Research Center Internal Report, unpublished, Lehigh University, Bethlehem, PA, (1990)

3. Botterill, J.S.M., van der Kolk, M., Elliot, D.E., McGuigan, S., "The Flow of Fluidised Solids," *Powder Tech.*, **6**, (1972), pp. 343-351

4. Botterill, J.S.M., and van der Kolk, M., "The Flow Properties of Fluidized Solids," *Chem. Eng. Progr. Sym Series*, **67**, (27), (1971), pp.70-76

5. Botterill, J.S.M., and Bessant, D.J., "The Flow Properties of Fluidized Solids," *Powder Tech.*, **8**, (1973), pp. 213-222

6. Botterill, J.S.M., Bessant, D.J., "The Flow Properties of Fluidized Solids," *Powder Tech.*, **14**, (1976), pp. 131-137

7. Botterill, J.S.M., Bessant, D.J., "The Flow Properties of Fluidized Solids," in *Proc. 'Pneumotransport 3' 3rd International Conference on the Pneumatic Transport of Solids in Pipes*, by BHRA Fluid Engineering, April 1976, Paper E3

8. Botterill, J.S.M., and Abdul-Halim, B.H., "The Open-Channel Flow of Fluidized Solids," *Powder Tech.*, **23**, (1979), pp. 67-78

9. Chandelle, V., "The Transportation of Granular Products in Airslides and Air-lifts," *Annales des Mines de Beligique*, **2**, (1971), pp. 191-208 [In French]

10. Descamps, P., and Jodlowski, C., "Principles of Pneumatic Transport and Fluidisation," *Air Industriel* (France), **11**, (1973), pp. 23-27 [In French]

11. Geldart D., "Types of Gas Fluidization," *Powder Tech.*, **7**, (1973), pp. 285-292

12. Ishida, M., and Shirai, T., "Velocity Distributions in the Flow of Solid Particles in an Inclined Open Channel," *J. Chem. Engr. Japan*, **12**, (1), (1979), pp. 46-50

13. Ishida, M., Hatano, H., Shirai, T., "The Flow of Solid Particles in an Aerated Inclined Channel," *Powder Tech.*, **27**, (1980), pp. 7-12

14. Ishida, M., and Hatano, H., "The Flow of Solid Particles in an Aerated Inclined Channel," *Advances in the Mechanics and the flow of Granular Materials*, **vol. II**, ed. by Shahinpoor, M., Transtech Publications, Clausthal-Zellerfeld, B.R.D., (1983), pp 565-575

15. Kozanoglu, B., "Transient Mixing of Solids in a Bubbling Fluidized Bed," PhD. Dissertation, Lehigh University, Bethlehem, PA, (1990)

16. Kuni, D., and Levenspiel, O., *Fluidization Engineering, 2nd ed.*, Butterworths, Boston, (1991)

17. Latkovic, D., "The Flow Characteristics of a Fluidized Bed in an Open Channel," M.S. Thesis, Lehigh Unversity, Bethlehem, PA, (1990)

18. McGuigan, S.J., and Pugh, R.R., "The Flow of Fluidized Solids in an Open Channel," in *Proc. 'Pneumotransport 3', 3rd International Conference on the Transport of Solids in Pipes*, by BHRA Fluid Engineering, Cranfield, April 1976, Paper E2

19. Metzner, A.B., Reed, J.C., "Flow of Non-Newtonian Fluids - Correlation of the Laminar, Transistion, and Turbulent Flow Regions," *AIChE Journal*, **1**, (4), (1955), pp. 434-440

20. Mooney, M., "Explicit Formulas for Slip and Fluidity," *Journal of Rheology*, **2**, (2), (1931), pp. 210-222

21. Mori, Y., Aoki, R., Oya, K., Ishikawa, H., "Transportation of Solid Material by an Air Slide Conveyor," *Kagaku Kogaku* (Japan), **19**, (1955), pp. 16-22, [In Japanese]

22. Bird, R.B., Stewart, W.E., Lightfoot, E.N., *Transport Phenomena*, John Wiley and Sons, Inc., New York, (1960)

23. Sahan, R., "Effects of Coal Properties and Process Variables on Cleaning Efficiency in a Fluidized Bed Separator," M.S. Thesis, Lehigh University, Bethlehem, PA, (1992)

24. Salmento, J., and Sahan, R., unpublished results, Lehigh University, Bethlehem, PA, (1992)

25. Siemes, W., "Conveying Granular Material in an Inclined Fluidized Bed," *Chemie-Ing. Tech.*, **31**, (3), (1959), pp. 212-213 [In German]

26. Siemes, W., and Hellmer, L., "Measurement of Fluidized Bed Viscosity in a Pneumatic Duct," *Chem. Eng. Sci.*, **17**, (1962), pp. 555-571 [In German]

27. Singh, B., Calcott, T.G., Rigby, G.R., "Flow of Fluidized Solids and Other Fluids in Open Channels," *Powder Tech*, **20**, (1978), pp. 99-113

28. Ulge, E.T., "Effect of Process Parameters on Segregation in a Fluidized Bed of Coal and Magnetite," M.S. Thesis, Lehigh University, Bethlehem, PA, (1991)

29. Wheeler, J.A., and Wissler, E.H., "The Friction Factor - Reynolds number Relation for the Steady Flow of Pseudoplastic Fluids through Rectangular Ducts," *AIChE Journal*, **11**, (2), (1965), pp. 207-216

30. Woodcock, C.R., and Mason, J.S., "Fluidised Bed Conveying - Art or Science?" in *Proc. 'Pneumotransport 3', 3rd International Conference on the Pneumatic Transport of Solids in Pipes*, by BHRA Fluid Engineering, Cranfield, April 1976, Paper E1

31. Woodcock, C.R., and Mason, J.S., "The Flow Characteristics of a Fluidised P.V.C. Powder in an Inclined Channel," in *Proc. Powder and Bulk Solids Handling and Processing*, Chicago, May 1977, pp. 466-475

32. Woodcock, C.R., and Mason, J.S., "The Modeling of Air-Assisted Bulk Particulate Solids Flow in Inclined Channels," in *Proc. 'Pneumotransport 4', 4th International Conference on the Pneumatic Transport of Solids in Pipes*, by BHRA Fluid Engineering, Cranfield, June 1978, Paper D2

Vita

Timothy J. Schmitt was born on August 3, 1968 in Lancaster, Pennsylvania, to Gervase A. and Catherine E. Schmitt.

On June 2, 1990, he received the Degree of Bachelor's of Science in Mechanical Engineering from Lehigh University.

Beginning June 4, 1990, he continued his education as a graduate student at Lehigh University and worked as a Research Assistant in the Energy Research Center at Lehigh University. On May 31, 1992, he received the degree of Master's of Science in Mechanical Engineering from Lehigh University.

END

OF

TITLE